IMPERIAL COLLEGE LONDON

Deciphering the Influence of Local Chain Order on Thermal Transport in Macromolecular Matter

Faisal Abdulaziz I Almana

Submitted for the degree of Doctor of Philosophy

Faculty of Engineering

Department of Materials

Declaration of Originality

I, Faisal Abdulaziz I Almana, declare that this thesis, "Deciphering the Influence of Local Chain Order on Thermal Transport in Macromolecular Matter" under the supervision of Professor Natalie Stingelin, Professor Martyn McLachlan, and Doctor Ajay Taraiya, and the work presented in it are my own. I confirm that:

- This work was done while in candidature for a research degree at this University.
- Where I have consulted the published work of others, this is always clearly attributed.
- Where I have quoted from the work of others, the source is always given. With the exception of such quotations, this thesis is entirely my own work.
- Where the thesis is based on work done by myself jointly with others, I have made clear exactly what was done by others and what I have contributed myself.

Copyright Declaration

The copyright of this thesis rests with the author. Unless otherwise indicated, its contents are licensed under a Creative Commons Attribution-Non Commercial-No Derivatives 4.0 International Licence (CC BY-NC-ND). Under this licence, you may copy and redistribute the material in any medium or format on the condition that; you credit the author, do not use it for commercial purposes and do not distribute modified versions of the work. When reusing or sharing this work, ensure you make the licence terms clear to others by naming the licence and linking to the licence text. Please seek permission from the copyright holder for uses of this work that are not included in this licence or permitted under UK Copyright Law.

Signed: Faisal Abdulaziz I Almana

Date: December 22nd , 2021

Abstract

The attractiveness of polymers generally stems from their lightweight, low cost, and offer freedom-of-design using large-scale manufacturing techniques. Their corrosion resistance, low dielectric constants among other attributes are appealing properties for specific applications such as heat exchangers for corrosive environments and heat sinks in compact electronic devices. However, polymers are considered thermal insulators, therefore these applications have been, primarily restricted to metals and their alloys. Nonetheless, our fundamental understanding of thermal transport in polymeric systems needs to be drastically improved to gain the capability to design systems for thermal applications from the outset. The abundance of variety of polymers systems renders this task highly challenging. Here, we use polymers with model functional groups such as poly(vinyl alcohol) (PVAL) to discuss the various effects of solid-state structure on overall thermal transport. Blending with an oligomer was shown to influence the local chain order via hydrogen bonding, and in turn, influencing the thermal conductivity. It was revealed that at low concentrations (5-15 wt.% of the oligomer), a localised extension of the PVAL backbone bonds occurred. However, with higher oligomer concentrations, the main change observed was a plasticising effect.

Organic/inorganic hybrid systems were studied next. They are an attractive new field of research as they offer tunability of a range of properties, yet the effects on thermal conductivity were yet to be investigated. The hybrid system based on PVAL / titanium oxide hydrate was revealed to have favourable thermal transport network despite having a lesser ordered molecular structure. This system was compared to a conventional PVAL – TiO_2 composite to draw contrasts with the formed structures.

Finally, a novel preparation of PVAL with Aramid nanofibers (ANF) films was studied and the effect on thermal conductivity was explored. A more intimate interaction between the ANF and PVAL chains compared to methods reported in literature was revealed using various vibrational and electron spectroscopy techniques. The effects on the thermal conductivity were more significant compared to the hybrid and blend systems. Overall similarities can be drawn between the three multicomponent systems, which allows us to establish design rules and broadly applicable structure-thermal conductivity relationships. Ultimately, we provided a general understanding on a broad range of systems that can be used to tune the thermal conductivity of macromolecules to the final required properties.

Acknowledgments

I would like to take this opportunity to express my deepest gratitude and appreciation to the people who have made my journey through this PhD enlightening, enjoyable, and stimulating. I would firstly like to thank my supervisors Natalie, Martyn and Ajay for the opportunity of working with them. Special appreciation goes to Natalie for her mentorship, kindness, generosity, and guidance throughout my years at Imperial. Her support to me was felt no matter where she was in the world and could always count on her through any issues that I have faced, both personal and academically. The many memories we have shared throughout the world are unforgettable especially the conferences and karaoke nights. She has genuinely made me a better scientist and more importantly, a better person. Thanks goes to Martyn who has been my supervisor at Imperial with Natalie away and for the use of his lab. I shall appreciate the countless moments of discussions and banter despite his questionable football allegiance. Finally, I would like to thank Ajay who was my mentor from SABIC. Our monthly calls was a sanity check and I have enjoyed our discussions greatly. I cannot wait to work further with him.

I would like to thank my collaborators Ahmad, Alex, Daron, Matthew, and Radek for their help in measuring the various samples I made in this thesis. I would also like to thank Weidong Tang and Dr. Oliver Fenwick for the initial thermal conductivity measurements. I would also like to thank Dr. Fin Giuliani & Prof. Milo Shaffer for allowing me access to their Raman microscope and Prof. Theo Tervoort for supplying the PPTA fibres for my experiments. Further thanks to Prof. Sophia Charalambous-Heyes for discussions on Raman spectroscopy and assistance in peak fitting. I would also like to thank Dr. Sarfraz Abbasi for various inputs and discussions throughout my PhD.

I would like to thank all my friends and colleagues at Imperial and GaTech who have made this PhD so much more stimulating and enjoyable. A huge thank you goes to: Ahmad, Jaspreet, Lucky, Riley, Huda, Becky, Stefan, David, Shengyang, Jon, Kevin, Sebastian, Bob, Julianna, Dimitra, Irene, Luca, Gianmaria, Claire, Ibrahim, Lin, Tian, Angel, Joel, Luke, Sam, Matayas, Francesco S, Notina, Charlotte, Martina, Bowen, Mat, Flo, Pete, Filip, William, Caoimhe, Aigerim, Kris, Alexandra, Minos, Dafni, Ashley, Jack, Benji, Martin, Ivy, Yuchen, and Francesco F. To all the GaTech group Aditi, Alex, Amalie, Aziz, Mark, Marlow, Connor, Tanner, Hongmo, Linda, Victoria, Seongmin, Francesco, Daron, Miguel, and Praetip. I wold also like to thank all the support staff, technicians and administrators in both RSM and MSRH.

I would also like to remember and thank Christina Kong for all the wonderful memories and her friendship. She will never be forgotten.

Finally, to all my family and friends outside of Imperial who have made London my second home: my parents and siblings, Ashi, Mugi, Nouf, Khaled, Abdullah, Abdulrahman, Abdulrahman, Ibrahim, D.K., Hayden, Anna, Star, and Jane

Special thanks goes to Ahmad, as he has been my colleague, my friend, and family during these past years in London. To all the never-ending memories we have made from nights out, to football games and concerts to just staying at home and chatting. I could not have made it through without your support.

Finally, this work could not be possible without the sponsorship and scholarship of SABIC and giving me this opportunity to pursue my PhD degree. I would like to thank my managers who have mentored me and supported me throughout my career at SABIC. Abdullah Al-Otaibi, Waleed Al-Lafi, Ziad Abanmi, Mark Vlaar, and Abdulrahman Al-Awwad.

Faisal Almana, 22nd December 2021

Contents

Abstract 3
Acknowledgments 4
Abbreviations: 17
1 Thermal Transport in Materials 19
1.1 Thermal conductivity in materials 19
1.2 Thermal conductivity in polymers 20
1.2.1 Single molecule chains 21
1.2.2 Monomer type (backbone) 21
1.2.3 Molecular weight 23
1.2.4 Inter-chain interactions 24
1.2.5 Morphology (semi-crystalline vs amorphous) 27
1.3 Increasing TC by polymer chain orientation 28
1.3.1 Fibres 29
1.3.2 Stretched films 30
1.4 Increasing TC by highly conductive fillers 30
1.4.1 Ceramics 31
1.4.2 Carbon-based fillers 32
1.4.3 Metals 33
1.4.4 Particle shape and size 33
1.4.5 Interfaces 34
1.4.6 Processing and anisotropy 35
1.5 Summary 36
1.6 Scope of the thesis 37
1.7 References 38
2 Materials and characterisation techniques 41
2.1 Materials and solutions 41
2.1.1 PVAL solutions in water 41
2.1.2 PVAL solutions in DMSO 41
2.1.3 Tetraethylene glycol (TEG) solutions 41
2.1.4 TiO_2 suspensions 42
2.1.5 Titanium oxide hydrates 42
2.1.6 PVAL / titanium oxide hydrate hybrids 43
2.1.7 Preparation of aramid nanofiber dispersions (ANF) 44
2.1.8 Preparation of PVAL/ANF solutions 45
2.2 Film deposition methods 46
2.2.1 Substrates 46

2.2.2 Spin coating 46
2.2.3 Drop casting 47
2.3 Solid – State Spectroscopy characterisation 48
2.3.1 Raman spectroscopy 48
2.3.2 Fourier transform infrared spectroscopy (FTIR) 52
2.3.3 Brillouin light scattering (BLS) spectroscopy 54
2.3.4 X-ray photoelectron spectroscopy (XPS) 55
2.4 Differential Scanning Calorimetry (DSC) 56
2.4.1 DSC Sample preparation 56
2.5 Scanning Electron Microscopy 56
2.6 Thermal conductivity: 3 – ω Technique 57
2.6.1 Sample preparation for 3 – ω 58
2.7 List of collaborators and contributors 60
2.8 References 61
3 Polymer/Oligomer Blends 63
3.1 Motivation 63
3.2 Solid-State Structure 64
3.2.1 Raman Spectroscopy 64
3.2.2 Fourier-Transform Infra-Red (FTIR) Spectroscopy 69
3.3 Differential Scanning Calorimetry (DSC) 73
3.4 Brillouin Light Scattering Spectroscopy (BLS) 76
3.5 Thermal conductivity (3-ω) 77
3.6 Conclusions 79
3.7 References 80
4 Organic / Inorganic Hybrids 82
4.1 Motivation 82
4.2 Solid-State Structure 83
4.2.1 Raman Spectroscopy 83
4.2.2 Fourier-Transform Infra-Red (FTIR) Spectroscopy 95
4.3 Differential Scanning Calorimetry (DSC) 98
4.4 X-ray photoluminescence spectroscopy (XPS) 101
4.5 SEM 105
4.6 Thermal conductivity (3-ω) 108
4.7 Conclusions 110
4.8 References 111
5 Polymer / polymer nanofiber system 114
5.1 Motivation 114

5.2 Solid-State Structure 115
5.2.1 Raman Spectroscopy 115
5.2.2 Fourier-Transform Infra-Red (FTIR) Spectroscopy 119
5.3 Differential Scanning Calorimetry (DSC) 122
5.4 X-ray photoluminescence spectroscopy (XPS) 125
5.5 SEM 127
5.6 Thermal conductivity (3-ω) 130
5.7 Conclusions 133
5.8 References 134
6 Summary and outlook 137
6.1 Summary 137
6.2 Outlook and future work 139
Appendix A 142
Appendix B 148
Appendix C 150
Appendix D 163
Appendix E 164
Talks, Posters, and Prizes 167
Talks 167
Posters 167
Prizes 167

List of Figures

Figure 1: Effect of monomers on thermal conductivity. (a) Presents the effect of an aromatic ring in the backbone. (b) Illustrates the effect of double bonds in the chain. (c) Shows the effect of oxygen in the backbone. (d) Presents the dependence on chain length rather than number of monomers. Reprinted from [18]. Copyright (2012) by the American Physical Society. 22
Figure 2: Thermal conductance of 100% cross-linked polymers. Thermal conductance simulation measurements based on different cross-linking agents on two PMMA polymer chains. The mass of the carbon atoms in the benzenes were either kept normal ("benzene"), doubled ("heavy benzene"), or halved ("light benzene"). The simulations were conducted with the three different variations of the chemical bonding. The squares represent all bonding (covalent) and nonbonding (VdW & columbic) types. The circles represent the nonbonding interactions of the cross linker being removed. With the triangles, all nonbonding interactions in the system have been removed (cross-linker and polymer chain). The results show that the shorter carbene cross-linker had the most positive effect on the thermal conductance. Adapted with permission from [29]. Copyright 2017 American Chemical Society. 25
Figure 3: Thermal conductance of 100% cross-linked polymers presenting how the inter-chain distance affects thermal transport. The graph is from the same study presented in Figure 2. Here, all bond interactions were included. It can be observed that the shorter the inter-chain distance due to the crosslinking species, the higher the calculated thermal conductance. Adapted with permission from [29]. Copyright 2017 American Chemical Society. 25
Figure 4: Thermal conductivities of amorphous polymer blends from Kim et al's. study [32]. Blending PAP with a strong hydrogen bond donor PAA gave the highest improvement (left panel). With PVAL, the improvement was more modest but still doubling the initial thermal conductivity (middle panel). With a large benzene ring between the hydroxyl group and the backbone, the PAA:PVPh blend showed a decrease in the measured TC (right panel). Reprinted by permission from Springer Nature: Nature Materials, High thermal conductivity in amorphous polymer blends by engineered inter-chain interactions, Gun-Ho Kim et al.[32] , Copyright 2014 Springer Nature. 26
Figure 5: Thermal conductivity of commercial amorphous and semi-crystalline polymers at room temperatures. Graph plotted using values derived from [31]. 28
Figure 6: Modelling calculations representing ratio of filler/matrix TC on composite TC. K_c is the TC of the composite, K_m is the TC of the matrix and K_f is the TC of the filler. From the graph, it is seen that that only at high volume fraction loadings that the composite start to benefit from the high thermal conductivity of the filler. Graph obtained with permission from [50] © 2011 IEEE. 31
Figure 7: $TiCl_4$ hydrolysis set up. A round bottom flask with the required amount of DIW is placed in an ice bath on top of a magnetic stirring stage. The $TiCl_4$ is measured with syringes and added to the column above. The valve at the neck is then slowly opened to allow a steady, 1 drop/sec flow to be introduced to the water in the flask. 43
Figure 8: PVAL / titanium oxide hydrate hybrid structure. On the left, a polynuclear titanium oxide hydrate connects to separate PVAL chains. In the middle, a mononuclear PVAL / titanium oxide hydrate network is illustrated. Covalent bonds are created between the titanium atoms and the PVAL as well as hydrogen bonds with the remaining hydroxyl groups. Some residual chlorine is present as well. The segments on the right depict unreacted PVAL chain with residual acetate. 44
Figure 9: PPTA para-aramid structure. The para structure relates to the amide groups being linked to the aromatic rings at the 1 and 4 positions. Hydrogen bonding occurs between the amine and carbonyl groups highlighted in red. I Reproduced from [9] with permission from the Royal Society of Chemistry. 45
Figure 10: Diagrams showing the stages of the spin coating technique. The solution is first placed on the substrate that is held by a rotating platform (a). The platform and the substrate are then spun at high speeds and at specified times to spread the solution. Most of the ink is ejected from the substrate in this stage (b). The solvent is then evaporated and a solid, dry, thin film is left on the substrate (c). 47

Figure 11: Diagram showing the stages of drop casting. The solution is first dropped on a clean substrate or crucible (a). Then the solvent slowly evaporates and a film starts to form (b). After all the solvent has been evaporated, a film is created on the substrate (c).....47
Figure 12: Schematic describing the different scattering events an incident photon can have when interacting with a molecule. Anti-stokes scattering on the left shows an increase of the photon's energy after interaction. In Rayleigh scattering, which is the most dominant type, the photon energy is constant and elastic scattering is observed. In Raman scattering, the incident photon loses energy and the scattered photon is observed to have less energy.....49
Figure 13: Raman spectra of silicon wafer and PVAL film deposited on silicon wafer. The signal from the silicon bands (900-1050 cm^{-1}) overshadow the PVAL band signals. 49
Figure 14: Raman spectra of 10% TEG film obtained from onto of the gold electrode on a 3-ω chip. The signal showed the distinct peaks of PVAL. 50
Figure 15: Energy state difference between Raman spectroscopy based on scattering and FTIR spectroscopy based on absorbance.....52
Figure 16: ATR-FTIR set-up depicting where the signal is generated and detected. The light source is positioned to obtain an evanescent wave within the sample. The penetration depth is 0.5 μm to 2 μm. 53
Figure 17: Side view (a) and top view (b) of a sample for 3-ω measurement. (a) Shows the substrate that is considered infinitely thick in comparison to the polymer film. The gold electrodes and heater lines are then evaporated on top. (b) Shows the electrodes and heater lines. The dimensions of the heater lines are crucial to the measurement as it is linked to the resistance and the voltage signal. Any fluctuation results in fluctuation in the measured signal.....59
Figure 18: A film with gold electrodes and heater lines deposited for 3-ω measurement. Four electrodes are used; two for the input current and two to measure the voltage difference. 59
Figure 19: PVAL (a) and TEG (b) chemical structure.....63
Figure 20: Theorised structure change based on introduction of TEG molecules in PVAL matrix 64
Figure 21: Raman spectra of a PVAL film. The spectra is divided into the main regions where characteristic vibrations were observed. The main contributor(s) to each band is highlighted above and can be observed with further detail in Table 1.....66
Figure 22: Raman spectra of PVAL - TEG blends. The key changes occur below 1500 cm^{-1}. The bands were split into three main regions of interest based on the C-C stretching (760-950 cm^{-1}), C-O stretching and O-H bending (1000 – 1200 cm^{-1}), and C-H and O-H bending (1250 – 1500 cm^{-1}). 66
Figure 23: Raman spectra of PVAL - TEG blends in the C-C stretching region. (a) The peaks are shifted to lower wavenumbers with increasing TEG content. The peak position shift of two of the peaks to show the trend is presented in (b). Error bars based on resolution of the apparatus. Further errors due to peak fitting are not represented in the graph. The dashed line is used to highlight the shift to lower wave numbers.....68
Figure 24: Raman spectra of PVAL - TEG blends in the C-O stretching and O-H bending region. (a). The intensity of peak 1126 cm^{-1} (linked to disordered segments) relative to peak 1143 cm^{-1} (linked to ordered segments) is the main change and illustrated in (b). The intensity of the 1126 cm^{-1} peak grows significantly compared to the peak at 1143 cm^{-1} in the 5 and 10 wt.% TEG samples before decaying exponentially. The dashed lines were drawn using an exponential decay function as a guide for the eye. 68
Figure 25: Raman spectra of PVAL - TEG samples in the C-H and O-H bending region (a). The peak at 1359 cm^{-1} was shifted to lower numbers with increasing TEG content. While the position of the peak at 1441 cm^{-1} was shifted, it was not comparably a large shift. However, the intensity ratio between the two peaks grows with increasing TEG. The amount of shift is illustrated in (b). Error bars based on resolution of the apparatus. Further errors due to peak fitting are not represented in the graph. The dashed lines were used as a guide for the eye by fitting the data with polynomial curves.....69

Figure 26: FTIR spectra of PVAL. The spectra is divided to the main regions where characteristic vibrations were observed. The main contributor(s) to each peak is indicated above and can be observed in further detail in Table 2. 70
Figure 27: FTIR of PVAL – TEG blends of different compositions. The changes observed are primarily with the pendant hydroxyl (3276cm^{-1}) and carbonyl from the residual acetate (1733 cm^{-1}). The other changes are in the C-O stretching around 1123 cm^{-1}. 70
Figure 28: FTIR spectra of the O-H peak shift between PVAL – TEG samples. Dotted line placed as reference at the PVAL peak centre. 72
Figure 29: FTIR O-H peak position based on TEG content. Error bars based on resolution of the instrument. Further errors due to peak fitting are not represented in the graph. The dashed line drawn as a guide to the eye with the data point from the 5 wt.% TEG film masked out as an outlier..... 72
Figure 30: FTIR spectra of C=O stretching peak between PVAL – TEG samples. The intensity of absorption seems to increase up to 15wt.% TEG then decrease. 72
Figure 31: DSC thermograms of PVAL – TEG blends for the first heating (a) and cooling cycles (b). 74
Figure 32: DSC thermograms of PVAL –TEG blends for the second heating (a) and cooling cycles (b). 74
Figure 33: Enthalpy of fusion of PVAL - TEG films with various TEG content. ΔH_{PVAL} measured from the first heating. Error bars based on systematic error of the DSC of a single measurement. 75
Figure 34: Calculated sound velocities of PVAL – TEG blends based on measured Brillouin shifts. The dashed line was added as a guide to the eye. 77
Figure 35: Thermal conductivity of PVAL – TEG blends at room temperature. Measured using 3-ω technique. Error bars based on three film samples measured at each loading. The dashed line was added as guide to the eye. 78
Figure 36: PVAL / titanium oxide hydrate hybrid structure. On the left, a mononuclear hybrid is shown which forms at low titanium oxide hydrate content. The schematic on the right shows a polynuclear PVAL / titanium oxide hydrate network that is observed at higher inorganic loadings. Covalent bonds are created between the titanium atoms and the PVAL as well as hydrogen bonds with the remaining hydroxyl groups. Some residual chlorine is present as well. 82
Figure 37: PVA-TiO_2 nanocomposite structure. TiO_2 particles infiltrate free volume in PVAL and interact with hydrogen bonds with the polymer's hydroxyl groups. Structure adapted from [10]. Copyright (2018) John Wiley and Sons. 83
Figure 38: Raman spectrum of PVAL. The spectra is divided into the main regions where characteristic vibrations were observed. The main contributor(s) to each band is highlighted above and further details are given in Table 2. 84
Figure 39: Raman spectrum of PVAL between 100 and 700 cm-1. The spectra is divided into the main regions where characteristic vibrations were observed. The main contributor(s) to each band is highlighted above and further discussed in Table 2. 85
Figure 40: Raman spectra of PVAL / titanium oxide hydrate hybrid films between 700 and 3200 cm^{-1}. The key changes occur below 1500 cm^{-1}. The bands were split into three main regions of interest based on the C-C stretching (760-950 cm^{-1}), C-O stretching and O-H bending (1000 – 1200 cm^{-1}), and C-H and O-H bending (1250 – 1500 cm^{-1}).The C-H peak around 2909 cm^{-1} appears to reduce in intensity with increasing inorganic loading. 85
Figure 41: Raman spectra of PVAL - TiO_2 composites between 700 and 3200 cm^{-1} at spots taken where no particles were visible under the microscope lens. The notation of the letter "M" next to each sample is in reference to "matrix". This notation will be used in all the following graphs. See Appendix C for microscope image. 86
Figure 42: Raman spectra of PVAL – TiO_2 composites between 700 and 3200 cm^{-1} at spots taken from where a particle was visible under the microscope lens. The notation of the letter "P" next to each sample is in reference to "particle". This notation will be used in all the following graphs. 86

Figure 43: Raman spectra of PVAL / titanium oxide hydrate hybrids in the C-C stretching region (a). The 853 cm^{-1} peak was shifted to lower wavenumbers with increasing inorganic content but the 936 cm^{-1} peak was shifted to higher Raman shifts (b). Error bars based on resolution of the apparatus. Further errors due to peak fitting are not represented in the graph. The dashed line is used to highlight the positive and negative shifts. 90
Figure 44: Raman Spectra of PVAL – TiO_2 composite films in the C-C stretching region. (a) Spectra taken in areas where no particles were observed and (b) in areas with visible particles. 90
Figure 45: Raman spectra of PVAL / titanium oxide hydrate hybrids in the C-O stretching and O-H bending region (a). The relatively large shift of the 1143 cm^{-1} peak is illustrated in (b). Error bars based on resolution of the apparatus. Further errors due to peak fitting are not represented in the graph. The dashed line is used to highlight the negative shift..... 91
Figure 46: Raman Spectra of PVAL – TiO_2 composite films in the C-O stretching and O-H bending region. (a) Regions where the matrix was dominant and (b) regions with visible particles. 91
Figure 47: Raman spectra of PVAL / titanium oxide hydrate hybrids in the C-H bending and O-H bending region (a). The peaks appear to be shifted to lower wavenumbers with the 1441 cm^{1} showing a larger shift (b). Above 50 vol.% Ti, the two peaks merge into one broad peak. Error bars based on resolution of the apparatus. Further errors due to peak fitting are not represented in the graph. The dashed line is used to highlight the negative shift..... 92
Figure 48: Raman Spectra of PVAL – TiO_2 composite films in the C-H bending and O-H bending region. (a) regions dominated by the matrix and (b) Regions where particles were observed. 92
Figure 49: Raman spectra of PVAL / titanium oxide hydrate hybrid films between 220 and 700 cm^{-1}. 94
Figure 50: Raman spectra of PVAL – TiO_2 composite films between 220 and 700 cm^{-1} taken where predominantly the matrix was observed. 94
Figure 51: Raman spectra of PVAL – TiO_2 composite films between 220 and 700 cm^{-1} in regions where the particles were observed. 94
Figure 52: FTIR spectra of PVAL. The spectra is divided into the main regions where characteristic vibrations are observed. The main contributor(s) to each peak are indicated. 95
Figure 53: FTIR spectra of PVAL / titanium oxide hydrate hybrid films. 96
Figure 54: FTIR spectra of PVAL - TiO_2 composite films. 96
Figure 55: PVAL / titanium oxide hydrate hybrid structure with a residual acetate group. 97
Figure 56: DSC thermograms of PVAL / titanium oxide hydrate hybrids showing the first heating (a) and cooling cycles (b). 99
Figure 57: DSC thermograms of PVAL – TiO_2 composites showing the first heating (a) and cooling cycles (b). 99
Figure 58: DSC thermograms of PVAL / titanium oxide hydrate hybrids showing the second heating (a) and cooling cycles (b). 100
Figure 59: DSC thermograms of PVAL – TiO_2 composites showing the second heating (a) and cooling cycles (b). 100
Figure 60: XPS spectra of PVAL / titanium oxide hydrate hybrid films focusing on the C1s region (a). A comparison of the carbon peak intensity is presented in (b) as a function of inorganic content. 102
Figure 61: XPS spectra of PVAL – TiO_2 composite films focusing on the C1s region (a). A comparison of the carbon peak intensity is presented in (b) as a function of inorganic content. 103
Figure 62: XPS spectra of PVAL / titanium oxide hydrate hybrid films focusing on the O1s region. 103
Figure 63: XPS spectra of PVAL – TiO_2 composite films focusing on the O1s region. 103
Figure 64: XPS spectra of PVAL / titanium oxide hydrate hybrid films focusing on the Ti2p region. 104
Figure 65: XPS spectra of PVAL – TiO2 composite films focusing on the Ti2p region. 104
Figure 66: SEM images of hybrid films 10 vol.% (a), 30 vol.% (b), and 50 vol.% titanium oxide hydrate (c) at 5K x magnification. 106

Figure 67: SEM images of nanocomposites of 10 wt.% (a), 30 wt.% (b), and 50 wt.% TiO_2 in PVAL (c) at 5K x magnification. 107
Figure 68: Thermal conductivity measurements for PVAL/titanium oxide hydrate hybrids and PVAL – TiO_2 composite films of varying inorganic content using the 3-ω technique. Error bars are based on measurements of three films for hybrids and two films for composites. Solid line based on rule of mixtures using 0.9 W/m.K as the value for the titanium oxide hydrate. Dashed line represents the relative unchanging TC of the PVAL/TiO_2 composite films with increasing inorganic content.# 109
Figure 69: Chemical structure of PPTA. Amide groups are situated between the aromatic rings in the backbone. The hydrogen inter-chain bonding is illustrated with dashed lines. Reproduced from [5] with permission from the Royal Society of Chemistry. 115
Figure 70: Raman spectra of PVAL and ANF between 600 and 1700 cm^{-1}. Observed peaks assigned to main contributor(s). Further details on peak assignments are described in Table 10 and Table 11. .. 116
Figure 71: Optical micrograph of a 2.5 wt.% ANF sample in PVAL. Film formation at this ANF loading was poor and separated islands seemed to form on the substrate. 117
Figure 72: Raman spectra of PVAL / ANF films between 600 cm^{-1} and 1700 cm^{-1}. The signal of the ANF appears to overshadow the PVAL signal at all composite compositions. 117
Figure 73: Raman spectra of PVAL / ANF films between 600 cm^{-1} and 1150 cm^{-1}. 117
Figure 74: FTIR spectra of neat ANF and PVAL. Contributors to each peak are indicated below the peaks. For detailed peak positions, see Table 12 and Table 13. 120
Figure 75: FTIR spectra of PVAL / ANF films of different composite compositions. 120
Figure 76: DSC thermograms of PVAL / ANF films of the first heating (a) and the first cooling (b) cycles. 123
Figure 77: DSC first heating thermograms of PVAL films with 88% and 99% degrees of hydrolysis. 124
Figure 78: DSC/TGA of 99% hydrolysed PVAL film drop cast from DMSO (a). DSC themrogram shown in black and TGA curve shown in red. First derivative of TGA curve (b). 124
Figure 79: XPS spectra of PVAL / ANF films in the C1s region. 126
Figure 80: XPS spectra of PVAL / ANF films in the O1s region. 126
Figure 81: XPS spectra of PVAL / ANF films in the N1s region. 126
Figure 82: SEM images of 2.5 wt.% ANF/PVAL (a), 5 wt.% ANF/PVAL (b), and 10 wt.% ANF/PVAL (c). 128
Figure 83: SEM images of 15 wt.% ANF/PVAL (a), 50 wt.% ANF/PVAL (b), and neat ANF film (c). 129
Figure 84: Thermal conductivity of PVAL / ANF films based plotted as a function of ANF concentration using the 3-ω technique. The 2.5 wt.% ANF/PVAL film and neat ANF film values are missing, as measurements could not be performed due to poor film quality. Error bars based on measurements of two films. Dashed line added as a guide by fitting a linear function. 5 wt.% ANF/PVAL film was masked in linear fit. 132
Figure 85: PVA / ANF thermal conductivity compared to Lewis - Nielsen model for composite using a 3.1 W/m.K value (black dashed line) and 0.04 W/m.K (red dashed line) as upper and lower limits, respectively. 132
Figure 86: Raman spectra of neat TEG and neat PVAL between 750 and 1850 cm^{-1}. TEG is liquid at room temperature and a droplet was used to capture spectra. PVAL film cast from 6 wt.% solution. 142
Figure 87: Raman spectra of neat TEG showing the peak fittings at each of the main band regions. 142
Figure 88: Raman spectra peak fitting of neat PVAL at different regions: (a) C-C stretching, (b) C-O stretching and O-H bending, (c) C-H and O-H bending, (d) C=O stretching and C-O asymmetric stretching, and (e) C-H stretching. Peak assignments are used in Chapter 3 and 4. 143

Figure 89: Raman spectra peak fitting of PVAL/TEG blends of different concentrations at the C-C stretching region. (a) 5 wt.% TEG, (b) 10 wt.% TEG, (c) 15 wt.% TEG, (d) 20 wt.% TEG, (e) 25 wt.% TEG, (f) 30 wt.% TEG, and (g) 50 wt.% TEG in PVAL. 144
Figure 90: Raman spectra peak fitting of PVAL/TEG blends of different concentrations at the C-O stretching and O-H bending region. (a) 5 wt.% TEG, (b) 10 wt.% TEG, (c) 15 wt.% TEG, (d) 20 wt.% TEG, (e) 25 wt.% TEG, (f) 30 wt.% TEG, and (g) 50 wt.% TEG in PVAL. 145
Figure 91: Raman spectra peak fitting of PVAL/TEG blends of different concentrations at the C-H bending and O-H bending region. (a) 5 wt.% TEG, (b) 10 wt.% TEG, (c) 15 wt.% TEG, (d) 20 wt.% TEG, (e) 25 wt.% TEG, (f) 30 wt.% TEG, and (g) 50 wt.% TEG in PVAL. 146
Figure 92: FTIR spectra peak fitting of PVAL at different regions of the spectrum: (a) O-H stretching, (b) C-H stretching, (c) C=O stretching, (d) C-H stretching, and (e) C-O and C-O-C stretching. 148
Figure 93: FTIR spectra peak fitting of PVAL/TEG blends for the O-H stretching band. (a) 5 wt.% TEG, (b) 10 wt.% TEG, (c) 15 wt.% TEG, (d) 20 wt.% TEG, (e) 25 wt.% TEG, (f) 30 wt.% TEG, and (g) 50 wt.% TEG in PVAL. 149
Figure 94: Raman spectra peak fitting of PVAL in the region between 100 and 700 cm-1 150
Figure 95: Raman spectra peak fitting of PVAL/titanium oxide hydrate hybrid film of different compositions at the C-C stretching region. (a) 10 vol.%, (b) 20 vol.%, (c) 30 vol.%, (d) 40 vol.%, (e) 50 vol.%, and (f) 80 vol.% titanium oxide hydrate in PVAL. 151
Figure 96: Raman spectra peak fitting of PVAL/titanium oxide hydrate hybrid film of different compositions at the C-O stretching and O-H bending region. (a) 10 vol.%, (b) 20 vol.%, (c) 30 vol.%, (d) 40 vol.%, (e) 50 vol.%, and (f) 80 vol.% titanium oxide hydrate in PVAL. 152
Figure 97: Raman spectra peak fitting of PVAL/titanium oxide hydrate hybrid film of different compositions at the C-H and O-H bending region. (a) 10 vol.%, (b) 20 vol.%, (c) 30 vol.%, (d) 40 vol.%, (e) 50 vol.%, and (f) 80 vol.% titanium oxide hydrate in PVAL. 153
Figure 98: Raman spectra peak fitting of PVAL/titanium oxide hydrate hybrid film of different compositions between 300 and 700 cm^{-1}. (a) 10 vol.%, (b) 20 vol.%, (c) 30 vol.%, (d) 40 vol.%, (e) 50 vol.%, and (f) 80 vol.% titanium oxide hydrate in PVAL. 154
Figure 99: Optical micrograph taken using Raman microscope of PVAL – TiO_2 composite. Points where it was considered to be predominantly the matrix or particle are indicated. 156
Figure 100: Raman spectra peak fits for PVAL - TiO2 composites of different compositions and taken where matrix “M” or particle “P” were observed in the C-C stretching region. (a) 10% TiO2/PVAL M, (b) 10% TiO2/PVAL P, (c) 30% TiO2/PVAL M, (d) 30% TiO2/PVAL P, (e) 50% TiO_2/PVAL M, and (f) 50% TiO_2/PVAL P. 157
Figure 101: Raman spectra peak fits for PVAL - TiO2 composites of different compositions and taken where matrix “M” or particle “P” were observed in the C-O stretching and O-H bending region. (a) 10% TiO2/PVAL M, (b) 10% TiO2/PVAL P, (c) 30% TiO2/PVAL M, (d) 30% TiO2/PVAL P, (e) 50% TiO_2/PVAL M, and (f) 50% TiO_2/PVAL P. 158
Figure 102: Raman spectra peak fits for PVAL - TiO2 composites of different compositions and taken where matrix “M” or particle “P” were observed in the C-O stretching and O-H bending region. (a) 10% TiO2/PVAL M, (b) 10% TiO2/PVAL P, (c) 30% TiO2/PVAL M, (d) 30% TiO2/PVAL P, (e) 50% TiO_2/PVAL M, and (f) 50% TiO_2/PVAL P. 159
Figure 103: Raman spectra peak fits for PVAL - TiO_2 composites of different compositions and taken where matrix “M” or particle “P” were observed between 300 and 700 cm^{-1}. (a) 10% TiO_2/PVAL M, (b) 10% TiO_2/PVAL P, (c) 30% TiO_2/PVAL M, (d) 30% TiO_2/PVAL P, (e) 50% TiO_2/PVAL M, and (f) 50% TiO_2/PVAL P. 160
Figure 104: XPS spectra of PVAL / boric acid films focusing on the C1s region (a). A comparison of the carbon peak intensity is presented in (b) as a function of inorganic content. 163
Figure 105: XPS spectra of PVAL / boric acid films focusing on the C1s region. 163
Figure 106: Raman spectra peak fitting of neat PVAL films 99% hydrolysed at different regions: (a) C-S stretching, (b) C-C stretching, (c) C-O stretching and O-H bending, (d) C-H and O-H bending .Peak assignments are used in Chapter 5. 164

Figure 107: Raman spectra peak fitting of neat ANF at different regions: (a) C-H bending, (b) C-C ring stretching, (c) C-C ring stretching and C-H in-plane bending, (d) C-C ring stretching and N-H bending and C-N stretching, (e) C-C ring stretching C=O stretching, C-N stretching, and N-H bending. 165
Figure 108: Optical micrographs of PVAL/ANF composite films with different concentrations. Images taken using Raman microscope lens with 100x objective. 166

List of Tables

Table 1: Comparison between FTIR and Raman spectroscopy 52
Table 2: Raman peak assignments of neat PVAL. 65
Table 3: Raman peak assignments of neat TEG 65
Table 4: FTIR band assignments of PVAL. 69
Table 5: Measured glass transitions, melting transitions and enthalpies of fusion of PVAL - TEG films 75
Table 6: Raman peak assignments form PVAL. The three peaks observed in the lower Raman shift are highlighted first. 84
Table 7: Peak assignment for anatase TiO_2 based on Raman of PVAL-TiO_2 composites. 93
Table 8: FTIR band assignments for PVAL. 95
Table 9: Measured glass transitions and melting temperatures of PVAL / titanium oxide hydrate hybrid films and PVAL – TiO_2 composite films. 100
Table 10: Raman peak position and assignment for PVAL. 116
Table 11: Raman peak position and assignment for ANF. 116
Table 12: FTIR band assignments for PVAL. 119
Table 13: FTIR band assignments for ANF. 119
Table 14: Observed glass transition, melting temperatures of PVAL / ANF films 124
Table 15: Raman peak fitting statistics for PVAL/TEG blends of different concentrations at the C-C stretching region. 147
Table 16: Raman peak fitting statistics PVAL/TEG blends of different concentrations at the C-O stretching and O-H bending region. 147
Table 17: Raman peak fitting statistics for PVAL/TEG blends of different concentrations at the C-H bending and O-H bending region. 147
Table 18: Raman peak fitting statistics for PVAL/titanium oxide hydrate hybrid film of different compositions at the C-C stretching region. 155
Table 19: Raman peak fitting statistics PVAL/ titanium oxide hydrate hybrid film of different compositions at the C-O stretching and O-H bending region. 155
Table 20: Raman peak fitting statistics for PVAL/ titanium oxide hydrate hybrid film of different compositions at the C-H bending and O-H bending region. 155
Table 21: Raman peak fitting statistics for PVAL/ titanium oxide hydrate hybrid film of different compositions at the between 300 and 700 cm^{-1}. 156
Table 22: Raman peak fitting statistics for PVAL - TiO_2 composites of different compositions at the C-C stretching region. 161
Table 23: Raman peak fitting statistics PVAL - TiO_2 composites of different compositions at the C-O stretching and O-H bending region. 161
Table 24: Raman peak fitting statistics for PVAL - TiO_2 composites of different compositions at the C-H bending and O-H bending region. 161
Table 25: Raman peak fitting statistics for PVAL – TiO_2 composites of different compositions between 300 and 700 cm^{-1}. 162
Table 26: Raman peak fitting statistics for PVAL 99% hydrolysed at different regions of the spectrum 164
Table 26: Raman peak fitting statistics for PVAL 99% hydrolysed at different regions of the spectrum 165

List of Abbreviations:

3-ω	Three omega method of thermal conductivity measurement
ABS	Acrylonitrile butadiene styrene
ANF	Aramid nanofibres
ATR	Attenuated Total Reflectance
BLS	Brillouin light scattering
CCD	Charge-coupled device
CNT	Carbon nanotube
C_p	Specific heat capacity
D	Sample dimension
D	Nanoparticle's diameter
DC	Degree of crosslinking
DIW	Deionised water
DMSO	Dimethyl sulfoxide
DSC	Differential Scanning Calorimetry
EDS	Energy dispersive X-ray spectroscopy
EG	Exfoliated graphite
EVA	Ethylene Vinyl Acetate
FSR	Free spectral range
FTIR	Fourier-Transform Infra-red
GnP	Graphene Nanoplatelets
H-Bond	Hydrogen Bond
HDPE	High Density Polyethylene
K	Thermal conductivity
K_c	Thermal conductivity of the composite
K_e	Electrons' contribution to thermal conductivity
K_{eff}	Effective thermal conductivity
K_f	Thermal conductivity of the filler
K_m	Thermal conductivity of the matrix
K_p	Phonons' contribution to thermal conductivity
KOH	Potassium hydroxide
L	Nanoparticle's length
LDPE	Low Density Polyethylene
LED	Light emitting diode
MPF or Φ_m	Maximum packing factor
MW	Weight-average molecular weight
MWCNT	Multi-walled carbon nanotube
q	Heat flux
PA	Polyamide
PAA	poly(acrylic acid)
PAP	poly(N-acryloyl piperidine)
PB	Polybutadiene
PBDT	poly(2,2′-disulfonyl-4,4′-benzidine terephthalamide)
PBO	Poly(p-phenylene-2,6-benzobisoxazole)
PBT	Polybutylene terephthalate
PBI	Polybenzimidazole
PC	Polycarbonate
PE	Polyethylene
PEEK	Polyether ether ketone
PEG	Polyethylene glycol
PEI	Polyetherimide
PET	Polyethylene terephthalate
PI	Polyimide

PIPD	Polyhydroquinone diimidazopyridine
POM	Poly(methylene oxide)
PP	Polypropylene
PPE	Poly(p-phenylene ether)
PPP	poly (p-phenylene)
PPS	Polyphenylene sulfide
PS	Polystyrene
PSU	Polysulfone
PPTA	poly(p-phenylene terephthalamide)
PVAL or PVA	poly(vinyl alcohol)
PVC	Poly vinyl chloride
PVPh	poly(4-vinyl phenol)
RA 2DIR	Relaxation-assisted two-dimensional infrared
RPM	Revolutions per minute
SAXS	Small-angle X-ray scattering
SEM	Scanning Electron Microscope
SERS	Surfaced Enhanced Raman Spectroscopy
SSNMR	Solid-state nuclear magnetic resonance
SWCNT	Single-walled carbon nanotube
T	Temperature
T_g	Glass-transition temperature
T_m	Melting temperature
TC	Thermal Conductivity
TDTR	Time-domain thermoreflectance
TEG	Tetraethyleneglycol
TEM	Transmission Electron Microscope
TEOS	Tetraethoxysilane
TGA	Thermal gravimetric analysis
TMM	Transfer Matrix Method
UHMWPE	Ultra-high-molecular-weight polyethylene
vdW	Van der Waal
vf or Φ	Volume fraction
W/m.K	Watts per meter Kelvin (units of TC)
WAXS	Wide-angle X-ray scattering
wt.%	Weight percentage
vol.%	Volume percentage
XPS	X-ray photoelectron spectroscopy
ΔT	Temperature gradient
Λ	Mean-free path of a phonon
ν	Speed of sound
ω	Angular frequency
ω_B	Brillouin shift
$\lambda_{incident}$	Wavelength of incident light
$\lambda_{scattered}$	Wavelength of scattered light

1 Thermal Transport in Materials

In order to study the effect of solid-state structure, chain morphology and confirmation on thermal conductivity (TC), an understanding of how thermal energy is transferred within a material must be established. A review of fundamental theories and current research is presented in the following sections. A description of how energy is transported in polymers is detailed, highlighting fundamental factors affecting the thermal conductivity. Furthermore, current and commercially available methods for altering thermal conductivity in polymer systems are examined, while highlighting some limitations of the findings and how this thesis is aiming to address them.

1.1 Thermal conductivity in materials

Thermal conductivity is the transport of thermal energy throughout a medium across a temperature gradient. This flow of energy is based on the atomic and molecular structures of the medium [1]. For bulk materials, Fourier's law defines this as:

$$q = -K\Delta T \tag{1.1}$$

Where q is the heat flux, K is the thermal conductivity and ΔT is the temperature gradient. K is a function of T if the temperature range is wide, yet can be considered constant for small ΔT [2]. For solid materials, the thermal conductivity is the sum of two main components:

$$K = K_p + K_e \tag{1.2}$$

Where K_p relates to conductivity by phonons and K_e relates to the electrons' contribution [1]. Phonons are defined as quantum mechanical vibrations of the crystal lattice or chemically bonded atoms that carry thermal energy through the material [3]. They are similar to photons as they have a particle-wave nature [4]. In metals, electrons are the primary thermal energy carriers and phonons' contribution is considered negligible. On the other hand, for dielectric materials, such as most ceramics and polymers, the contribution of electrons is ignored due to the lack of free electrons. Therefore, thermal energy propagation via phonons is the primary heat transfer mechanism [1].

Phonons can be represented by a sound wave, hence the term "acoustical phonons" being used to identify them, as they travel at the speed of sound within a material [1]. These waves are of

relatively low frequencies (<100 kHz) and travel through crystal planes and chemical bonds between atoms. Phonons in a material can interact, exchange or dissipate their energy. These occasions are described as phonon scattering events [5, 6]. They can be scattered by other phonons, lattice defects in crystalline structures, molecular chain bends in polymers, interfaces between phases, or impurities [6-8].

The phonon's heat conductivity equation can be derived from the kinetic theory of gasses to this simple form:

$$K_p = \frac{C_v \upsilon \Lambda}{3} \tag{1.3}$$

Where C_v is the specific heat capacity at constant volume, υ is the speed of sound and Λ is the phonon's mean-free path: the average distance a phonon can travel before being scattered. The specific heat capacity can be considered as how fast the material can acquire or lose thermal energy [9]. The dimensions of the sample relative to the mean-free path, governs the transport regime. If the dimension D >> Λ, the transport is termed "diffusive". This leads to overall lower TC, as phonons would face more scattering events. On the other hand, when D < Λ, "ballistic" thermal transport is occurring, and high TC is achieved [1, 6]. Thus, one of the strategies of increasing TC is increasing Λ by reducing phonon scattering events; *i.e.* making the phonons travel more efficiently through the material [4].

1.2 Thermal conductivity in polymers

Polymers are materials consisting of long chains of repeating units called monomers. Chains can range from a few monomers (oligomers) to more than thousands in ultra-high molecular-weight polyethylene (UHMWPE). Bulk polymers contain a large number of these long chains interacting with each other. Polymers can also be considered in simplistic form as cooked spaghetti with many chains interacting with each other in a random fashion. The relative randomness of the structure is the reason behind many polymers being low in TC as phonons cannot pass throughout the material without facing many scattering events [4, 5]. However, polymers can be described by several parameters such as the monomer type, number of monomers, and tacticity to name but a few. Polymer chains can also be either linear (high density polyethylene, HDPE) or branched (low density polyethylene, LDPE). The simplest, and most widely spread polymer type is HDPE, which is a linear chain of carbon atoms covalently bonded with hydrogen atoms on each side [10]. These different parameters

can all influence the thermal transport in polymers and are vital to be understood to design polymer systems from on the onset.

1.2.1 Single molecule chains

To understand TC of bulk polymers, it is important to understand how a single chain transports thermal energy. Based on observations on one-dimensional materials, it is hypothesised that single polymer chains may have very high thermal conductivities [11]. This was shown theoretically that a single PE chain can have TC as high as 300 W/m.K, noticeably higher than some metals (consider aluminium at 237 W/m.K) [12, 13]. In another molecular dynamics simulation study, single-chain stretched poly(p-phenylene terephthalamide) (PPTA) and a (poly(2,2′-disulfonyl-4,4′-benzidine terephthalamide)) (PBDTA) derivative was calculated to be ~148 W/m.K and ~120 W/m.K respectively [14]. The PBDTA derivative had the disulfonyl groups substituted with hydrogen.

In the case of shorter chains such as oligomers, a study of energy transport along organic chains with different lengths and end-groups was made [15]. The oligomers were placed in a solution to isolate them, and in turn, removing phonon-phonon scattering events. To measure the energy transport, one end-group was excited by a wave, and the time taken to reach the other end was recorded by a method of wave detection (relaxation-assisted two-dimensional infrared spectroscopy (RA 2DIR)). The results show ballistic transport along the chain (1440 m/s) then the transport regime turns into slow diffusive (130 m/s) at the end-groups. Furthermore, energy transport velocity was observed to be primarily dependant on the chain length rather than the end-group type [15]. The results complement previous theoretical studies that single chains of carbon covalently bonded are extremely good energy carriers [12, 16].

1.2.2 Monomer type (backbone)

By perceiving heat transport as vibrations and waves, it is clear to see that rigid structures are better at conduction than flexible structures [5]. In a long, flexible polymer chain, bends will exist along its length, creating phonon scattering points hindering phonon propagation. In a flexible polymer, typically, the phonon's mean free path Λ is less than 10 nm or a few monomers in length [17]. Changing the monomer type, can introduce stiffness to the polymer chain, which changes the overall bulk properties such as melt temperature, elastic modulus, etc. Double bonds, oxygen atoms and aromatic rings in the backbone all introduce some degree of rigidity [10].

This is presented in the study by Liu and Yang, where the role of monomer type and hence backbone rigidity on TC was investigated [18]. Single chain polymers made from eight different monomer types were simulated. Figure 1 presents their findings. The polymers were:

- Polyethylene (PE) (simple carbon-carbon bonds as reference)
- Polyacetylene (double bonds along the backbone chain)
- Polybutadiene (PB) (alternating double and single bonds along the backbone)
- Poly(methylene oxide) (POM) and Polyethylene glycol (PEG) (oxygen in the backbone)
- Polybenzimid, Poly(p-phenylene (PPP) and Poly(phenylene ether) (PPE) (aromatic rings in the backbone)

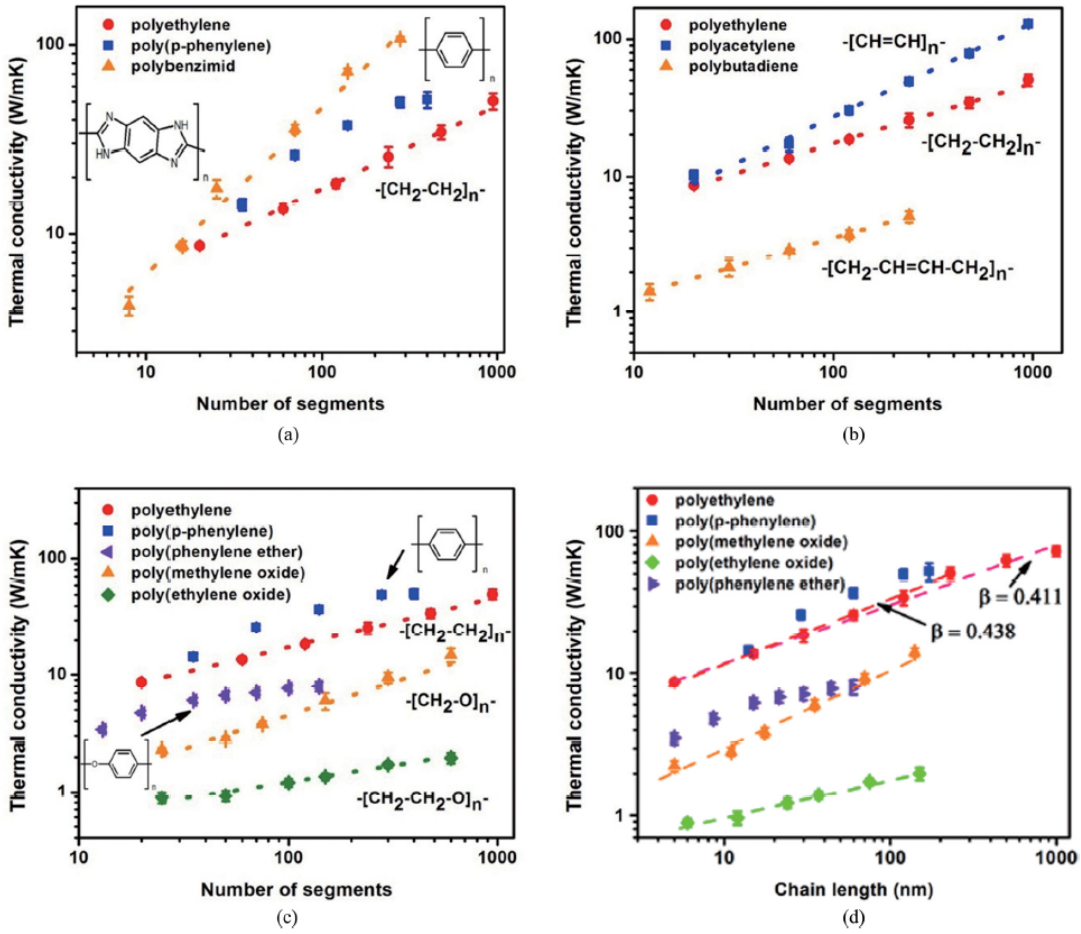


Figure 1: Effect of monomers on thermal conductivity. (a) Presents the effect of an aromatic ring in the backbone. (b) Illustrates the effect of double bonds in the chain. (c) Shows the effect of oxygen in the backbone. (d) Presents the dependence on chain length rather than number of monomers. Reprinted from [18]. Copyright (2012) by the American Physical Society.

The results concluded that a polymer chain with an aromatic ring in the backbone was up to 5 times higher in TC than a simple PE chain due to higher rigidity, (Figure 1 a). Having double bonds along the entire chain increases TC, yet isolated double bonds reduces TC due to "bond-disorder", (Figure 1 b). Oxygen in the backbone creates "mass-disorder" and reduces TC as well, (Figure 1 c) [18].

The effect of chain stiffness was examined using molecular dynamics simulations in another study [19]. Using PE, different possible scenarios were simulated and their effect on TC was calculated. The scenarios were chain morphology, temperature range, density of chains, and chain stiffness. The conclusions showed that the intra-chain interaction was the dominant factor in TC similar to the findings presented earlier by Rubtsova *et al*. [15]. A notable observation from the study was that larger backbone stiffness resulted in anisotropic increase in TC. This is due to the rigid chains being aligned in one direction without bends. The increase in TC was observed in the chain direction [19]. Further to chain rigidity, single chain rotation was studied using molecular dynamics more recently [14]. PPTA and PBDT derivatives were simulated to have different degrees of chain rotation factors that they have introduced for this study. It was found that chain rigidity was directly proportional to higher thermal conductivities due to more efficient phonon transport in the form of high group velocities and higher larger mean free path [14].

1.2.3 Molecular weight

Further to the type of monomer, polymers are defined by their molecular weights (MW) which affects macro-properties such as mechanical and viscoelastic properties [10]. Naturally, MW would affect TC as well. This stems from understanding that phonons along the chain are transported by strong, intramolecular covalent bonds more efficiently than weaker intermolecular bonds such as van der Waals (vdW) [5]. Furthermore, phonons will be scattered by the chain ends and having higher MW reduces the total number of chain ends [17, 20]. The chain ends' effect was observed in Rubtsova *et al*. where the velocity of energy transport was reduced from ballistic to diffusive [15]. The effect of MW was also presented in Figure 1. TC increased linearly with the increased repeating units (MW) for modelled single chains [19].

Work on bulk Polystyrene (PS) found that higher MW yielded higher TC [21]. It supports that phonons travel more efficiently along a single chain rather than between chains. Further theoretical studies show that the positive effect of higher MW holds for linear polymers rather than branched polymers [22]. This was later supported empirically, due to branches acting as

scattering points for phonons reducing their mean-free path [23]. A more recent study using molecular dynamic simulations of different bottle-brush polymers show significant decrease in TC with increasing side chain lengths [24]. This signifies that phonons would travel more efficiently through the backbone in an aligned polymer.

1.2.4 Inter-chain interactions

Further to studies on single chains, bulk polymers have several inter-chain interactions that give rise to many intrinsic polymer properties [10]. As presented earlier, intramolecular covalent bonds are excellent in thermal energy transport, yet when phonons reach chain ends, energy is dissipated. Moreover, phonons travel less efficiently over weaker intermolecular bonds.

Strengthening the intermolecular bonds by crosslinking, hence having strong covalent bond reinforcement between chains signifies better TC. However, experimentally, the results fluctuated in affecting TC [25]. In another study, PE and PS chains were simulated and their degree of crosslinking varied. By doing so, it was found that crosslinks influenced TC positively in high degree-of-crosslinking (DC) (>20%). The interpretation stems from that crosslinking contributes to TC in two ways: positively influencing, in increased covalent bonds, or negatively contributing, as increased phonon structural scattering points. The increase in TC is still relatively low for PE (from 0.2 to 0.6 W/m.K at 80% DC) and negligible for PS [26].

On the other hand, some simulation studies show a decrease in the TC after crosslinking [27]. Experimental work also show a decrease in TC with the increase of DC in HDPE using a peroxide cross linker. It is suggested that this is due to the reduction overall crystallinity of the material [28]. The fluctuation between the results of the effect of crosslinking on TC was investigated recently by Rashidi *et al.* [29]. The work focuses on understanding how different cross-linking agents affect thermal conductance. Two PMMA polymer chains were simulated and cross-linked with different chemical moieties. The length of the crosslink was found to be significant in thermal transport. Shorter covalent links were not only created, but also allowed further interactions of inter-chain bonds such as Van der Waals (VdW). Their work is summarised in Figure 2 & Figure 3. The work clarifies the discrepancies between several experimental crosslinking studies on TC.

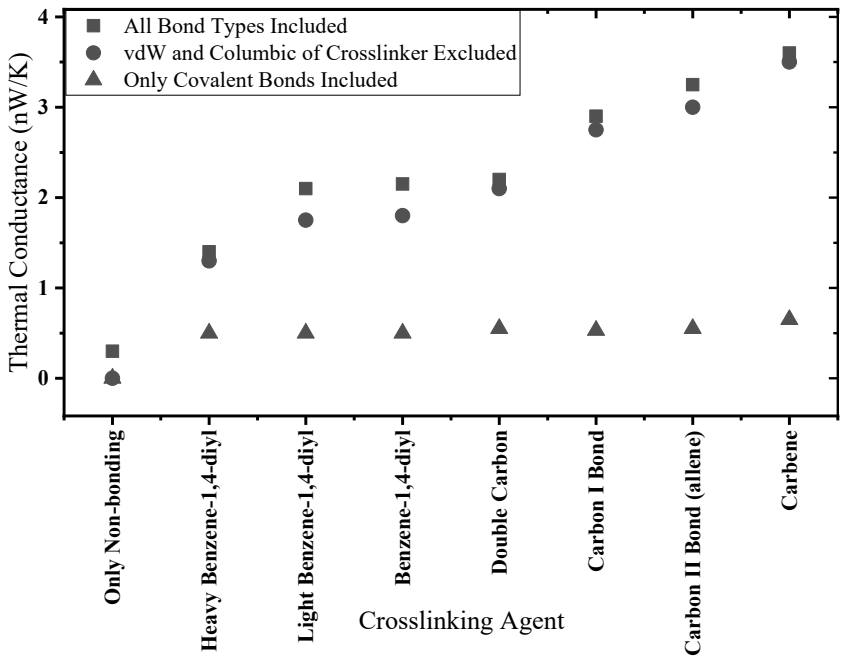


Figure 2: Thermal conductance of 100% cross-linked polymers. Thermal conductance simulation measurements based on different cross-linking agents on two PMMA polymer chains. The mass of the carbon atoms in the benzenes were either kept normal ("benzene"), doubled ("heavy benzene"), or halved ("light benzene"). The simulations were conducted with the three different variations of the chemical bonding. The squares represent all bonding (covalent) and nonbonding (VdW & columbic) types. The circles represent the nonbonding interactions of the cross linker being removed. With the triangles, all nonbonding interactions in the system have been removed (cross-linker and polymer chain). The results show that the shorter carbene cross-linker had the most positive effect on the thermal conductance. Adapted with permission from [29]. Copyright 2017 American Chemical Society.

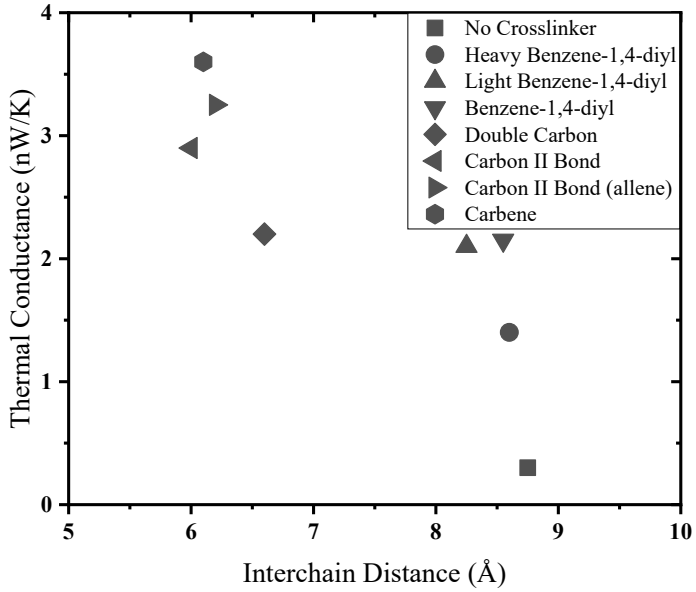


Figure 3: Thermal conductance of 100% cross-linked polymers presenting how the inter-chain distance affects thermal transport. The graph is from the same study presented in Figure 2. Here, all bond interactions were included. It can be observed that the shorter the inter-chain distance due to the crosslinking species, the higher the calculated thermal conductance. Adapted with permission from [29]. Copyright 2017 American Chemical Society.

Furthermore, observing polymers that create hydrogen-bonds between their chains, which are stronger than VdW, such as PA 6,6 is still not significant in measure (0.41 W/m.K) [30, 31]. However, the effect of inter-chain bonding on TC show that having hydrogen bonds (H-bonds) on their own is not enough [32]. How the H-bond donor or acceptor is linked to the backbone and the density of the bonds affect TC significantly. Kim *et al*. in their study used an H-bond-accepting polymer (poly (N-acryloyl piperidine)) (PAP) with different H-bond donating polymers: poly (acrylic acid) (PAA), PVAL, and poly(4-vinyl phenol) (PVPh). Their variable was how the H-bond donating part, in this case (OH), was linked to the backbone [32]. In PAA and PVAL, the hydroxyl group is closely connected to the polymer backbone. In PVPh, the hydroxyl group is attached via a benzene ring to the backbone.

Further to the H-bonds, they kept the MW of the H-bond donating polymer relatively low in comparison to the PAP. The idea behind this was to keep both polymer chains extended by means of high H-bond densities, improving both the intra and inter-chain thermal energy transfers. Their method was believed to only function with miscible blends, as the bonds would be distributed homogenously in the polymer and not at the interfaces between phases. The results show that the higher H-Bond density (PAP: PAA, ΦPAP 0.3) gave the highest TC improvement. Their results are presented in Figure 4. It was interpreted that at that volume fraction, the chains where most extended giving rise to the highest positive improvement to TC [32].

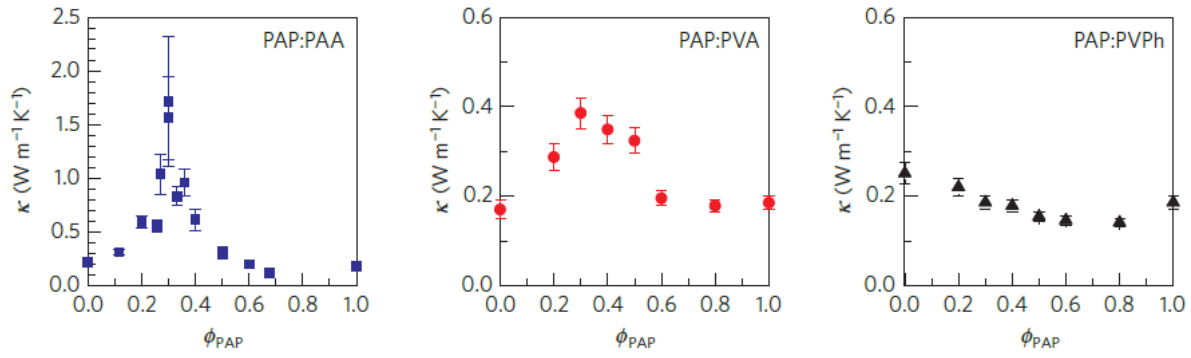


Figure 4: Thermal conductivities of amorphous polymer blends from Kim *et al's.* study [32]. Blending PAP with a strong hydrogen bond donor PAA gave the highest improvement (left panel). With PVAL, the improvement was more modest but still doubling the initial thermal conductivity (middle panel). With a large benzene ring between the hydroxyl group and the backbone, the PAA:PVPh blend showed a decrease in the measured TC (right panel). Reprinted by permission from Springer Nature: Nature Materials, High thermal conductivity in amorphous polymer blends by engineered inter-chain interactions, Gun-Ho Kim *et al*.[32] , Copyright 2014 Springer Nature.

A more recent study looked at the effect of blending PEG of multiple MWs and ratios with PVAL [33]. The hypothesis was similar to what was stated by Kim *et al.*'s [32] in that heat conduction pathways would be created via the extension of polymer chains using the stronger H-bond interactions. The main conclusions found in the study was that the lower molecular weight PEGs (400 g/mol in this case) had a more positive effect on the system's TC. The higher MW (1000, 20,000 & 200,000 g/mol) created agglomerates and phase separation between the two polymers which reduced TC. As for the lower MW, it created a large number of thermal bridges via the hydrogen bonds as well as being miscible. When varying the ratio of PEG to PVAL, they found that the conductivity increases then decrease similar to the trends in the amorphous blends (PAP:PAA and PAP:PVA) presented in Figure 4 [32]. Further to the PVAL / PEG study, several smaller ethylene glycols such as (diethylene glycol (DEG), tetraethylene glycol (TEG) and hexaethylene glycol (HEG)) were blended with PVAL [34]. It was found that the shorter DEG had the most positive effect on the system's TC by reaching 0.52 W/m.K in comparison to 0.32 W/m.K in neat PVAL [34].

Further to studies mentioned, another method of inducing localised stretching of polymer chains is ionising polyelectrolytes [35]. Their results show that due to the electrostatic repulsion of the ions, the chains became stiffer and extended which increased the measured TC from 0.36 W/m.K in a pH 1 environment to ~ 1.2 W/m.K at pH 12. However, this magnitude of increase in the result was observed only in the spin-coated samples of the study. While the blade-coated (thicker films and slower in solvent evaporation) showed an increase, albeit to a lower extent (~ 0.6 W/m.K). This is due to the chains having a longer time to relax and coil back to a more thermodynamically favourable position [35].

1.2.5 Morphology (semi-crystalline vs amorphous)

From a morphology standpoint, polymers can be divided into two forms: amorphous or semi-crystalline. Amorphous polymers are considered to have random chains entangled and interacting with each other with no long-range order. In semi-crystalline polymers, ordered parts, called lamellae or spherulites, are embedded in the amorphous polymer matrix [10]. Hence, a semi-crystalline can be considered as a two-phase material. A study presented that semi-crystalline polymers have higher TC compared to amorphous polymers. This is due to ordered sections leading to more efficient phonon transport [17]. Figure 5 presents some commercial polymers and the difference of their thermal conductivities based on their morphologies. As observed from the graph, amorphous polymers have relatively equal thermal

conductivities. However, in semi-crystalline polymers, the values span a wider range. TC is believed to increase with increasing degrees of crystallinity (the ratio of crystalline phases to amorphous) [17]. This is also apparent in HDPE where it has the highest TC due to the linearity of its chains leading to high degrees of crystallinity.

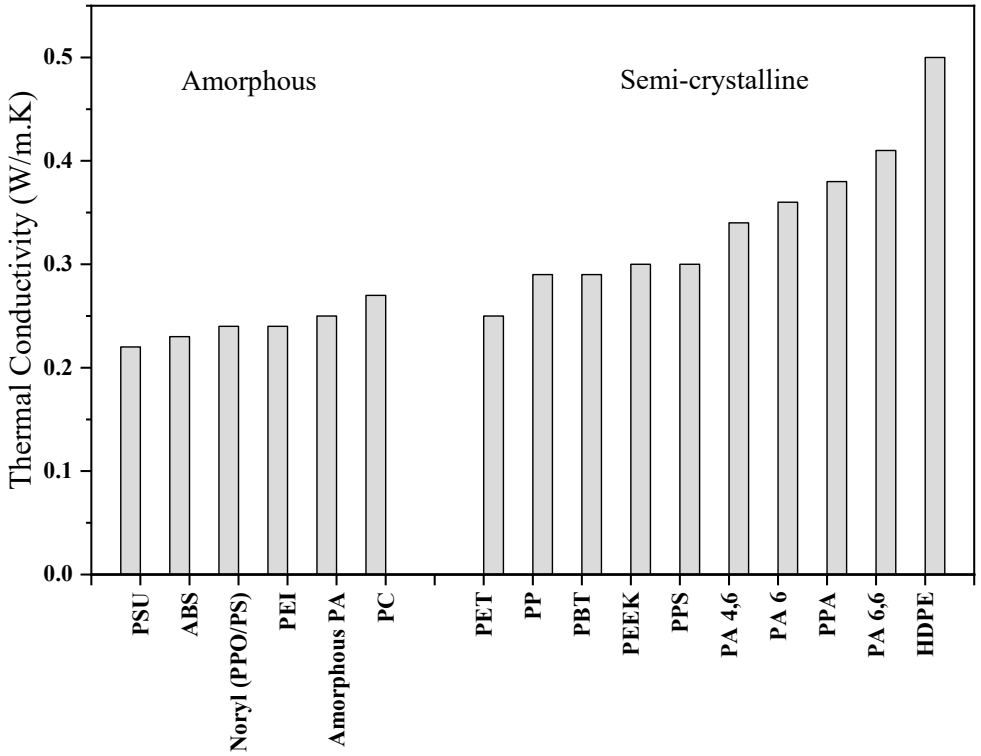


Figure 5: Thermal conductivity of commercial amorphous and semi-crystalline polymers at room temperatures. Graph plotted using values derived from [31].

1.3 Increasing TC by polymer chain orientation

Expanding on the studies shown in Section 1.2 that aligned chains have high TC, this section highlights chain alignment methods observed in industry. The role of chain alignment has been previously exploited to increase elastic modulus, which is demonstrated in different industrial fibres: such as UHMWPE, Polyhydroquinone diimidazopyridine (PIPD (M5)), PPTA, and Poly(p-phenylene-2,6-benzobisoxazole) (PBO) [10]. Such fibres are created by very high draw ratios (20 – 400 times) and are mainly processed from solutions rather than melt; owing to their high molecular weights, that increases viscosity. Additionally, stretching increases crystallinity in polymers, thus reiterating that it will enhance TC for semi-crystalline polymers [10].

1.3.1 Fibres

An early study focused on commercial high modulus fibres, mainly UHMWPE, with different draw ratios. It was found that conductivity was up to 60 W/m.K [36]. A more recent study revisited high modulus fibres and included nine different polymers such as (PIPD (M5)) and Kevlar. The method used for measuring thermal conductivity was time-domain thermoreflectance (TDTR), which measured conductivity along the fibres' axis (different from the previous study [36]). At room temperature, liquid crystal PBO fibres showed the highest conductivity at ~ 20 W/m.K, UHMWPE was less at ~ 15 W/m.K [37]. Yet these are two orders of magnitude higher than average bulk polymers seen in Figure 5.

A significant experiment followed on from those studies and sought to improve TC by reducing the defects along the fibres [38]. PE nanofibers were created by growing from a gel and drawing for up to 400 times. The fibres created were highly conductive with TC reported at ~ 104 W/m.K. The work confirms that highly aligned polymer chains, and reduction of impurities such as voids and bends, make excellent phonon transport media. It also proved that carbon-carbon covalent bonds can be as efficient as some metals in thermal transportation [38]. Yet, they were only able to reduce the impurities by reducing the scale drastically with very high draw ratios.

Electrospinning is another method of creating highly oriented polymer fibres using an electrical field. Studies on PEG have shown that highly oriented fibres can reach thermal conductivities of around 28 W/m.K in comparison to 0.2 W/m.K in bulk PEG [39, 40].

Another study on nanofibres was done using polythiophene (PT) as the focus [41]. Arrays of PT nanofibres were made by electropolymerisation on a nano-template. The chains obtained were highly oriented along the fibre axis yet still amorphous. TC of the arrays were found to be ~ 4.4 W/m.K and consistent over multiple cycles at 200^{o}C signifying their practical use in sensors [41]. The rigid backbone and the conjugated structure of polythiophene add to the high melting point and thermal stability thus making it suitable for high temperature applications [42].

1.3.2 Stretched films

Similar to fibres, stretched films are considered as highly oriented materials. They have their own practical advantages over fibres especially in heat dissipation purposes, as those applications are directly linked to surface area. Early experiments made on UHMWPE highly oriented strips were conducted to measure TC [43]. The implemented method to measure the thermal diffusivity used a point source heater then fitted the spatial infrared radiation to a solution of the heat equation. They recorded thermal conductivities of 37.5 W/m.K due to the highly aligned nature of the films [43].

A more recent study made UHMWPE films from a sol-gel solution with different draw ratios [44]. Very high mechanical stretching rates, up to 125 times were needed to reach 15.38 W/m.K. However, at a draw ratio of 25, a significant increase was reached with a TC of 11.66 W/m.K [44].

However, the drawback of highly aligned chains in fibres, stretched films or nanofiber arrays, is the method of production that requires high draw ratios from solution. Such methods are not suitable to the mass-market production such as roll-to-roll for solution-processed materials or injection moulding for melt processed polymers. Nevertheless, these studies are crucial in understanding that high thermal conductivities could be achieved with increased chain alignment.

1.4 Increasing TC by highly conductive fillers

In current commercial products, thermally conductive polymer products are based on composites. They are available either as electrically isolative or both thermally and electrically conductive. The latter products are higher in TC, as the fillers used have higher TC to begin with (compare up to 100 W/m.K for both electrically and thermally conductive to 1-10 W/m.K in electrically isolative) [45]. Adding highly conductive fillers is a simpler method than mechanical stretching for improving polymer TC.

Different models predicting thermal behaviour of composites show various degrees of agreement with empirical data [46-48]. A basic model predicts that the TC of a composite would increase linearly with the TC of the filler. However, this does not hold for K_f/K_m ratios greater than 100 as the trend plateaus [47]. Where K_f is the TC of the filler and K_m is the TC of the matrix. Figure 6 better describes the variation based on the ratios. Furthermore, a very high loading of the filler must be achieved before realising the full potential of the filler's thermal conductivity [4, 47]. Further to the models, several studies' results of thermally

conductive polymer composites was compiled by Guo *et al*. [49]. It shows discrepancies between the composites TC and the rule of mixtures despite having an overall positive impact on the end system.

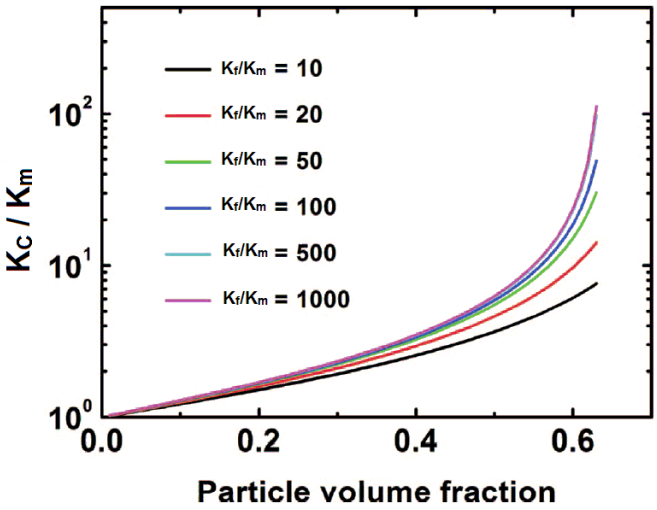


Figure 6: Modelling calculations representing ratio of filler/matrix TC on composite TC. K_c is the TC of the composite, K_m is the TC of the matrix and K_f is the TC of the filler. From the graph, it is seen that that only at high volume fraction loadings that the composite start to benefit from the high thermal conductivity of the filler. Graph obtained with permission from [50] © 2011 IEEE.

Generally, it is believed that the TC of a composite is based on the TC of both the matrix and the filler. It is also significantly affected by the filler's loading, shape, size, dispersion as well as the matrix/filler thermal interface [48-50]. The following subsections will cover the main filler types of ceramics, carbon-based and metals as well as their respective benefits and limitations.

1.4.1 Ceramics

Polymer/ceramic composites can be split into three main categories for simplicity: oxides, nitrides, and carbides. Some oxides are apparent in industrial polymer/ceramic composite products such as SiO_2 in epoxies, ZnO in rubber tyres, and Al_2O_3 [50]. However, as one of the main applications of high thermally conductive polymers is the electronic market, these ceramics have some drawbacks. SiO_2 has low TC (~1.5 W/m.K), ZnO is intrinsically a semiconductor, and Al_2O_3 has a relatively high dielectric constant [49, 50].

Another type of ceramics more commonly used are nitrides [50]. AlN is of interest because of its high TC, but similar to Al_2O_3, it has a high dielectric constant - making it unsuitable to electronic devices. BN is even more appealing to the composite industry, especially due to the low density and high temperature resistance. Furthermore, its main stable shape is a hexagonal

crystal that creates powder platelets - leading to improved processing performance [50]. It has also been made into nanotubes and nanosheets, which enable less filler loading in weight percentage yet, improve TC [51].

Carbides such as silicon carbide (SiC) have high intrinsic TC and high thermal stability [49]. However, similar to ZnO, it is considered as a semi-conductor, which limits its applications in dielectric materials [50]. Furthermore, carbides are considered to have high hardness thus making them detrimental to melt processing equipment [52].

Intrinsic TC is only one factor required to have a highly conductive composite. A study evaluated the TC of composites made with different ceramic fillers with the difference between the fillers being solely based on their intrinsic TCs [53]. The ceramics used were Al_2O_3, BN, TiB2, and SiC all in an epoxy matrix. The result show that TC increases with higher filler loading, as hypothesized. Surprisingly the difference between Al_2O_3, TiB2, and SiC is negligible at similar loading values, despite the difference in their intrinsic thermal conductivities. Those three fillers reached a maximum of ~ 4 W/m.K at maximum loading of 45%. BN on the other hand, could be packed until 65% with TC value measured at 13 W/m.K. It is credited to the relatively soft nature of BN platelets, which allowed them to deform in the matrix and increased their packing factor, hence their contact area [53]. Nonetheless, such ceramics are relatively hard and are abrasive to the processing equipment leading to much higher production costs. Furthermore, a high loading increases the weight of the product, reduces some mechanical properties as well an increase in price, which are generally unfavourable [49].

1.4.2 Carbon-based fillers

An extensive review into carbon nanotubes (CNT) / polymer nanocomposites was published in 2011 [54]. Theoretically, single-walled carbon nanotube (SWCNT) should have a TC value of 6600 W/m.K at room temperature [55]. On the other hand, experimental values for MWCNT show that the value is closer to 3000 W/m.K, which is still one of the highest values for materials [56]. Similarly to ceramics, despite the fact of their high TC, CNT or other carbon-based filled polymer composites do not follow the theoretical rule of mixtures. The review by Han and Fina illustrated that discrepancy by comparing several results of carbon based composites with theoretical limits [54]. Undesirably, the measured result seem to be closer to the lower bound limit [54].

1.4.3 Metals

The addition of metallic particles not only increases the TC, but also the electrical conductivity. As mentioned earlier, the TC of electrically conductive material can range an order of magnitude greater than electrically isolative [45]. The large discrepancy is due to that the free electrons in metals are the main thermal energy carriers that travel much faster than phonons. However, this limits the applications in dielectric applications, but can be beneficial for heat management applications such as heat exchangers [49]. Furthermore, the addition of high density metallic fillers increases the total weight of the composite thus losing on the light-weighting advantage of polymers [54].

Metal powder and carbon-based filler hybrids have been studied to achieve a balance from both types of fillers [57]. The results show significant improvement in TC measured. It is believed that the presence of metal powder alone, below the 'percolation threshold' would not improve the transfer of thermal energy. This is due to the difference between the thermal carriers (electrons in metals and phonons in polymers) creating a thermal barrier. With the inclusion of MWCNT however, the transfer was enhanced as both the Al powder and MWCNT created a network of conductivity in the matrix [57].

1.4.4 Particle shape and size

Physically, a large interface area would increase phonon scattering and reduce TC, giving rise to the theoretical outcome that having large sized fillers would reduce the interfacial area and improve TC [50]. Furthermore, it is generally believed that usually fillers and polymers have mismatching polarities, the dispersion of nanofillers is difficult as agglomerates are created [49].

This is observed in the results of an experiment where for the same AlN, particles with average diameter 22 μm showed higher thermal conductivities at the same filler loading than particles with 4 μm diameter [58]. Yet, the results of several papers conclude that finer fillers are the recommended size for higher conductivity [59-61]. Those papers hypothesize that smaller particles can create thermal pathways (percolation networks) and hence reduce matrix/filler interface making thermal transport across the filler mainly. As observed, there are some discrepancies in particle size recommendations. The type of filler and its shape will govern the recommended size together with how well it bonds with the matrix. This is also seen in some studies on polymer/ceramic composites in that an increase then a decrease of the TC was

observed with increasing filler loading. This was attributed to the fillers creating agglomerates in the polymer matrix [62, 63]. This could be due to the processing methods used as they were electrospun in [62] and 3D printed in [63].

Lee *et al.* studied the effects of adding two different ceramic fillers to a HDPE matrix to create a hybrid thermal pathway and network [58]. AlN spheres with either SiC whiskers, or woolastonite were examined. The work was based on creating a thermal path network with a hybrid of filler shapes (spherical and acicular) to reduce filler content. The results show that for AlN spheres with woolastonite hybrid filler show an improved TC value even below the maximum packing factor (MPF) of the filler (60% in this case) despite the lower inherent conductivity of woolastonite. Above the MPF, the effect was negative as the AlN network was already existing. With SiC, that has higher TC than woolastonite, the effect was prominent throughout filler loading range.

To aid in creating percolation networks, some work have shown that adding the inorganic filler to an immiscible blend of two polymers will make the filler assemble at the interface between the two polymer phases, thus a network is introduced with low filler loading [50].

As for metallic powder filled polymers, the main conclusions were, similar to ceramic filled polymers, where the shape of the filler affects the packing factor and hence the thermal and electrical properties. The percolation threshold depends on the particle shape and size distribution [64].

1.4.5 Interfaces

Adding a high thermally conductive material will improve heat transport in the composite as thermal carriers travel faster in the filler than the polymer. Consequently, that difference in the phonon spectra (or electrons and phonons) introduces thermal resistance – known as the Kapitza thermal resistance [65]. Additionally, the interface will act as a phonon scattering point. This is one of the reasons believed why TC does not strictly follow the rule of mixtures [4]. If filler loading is low, the particles will be isolated in the matrix and a travelling phonon would face multiple matrix/filler interfaces and be scattered easily. If the loading is above the percolation threshold, a network of conductive fillers is created, thus the phonon will travel through this network instead of the matrix [4]. In order to maximise TC in a composite, one must maximise the thermal pathway network, minimise the thermal resistance of the filler and decrease the thermal resistance at the interfaces [66]. This is one of the reasons why high loadings of fillers is usually required to create a thermally conductive composite.

Various surface treatments on BN in an epoxy matrix were investigated in an experiment [66]. The results show significant improvement especially with silane treatment. It is believed that covalent bonds have formed between the filler and the matrix through the interface layer hence the higher conductivity [66]. It is worth noting that the results mentioned hold only for high filler loadings (57 wt.%).

Another study was done where ZnO particles in EVA matrix were used with several modifying and coupling agents [67]. The results show that conductivity was improved with all the studied treatments in varying degrees. Most treatments increased TC with the amount of modifying agent until an optimum point before decreasing. Signifying that with the added thickness of the interfacial layer, another thermal barrier was created. The best interface modifiers found in the experiment are the ones that created a covalent bond between the matrix and the filler [66, 67].

Another dimension of the metal powder/carbon based fillers study mentioned earlier, was modifying the filler/matrix interface [57]. For MWCNT, an electrostatically bonding improvement showed a 50% enhancement in TC. Yet, for that report's most positive result in TC, the 40% exfoliated graphite, an electrostatic attachment actually reduced the measured value. Metal coated carbon nanofibres such as Ag, Cu and Ni were experimented as well, however the result showed decrease in TC compared to untreated fibres [57].

1.4.6 Processing and anisotropy

Similar to chain alignment and stretching mentioned in the previous section, anisotropy is apparent in almost all polymer composites. Hence, the reporting of in-plane and out-of-plane measurements in data sheets of commercial thermal conductive polymers is essential. This emphasizes the effect of careful processing on the properties required for the final application.

Anisotropy was studied in the measurements of thermal diffusivity in BN filled PI films [68]. Focusing on the effects of the filler size, orientation, aggregation and chain rigidity of the polymer matrix. The results show high anisotropy in particles with high aspect ratios, as they are easily oriented during processing. Less anisotropy was found in aggregates and small flakes. Furthermore, using the more rigid polymer chains of PI gave rise to even higher anisotropy for the same filler as the chains also orient during processing [68]. These effects could explain some of the discrepancies observed in filler-size' effect mentioned earlier as different methods used in those studies could be biased to certain planes.

1.5 Summary

This review presented various methods of how polymer TC could be tuned. To increase TC, the focus was to increase the mean free path of phonons travelling through the polymer by reducing scattering events. The stretching of polymer chains lead to higher TC as observed in simulations on single molecules or fibres [12, 14, 38]. This is due to the high efficiency in thermal transport of carbon-carbon covalent bonds along the chains [15]. However, this increase in the property was observed anisotropically for fibres and foils. This is unfavourable in mass production as it limits some design aspects of the polymer products.

In commercial products, polymer matrix composites are readily available. Nonetheless, ceramic as well as metal fillers are abrasive to the processing equipment leading to much higher production costs [50]. Furthermore, high filler loading is usually required (>30 wt.%) to achieve thermal networks which leads heavier products [49, 54] Studies have shown that reduction in filler loading can be achieved by mixing two different fillers together or modifying the matrix/filler interface [58, 66]. But careful consideration to the coupling agent as well as the thickness of the interfacial layer is still problematic [67]. Furthermore, almost all polymer composites come with a high degree of anisotropy due to the shape of the fillers which raises limitations in product manufacturing and design [68].

Modifying intermolecular interaction is an upcoming route for tuning and improving polymer TC as observed in [32-34]. It was shown how designing polymer blend systems from the outset could tune the thermal pathways and manipulate the chain conformation. Moreover, the findings from crosslinking simulations and experimental studies show a different route in achieving an isotropic increase of TC [26, 29]. These routes give insight on how thermal energy is transported in a polymer system and how it is possible to create efficient phonon pathways.

1.6 Scope of the thesis

This thesis provides insight using polymers with model functional groups (PVAL), to discuss the various way in which solid-state structure is linked to overall thermal transport. This is achieved by using the same base polymer and keeping the processing of the samples invariable, thus, only the influence of the changes in structure is observed. We present novel multicomponent systems that are theorised to create unique solid-structures and in turn, tune the thermal transport.

Chapter 3 follows from the work of [32] on amorphous polymer blends and [33] on the important of hydrogen bonding and short polymer chains by using a polymer / oligomer blend. The addition of the relatively small molecules to the polymer matrix can influence local order as it is theorised to introduce localised chain extensions of the polymer matrix. In **Chapter 4**, organic / inorganic hybrids are investigated. New material properties are achieved by creating new chemical bonds between mixtures of two dissimilar materials. This produces a macromolecular network with attractive and tuneable properties. The unique structure is compared to a conventional composite to highlight the differences in the thermal conductivity based on solid-state structure and phonon pathways.

A polymer / polymer nanofibers system is proposed in **Chapter 5** using aramid nanofibers (ANF). The strong hydrogen bonding between the ANF and the PVAL is expected to present a distinctive structure that is more favourable to phonon transport. Comparing the rigid molecules of ANFs to the more flexible TEG oligomer, a larger impact on the thermal conductivity is predicted. Furthermore, as the structural changes proposed in this thesis are expected to be homogenous across the samples and systems, the thermal conductivity is expected to be isotropic. Finally, in **Chapter 6** we conclude with a summary and future outlook of the work in tuning the thermal conductivity of macromolecules to the final required properties.

1.7 References

1. Balandin, A.A., *Thermal properties of graphene and nanostructured carbon materials.* Nature Materials, 2011. **10**(8): p. 569-581.
2. Cahill, D.G., *Thermal conductivity measurement from 30 to 750 K: the 3ω method.* Review of Scientific Instruments, 1990. **61**(2): p. 802-808.
3. Regner, K.T., et al., *Broadband phonon mean free path contributions to thermal conductivity measured using frequency domain thermoreflectance.* Nature Communications, 2013. **4**: p. 1640.
4. Mehra, N., et al., *Chapter 3 - Thermal Conduction in Polymer Composites*, in *Polymer-Based Multifunctional Nanocomposites and Their Applications*, K. Song, C. Liu, and J.Z. Guo, Editors. 2019, Elsevier. p. 77-110.
5. Henry, A., *Thermal Transport in Polymers*. Vol. 17. 2014.
6. Qian, X., J. Zhou, and G. Chen, *Phonon-engineered extreme thermal conductivity materials.* Nature Materials, 2021. **20**(9): p. 1188-1202.
7. Callaway, J., *Model for Lattice Thermal Conductivity at Low Temperatures.* Physical Review, 1959. **113**(4): p. 1046-1051.
8. Parrott, J.E., *Thermal conductivity of solids / J.E. Parrott and Audrey D. Stuckes*. Applied physics series (Pion (Firm)) ; 8., ed. A.D. Stuckes. 1975, London: Pion.
9. Pop, E., V. Varshney, and A.K. Roy, *Thermal properties of graphene: Fundamentals and applications.* MRS Bulletin, 2012. **37**(12): p. 1273-1281.
10. Chanda, M. and S.K. Roy, *Plastics Technology Handbook, Fourth Edition*. 2006: CRC Press.
11. Fermi, E., J. Pasta, and S. Ulam, *Los Alamos Report No. LA1940: Studies on nonlinear problems.* 1955.
12. Henry, A. and G. Chen, *High thermal conductivity of single polyethylene chains using molecular dynamics simulations.* Phys Rev Lett, 2008. **101**(23): p. 235502.
13. Lienhard, J.H., *A Heat Transfer Textbook*. Fourth Edition ed. 2011, New York: Dover Publications.
14. Ma, H. and Z. Tian, *Chain rotation significantly reduces thermal conductivity of single-chain polymers.* Journal of Materials Research, 2019. **34**(1): p. 126-133.
15. Rubtsova, N.I., et al., *Room-temperature ballistic energy transport in molecules with repeating units.* The Journal of Chemical Physics, 2015. **142**(21): p. 212412.
16. Henry, A., et al., *1D-to-3D transition of phonon heat conduction in polyethylene using molecular dynamics simulations.* Physical Review B, 2010. **82**(14): p. 144308.
17. Choy, C.L., *Thermal conductivity of polymers.* Polymer, 1977. **18**(10): p. 984-1004.
18. Liu, J. and R. Yang, *Length-dependent thermal conductivity of single extended polymer chains.* Physical Review B, 2012. **86**(10): p. 104307-104315.
19. Zhang, T. and T. Luo, *Role of Chain Morphology and Stiffness in Thermal Conductivity of Amorphous Polymers.* The Journal of Physical Chemistry B, 2016. **120**(4): p. 803-812.
20. Anderson, D.R., *Thermal Conductivity of Polymers.* Chemical Reviews, 1966. **66**(6): p. 677-690.
21. Ueberreiter, K. and S. Purucker, *Spezifische Wärme, spezifisches Volumen, Temperatur- und Wärmeleitfähigkeit von Hochpolymeren.* Kolloid-Zeitschrift, 1955. **144**(1): p. 120-125.
22. Hansen, D. and C.C. Ho, *Thermal conductivity of high polymers.* Journal of Polymer Science Part A: General Papers, 1965. **3**(2): p. 659-670.
23. Tomlinson, J.N., D.E. Kline, and J.A. Sauer, *Effect of nuclear radiation on the thermal conductivity of polyethylene.* Polymer Engineering & Science, 1965. **5**(1): p. 44-48.
24. Ma, H. and Z. Tian, *Effects of polymer topology and morphology on thermal transport: A molecular dynamics study of bottlebrush polymers.* Applied Physics Letters, 2017. **110**(9): p. 091903.
25. Yamamoto, O. and H. Kambe, *Thermal Conductivity of Cross-linked Polymers. A Comparison between Measured and Calculated Thermal Conductivities.* Polymer Journal, 1971. **2**: p. 623-628.
26. Kikugawa, G., et al., *Effect of crosslink formation on heat conduction in amorphous polymers.* Journal of Applied Physics, 2013. **114**(3): p. 034302 -034306.

27. Ni, B., T. Watanabe, and S.R. Phillpot, *Thermal transport in polyethylene and at polyethylene–diamond interfaces investigated using molecular dynamics simulation.* Journal of Physics: Condensed Matter, 2009. **21**(8): p. 084219-084227.
28. Yu, S., et al., *Thermal conduction behaviors of chemically cross-linked high-density polyethylenes.* Thermochimica Acta, 2014. **583**: p. 67-71.
29. Rashidi, V., et al., *Thermal Conductance in Cross-linked Polymers: Effects of Non-Bonding Interactions.* The Journal of Physical Chemistry B, 2017. **121**(17): p. 4600-4609.
30. Steiner, T., *The hydrogen bond in the solid state.* Angewandte Chemie International Edition English, 2002. **41**(1): p. 49-76.
31. Mercx, F., *The Effect of In-Plane and Through-Plane Thermal Conductivity on LED Heatsink Performance*, in *AMI - Conductive Plastics 2015*. 2015, AMI.
32. Kim, G.H., et al., *High thermal conductivity in amorphous polymer blends by engineered interchain interactions.* Nature Materials, 2015. **14**(3): p. 295-300.
33. Mehra, N., L. Mu, and J. Zhu, *Developing heat conduction pathways through short polymer chains in a hydrogen bonded polymer system.* Composites Science and Technology, 2017. **148**: p. 97-105.
34. Mehra, N., M.A. Kashfipour, and J. Zhu, *Filler free technology for enhanced thermally conductive optically transparent polymeric materials using low thermally conductive organic linkers.* Applied Materials Today, 2018. **13**: p. 207-216.
35. Shanker, A., et al., *High thermal conductivity in electrostatically engineered amorphous polymers.* Science Advances, 2017. **3**(7): p. 1700342-1700350.
36. Fujishiro, H., et al., *Thermal Conductivity and Diffusivity of High-Strength Polymer Fibers.* Japanese Journal of Applied Physics, 1997. **36**(9R): p. 5633 - 5637.
37. Wang, X., et al., *Thermal Conductivity of High-Modulus Polymer Fibers.* Macromolecules, 2013. **46**(12): p. 4937-4943.
38. Shen, S., et al., *Polyethylene nanofibres with very high thermal conductivities.* Nature Nanotechnology, 2010. **5**(4): p. 251-255.
39. Kakade, M.V., et al., *Electric Field Induced Orientation of Polymer Chains in Macroscopically Aligned Electrospun Polymer Nanofibers.* Journal of the American Chemical Society, 2007. **129**(10): p. 2777-2782.
40. Lu, C., et al., *Thermal conductivity of electrospinning chain-aligned polyethylene oxide (PEO).* Polymer, 2017. **115**: p. 52-59.
41. Singh, V., et al., *High thermal conductivity of chain-oriented amorphous polythiophene.* Nature Nanotechnology, 2014. **9**(5): p. 384-390.
42. Mohammad, F., P.D. Calvert, and N.C. Billingham, *Thermal stability of electrochemically prepared polythiophene and polypyrrole.* Bulletin of Materials Science, 1995. **18**(3): p. 255-261.
43. Mergenthaler, D.B., et al., *Thermal conductivity in ultraoriented polyethylene.* Macromolecules, 1992. **25**(13): p. 3500-3502.
44. Ghasemi, H., et al. *High thermal conductivity ultra-high molecular weight polyethylene (UHMWPE) films*. in *Fourteenth Intersociety Conference on Thermal and Thermomechanical Phenomena in Electronic Systems (ITherm)*. 2014.
45. Sherman, L. *Plastics That Conduct Heat*. 2001 [cited 2018 28/2/2018]; Available from: https://www.ptonline.com/articles/plastics-that-conduct-heat.
46. Liang, J.Z. and G.S. Liu, *A new heat transfer model of inorganic particulate-filled polymer composites.* Journal of Materials Science, 2009. **44**(17): p. 4715-4720.
47. Bigg, D.M., *Thermal conductivity of heterophase polymer compositions*, in *Thermal and Electrical Conductivity of Polymer Materials*. 1995, Springer Berlin Heidelberg: Berlin, Heidelberg. p. 1-30.
48. Nielsen, L.E., *The thermal and electrical conductivity of two-phase systems.* Industrial Engineering Chemistry Fundamentals, 1974. **13**(1): p. 17-20.
49. Guo, Y., et al., *Factors affecting thermal conductivities of the polymers and polymer composites: A review.* Composites Science and Technology, 2020. **193**: p. 108134 - 108159.
50. Huang, X., P. Jiang, and T. Tanaka, *A review of dielectric polymer composites with high thermal conductivity.* IEEE Electrical Insulation Magazine, 2011. **27**(4): p. 8-16.

51. Zhi, C., et al., *Towards Thermoconductive, Electrically Insulating Polymeric Composites with Boron Nitride Nanotubes as Fillers.* Advanced Functional Materials, 2009. **19**(12): p. 1857-1862.
52. Bansal, N.P., *Handbook of ceramic composites*. 2005, Boston: Kluwer Academic Publishers.
53. Hill, R.F. and S.H. Peter, *Thermal Conductivity of Platelet-Filled Polymer Composites.* Journal of the American Ceramic Society, 2002. **85**: p. 851-857.
54. Han, Z. and A. Fina, *Thermal conductivity of carbon nanotubes and their polymer nanocomposites: A review.* Progress in Polymer Science, 2011. **36**(7): p. 914-944.
55. Berber, S., Y.-K. Kwon, and D. Tománek, *Unusually High Thermal Conductivity of Carbon Nanotubes.* Physical Review Letters, 2000. **84**(20): p. 4613-4616.
56. Kim, P., et al., *Thermal Transport Measurements of Individual Multiwalled Nanotubes.* Physical Review Letters, 2001. **87**(21): p. 215502-215506.
57. Ghose, S., et al., *Thermal conductivity of ethylene vinyl acetate copolymer/nanofiller blends.* Composites Science and Technology, 2008. **68**(7-8): p. 1843-1853.
58. Lee, G.-W., et al., *Enhanced thermal conductivity of polymer composites filled with hybrid filler.* Composites Part A: Applied Science and Manufacturing, 2006. **37**(5): p. 727-734.
59. Lu, X. and G. Xu, *Thermally Conductive Polymer Composites for Electronic Packaging.* Journal of Applied Polymer Science, 1997. **65**: p. 2733-2738.
60. Kemaloglu, S., G. Ozkoc, and A. Aytac, *Thermally conductive boron nitride/SEBS/EVA ternary composites: "Processing and characterization".* Polymer Composites, 2009: p. 1398-1408.
61. Zhou, W., et al., *A novel fiber-reinforced polyethylene composite with added silicon nitride particles for enhanced thermal conductivity.* Composites Part A: Applied Science and Manufacturing, 2009. **40**(6-7): p. 830-836.
62. Zhang, D.-L., et al., *Enhanced thermal conductivity and mechanical property through boron nitride hot string in polyvinylidene fluoride fibers by electrospinning.* Composites Science and Technology, 2018. **156**: p. 1-7.
63. Guiney, L.M., et al., *Three-Dimensional Printing of Cytocompatible, Thermally Conductive Hexagonal Boron Nitride Nanocomposites.* Nano Letters, 2018. **18**(6): p. 3488-3493.
64. Mamunya, Y.P., et al., *Electrical and thermal conductivity of polymers filled with metal powders.* European Polymer Journal, 2002. **38**(9): p. 1887-1897.
65. Liao, B. and G. Chen, *Nanocomposites for thermoelectrics and thermal engineering.* MRS Bulletin, 2015. **40**(09): p. 746-752.
66. Xu, Y. and D.D.L. Chung, *Increasing the thermal conductivity of boron nitride and aluminum nitride particle epoxy-matrix composites by particle surface treatments.* Composite Interfaces, 2012. **7**(4): p. 243-256.
67. Lee, B. and G. Dai, *Influence of interfacial modification on the thermal conductivity of polymer composites.* Journal of Materials Science, 2009. **44**(18): p. 4848-4855.
68. Tanimoto, M., et al., *Anisotropic Thermal Diffusivity of Hexagonal Boron Nitride-Filled Polyimide Films: Effects of Filler Particle Size, Aggregation, Orientation, and Polymer Chain Rigidity.* ACS Applied Material & Interfaces, 2013. **5**(10): p. 4374-4382.

2 Materials and characterisation techniques

2.1 Materials and solutions

2.1.1 PVAL solutions in water

PVAL was purchased from Sigma – Aldrich. Mowiol®18-88 that is 88% hydrolysed and has a weight-average molecular weight, $M_w \approx 130{,}000$ g/mol. It was used to prepare the PVAL - tetraethylene glycol (TEG) blends, PVAL / titanium oxide hydrate hybrids, and PVAL – TiO_2 composites. The concentration of PVAL used was 60 mg/ml for all materials systems, by dissolving the required amount in deionised water (DIW). The PVAL solution was kept stirring at 90°C overnight at 400 rpm to dissolve the polymer completely. It was then stored in a refrigerator until being used when it was allowed to reach room temperature before mixing with other solutions. Prior to mixing, the solution was filtered using a Supor® syringe filter with a pore size of 0.45 μm.

2.1.2 PVAL solutions in DMSO

PVAL was purchased from Sigma – Aldrich with average $M_w \approx 130{,}000$ g/mol and 99% hydrolysed. PVAL was dissolved in dimethyl sulfoxide (DMSO) purchased from VWR which has < 0.03% water. The required amount of PVAL was added to DMSO and mixed at 70°C for 2 hours to obtain homogenous, clear solutions with concentrations of 40 mg/ml. Solutions were then filtered using a nylon syringe filter with a pore size of 0.45 μm. This PVAL solution was used for the PVAL – Aramid nanofibers (ANF) systems. Solutions were stored at room temperature.

2.1.3 Tetraethylene glycol (TEG) solutions

TEG was purchased from Sigma-Aldrich with a number-average molecular weight M_n of 200 g/mol. The required amount was added to DIW to create a 6 wt.% solution. The solutions were kept stirring for at least 1 hour before mixing. They were stored in a refrigerator and allowed to reach room temperature before usage.

2.1.4 TiO_2 suspensions

Titanium(IV)oxide anatase nanopowder with < 25 nm particle size was purchased from Sigma – Aldrich. The required amount was added to DIW to create a 5 wt.% suspension. The suspension was sonicated for 20 minutes, and then stirred for one hour to prevent large agglomerates to form. It was then extracted by pipettes while it was being stirred and mixed with PVAL solutions to create PVAL – TiO_2 composite solutions.

2.1.5 Titanium oxide hydrates

Titanium oxide hydrates were used to prepare organic / inorganic hybrids as described by Russo *et al.*[1] and other studies [2-4]. The titanium oxide hydrate is prepared via the hydrolysis of the titanium precursor. The precursor used here is titanium tetrachloride, $TiCl_4$, 99.9 % trace metal basis purchased from Sigma - Aldrich. The hydrolysis step is fast due to the halide nature of the precursor and is highly exothermic. The required amount of precursor was placed in a column and slowly added (~1 drop/second) in to a round bottom flask with the required amount of water to create a 2 M concentration of Ti in the final solution. To avoid the condensation of the metal oxide hydrate, the flask was placed in an ice bath and a magnetic stirrer is used for agitation [1, 3, 5]. The set-up is shown in Figure 7 below. The hydrolysis in its simplistic form can be described as follows:

$$TiCl_4 + XH_2O \rightarrow TiO_xH_{2X-4} + 4HCL \quad (2.1)$$

However, the hydrolysis reaction can be very complex as to whether mononuclear or polynuclear species of the hydrate are created. A more realistic hydrolysis reaction was described by Nussbaumer *et al.* [6] :

$$TiCl_4 + (a+b)H_2O \rightarrow TiO_a(OH)_bCl_c^{\alpha} + (2a+b)H^+ + (4-c)Cl^- \quad (2.2)$$

Where $\alpha = 4 - 2a - b - c$.

The hydrate solution was prepared and stored in a freezer at -5ºC to avoid such hydrolysis reactions and the creation of titanium dioxide particles.

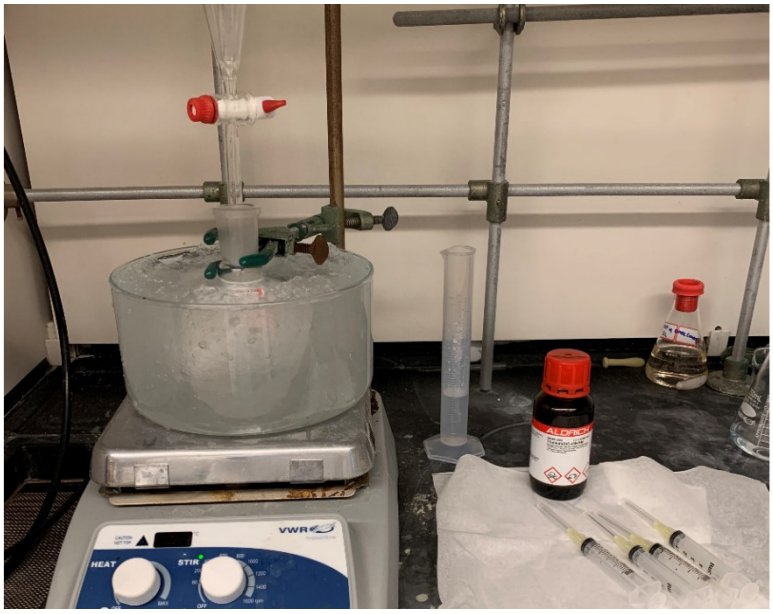


Figure 7: $TiCl_4$ hydrolysis set up. A round bottom flask with the required amount of DIW is placed in an ice bath on top of a magnetic stirring stage. The $TiCl_4$ is measured with syringes and added to the column above. The valve at the neck is then slowly opened to allow a steady, 1 drop/sec flow to be introduced to the water in the flask.

2.1.6 PVAL / titanium oxide hydrate hybrids

Russo *et al.* first introduced the preparation of PVAL / titanium oxide hydrate hybrids [5]. They are based on the condensation of the functional groups of the PVAL and titanium oxide hydrate by creating new covalent bonds between the polymer and the inorganic component. Mononuclear or polynuclear amorphous networks can thus be created between the PVAL chains and the inorganic species. Indeed, only at high inorganic content (>80% vol.), titanium oxide nanoparticles can be observed, [3] while PVAL – titanium oxide hydrate networks resemble a cross-linked polymer system as reported in previous studies and shown further in this thesis [1-4]. Figure 8 illustrates the hybrid structure.

The hydrate solutions were removed from the freezer and allowed to reach room temperature before mixing. PVAL solutions with 6 wt.% concentration were mixed with 1 M titanium oxide hydrate solutions to create the hybrids. The solutions were kept stirring at room temperature for one hour before deposition to ensure homogeneity. However, these hybrid solutions are not stable for long periods as condensation reactions may occur. This can lead to a gel is after a few hours of stirring especially at lower inorganic content (10-30% vol.). All hybrid films were left to age in a desiccator for ~7 days [4]. Films were then hydrothermally annealed in a humidity oven at 80ºC for 1 minute to promote further condensation reactions and remove residual chlorine before any measurements were performed [2, 4].

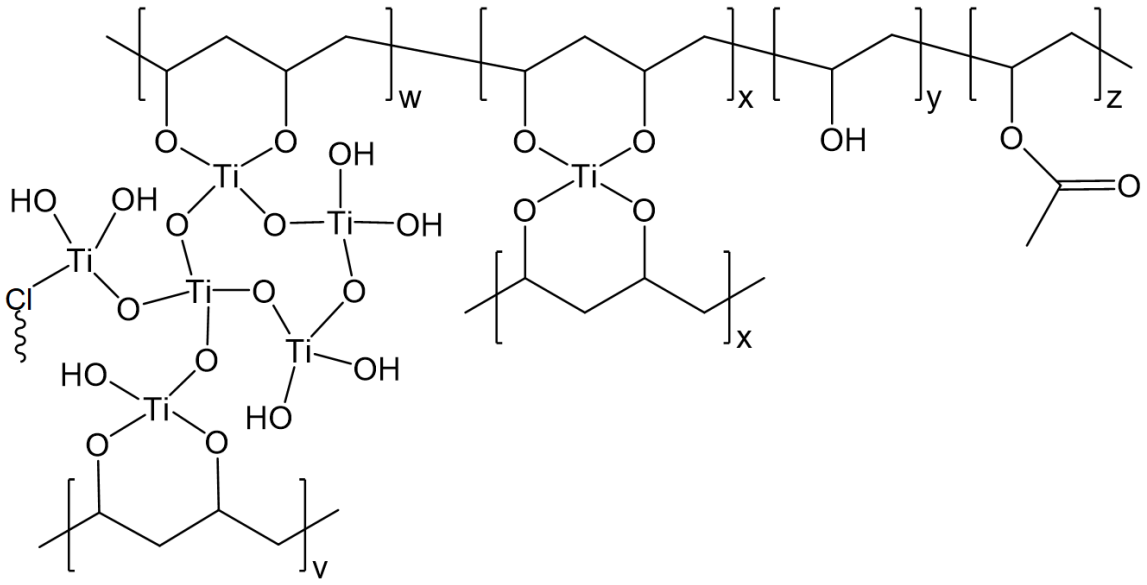


Figure 8: PVAL / titanium oxide hydrate hybrid structure. On the left, a polynuclear titanium oxide hydrate connects to separate PVAL chains. This polynuclear form is more likely to be present in higher inorganic content hybrids. In the middle, a mononuclear PVAL / titanium oxide hydrate network is illustrated. Covalent bonds are created between the titanium atoms and the PVAL as well as hydrogen bonds with the remaining hydroxyl groups. Some residual chlorine is present as well. The segments on the right depict unreacted PVAL chain with residual acetate.

2.1.7 Preparation of aramid nanofiber dispersions (ANF)

Aramid (p-phenylene terephthalamide (PPTA)) nanofibers are prepared following the method first described by Yang, M. *et al.* [7]. It was shown that by adding aramid microfibers in a solution of DMSO and potassium hydroxide (KOH), a controlled, slow deprotonation of the N-H bond follows. This breaks down the intermolecular hydrogen bonds. Figure 9 depicts the structure of PPTA molecules. Further electrostatic repulsion between the molecules, creates a stable dispersion of aramid nanofibres [7]. Further experimentation by Yang, B. *et al.* [8], presented faster methods to obtain such ANF fibres by either mechanical agitation, higher temperatures, or reduction of viscosity. The method used in this thesis was by mechanical agitation using a sonication bath and a slightly elevated temperature. Twaron 1055 yarn para-aramid fibres were obtained from Teijin Aramid. A solution of DMSO and required amount of KOH were left to dissolve for 20 minutes at 45ºC. Aramid fibres were cut to ease initial dispersion then added to the solution. After all the fibres were added, the bottle was moved to a sonication bath and was agitated for one hour to break up most of the fibres and speed up the process of deprotonation. The bottle was then moved to a stirring hot plate at 45ºC and kept stirring overnight until a clear, dark red solution was obtained. The final concentration was 2 mg/ ml. The dispersion was stored at room temperature.

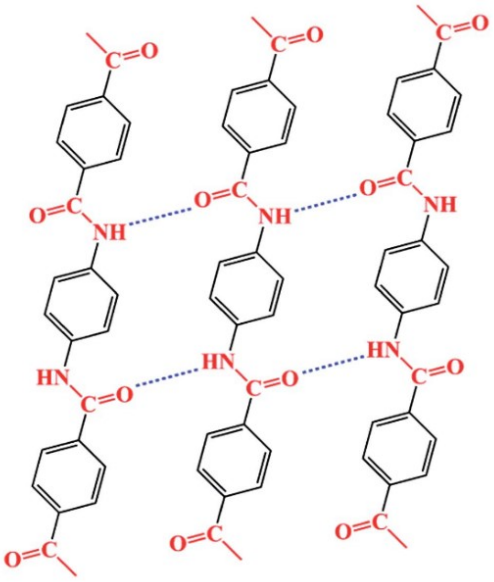


Figure 9: PPTA para-aramid structure. The para structure relates to the amide groups being linked to the aromatic rings at the 1 and 4 positions. Hydrogen bonding occurs between the amine and carbonyl groups highlighted in red. I Reproduced from [9] with permission from the Royal Society of Chemistry.

2.1.8 Preparation of PVAL/ANF solutions

Previous studies using ANFs with polymers have a step of isolating and protonating the ANFs before incorporating them in different systems [7, 8, 10, 11]. The isolation step was usually prepared by solvent substitution, and then followed by vacuum assisted filtration. In this thesis, no isolation step was taken. In Yang, M. *et al.'s* work, the ANFs appear to have a distribution of lengths from 200 nm up to 10 µm after protonation [7]. Due to that, the ANF dispersion was first filtered using a syringe filter with a nylon membrane having a pore size of 0.45 µm to limit the length of the dispersed fibres. The filtered dispersion was then mixed with PVAL in DMSO solution at room temperature. The solutions were kept stirring for one hour before deposition. However, similar to the PVAL / titanium oxide hydrate hybrid solutions, they were not stable for long times and a gel seems to be formed within the solution after one day. This is especially prominent with low ANF loading of 2.5 wt.%. Spin coated films prepared from these solutions were further annealed at 75°C for 3 minutes to speed up the solvent evaporation as DMSO has a high boiling point.

2.2 Film deposition methods

Throughout this thesis, two main film deposition techniques have been used. It is crucial to note that the dynamics of film formation is directly related to the properties observed and each technique would produce films with different features. It is also worth noting the similarities between the solution processing techniques used here and their counterparts in melt processing. For example, spin coating, where the solvent evaporates quickly, is similar to the fast quenching of molten polymer in injection moulding. Drop casting on the other hand, would be similar to compression moulding with the slow cooling rate [12].

2.2.1 Substrates

Glass substrates have been purchased from VWR in the form of microscope slides. They are 1mm thick and have been cut to 10 x 10 mm squares. These were cleaned in a sonication bath with acetone and isopropanol for 10 minutes and then dried with nitrogen. After drying, they were placed in the UV-ozone chamber to activate the surface before depositions. Silicon and sapphire substrates were used for the 3-ω technique. Undoped silicon wafers were purchased from University Wafers with a crystal orientation <100>, > 20,000 Ω resistance and 525 μm thickness. They were cut into 10 x 10 mm squares and cleaned as the glass substrates before film depositions. Sapphire substrates were purchased from Ossila with a surface orientation in the C-plane. The dimensions were 1.1 mm thick, 20 mm width and 15 mm length. They had a coarse finish with a surface roughness of ~ 0.7 nm. These were not cut further and were cleaned as the rest of the substrates.

For drop cast films, PS crucibles, either a petri dish of 55 mm diameter or a square container with 15 x 15 x 10 mm dimensions, were purchased from VWR and cleaned with isopropanol and dried with nitrogen before casting the solutions in them.

2.2.2 Spin coating

Spin coating is a useful technique when a small area film needs to be prepared. The solution (or ink) is dropped on the substrate and the centripetal force is used to spread it. This creates an even thin film after all the remaining solvent has evaporated. The desired thickness can be obtained by controlling the speed of rotation (faster spinning leads to thinner films) and the viscosity of the ink (more viscous solutions, lead to thicker films). The fast spinning and evaporation rate, freezes molecules in a higher entropy state. Furthermore, most of the solution is lost during the spreading stage, which could be costly for expensive materials [13]. Figure ***10*** describes the three stages of spin coating.

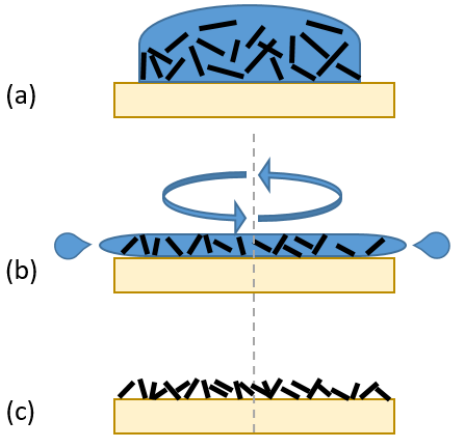


Figure 10: Diagrams showing the stages of the spin coating technique. The solution is first placed on the substrate that is held by a rotating platform (a). The platform and the substrate are then spun at high speeds and at specified times to spread the solution. Most of the ink is ejected from the substrate in this stage (b). The solvent is then evaporated and a solid, dry, thin film is left on the substrate (c).

2.2.3 Drop casting

Drop casting is one of the simpler methods of preparing a film from solution. The solution is dropped on a substrate or in a crucible and the solvent evaporates after time and a film is left behind. The rate of evaporation can be increased by placing the substrate on a hot plate and increasing the temperature. This would also affect the formation and structure of the film. With this method, hardly any material is lost and usually thick films are prepared. However, the films are usually not homogenous in thickness and it is slow in comparison to spin coating. Figure ***11*** illustrates the stages of drop casting.

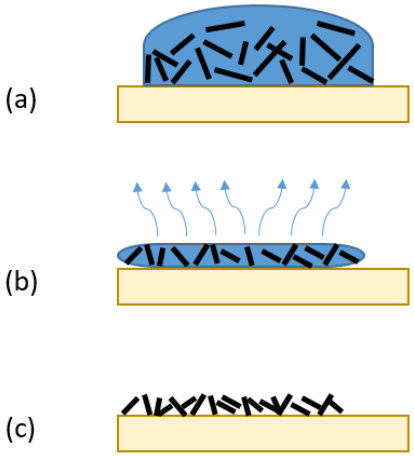


Figure 11: Diagram showing the stages of drop casting. The solution is first dropped on a clean substrate or crucible (a). Then the solvent slowly evaporates and a film starts to form (b). After all the solvent has been evaporated, a film is created on the substrate (c)

2.3 Solid – State Spectroscopy characterisation

2.3.1 Raman spectroscopy

Raman spectroscopy is an electromagnetic vibrational spectroscopy technique used in the analysis of materials. It based on the interaction between electromagnetic waves and the vibrations of atoms and molecules in a material. The energies of molecular and atomic vibrations of organic materials are usually in the range of visible and near infrared electromagnetic waves. The interactions detected are either absorption or scattering. Such vibrational spectroscopy techniques are non-destructive, reasonably quick (in the order of seconds or minutes), and can be obtained from gasses, liquids or solids. It is mainly used on organic or inorganic materials but metallic materials are incompatible as they mostly reflect the incident light [14].

Choosing the right laser wavelength is dependent on the material being investigated [14, 15]. If the sample is thin enough, background photoluminescence from the substrate can occur and thus shadowing material's signal [15]. As light interacts with a material, it can be either reflected, absorbed or scattered. When the incident light is scattered after interacting with a material, it can do so either elastically or inelastically. Elastic scattering is where the energy is conserved but a change in direction occurs. This is also called Rayleigh scattering. For inelastic scattering, the scattered light can have a higher or lower energy than the incident light. Considering that the inelastic scattered photons can have a higher or lower energy than the incident photon, Raman scattering is thus split into Stokes Scattering ($\lambda_{scattered} > \lambda_{incident}$) and anti-Stokes scattering ($\lambda_{scattered} < \lambda_{incident}$). Figure 12 below illustrates these conditions. As the intensity of anti-Stokes scattering is usually much lower than Stokes scattering, most Raman spectra are obtained by detecting the latter [14, 16]. In order for a molecule vibration to exhibit Raman scattering, must have vibrational modes that are Raman active. Vibrational modes in molecules can be either stretching or bending of bonds between nuclei. A change in polarizability in a molecule based on the stretching or bending of bonds renders the vibrational mode Raman active. A change in the dipole moment on the other hand makes the mode Infrared active [14]. In some cases, the incident photon's energy corresponds with an optical transition of the material. This results in a much stronger Raman signal and is called resonance Raman scattering [17].

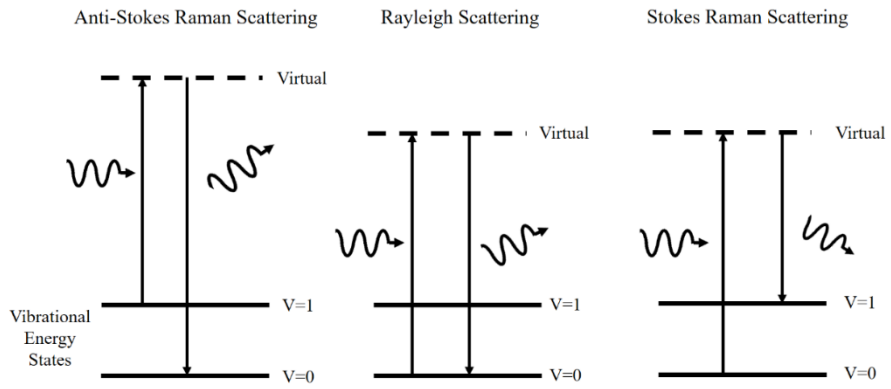


Figure 12: Schematic describing the different scattering events an incident photon can have when interacting with a molecule. Anti-stokes scattering on the left shows an increase of the photon's energy after interaction. In Rayleigh scattering, which is the most dominant type, the photon energy is constant and elastic scattering is observed. In Raman scattering, the incident photon loses energy and the scattered photon is observed to have less energy.

Most Raman instruments use an optical microscope to focus the incident beam on the sample. Hence the name Raman microscopy. Simply described, the incident photons are a continuous laser beam focused by an optical microscope on the sample. The same lens then collects the scattered photons. Those photons are passed through a holographic filter to separate them from the incident high intensity laser beam. They are then passed through a diffraction grating before reaching a charge-coupled device (CCD) detector. [14]

2.3.1.1 Choosing the right substrate and wavelength for Raman

At first, silicon wafers were used as substrates for the films. The results from that showed the Si spectra overlapping the PVAL trace as it had a stronger observed signal [18]. This is shown in Figure 13.

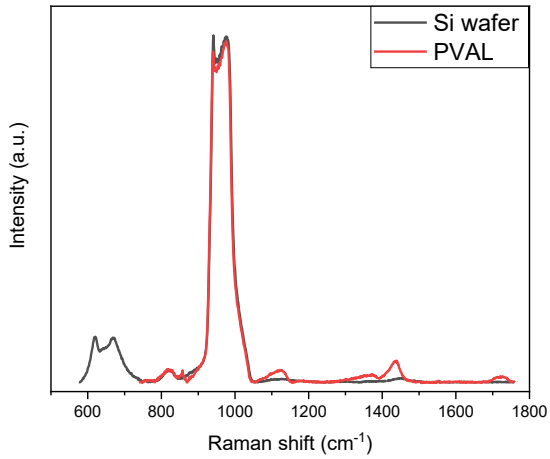


Figure 13: Raman spectra of silicon wafer and PVAL film deposited on silicon wafer. The signal from the silicon bands (900-1050 cm^{-1}) overshadow the PVAL band signals.

The same issue happened when a quartz substrate was used. The quartz's signal overshadowed the PVAL bands and differences could not be discerned.

Further investigation on the above showed how the substrate affects the obtained Raman signal and which substrate is best used based on the sample/material being measured [18]. Merlen *et al.* [19], showed how a simple substrate used for Surfaced Enhanced Raman Spectroscopy (SERS) can be prepared. A glass substrate sputtered with a thin layer of gold can create a SERS effect. By depositing the correct thickness of gold in relation to the wavelength of the excitation laser used in Raman spectroscopy, a characteristic Raman signal can be obtained. Then the parameters of the laser power, accumulation time and number of accumulations can be varied to obtain a clearer signal.

To test this, a previously prepared film of 10% wt. TEG in PVAL on a 3-ω chip was used. The chip had a pre-patterned gold electrodes and the film was deposited on top by spin coating. The laser can be focused on the part of the film above the gold electrode to observe the SERS effect. The Raman spectra obtained can be seen in Figure 14.

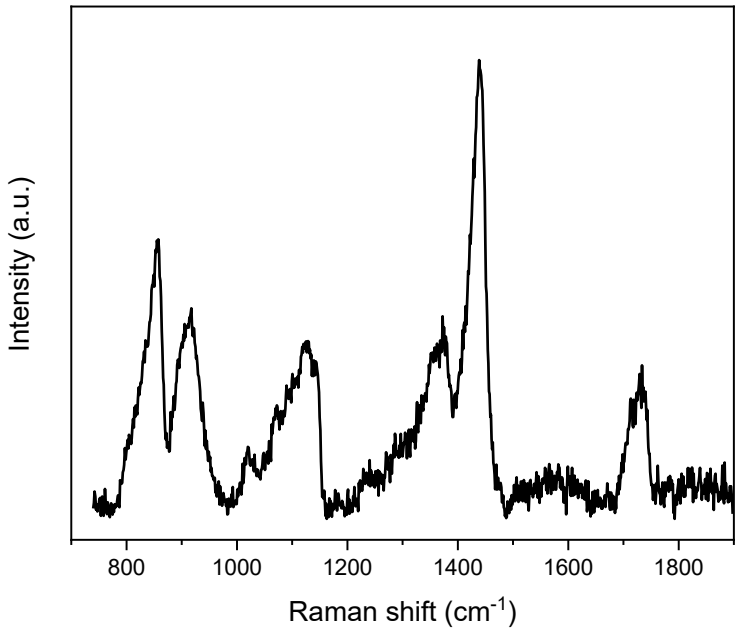


Figure 14: Raman spectra of 10% TEG film obtained from onto of the gold electrode on a 3-ω chip. The signal showed the distinct peaks of PVAL.

2.3.1.2 Raman sample preparation

To prepare the correct substrates, microscope glass slides were cut in to squares of 10 x 10 mm. They were then cleaned with acetone and isopropanol in a sonication bath for 10 minutes each. Then mounted on SEM stubs and placed in a gold sputtering apparatus (Emitech K675x). Sputtering times used were 45 seconds coating time for the 785 nm laser or 30 seconds when using the 633 nm laser. All substrates prepared using 40 mA of current and under $5x10^{-2}$ mbar pressure. Parameters used following work found in [19]. The SERS substrates prepared by the parameters above were used for all Raman measurements. Solutions were prepared and deposited directly on the gold films by spin coating and stored in desiccators for at least two days before measurements. Hybrid samples were kept for 1 week before hydrothermal annealing similar to other measurements.

2.3.1.3 Raman signal acquisition

Renishaw inVia Raman microscope was used for all samples. As two different equipment were used during this study, two different lasers were used; 785 nm and 633 nm HeNe lasers based on availability. The gold sputtering thickness was chosen according to the laser source used. The lens used to focus the laser was 100x objective. Microscope calibrated with Si reference and CCD, optics, and grid were auto aligned and calibrated using WiRE™ software before each session. The spectral resolution for both apparatuses was 0.5 cm^{-1} based on the diffraction grating, detector, and optical setup. Value of resolution given by equipment manufacturer [20]. For the PVAL –TEG blends, PVAL / titanium oxide hydrate hybrids, and PVAL – TiO_2 composites, 30 seconds acquisition time and four accumulations were used. For the PVAL – ANF systems, 50 seconds and 5 accumulations were used instead. Laser power was at 100% for the PVAL – TEG samples but reduced to 50% for PVAL – ANF systems and 10% for the hybrids and composites.

2.3.1.4 Raman signal processing

Only cosmic ray anomalies were removed using the WiRE™ software, all other signal processing were done using Origin. Spectra was smoothed using the Savitzky-Golay method, 10 pts window and a 2^{nd} order polynomial. Baselines were removed using asymmetric least squares method with asymmetric factor 0.0001, threshold: 0.02, smoothing factor: 4, and 10 iterations. Normalisation of PVAL – TEG blends was made by dividing with the peak at 2800 cm^{-1} and all the rest normalised between 0 – 100 for clearer representation. Peak fittings were performed using Voigtan profiles using Origin software on all vibration modes for consistency. The peak fitting were performed on windows of the spectra (e.g. from 700-1000 cm^{-1}) and the

least amount of peaks were chosen based on previous literature and the current signals to have the best fit. Some iterations on the peak fitting parameters were done to reach the best R squared value (e.g. no negative intensity peaks were allowed).

2.3.2 Fourier transform infrared spectroscopy (FTIR)

Similar to Raman Spectroscopy, FTIR, is an electromagnetic vibrational spectroscopy technique to characterise materials. It is based on the interactions between light and atomic and molecular vibrational modes [14]. Table 1 and Figure 15 below summarise the differences between Raman and FTIR spectroscopy.

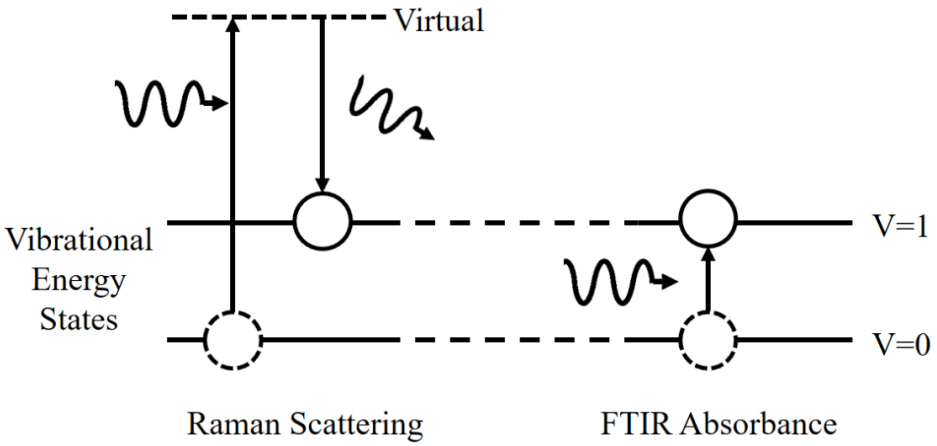


Figure 15: Energy state difference between Raman spectroscopy based on scattering and FTIR spectroscopy based on absorbance.

Table 1: Comparison between FTIR and Raman spectroscopy

	FTIR	**Raman**
Light source wavelength	Globar (heated silicon carbide) 2500 – 25000 nm	Laser in visible-IR region (most common are 532nm, 638nm, 785nm and 1064nm)
Based on	Light absorption	Light scattering
Vibrational active modes	Change in dipole moment	Change in polarizability
Molecular bond types	Ionic bonds give strong signals	Covalent bonds give strong signals

2.3.2.1 Attenuated Total Reflectance FTIR – (ATR-FTIR)

ATR is one of the more common setups for obtaining an IR spectrum. It is based on the total internal reflectance of the IR light inside a crystal with high refractive index such as diamond or germanium. The alignment of the incident angle is critical to create the evanescent wave just above the crystal where the sample is placed. The penetration depth is around 0.5 µm to 2 µm thus making it suitable for thin films or laminates [21]. The diagram in Figure 16 describes the set-up.

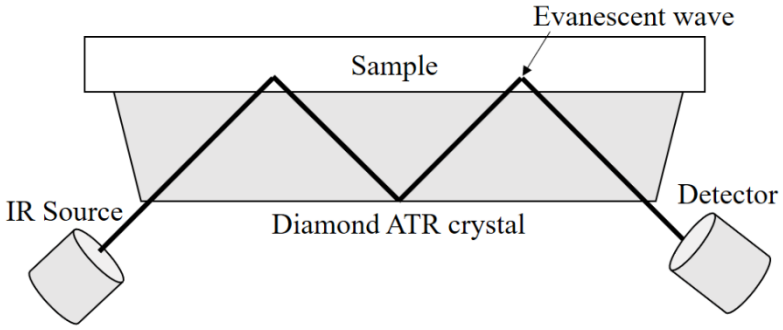


Figure 16: ATR-FTIR set-up depicting where the signal is generated and detected. The light source is positioned to obtain an evanescent wave within the sample. The penetration depth is 0.5 µm to 2 µm.

2.3.2.2 FTIR Sample preparation & signal acquisition

PVAL – TEG, PVAL – TiO_2 composites, and PVAL / titanium oxide hydrate hybrids were all drop cast from solution in PS square crucibles. PVAL – ANF samples were drop cast on clean glass slides as DMSO dissolves PS. They were then stored in a dissector for around 3 days before measurements. The equipment used was Agilent Cary-630 FTIR with a diamond ATR crystal. Film samples (~1 µm) were peeled off from the PS crucibles, placed on top of the ATR crystal. PVAL – ANF films were placed directly face down on the crystal. Signals obtained in transmission mode between 4000 – 650 cm^{-1}, resolution of 2 cm^{-1} and with 32 scans. Background signal was obtained before each measurement.

2.3.3 Brillouin light scattering (BLS) spectroscopy

BLS spectroscopy is another electromagnetic spectroscopic technique based on the inelastic scattering of light similar to Raman spectroscopy. However, Raman scattering is between the incident light and molecules but BLS, it is between the light and the acoustic phonons in the material [22, 23]. It is an alternate, non-destructive method of measuring the elastic modulus as opposed to the more traditional tensile test [24]. Here, contrasts based on changes of mechanical properties are utilised to characterise the material rather than chemical composition observed in Raman. This is given by the following relationship:

$$\omega_B = \frac{2\,n}{\lambda}\sqrt{\frac{M}{\rho}}\,\sin(\frac{\theta_s}{2}) \qquad (2.3)$$

Where ω_B is the Brillouin shift, n & ρ are the material's refractive index and density respectively, λ is the excitation wavelength, M is longitudinal modulus, and θ_s is the scattering angle [22].

2.3.3.1 BLS sample preparation and data analysis

Only PVAL – TEG systems were measured using BLS. Other systems proved difficult to obtain the correct thicknesses and film quality for a clean signal. The films were prepared by spin coating to have as similar properties as possible to samples prepared for Raman and thermal conductivity measurements. PVAL – TEG samples were spin coated on clean glass substrates to obtain thicknesses greater than 1μm. An excitation laser from a cobalt source was used generating a 561 nm wavelength. An oil emersion objective lens (UPlanSApo 60x, NA =1.35) was used to avoid reflectance of scattered light due to large refractive index mismatch between the film and the air. PVAL – TiO_2 composites and PVAL – ANF films could not be produced without altering the concentrations of the solutions which will change observed signals from the films made previously. PVAL / titanium oxide hydrate hybrids films could be made by spin coating multilayers of the films to create a 1 μm film, however the signal showed some reflection that could be due to the Fabry-Pérot oscillations and the excitation laser falling on a trough of those oscillations.

The Brillouin shifts were calculated from the spectra using the method found in [22]. It is based on the distances between the Rayleigh, Stokes and anti-Stokes peaks measured. It is given as follows:

$$\omega_B = \frac{1}{2}\,(FSR - \Delta\mathrm{f}) \qquad (2.4)$$

Where FSR is the free spectral range (the distance between the first and 2nd Rayleigh peaks) and Δf is the distance between the first anti-Stokes peak and the second Stokes peak. A detailed description of the method can be found in [22].

To calculate the sound velocities, a system-based approach was used to calibrate the Brillouin shifts with six known materials: DIW, Methanol, 1-Propanol, Ethanol, Glycerol, and Mono Ethylene glycol. The corresponding velocities were then corrected with their refractive indices and a regression line was made. For the BLS system used here, the equation was

$$V = 277.21 \times \omega_B \qquad (2.5)$$

2.3.4 X-ray photoelectron spectroscopy (XPS)

X-ray photoelectron spectroscopy technique based on the interaction of x-rays and the electron shell around the atoms in a sample. It is surface sensitive and information is taken from the top few nanometres of the film. The electrons are emitted due to the energy of the incident beam and are knocked out of the electron shell. A detector then separates the electrons based on their kinetic energies and counts them. From the measured kinetic energy E_k, the electron binding energy E_b can be calculated using the following equation:

$$E_b = h\upsilon - E_k - \Phi \qquad (2.5)$$

Where h is Plank's constant, ν is the frequency and Φ is a parameter related to the energy required for the electron to escape from the surface. Information on stoichiometry, composition, chemical and electronic states of the material can be inferred from the spectra [14].

Samples were prepared by spin coating on glass substrates similar to Raman and thermal conductivity measurements. PVAL / titanium oxide hydrate hybrids samples were aged for 1 week in a desiccator before annealing similar to the rest of the measurements.

2.4 Differential Scanning Calorimetry (DSC)

DSC is a thermal analysis technique used in this thesis. DSC is used to measure several properties such as reaction temperature, phase changes, specific heat as well heat of reaction temperatures [25]. The setup of a DSC falls under two groups: heat flux or power compensated. The former measures the heat flow between a sample and reference placed in the same furnace in order to keep the differential temperature between them equalling zero. The power compensated setup has the sample and reference in two separate furnaces and the power required to keep the temperature at equilibrium is recorded as heat flow [25]. The focus of this study is on measuring the critical temperatures such as the glass transition and melting temperatures (T_g & T_m respectively) to characterize the polymer blends. Such transition temperatures are effected by the interactions between the polymer molecules and therefore have a direct physical meaning to the signals obtained [26].

2.4.1 DSC Sample preparation

PVAL – TEG, PVAL – TiO_2 composites, and PVAL / titanium oxide hydrate hybrids were all drop cast from solution in PS square crucibles. PVAL – ANF samples were drop cast on clean glass slides as DMSO dissolves PS. They were then stored in a dissector for 7 days before measurements. The films were then peeled from the PS containers, cut into strips using a razor blade and placed in the standard aluminium DSC crucibles (40 µl). The weight of each sample ranged between 3 – 5 mg. The PVAL – ANF films were scraped off using a razor then placed in the DSC crucibles.

2.5 Scanning Electron Microscopy

Scanning electron microscopy (SEM) uses an electron beam that is rastered on the surface of the sample to obtain an image. Electrons interact with the sample in various ways and different information can be obtained. For example, secondary electrons coming from the first ~100nm of the surface can give information on the topography. These are created by inelastic scattering of the electrons and the surface. The contrast is based on the number of electrons reaching the detector. Another type of interaction is backscattered electrons. These come from elastic scattering of the electrons and the atoms and are generated from deeper in the film ~1 µm. Heavier atoms scatter more electrons and thus giving information on the composition [14].

2.6 Thermal conductivity: 3 – ω Technique

To measure a material's thermal conductivity, several methods have been developed. These methods can be grouped under two main umbrellas: steady state or transient methods. Steady state techniques are mainly based on obtaining thermal conductivity from Fourier's law of thermal conductivity [27].

Transient methods on the other hand, measure thermal conductivity from temporary signals. These signals are then processed and analysed to obtain the thermal conductivity. Examples of such signals are thermal conductance and thermal diffusivity.

Steady state techniques are generally more accurate; however, they take longer to conduct the measurement, as thermal equilibrium must be achieved at each sampling point. Transient methods are relatively lower in price and signals can be obtained rather quickly. The slight disadvantage is that analysis of the signals can be more complicated [27].

The 3 – ω technique is a transient thermal conductivity measurement technique. It is mainly used for thin films (<10 μm) and with relatively low thermal conductivities (0.2 – 20 W/m.K) thus making it well suited for polymer thin films [27]. The sample film is deposited on a substrate that is considered to have infinite thickness compared to the sample (~100nm for the film and >500 μm for the substrate). The substrate's thermal information and thickness is well characterised and is used as the reference in the post measurement calculations. Typically, metal electrodes (gold in all these measurements) and heater lines are deposited on top of the polymer film. See Figure 17 and Figure 18 below for illustration.

In a typical 3 – ω setup, an AC current with a given angular frequency ω.

$$I = I_o \cos(\omega t) \tag{2.7}$$

This current, in turn results in periodic Joule heating of the line at angular frequency 2 ω and a phase lag of φ.

$$\Delta T = \Delta T_0 \cos(2\omega + \varphi) \tag{2.8}$$

The phase shift is dependent on the geometry of the heater line, its thermal properties, and the thermal properties of the film underneath. Due to the change of the temperature of the heater line, an oscillating change in its resistance follows at 2 ω.

$$R = R_o(1 + \beta \Delta T) \tag{2.9}$$

Based on Ohm's law: $V = IR$, an amplitude modulated voltage signal is obtained with components at 1ω and 3ω. However, the amplitude at the first harmonic is orders of magnitude larger than at 3ω, so a lock-in amplifier is used to modulate it [28-30]. If the measurement was taken at two different frequencies, the thermal conductivity (K) can be calculated using the following equation from [29]:

$$K = \frac{V^3 \ln\frac{f_2}{f_1}}{4\pi I R^2 (V_{3,1} - V_{3,2})} \frac{dR}{dT} \qquad (2.10)$$

Where V is the voltage across the line at ω. R is the heater line resistance, $V_{3,1}$ is the voltage at 3ω at frequency f_1 and $V_{3,2}$ is the voltage at frequency f_2. dR/dT is the slope of the heater line's calibration at the temperature of measurement [29].

2.6.1 Sample preparation for 3 – ω

An undoped Si wafer with high resistivity and no SiO_X layer was used as a substrate. This was considered as the reference point with a known thermal properties and thickness. The thickness of the Si substrate was considered infinitely larger than the sample deposited on top (compare 525 μm to 200 nm). The polymer film was then deposited on top by spin coating. The gold electrodes and heater lines were deposited on top of the film by evaporation and a shadow mask for patterning. The mask has heater lines with different widths to allow for a range of resistances based on the expected thermal conductivities of the samples measured. The thinner the line, the higher the resistance and temperature increase and vice versa. The voltage measurements were taken at several points by varying the input's current frequency. The frequency was varied with 60 Hz steps from 200 – 2000 Hz with an amplitude of 40 or 60 mA based on the thickness of the heater line used. A typical signal would show a linear decay of the voltage's amplitude and an increase in the phase lag with increasing frequency. The thickness was then measured using a profilometer. The profilometer was used to measure the thicknesses of the PVAL – TEG systems. For the PVAL / titanium oxide hydrate hybrids, composites and PVAL – ANF systems, the Transfer Matrix Method (TMM) was used using UV-Vis transmission data. A detailed description of the method can be studied in [3]. This method proved to be more accurate as it acquires the signal from the entire surface are of the film instead of several points using a contact profilometer. To obtain that, crystal sapphire substrates were used instead of the opaque silicon wafers. The film deposition, electrode deposition, and voltage measurements remained the same.

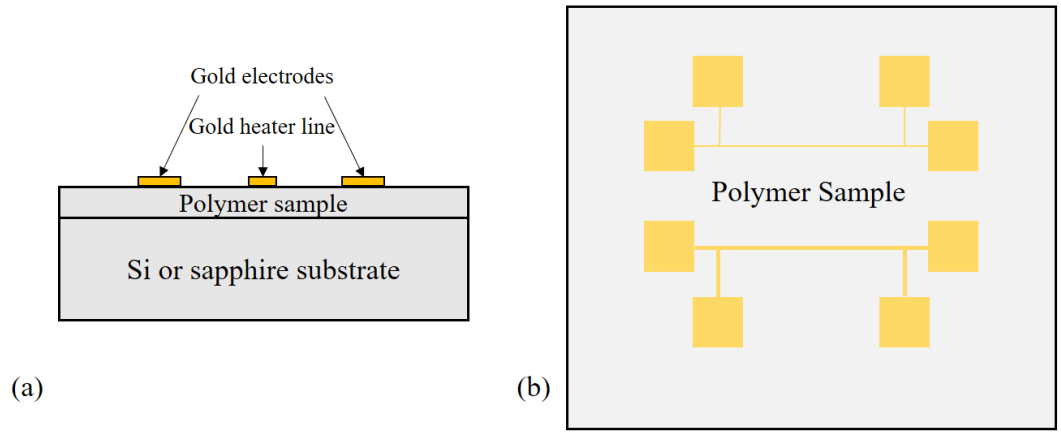


Figure 17: Side view (a) and top view (b) of a sample for 3-ω measurement. (a) Shows the substrate that is considered infinitely thick in comparison to the polymer film. The gold electrodes and heater lines are then evaporated on top. (b) Shows the electrodes and heater lines. The dimensions of the heater lines are crucial to the measurement as it is linked to the resistance and the voltage signal. Any fluctuation results in fluctuation in the measured signal.

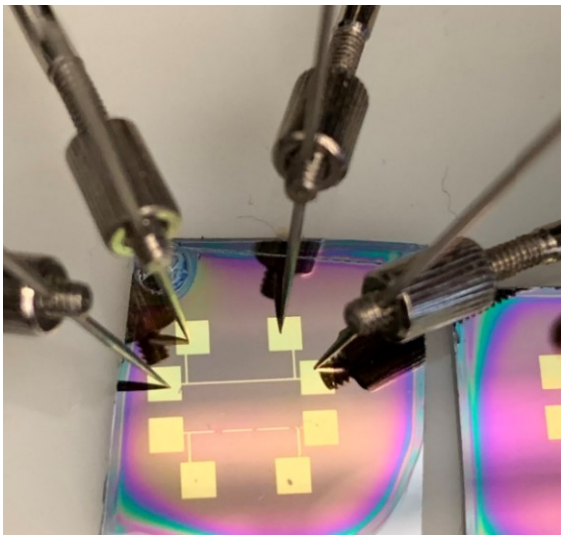


Figure 18: A film with gold electrodes and heater lines deposited for 3-ω measurement. Four electrodes are used; two for the input current and two to measure the voltage difference.

2.7 List of collaborators and contributors

- Thank you to Prof. Sophia Charalambous-Heyes for discussions on Raman spectroscopy and assistance in peak fitting.
- Thank you to Mr. Matthew S'ng Ming Hao, Dr. Radek Machan, and Prof. Peter Török, School of Physical and Mathematical Sciences, Nanyang Technological University, Singapore, for the BLS and sound velocity measurements.
- Thank you to Mr. Alex Balzer, Department of Chemical and Bimolecular Engineering, Georgia Institute of Technology, GA, USA, for the TGA measurements, XPS measurements and preparation of the PVAL / boric acid films for XPS measurement, and for drawing the hybrid images and structures.
- Thank you to Mr. Ahmad Alraddadi, Department of Materials, Imperial College London, London, UK, for the SEM images.
- Thank you to Mr. Daron Spence and Prof. Shannon Yee, School of Material Science and Engineering, Georgia Institute of Technology, GA, USA, for the electrode depositions, thermal conductivity measurements, and post-measurements calculations.

2.8 References

1. Russo, M., *Titanium Oxide Hydrates: Optical Properties and Applications*, in *Department of Materials*. 2010, Imperial College London.
2. Votta, I., *Titanium-Oxide-Hydrates Based Organic/Inorganic Molecular Hybrids produced via Sol-Gel Processing*, in *Department of Materials*. 2017, Imperial College London.
3. Bachevillier, S., *Solution-Processed Photonics for Light and Heat Management*, in *Department of Materials*. 2019, Imperial College London.
4. Strang, A., *Organic/Inorganic Hybrid Material for Solution-Processed Photonics Applications*, in *Department of Materials*. 2015, Imperial College London.
5. Russo, M., et al., *One-pot synthesis of polymer/inorganic hybrids: toward readily accessible, low-loss, and highly tunable refractive index materials and patterns.* Journal of Polymer Science Part B: Polymer Physics, 2012. **50**(1): p. 65-74.
6. Nussbaumer, R.J., P. Smith, and W.R. Caseri, *Transparent, Anatase-Free TiO2 Nanoparticle Dispersions.* Journal of Nanoscience and Nanotechnology, 2006. **7**: p. 2422 - 2432.
7. Yang, M., et al., *Dispersions of Aramid Nanofibers: A New Nanoscale Building Block.* ACS Nano, 2011. **5**(9): p. 6945-6954.
8. Yang, B., et al., *Timesaving, High-Efficiency Approaches To Fabricate Aramid Nanofibers.* ACS Nano, 2019. **13**(7): p. 7886-7897.
9. Fan, J., et al., *Aramid nanofiber-functionalized graphene nanosheets for polymer reinforcement.* Nanoscale, 2012. **4**(22): p. 7046-7055.
10. Guan, Y., et al., *Aramid nanofibers and poly (vinyl alcohol) nanocomposites for ideal combination of strength and toughness via hydrogen bonding interactions.* Composites Science and Technology, 2017. **144**: p. 193-201.
11. Songfeng, E., et al., *Enhancing mechanical strength and toughness of aramid nanofibers by synergetic interactions of covalent and hydrogen bonding.* Composites Part A: Applied Science and Manufacturing, 2020. **137**: p. 106031-106042.
12. Kutz, M., *Applied Plastics Engineering Handbook: Processing, Materials, and Applications*. 2016, Norwich: Elsevier Science & Technology Books.
13. Griffin., J., H. Hassan., and E. Spooner. *Spin Coating: A Guide to Theory and Techniques*. 2018 [cited 2018 1/23/2018]; Available from: https://www.ossila.com/pages/spin-coating.
14. Leng, Y., *Materials Characterization: Introduction to Microscopic and Spectroscopic Methods*. 2013, Wiley - VCH.
15. Tuschel, D., *Selecting an excitation wavelength for raman spectroscopy.* Spectroscopy, 2016. **31**(3): p. 14-23.
16. Wood, S., J.R. Hollis, and J.-S. Kim, *Raman spectroscopy as an advanced structural nanoprobe for conjugated molecular semiconductors.* Journal of Physics D: Applied Physics, 2017. **50**(7): p. 073001-073062.
17. Smith, E. and G. Dent, *Modern Raman Spectroscopy: A Practical Approach*. 2005, England: John Wiley & Sons Incorporated.
18. Mikoliunaite, L., et al., *The substrate matters in the Raman spectroscopy analysis of cells.* Scientific Reports, 2015. **5**(1): p. 13150-13159.
19. Merlen, A., et al., *Surface Enhanced Raman Spectroscopy of Organic Molecules Deposited on Gold Sputtered Substrates.* Nanotechnology, 2009. **20**(21): p. 215705-215712.
20. Renishaw, *inVia™ confocal Raman microscope*. 2019.
21. Milosevic, M., *Internal Reflection and ATR Spectroscopy*. 2012, John Wiley & Sons.
22. Wu, P.-J., et al., *Water content, not stiffness, dominates Brillouin spectroscopy measurements in hydrated materials.* Nature Methods, 2018. **15**(8): p. 561-562.
23. Poon, C., et al., *Brillouin imaging for studies of micromechanics in biology and biomedicine: from current state-of-the-art to future clinical translation.* Journal of Physics: Photonics, 2020. **3**(1): p. 012002-012026.
24. Bottani, C.E. and D. Fioretto, *Brillouin scattering of phonons in complex materials.* Advances in Physics: X, 2018. **3**(1): p. 606-632.

25. Perez, M., O. Lame, and A. Deschamps, *Global Techniques for Characterizing Phase Transformations - A Tutorial Review.* Advanced Engineering Materials, 2010. **12**(6): p. 433-446.
26. Schick, C., *Differential scanning calorimetry (DSC) of semicrystalline polymers.* Analytical and Bioanalytical Chemistry, 2009. **395**(6): p. 1589-1611.
27. Yüksel, N., *The Review of Some Commonly Used Methods and Techniques to Measure the Thermal Conductivity of Insulation Materials*, in *Insulation Materials in Context of Sustainability*. 2016, IntechOpen.
28. Cahill, D.G., *Thermal conductivity measurement from 30 to 750 K: the 3ω method.* Review of Scientific Instruments, 1990. **61**(2): p. 802-808.
29. Cahill, D.G. and R.O. Pohl, *Thermal conductivity of amorphous solids above the plateau.* Physical Review B, 1987. **35**(8): p. 4067-4073.
30. Linseis, V., et al., *Platform for in-plane ZT measurement and Hall coefficient determination of thin films in a temperature range from 120 K up to 450 K.* Journal of Materials Research, 2016. **31**(20): p. 3196-3204.

3 Polymer/Oligomer Blends

3.1 Motivation

Blending PVAL with TEG is expected to alter the polymer's chain conformation and structure. Moreover, TEG is predicted to create strong hydrogen bonding with PVAL due to the pendant hydroxyl groups, and thus altering the thermal energy pathways [1-3]. The study by Kim *et al*. [1] showed how the strong hydrogen bonding between a high molecular weight polymer and a lower molecular weight polymer could be used to tune the system's thermal conductivity. In the study by Mehra *et al*. [2], it was found that by blending short PEG chains into the matrix of long PVAL chains, an increase in thermal conductivity was achieved. In that study it was found that the shortest PEG molecule (1000 g/mol) resulted in the highest increase in thermal conductivity [2]. Here, we incorporated even shorter ethylene glycol molecules in the form of TEG to tune the structure. The addition of the relatively small molecules to the polymer matrix can influence local order. This is theorised to introduce localised extension of PVAL chains and reduction of chain bends by TEG molecules with strong interaction between the functional groups. Figure 19 (a) and (b) illustrate the chemical structure of PVAL and TEG, respectively. Figure 20, illustrates the theorised change in solid-state structure of the PVAL due to the addition of TEG.

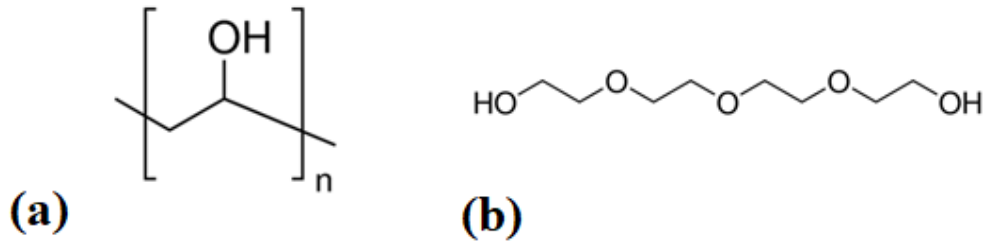


Figure 19: PVAL (a) and TEG (b) chemical structure

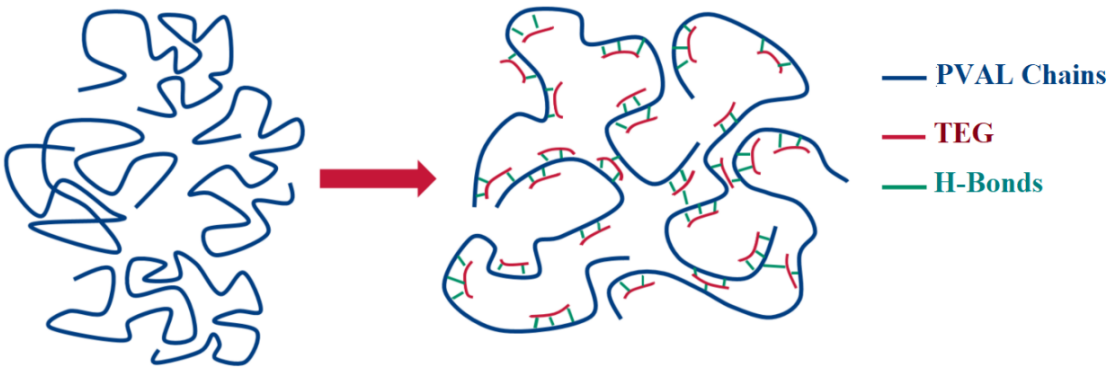


Figure 20: Theorised structure change based on introduction of TEG molecules in PVAL matrix

3.2 Solid-State Structure

The theorised changes in structure by the introduction of TEG (illustrated in Figure 20) is difficult to observe as an image due to the low atomic weight of the chemical elements in the system (C, O, and H). As a result, there is hardly any contrast difference between these elements e.g. when using SEM. Therefore, different spectroscopic techniques are utilised here to study and infer the changes in solid-state structure.

3.2.1 Raman Spectroscopy

As Raman spectroscopy can probe the changes in the C-C bonds in the polymer backbone as well as the pendant hydroxyl groups, it was used here to observe the changes on PVAL. Table ***2*** shows the peak positions and assignments of PVAL films (peak fitting can be found in Appendix A). Figure 21 shows the Raman spectra of neat PVAL. The spectra was split into several bands assigned to the different vibrational modes. The spectra from a TEG droplet can be seen in Figure 86 in Appendix A. The peak positions and assignments are presented in Table ***3***. R squared value of peak fitting of PVAL was 0.9993 , 0.9979, and 0.9993 for the 700 – 1000 cm^{-1}, 1000 – 1200 cm^{-1} , and 1300 - 1500 cm^{-1} parts of the spectrum respectively. The peak fit with lowest R squared value of 0.9826 was for the 50 wt.% TEG film in the 1000 – 1200 cm^{-1} window. The rest of the R squared values fall between these two. (Peak fitting curves and statistics can be found in Appendix A)

Table 2: Raman peak assignments of neat PVAL.

Peak Centres (cm^{-1})	Assignment	Reference
853 (shoulders at 808 & 836)	C-C stretching	[4-6]
898	C-C stretching	[4, 6]
936	C-C stretching	[4, 5]
1022	C-O stretching O-H bending	[4, 7]
1070	C-O stretching O-H bending	[4-6]
1098	C-O stretching O-H bending	[4-6]
1126	C-O stretching O-H bending	[4, 6, 8]
1143	C-O stretching C-O stretching	[4-6, 8, 9]
1359	C- bending O-H bending	[4, 5, 7, 9]
1441	C- bending O-H bending	[4, 5, 7, 9]
1657	C=O stretching (residual acetate)	[9]
1732 (shoulder at 1711)	C=O stretching (residual acetate)	[9]
1882	C-O asymmetric stretching (residual acetate)	[9]
2909	C-H stretching	[4]
2936	C-H stretching	[4]

Table 3: Raman peak assignments of neat TEG

Peak Centres (cm^{-1})	Assignment	Reference
839 (shoulders at 810)	C-H rocking	[10, 11]
887 (shoulder at 869)	C-H rocking (C-O)	[10, 11]
923	C-H (C-O)	[11]
1072 (shoulder at 1035)	C-O C-H	[10, 11]
1131	C-C C-H	[10, 11]
1239	C-H , C-H	[10, 11]
1284	C-H , C-H	[10, 11]
1452	C-H	[10, 11]
1473	C-	[10, 11]

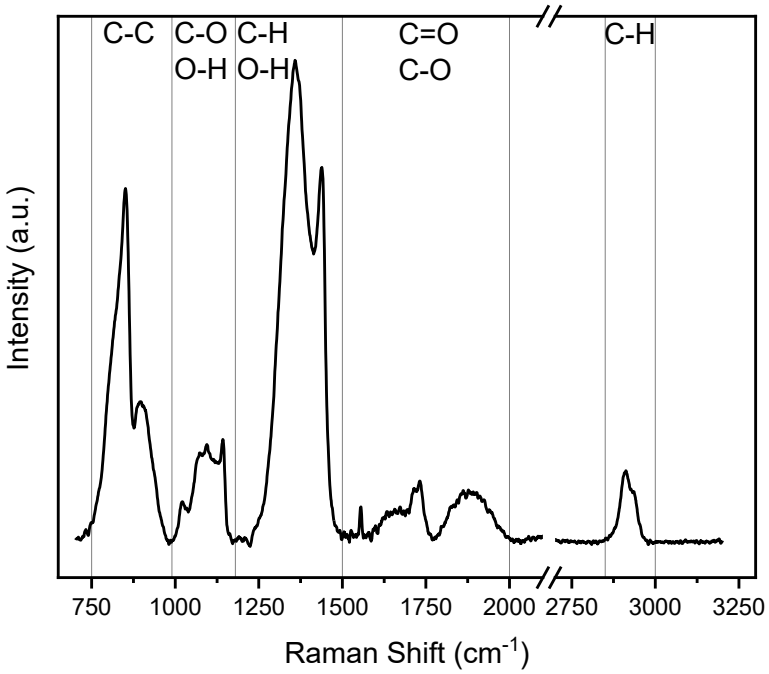


Figure 21: Raman spectra of a PVAL film. The spectra is divided into the main regions where characteristic vibrations were observed. The main contributor(s) to each band is highlighted above and can be observed with further detail in Table 2.

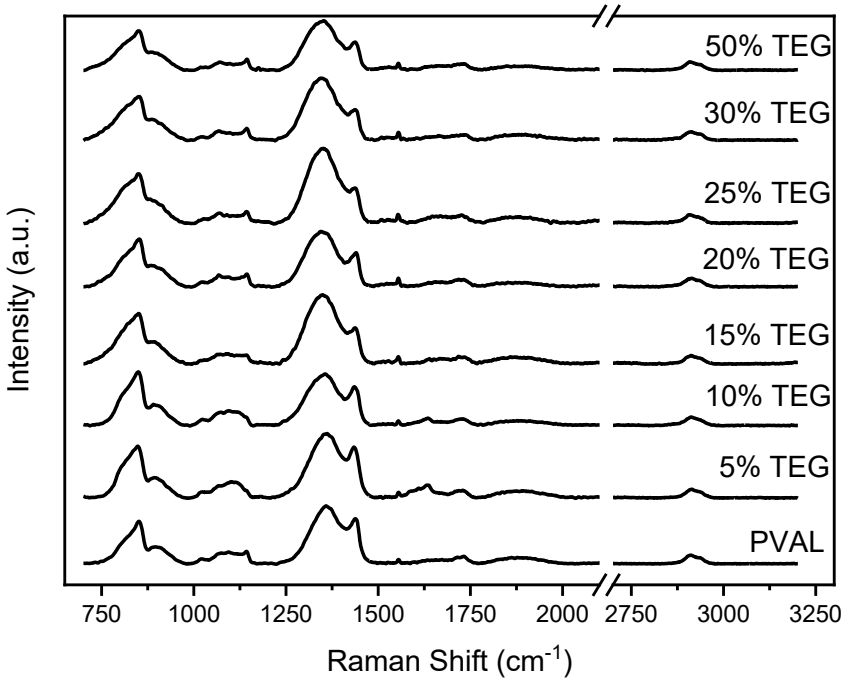


Figure 22: Raman spectra of PVAL - TEG blends. The key changes occur below 1500 cm^{-1}. The bands were split into three main regions of interest based on the C-C stretching (760-950 cm^{-1}), C-O stretching and O-H bending (1000 – 1200 cm^{-1}), and C-H and O-H bending (1250 – 1500 cm^{-1}).

Figure 22 displays the Raman spectra of the PVAL – TEG films on gold SERS substrates. The addition of TEG to the PVAL films has influences on the three main regions in the 750-1550 cm^{-1} range. The C-H stretching bands at 2909 and 2936 cm^{-1} show no significant changes.

For the C-C stretching bands (760-950 cm^{-1}), a broadening of the 853 cm^{-1} peak and a shift of its shoulders towards lower wavenumbers is observed upon addition of TEG. This is illustrated in further detail in Figure 23. This shift is indicative of an elongation of the C-C bond and is similar to a tensile stretch on the film sample as seen from studies on PE [12, 13].

Figure 24 describes the C-O stretching and O-H bending region between 1000 and 1200 cm^{-1}. The signal intensity here is relatively low in comparison to the other bands, which is due to the nature of the molecular vibrations. The 5, 10, 15 wt.% TEG samples reflect an increase in the middle peaks (1098 and 1126 cm^{-1}) while the intensity of the 1143 cm^{-1} peak was decreasing. This is indicative of a lower degree of local order [5, 6, 8, 14]. This change is likely due to the formation of new hydrogen bonds between the PVAL and TEG molecules that lead to backbone torsion. This in turn, would disrupt inter and intrachain hydrogen bonding of PVAL. However, as more TEG molecules were introduced, that effect is reduced and the peaks appear at similar positions as neat PVAL. This could be due to TEG molecules aggregating and creating relatively phase-pure domains within the PVAL matrix. Leading to a relatively heterogeneous distribution of the TEG molecules [1, 2]. However, Raman provides information on local-order that can be interpreted rather than long-range order and morphology.

In the third region of interest, C-H bending and O-H bending region between 1250 and 1500 cm^{-1}, the 1359 cm^{-1} peak has been shifted to lower numbers in all TEG samples. The peak centred at 1356 cm^{-1} is shifted due to new hydrogen bond formation between the PVAL and TEG molecules. The 1441 cm^{-1} peak shows minimal shift (~3-5 cm^{-1}) in relation to loading of TEG but a shift to lower numbers nonetheless. Figure 25 illustrates these changes. Another change is that the relative intensity between the 1356 and 1441 peaks is increasing. This could be linked to the reduction in local range order due to the formation of hydrogen bonds and the disruption of inter and intrachain interaction of PVAL molecules [4, 6, 14].

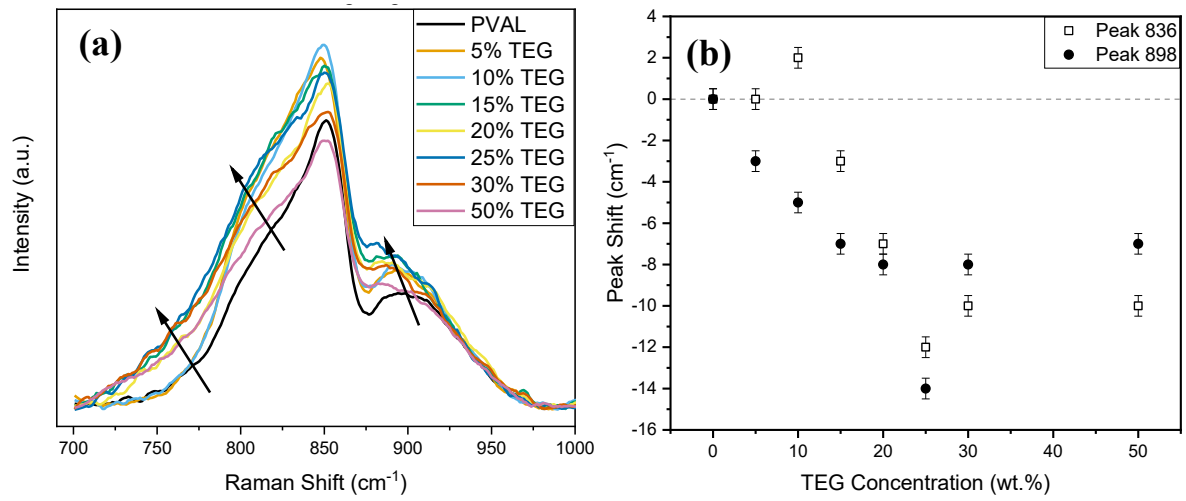


Figure 23: Raman spectra of PVAL - TEG blends in the C-C stretching region. (a) The peaks are shifted to lower wavenumbers with increasing TEG content. The peak position shift of two of the peaks to show the trend is presented in (b). Error bars based on resolution of the apparatus. Further errors due to peak fitting are not represented in the graph. The dashed line is used to highlight the shift to lower wave numbers.

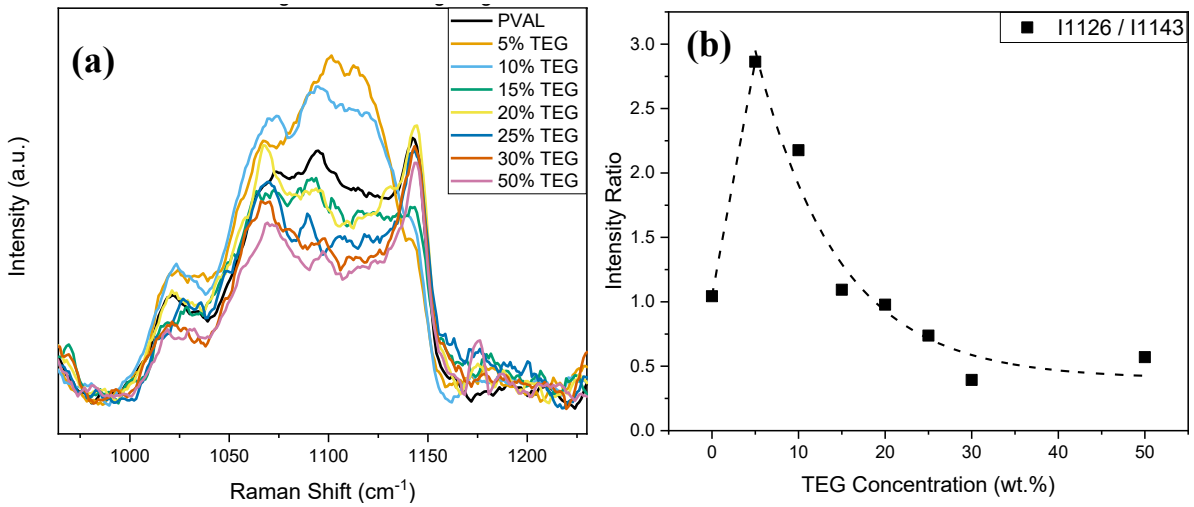


Figure 24: Raman spectra of PVAL - TEG blends in the C-O stretching and O-H bending region. (a). The intensity of peak 1126 cm^{-1} (linked to disordered segments) relative to peak 1143 cm^{-1} (linked to ordered segments) is the main change and illustrated in (b). The intensity of the 1126 cm^{-1} peak grows significantly compared to the peak at 1143 cm^{-1} in the 5 and 10 wt.% TEG samples before decaying exponentially. The dashed lines were drawn using an exponential decay function as a guide for the eye.

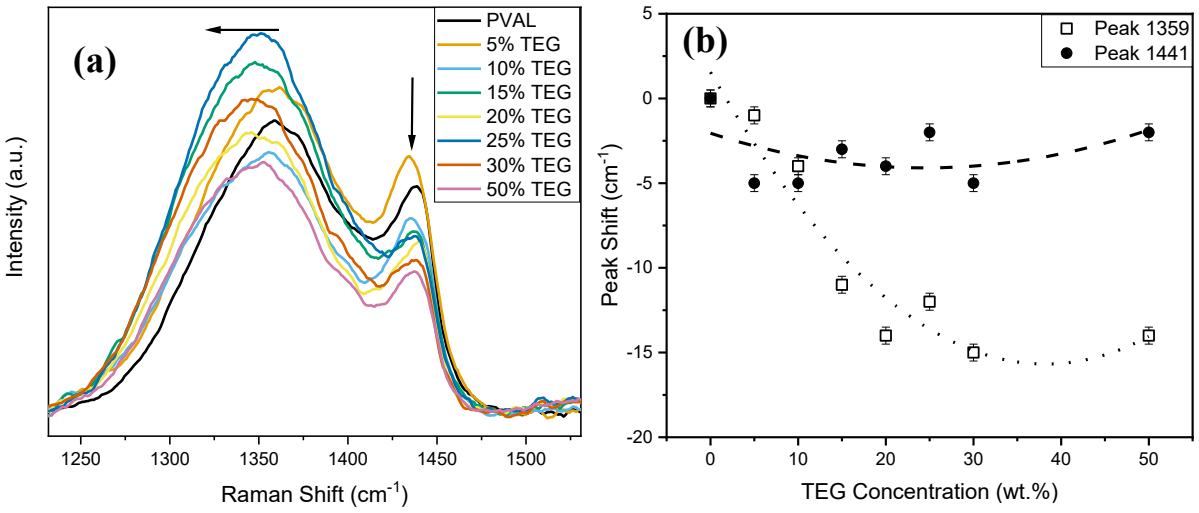


Figure 25: Raman spectra of PVAL - TEG samples in the C-H and O-H bending region (a). The peak at 1359 cm^{-1} was shifted to lower numbers with increasing TEG content. While the position of the peak at 1441 cm^{-1} was shifted, it was not comparably a large shift. However, the intensity ratio between the two peaks grows with increasing TEG. The amount of shift is illustrated in (b). Error bars based on resolution of the apparatus. Further errors due to peak fitting are not represented in the graph. The dashed lines were used as a guide for the eye by fitting the data with polynomial curves.

3.2.2 Fourier-Transform Infra-Red (FTIR) Spectroscopy

Table 4 below shows the assignment of bands observed using FTIR for the neat PVAL film (peak fitting can be found in Appendix B). Figure 26 shows the FTIR spectra of a neat PVAL film with the bands split up and contributors to each band is highlighted. For FTIR, the interactions on the pendant hydroxyl group are much more prominent than the C-C bonds, as the latter is not infrared active. Interactions between the functional groups can thus be observed by using FTIR.

Table 4: FTIR band assignments of PVAL.

Band centres (cm^{-1})	**Assignment**	**Reference**
3276	O-H stretching inter and intrachain	[15, 16]
2937, 2905	C-H stretching	[15, 16]
1733, 1709	C=O stretching (residual acetate)	[16]
1430	C-H stretching	[15, 16]
1123	C-O stretching (ordered segments)	[15, 16]
1083, 1051, 1021	C-O-C stretching	[16]

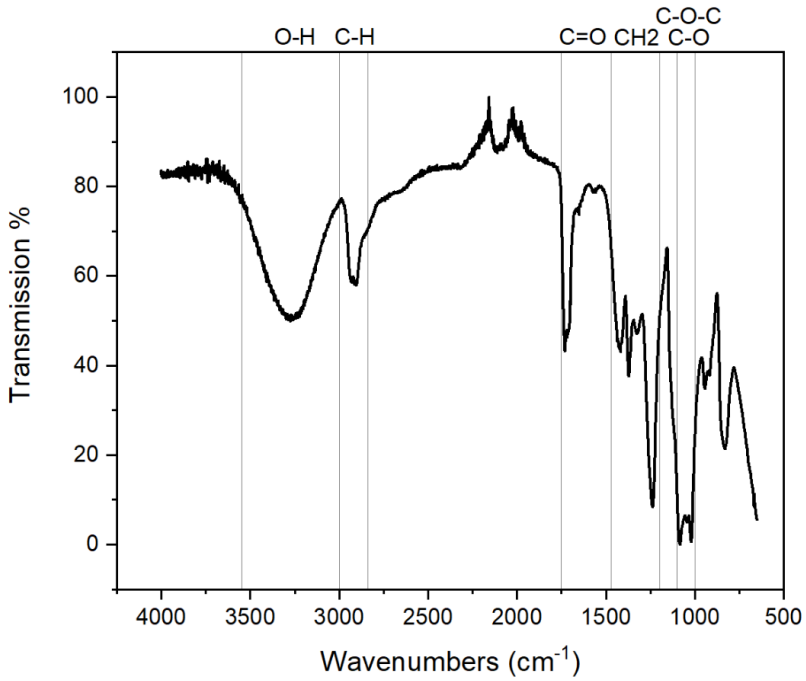


Figure 26: FTIR spectra of PVAL. The spectra is divided to the main regions where characteristic vibrations were observed. The main contributor(s) to each peak is indicated above and can be observed in further detail in Table 2.

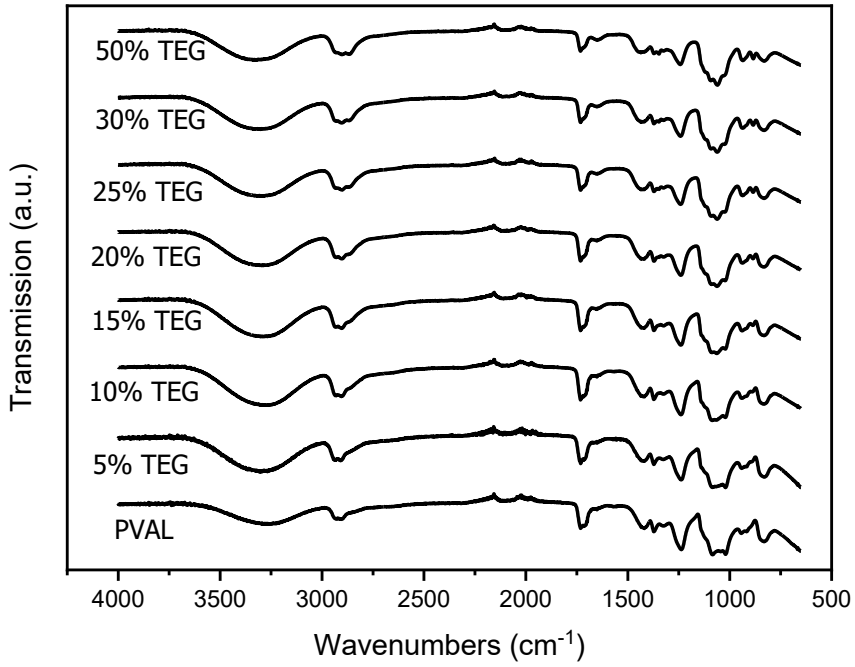


Figure 27: FTIR of PVAL – TEG blends of different compositions. The changes observed are primarily with the pendant hydroxyl (3276cm^{-1}) and carbonyl from the residual acetate (1733 cm^{-1}). The other changes are in the C-O stretching around 1123 cm^{-1}.

Comparing the FTIR spectra of PVAL – TEG films of different compositions (Figure 27), the traces look very similar. The largest difference is with the O-H peak, which is shifted to higher wavenumbers. The C-H band has a higher intensity at 2865 cm^{-1}, but no shifts in peak positions. In some of the other bands such as 1733 and 1430 cm^{-1}, the peaks appear to be shifted but they are within the resolution of the measurement apparatus, which is 2 cm^{-1}.

The hydroxyl bond peak is shifted to higher wavenumber (from 3276 cm^{-1} in neat PVAL to 3318 cm^{-1} in the 50 wt.% TEG) as shown in Figure 28. The shift to higher wavenumbers indicates a reduction in the overall hydroxyl hydrogen bond strength [1, 2]. It seems to follow a linear trend with the addition of TEG molecules with the exception of the 5 wt.% TEG sample. This is illustrated in Figure 29. The 5 wt.% TEG could be an outlier or it may be that the hydrogen bonding had a significant effect in this sample e.g. because of formation of a solid solution. The main strength of the hydrogen bond signal comes from PVAL inter and intrachain interactions [16]. The addition of TEG seems to infiltrate those hydrogen bonds and creates new ones with the ether group (middle of TEG molecule) and hydroxyl group (ends of TEG molecule) [2].

There was also an apparent increase then reduction in intensity of the C=O peak around 1700 cm^{-1} with increasing amount of TEG (Figure 30). This peak results from the residual acetate in the PVAL and is reduced, indicating there are less total carbonyl groups in the system with increasing TEG loading [16, 17]. Further changes to the C-O-C band were observed which are likely due to the interaction of the pendant hydroxyl group with the TEG. The shift is also indicative of change in observed local order [15, 16]. However, as the FTIR measurement obtains the signal from a small area, it cannot be concluded that the changes here are of long-range order. The changes are noted to be on short-range similar to the changes observed in Raman above.

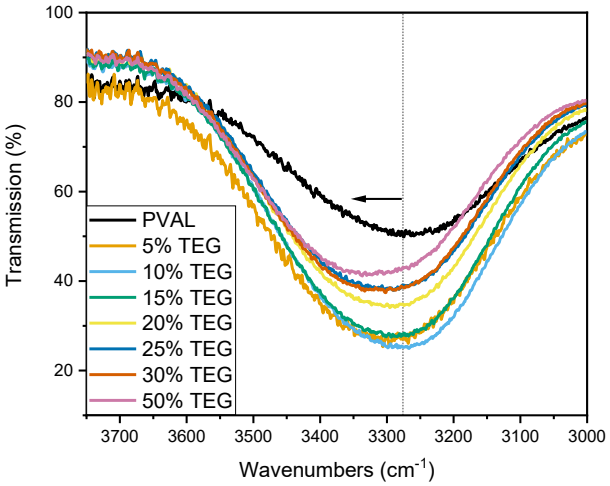


Figure 28: FTIR spectra of the O-H peak shift between PVAL – TEG samples. Dotted line placed as reference at the PVAL peak centre.

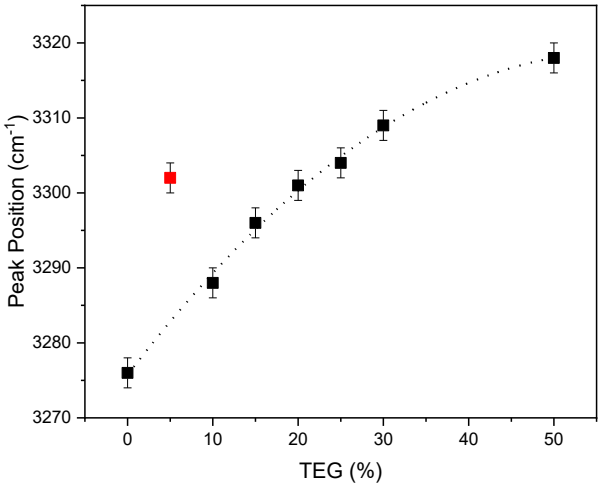


Figure 29: FTIR O-H peak position based on TEG content. Error bars based on resolution of the instrument. Further errors due to peak fitting are not represented in the graph. The dashed line drawn as a guide to the eye with the data point from the 5 wt.% TEG film masked out as an outlier.

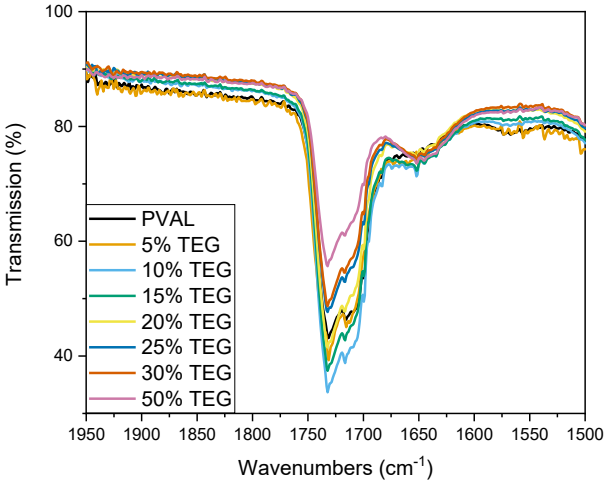


Figure 30: FTIR spectra of C=O stretching peak between PVAL – TEG samples. The intensity of absorption seems to increase up to 15wt.% TEG then decrease.

3.3 Differential Scanning Calorimetry (DSC)

Figure 31 (a) and (b) show the DSC thermograms for the first heating and first cooling of the PVAL – TEG systems, respectively. Figure 32 (a) and (b) show the second heating and cooling cycles of the PVAL – TEG systems, respectively. In Figure 31 (a), two endothermic peaks are centred at 77 ºC and at 187ºC in the PVAL trace. These are respectively, residual water evaporation (from the solvent) and the melting temperatures of PVAL. The samples were kept in a desiccator before measurements, but due to the hygroscopic nature of PVAL, water retention still occurred. This water evaporation endothermic peak obscures the glass transition temperature in this first heating cycle [18]. However, a clear T_g can be observed in the second heating cycle where a characteristic step change is seen. The transition temperatures are recorded in Table 5. It can be observed that with the addition of TEG molecules, the T_g is decreased from 65 ºC in neat PVAL to 27 ºC in the 50 wt.% TEG sample. TEG molecules appear to interrupt the intermolecular hydrogen bonds of the PVAL acting as a plasticizer for PVAL. This increases the inter-chain mobility thus requiring less energy to transition from the glassy state to the rubbery state [17, 19]. It must be noted that this change in solid-state structure and the plasticising affect by the TEG molecules are detected after a slow melting cycle only; i.e. the films are melt processed rather than solution processed in the second heating cycle. The addition of TEG to PVAL appears to have a nucleating affect during the cooling cycle as it crystallises earlier (Figure 31 b) Additional information can be obtained from the melting temperature, where the crystalline phase of PVAL transitions into a liquid phase [2, 19]. The melting temperature and the enthalpy of fusion are recorded in In the first heating cycle, the melting point is slightly increased upon addition of TEG but not significantly up to 25 wt.% TEG. At 30 and 50 wt.% TEG, the melting point is observed at ~205 ºC; an increase of around 20 ºC. The other noticeable feature is the slight increase then decrease of the melting peak (representing the enthalpy of fusion) with increasing TEG content, signifying the reduction of the crystalline fraction in the overall film above 15 wt.% TEG. This trend is presented in Figure ***33***. This may be expected due to the plasticising effect of the TEG on PVAL, disruption of the crystal growth upon TEG addition leading to a larger amorphous fraction [17, 19].

Another piece of information that can be obtained from DSC measurement is the miscibility of the blend. In fully miscible blends of two different polymers, the melting point is based on the ratio of the blend and generally follows a linear trend. PPE/PS is considered a classic example of a fully miscible blend [20]. Focus here was on the glass transition. A single T_g is observed which indicates some degree of miscibility. Furthermore, the changes in T_g and T_m is retained in the second heating cycle further supporting the view of strong hydrogen bonds between PVAL – TEG, the retention of TEG within the system, and the retention of the thermoplastic behaviour of PVAL [20].

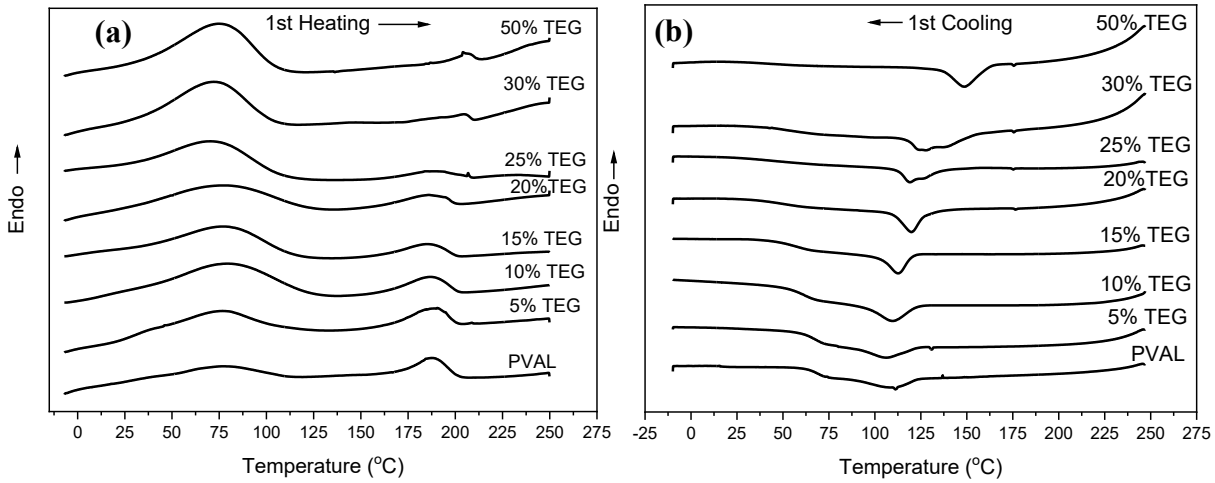


Figure 31: DSC thermograms of PVAL – TEG blends for the first heating (a) and cooling cycles (b).

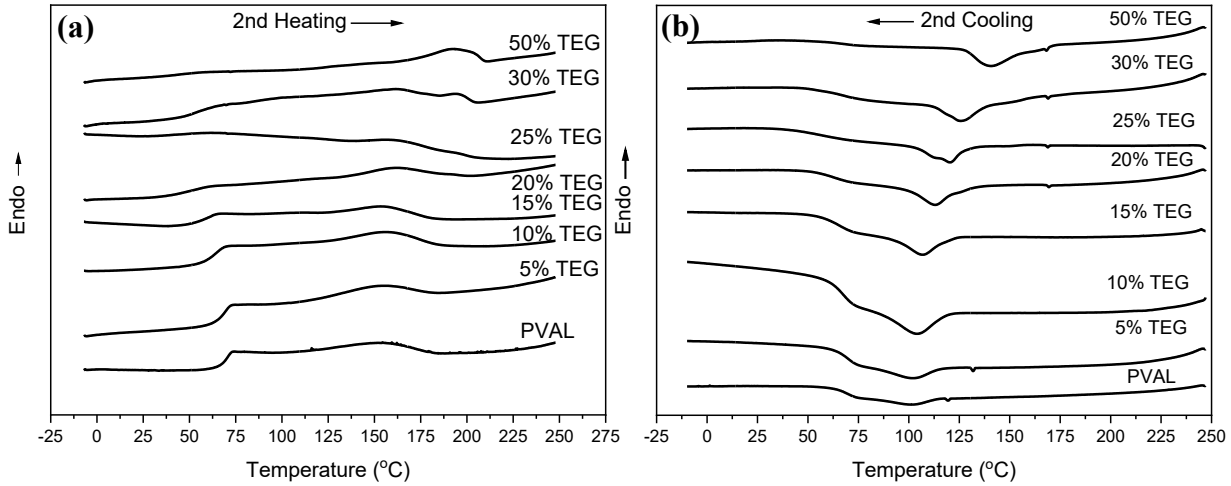


Figure 32: DSC thermograms of PVAL –TEG blends for the second heating (a) and cooling cycles (b).

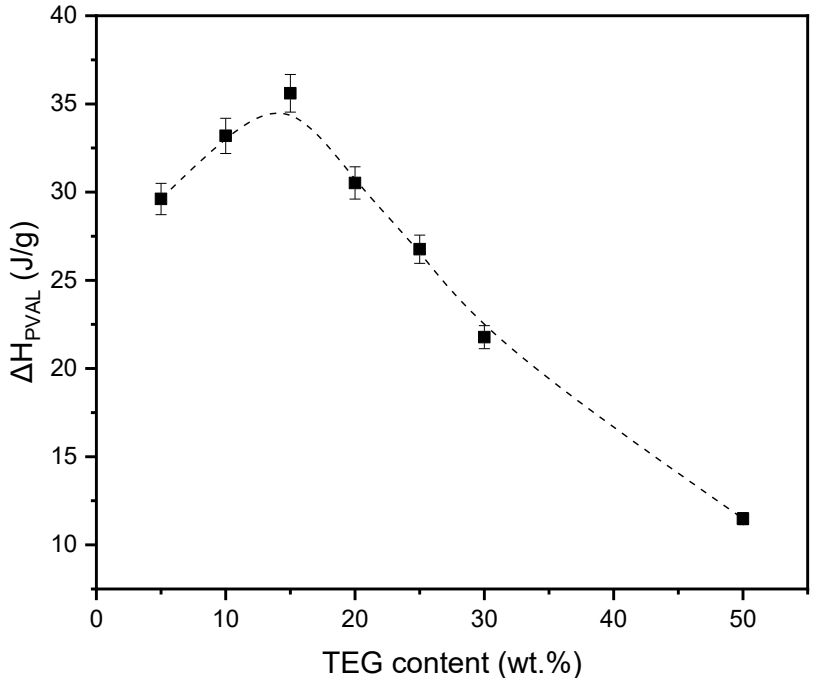


Figure 33: Enthalpy of fusion of PVAL - TEG films with various TEG content. ΔH_{PVAL} measured from the first heating. Error bars based on systematic error of the DSC of a single measurement.

Table 5: Measured glass transitions, melting transitions and enthalpies of fusion of PVAL - TEG films

Sample	**T_w* (ºC) (1st heating)**	**T_m (ºC) (1st heating)**	**ΔH_{PVAL} (J/g)** (1st heating)**	**T_g (ºC) (2nd heating)**	**T_m (ºC) (2nd heating)**
PVAL	77	187	30	65	152
5% TEG	76	188	33	63	154
10% TEG	76	186	36	56	156
15% TEG	76	184	31	48	153
20% TEG	76	186	27	36	161
25% TEG	70	188	22	26	160
30% TEG	72	204	11	51	161 (193)
50% TEG	74	205	12	27	193

*T_w is the peak associated with water evaporation. Temperature recorded as the peak position.

** Enthalpy of fusion normalised by weight fraction of PVAL for the first heating.

3.4 Brillouin Light Scattering Spectroscopy (BLS)

Using BLS, the Brillouin shifts were calculated for the PVAL – TEG films using the method described in [21]. The samples had to be of relatively large thickness to obtain a good signal in comparison to the other spectroscopy techniques used in this thesis. This is to allow the excitation laser beam focus to be within the material, avoiding the edge effects of the oil and substrate. Such films were prepared by spin coating so the observed properties should be comparable. For the 20 wt.% TEG sample, the thickness was not sufficient to obtain a clean signal so it was not included in the sound velocity calculations. Figure 34 shows the calculated sound velocities of the films deduced from their Brillouin shifts. The sound velocities here are considered to have contributions from both longitudinal and transverse directions. The apparent sound velocity appears to increase slightly at 5 and 10 wt.% TEG before being significantly reduced at higher loadings. At increasing TEG content (> 15 wt.%), TEG starts to act as a plasticiser and the mechanical properties are reduced due to that effect, in agreement with the decreased T_g that was measured in the DSC. However, at low loadings, the sound velocity appears to increase, signifying a higher phonon group velocity due to a change in solid-state structure. This could also be a slight error from the measurement, as the films absorb moisture and that can affect the measured Brillouin shift. This has not been quantified here systematically. From Raman, higher degree of disorder is observed at these TEG loadings (5 and 10 wt. %). The intensity ratio between the peak attributed to less ordered segments and more ordered segments followed a very similar trend (Figure 24 b). From, FTIR, the 5 wt.% TEG sample showed a significant change in the O-H stretching band as well (Figure 28 b). This suggests that a more localised order is created in such systems due to the strong interaction between TEG molecules and PVAL chains. This in turn, makes the system slightly more favourable to a phonon's path within the material.

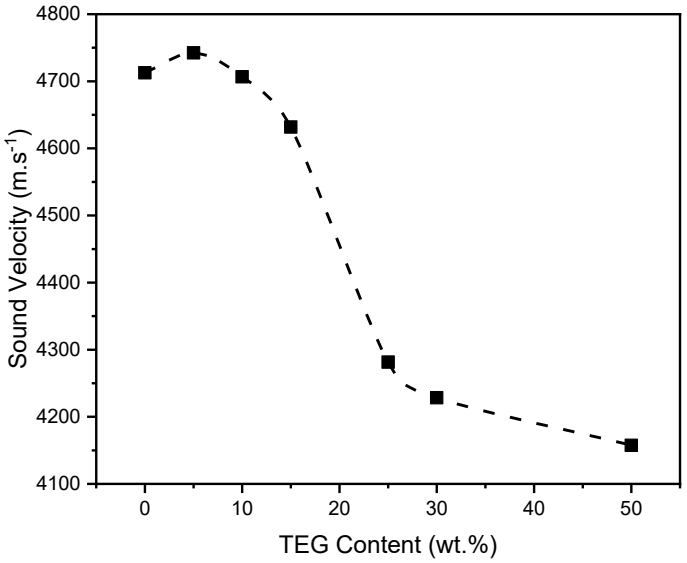


Figure 34: Calculated sound velocities of PVAL – TEG blends based on measured Brillouin shifts. The dashed line was added as a guide to the eye.

3.5 Thermal conductivity (3-ω)

Figure 35 shows the through-plane thermal conductivities of PVAL – TEG films. Error bars are based on the variation between three films measured at each loading. The neat PVAL's film thermal conductivity was measured to be ~ 0.32 W/m.K, in agreement with [2, 3, 22, 23]. With the addition of TEG, the thermal conductivity slightly increased to ~ 0.36 W/m.K before decreasing at loadings above 20 wt.% TEG. This may tentatively be attributed to TEG molecules intermixing with the PVAL matrix, with the strong interactions that form creating small thermal bridges [1-3, 22, 24]. This is also comparable to the trend observed in a similar system study between PVAL and ethylene glycols of different lengths [22]. Specifically the changes are in agreement with the creation of thermal bridges made of TEG due to the strong interaction of the hydroxyl groups observed in Raman, FTIR, and BLS measurements described above. This view is supported by the fact that the C-C backbone seems to extend due to hydrogen bond formation, as observed in the Raman measurements. This is analogous to creating mini splints along the backbone of the PVAL and keeping them in a stretched position at several points. The trend is also very similar to the calculated sound velocities as the thermal conductivity is directly related to the phonons' group velocity (see Figure 34) [25]. The increase in TC is likely due to the changes in the local polymer chain arrangement, as it does not follow the rule of mixtures [22]. However, with increasing amounts of TEG, the thermal conductivity is reduced as more TEG molecules interact with each other and create clusters and agglomerates within the PVAL matrix [1, 2, 22].

Moreover, above 20 wt.% TEG, the addition of TEG acts as a plasticiser and reduces the crystallinity of the PVAL film. This can be observed in DSC by the reduction of the melting endotherm. The sound velocity measurements give further evidence of this effect. The phonon's mean free path appears to be hindered in comparison to films with higher loadings, leading to a reduction of the system's thermal conductivity. Above 20 wt.% TEG, the low molecular order in the system results in more phonon scattering events thus reducing the phonon mean free path and overall thermal conductivity. This effect has been observed in different studies of filler-free blends and how the thermal conductivity can be tuned by the amount of small molecules added [1, 2, 22].

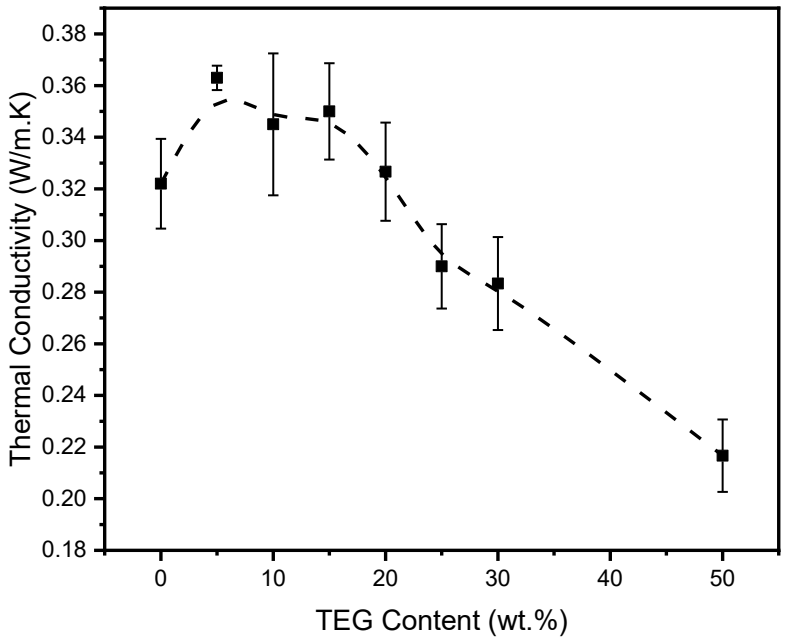


Figure 35: Thermal conductivity of PVAL – TEG blends at room temperature. Measured using 3-ω technique. Error bars based on three film samples measured at each loading. The dashed line was added as guide to the eye.

3.6 Conclusions

It was shown that with the addition of TEG molecules to PVAL, the thermal conductivity could be tuned. This was attributed to changes in solid-state structure, making it distinct from approaches that use highly conductive fillers to create a composite. From Raman spectroscopy, localised extension of the PVAL backbone was observed as well as changes in the local order due to hydrogen bonding. FTIR spectroscopy assisted to identify the extent of hydrogen bonding, and how the functional groups of TEG and PVAL interact with each other. The miscibility of the blend and the effect of hydrogen bonding on the polymer chain mobility were deduced from DSC data. A reduction in the overall crystallinity was observed, signifying that with the addition of TEG a system with a lager molecular disorder is created. From the BLS shifts, the sound velocities were calculated which are directly related to the phonons' mean free path. This was related to the observed changes in thermal conductivity of such blends. The similarity in the trend of thermal conductivity with composition and sound velocity with composition suggests that the interactions between PVAL and TEG and the changes in structure affect the phonon mean free path. Thereby, we assume the systems to be isotropic. Surprisingly, the magnitude of the changes in thermal conductivity is not as significant as seen in similar studies. This could be due to different sample preparations, measurement setups and the type of molecules used. Larger effect may be introduced using a more rigid small molecule that can still strongly interact with PVAL.

3.7 References

1. Kim, G.H., et al., *High thermal conductivity in amorphous polymer blends by engineered interchain interactions.* Nature Materials, 2015. **14**(3): p. 295-300.
2. Mehra, N., L. Mu, and J. Zhu, *Developing heat conduction pathways through short polymer chains in a hydrogen bonded polymer system.* Composites Science and Technology, 2017. **148**: p. 97-105.
3. Mehra, N., et al., *Moisture driven thermal conduction in polymer and polymer blends.* Composites Science and Technology, 2017. **151**: p. 115-123.
4. Thomas, P.S. and B.H. Stuart, *A Fourier transform Raman spectroscopy study of water sorption by poly(vinyl alcohol).* Spectrochimica Acta Part A: Molecular and Biomolecular Spectroscopy, 1997. **53**(13): p. 2275-2278.
5. Yang, C.-C., et al., *Study of poly(vinyl alcohol)/titanium oxide composite polymer membranes and their application on alkaline direct alcohol fuel cell.* Journal of Power Sources, 2008. **184**(1): p. 44-51.
6. Dodda, J.M., et al., *Comparative study of PVA/SiO2 and PVA/SiO2/glutaraldehyde (GA) nanocomposite membranes prepared by single-step solution casting method.* Journal of Materials Science, 2015. **50**(19): p. 6477-6490.
7. Gauthier, M.A., et al., *Degree of crosslinking and mechanical properties of crosslinked poly(vinyl alcohol) beads for use in solid-phase organic synthesis.* Polymer, 2004. **45**(24): p. 8201-8210.
8. Yang, C.-C., Y.J. Li, and T.-H. Liou, *Preparation of novel poly(vinyl alcohol)/SiO2 nanocomposite membranes by a sol–gel process and their application on alkaline DMFCs.* Desalination, 2011. **276**(1): p. 366-372.
9. Madhuri, S.N., K.S. Hemalatha, and K. Rukmani, *Preparation and investigation of suitability of gadolinium oxide nanoparticle doped polyvinyl alcohol films for optoelectronic applications.* Journal of Materials Science: Materials in Electronics, 2019. **30**(9): p. 9051-9063.
10. El Hadri, M., et al., *Raman spectroscopy investigation of mono- and diacyl-polyoxyethylene glycols.* Vibrational Spectroscopy, 2013. **64**: p. 78-88.
11. Koenig, J.L. and A.C. Angood, *Raman spectra of poly(ethylene glycols) in solution.* Journal of Polymer Science Part A-2: Polymer Physics, 1970. **8**(10): p. 1787-1796.
12. Kida, T., Y. Hiejima, and K.-h. Nitta, *Raman Spectroscopic Study of High-density Polyethylene during Tensile Deformation.* International Journal of Experimental Spectroscopic Techniques, 2016. **1**(1): p. 1-6.
13. Hiejima, Y., et al., *Microscopic structural changes during photodegradation of low-density polyethylene detected by Raman spectroscopy.* Polymer Degradation and Stability, 2018. **150**: p. 67-72.
14. Martinelli, A., et al., *Structural analysis of PVA-based proton conducting membranes.* Solid State Ionics, 2006. **177**(26–32): p. 2431-2435.
15. Costa, H.S., et al., *Sol–gel derived composite from bioactive glass–polyvinyl alcohol.* Journal of Materials Science, 2007. **43**(2): p. 494-502.
16. Mansur, H.S., et al., *FTIR spectroscopy characterization of poly (vinyl alcohol) hydrogel with different hydrolysis degree and chemically crosslinked with glutaraldehyde.* Materials Science and Engineering: C, 2008. **28**(4): p. 539-548.
17. Falqi, F.H., et al., *Preparation of Miscible PVA/PEG Blends and Effect of Graphene Concentration on Thermal, Crystallization, Morphological, and Mechanical Properties of PVA/PEG (10 wt%) Blend.* International Journal of Polymer Science, 2018. **2018**: p. 8527693 - 8527703.
18. Panero, S., et al., *Silica-Added, Composite Poly(vinyl alcohol) Membranes for Fuel Cell Application.* Journal of The Electrochemical Society, 2005. **152**(12): p. A2400 - A2405.
19. Liu, P., et al., *A novel poly (vinyl alcohol)/poly (ethylene glycol) scaffold for tissue engineering with a unique bimodal open-celled structure fabricated using supercritical fluid foaming.* Scientific Reports, 2019. **9**(1): p. 9534-9546.
20. Utracki, L.A. and C.A. Wilkie, *Polymer Blends Handbook*. 2 ed. 2014: Springer, Dordrecht.

21. Wu, P.-J., et al., *Water content, not stiffness, dominates Brillouin spectroscopy measurements in hydrated materials.* Nature Methods, 2018. **15**(8): p. 561-562.
22. Mehra, N., M.A. Kashfipour, and J. Zhu, *Filler free technology for enhanced thermally conductive optically transparent polymeric materials using low thermally conductive organic linkers.* Applied Materials Today, 2018. **13**: p. 207-216.
23. Xie, X., et al., *Thermal Conductivity, Heat Capacity, and Elastic Constants of Water-Soluble Polymers and Polymer Blends.* Macromolecules, 2016. **49**(3): p. 972-978.
24. Rashidi, V., et al., *Thermal Conductance in Cross-linked Polymers: Effects of Non-Bonding Interactions.* The Journal of Physical Chemistry B, 2017. **121**(17): p. 4600-4609.
25. Balandin, A.A., *Thermal properties of graphene and nanostructured carbon materials.* Nature Materials, 2011. **10**(8): p. 569-581.

4 Organic / Inorganic Hybrids

4.1 Motivation

It was observed in Chapter 3 how engineering inter-chain interactions could influence the local chain order and conformation. Another method of influencing chain interactions is the creation of a cross-linked network. Organic / inorganic hybrids are an attractive way of realising promising properties out of materials. This is achieved by creating new chemical bonds between mixtures of two dissimilar materials. It differs from a conventional composite which is considered as a dispersion of particles within a matrix [1-3]. PVAL / titanium oxide hydrate hybrids have been studied for their optical properties and their applications in photonic structures, yet the effect of the structure on the thermal conductivity is yet to be investigated [4-9]. The theorised structure of the PVAL / titanium oxide hydrate hybrid is illustrated in Figure 36. To differentiate between the PVAL hybrid structure and a conventional PVAL composite comprised of TiO_2 nanoparticles, side-by-side comparisons were conducted and studied. An illustration of the PVAL – TiO_2 composite is shown in Figure 37.

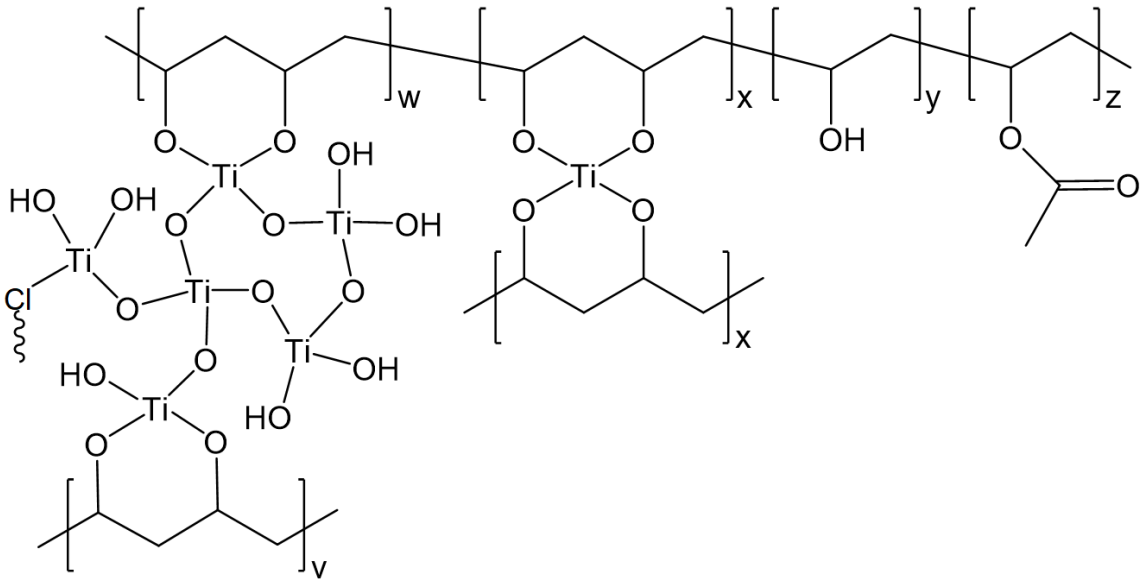


Figure 36: PVAL / titanium oxide hydrate hybrid structure. On the left, a polynuclear titanium oxide hydrate connects to separate PVAL chains. This polynuclear form is more likely to be present in higher inorganic content hybrids. In the middle, a mononuclear PVAL / titanium oxide hydrate network is illustrated. Covalent bonds are created between the titanium atoms and the PVAL as well as hydrogen bonds with the remaining hydroxyl groups. Some residual chlorine is present as well. The segments on the right depict unreacted PVAL with residual acetate.

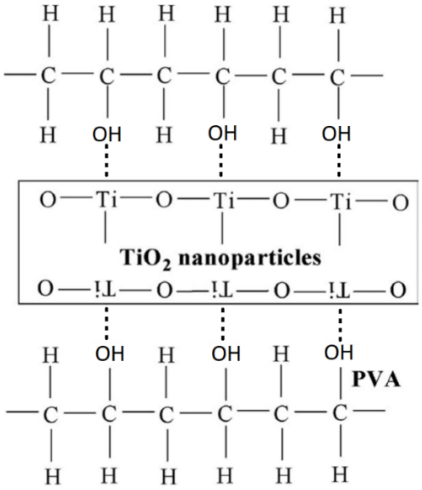


Figure 37: PVA-TiO_2 nanocomposite structure. TiO_2 particles infiltrate free volume in PVAL and interact with hydrogen bonds with the polymer's hydroxyl groups. Structure adapted from [10]. Copyright (2018) John Wiley and Sons.

4.2 Solid-State Structure

The changes in the structure due to the introduction of the titanium oxide hydrate creates a cross-linked network with PVAL as shown in Figure 36. This schematical structure has been studied before for its optical properties in photonic crystals and Bragg mirrors applications [4-9]. In this thesis, several alternative characterisation techniques were employed to study the changes in solid-state structure and draw contrasts with PVAL - TiO_2 composites to highlight the differences in the created structures. Spectroscopic techniques were utilised as in the PVAL – TEG blends in Chapter 3. X-ray photoelectron spectroscopy was also used here to study the differences between the organic / inorganic hybrids and the composites.

4.2.1 Raman Spectroscopy

Raman spectroscopy was employed to probe the changes in the backbone as well as the pendant groups. We, thereby, focused on the changes due to the formation of the organic/inorganic hybrid structure and compared it with a conventional composite. Table 6 presents the peak assignments for PVAL films, extended from the in Chapter 3 to include the region between 100 and 700 cm^{-1}. (Peak fitting can be found in Appendix C). Figure 38 shows the Raman spectrum of PVAL film in the region between 750 and 3200 cm^{-1}. Figure 39 shows the spectrum of PVAL film in the 100 to 700 cm^{-1} region. R squared value of peak fitting of PVAL was 0.9784, 0.9993 , 0.9979, and 0.9993 for the 400 – 700 cm^{-1}, 700 – 1000 cm^{-1}, 1000 – 1200 cm^{-1} , and 1300 - 1500 cm^{-1} parts of the spectrum respectively. The peak fit with lowest R squared value of 0.9383 was for the 50 % hybrid film in the 400 – 700 cm^{-1} window.

The rest of the R squared values fall between these two. (Peak fitting curves and statistics can be found in Appendix C)

Table 6: Raman peak assignments form PVAL. The three peaks observed in the lower Raman shift are highlighted first.

Peak Centres (cm^{-1})	Assignment	Reference
414	C-O wagging and bending	[11]
481	C-O bending out of plane	[11]
635	O-H wagging and twisting	[11]
853 (shoulders at 808 & 836)	C-C stretching	[12-14]
898	C-C stretching	[12, 14]
936	C-C stretching	[12, 13]
1022	C-O stretching O-H bending	[12, 15]
1070	C-O stretching O-H bending	[12-14]
1098	C-O stretching O-H bending	[12-14]
1126	C-O stretching O-H bending	[12, 14, 16]
1143	C-O stretching C-O stretching	[11-14, 16]
1359	C- bending O-H bending	[11-13, 15]
1441	C- bending O-H bending	[11-13, 15]
1657	C=O stretching (residual acetate)	[11]
1732 (shoulder at 1711)	C=O stretching (residual acetate)	[11]
1882	C-O asymmetric stretching (residual acetate)	[11]
2909	C-H stretching	[12]
2936	C-H stretching	[12]

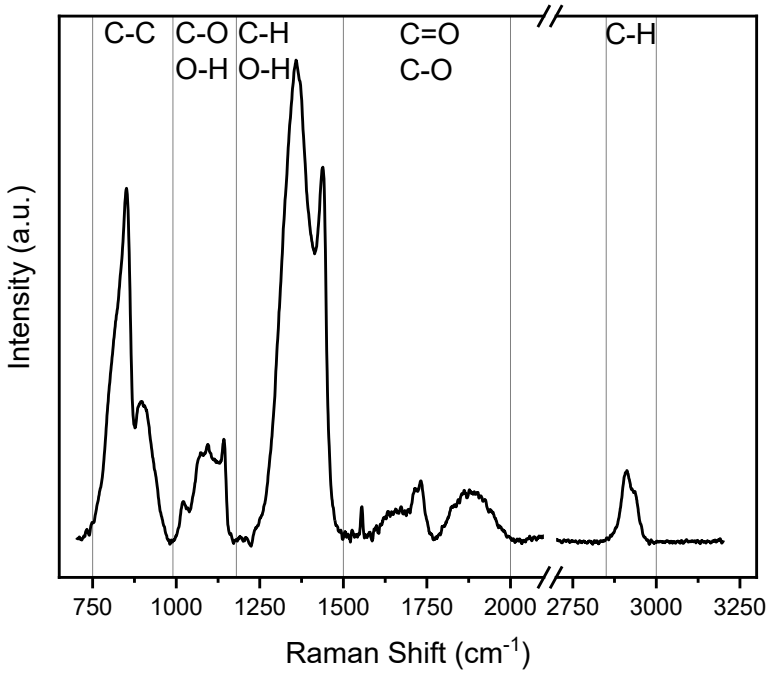


Figure 38: Raman spectrum of PVAL. The spectra is divided into the main regions where characteristic vibrations were observed. The main contributor(s) to each band is highlighted above and further details are given in Table 2.

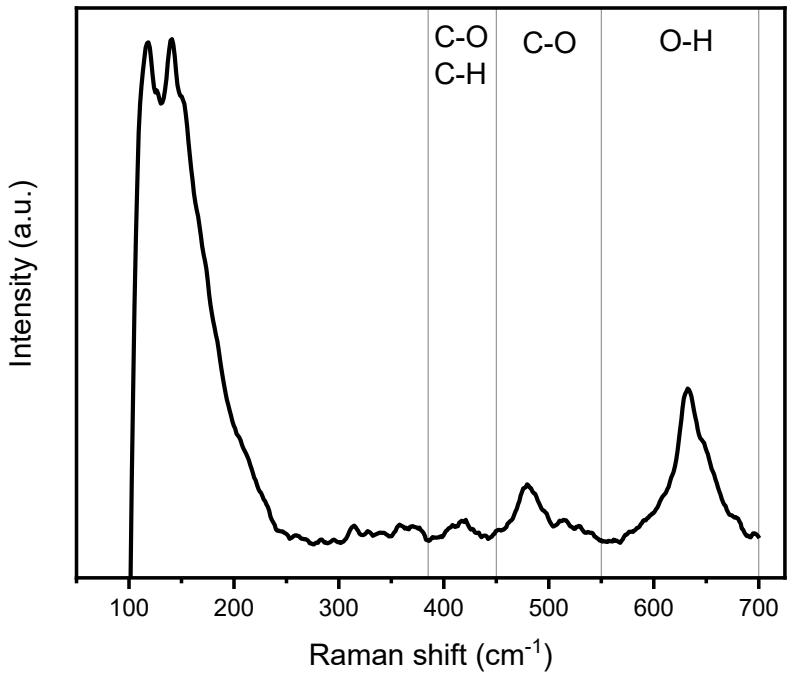


Figure 39: Raman spectrum of PVAL between 100 and 700 cm-1. The spectra is divided into the main regions where characteristic vibrations were observed. The main contributor(s) to each band is highlighted above and further discussed in Table 6.

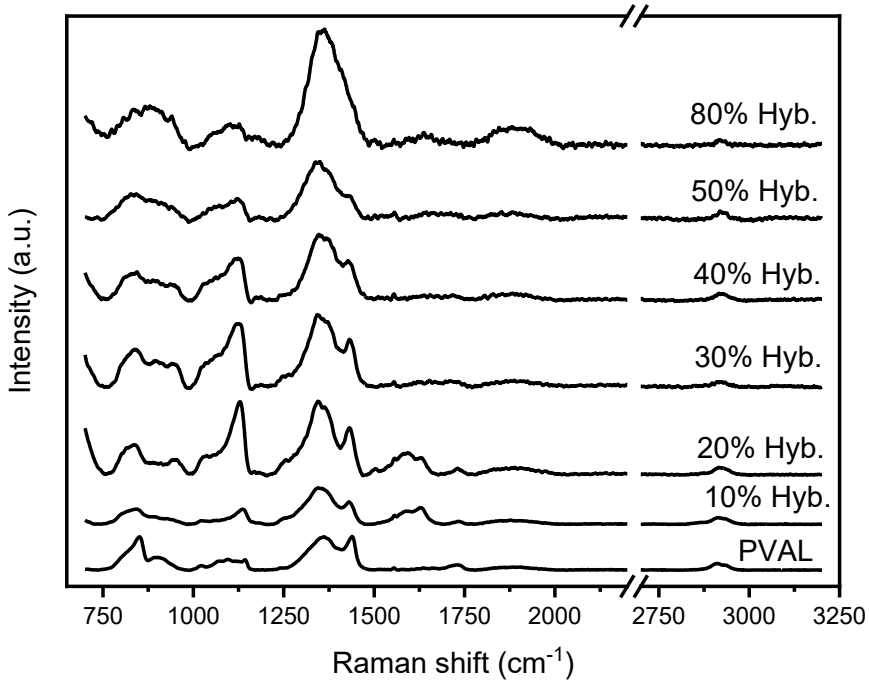


Figure 40: Raman spectra of PVAL / titanium oxide hydrate hybrid films between 700 and 3200 cm-1. The key changes occur below 1500 cm-1. The bands were split into three main regions of interest based on the C-C stretching (760-950 cm-1), C-O stretching and O-H bending (1000 – 1200 cm-1), and C-H and O-H bending (1250 – 1500 cm-1).The C-H peak around 2909 cm-1 appears to reduce in intensity with increasing inorganic loading.

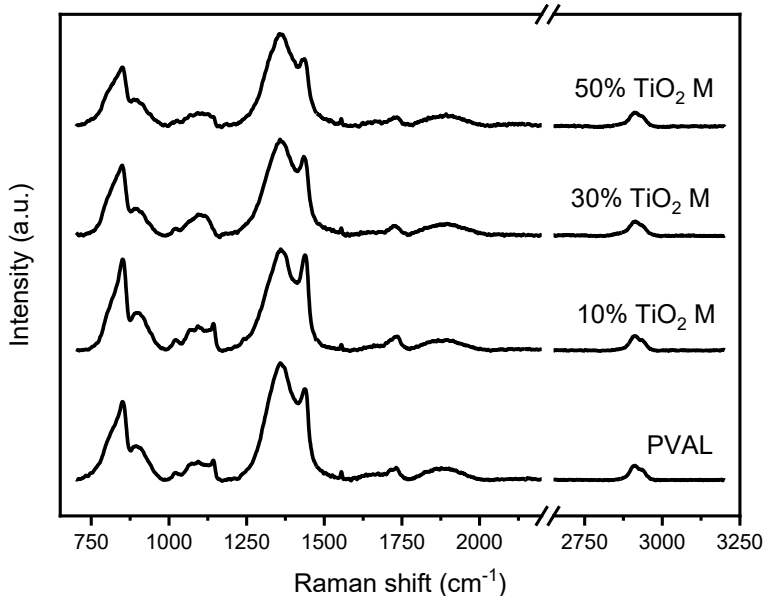


Figure 41: Raman spectra of PVAL - TiO_2 composites between 700 and 3200 cm^{-1} at spots taken where no particles were visible under the microscope lens. The notation of the letter "M" next to each sample is in reference to "matrix". This notation will be used in all the following graphs. See Appendix C for microscope image.

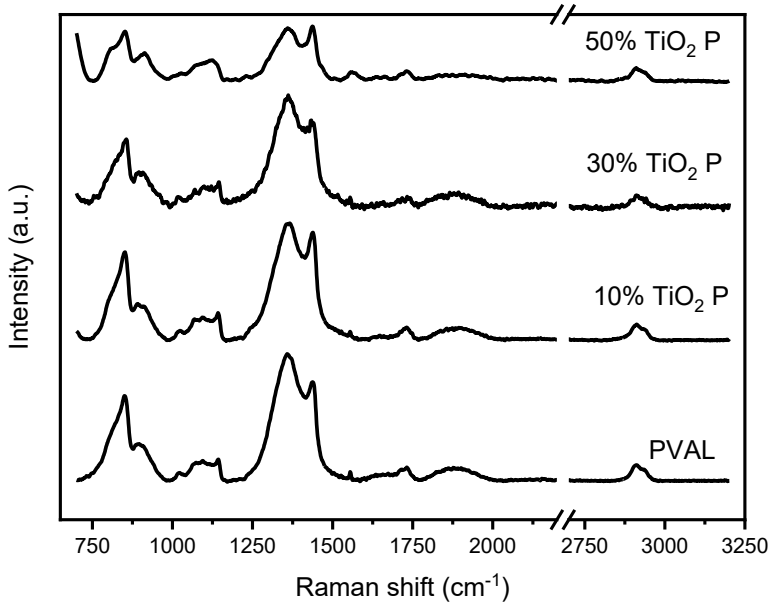


Figure 42: Raman spectra of PVAL – TiO_2 composites between 700 and 3200 cm^{-1} at spots taken from where a particle was visible under the microscope lens. The notation of the letter "P" next to each sample is in reference to "particle". This notation will be used in all the following graphs.

To simplify the analysis, the Raman spectra were split into two main ranges of interest: one from 100 to 700 cm^{-1} and the other from 750 to 3200 cm^{-1}. The former region is where the Ti-O vibrations were expected based on literature and the latter is where PVAL vibrations are primarily observed. Figure 40 displays the Raman spectra of the PVAL / titanium oxide hydrate hybrid films on gold SERS substrates. The creation of the hybrid structure has significant changes in all the regions in the 750-1550 cm^{-1} range. The C-H stretching bands at 2909 and 2936 cm^{-1} show no significant changes except a reduction in intensity with increasing Ti content. Note that the residual acetate peaks (1600 – 2000 cm^{-1} window) are still apparent in the hybrids however weaker. The 10 and 20 vol.% Ti hybrids have two large peaks in that region at 1593 cm^{-1} and 1630 cm^{-1}. These are characteristic of C=C stretching in the PVAL backbone and typically occur during thermal degradation of the polymer [17, 18]. In studies on thermochromism of PVAL / titanium oxide hydrate hybrids, it was for instance observed that the hybrid structure accelerates the thermochromic behaviour of PVAL and allows it to occur at a lower temperature (in neat PVAL it was at 200 ^{o}C) [7]. The thermochromic response of PVAL was due to the increase of unsaturated bonds in the backbone (i.e. C=C in the backbone) at high temperatures [7]. The signals seen here could be from the increased temperature by the laser as this characteristic C=C vibration was not observed in other spectroscopic techniques. Furthermore, the laser power was reduced for the hybrid samples with greater than 30 vol.% Ti. Figure 41 & Figure 42 show the Raman spectra of the PVAL – TiO2 composite films where the microscope was focused on the PVAL (matrix) or particles, respectively. Some differences between the spectra can be observed but not with the significant changes that are detected with the hybrid films.

For the C-C stretching bands (760-950 cm^{-1}), the spectra are presented in further detail in Figure ***43*** for the PVAL / titanium oxide hydrate hybrid films. It is clear that a significant change occurs on these bands as they appear to be separated at low loadings then coalesce in one broad peak above 40 vol.% Ti. Contrary to a shift to lower numbers indicating an increase in bond length, a shift to higher number is indicative of compression of the bonds and some molecular restriction [19, 20]. The shift to higher numbers observed in the hybrids could thus suggest that the C-C stretching vibration has been restricted in motion due to the creation of covalent bonds with the titanium. Moreover, the contraction observed of the C-C backbone may furthermore suggest that the Ti is covalently bonded to two neighbouring pendant oxygen atoms from the PVAL as represented in Figure 36.

Conversely, the PVAL – TiO_2 composites does not show such a shift in those bands with addition of TiO_2 nanoparticles. This can be observed in detail in Figure 44. It is observed that there is only a shift to lower numbers indicating a slight extension of the backbone due to the incorporation of the filler, similar to what was seen in with the PVAL – TEG system.

Figure 45 follows the C-O stretching and O-H bending region between 1000 and 1200 cm^{-1} for the PVAL / titanium oxide hydrate hybrid films. For all hybrid compositions, the signal intensity appears to be higher than for the neat PVAL film. This may be indicative for strong interactions that form between the titanium atoms and the oxygen atoms in the pendant groups. For all hybrid compositions, the peaks at 1098 and 1126 cm^{-1} appear to have the highest intensity. Furthermore, the intensity of the 1143 cm^{-1} peak appears to disappear. As deduced from previous studies and earlier in this thesis, this change and increase in the 1098 and 1126 cm^{-1} peaks is suggestive of a lower degree of local order in PVAL. [13, 14, 16, 21]. This change may be anticipated as the hybrid creates a cross-linked network via the oxygen atoms, which would decrease local order [4, 8, 11, 22]. Furthermore, the reduction in local order is observed at all inorganic content of the hybrid films indicating a relatively homogenous distribution of the cross-linked network in agreement with the reported optical properties [4-6, 22]. Still, the Raman signal was taken from small points over the film and may not be representative of the whole film. Therefore, only information on local order rather can be inferred.

For the composites on the other hand, no shift is observed, independent of particle content. That region is presented in further detail in Figure 46. Indeed, at 10 wt.% TiO_2 a strong 1144 cm^{-1} peak was still observed which could suggest that the particles acted as nucleating sites for the PVAL crystals [21]. However, at higher loadings the 1098 and 1126 cm^{-1} peaks are more apparent, which suggest lesser local order. This change signifies the hydrogen bonding between the TiO_2 particles and the PVAL matrix but no indication for strong covalent bonding is found as for the hybrids.

In the third region of interest, the C-H bending and O-H bending between 1250 and 1500 cm^{-1}, at 1356 and 1441 cm^{-1} both peaks were shifted to lower wavenumbers in all PVAL / titanium oxide hydrate hybrid films. Figure 47 illustrates these changes. The 1441 cm^{-1} is reduced in intensity and shifted to lower wavenumbers which is indicative of formation of bonds between the hydroxyl group and the titanium oxide hydrate [11]. The shift is also observed for the 1356 cm^{-1} peak that is coupled to the 1441 cm^{-1} peak . The shifts due to strong interactions

between the titanium oxide hydrate and the PVAL are similar to what was observed in crosslinking studies of PVAL in literature [14, 15, 21]. A sol-gel study of PVAL-SiO_2 also showed a similar trend, however, the loading used in that study were much lower (only up to 15wt.%) [16]. Here, with high loadings (> 40 vol.% Ti) the two peaks appear to coalesce into one large peak or 50 & 80 vol.% Ti hybrid films.

For the PVAL – TiO_2 composite films in that region, hardly any shift of those peaks is observed. This is shown in detail in Figure 48. The main change noticed here is the reduction of intensity in the 1441 cm^{-1} peak relative to the 1356 cm^{-1} peak with increasing TiO_2 loading. This is similar to what was observed in the PVAL – TEG system studied in Chapter 3 and other studies of PVAL and inorganic filler membranes. It is linked with hydrogen bond formations between the matrix and the filler [11, 13, 14, 23].

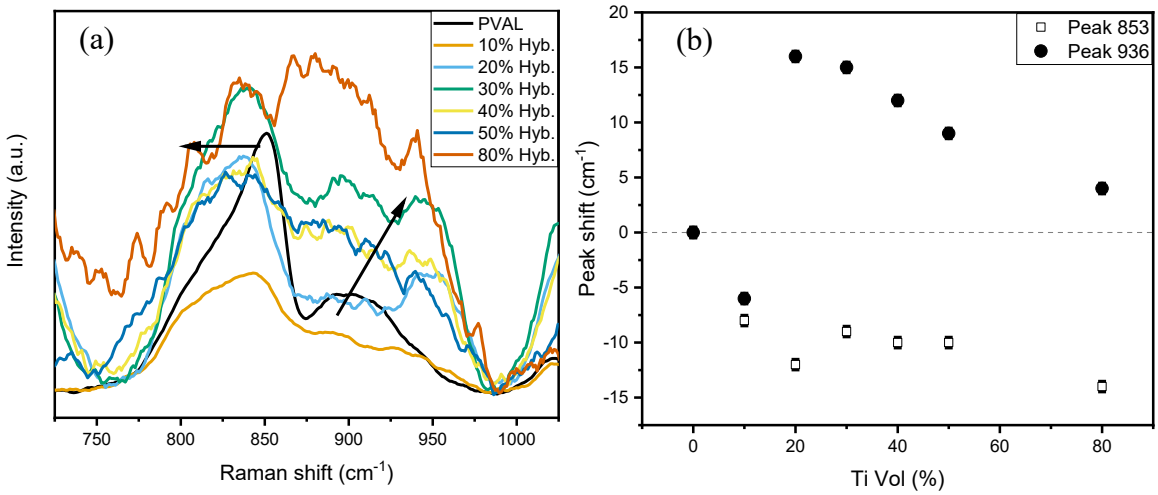


Figure 43: Raman spectra of PVAL / titanium oxide hydrate hybrids in the C-C stretching region (a). The 853 cm^{-1} peak was shifted to lower wavenumbers with increasing inorganic content but the 936 cm^{-1} peak was shifted to higher Raman shifts (b). Error bars based on resolution of the apparatus. Further errors due to peak fitting are not represented in the graph. The dashed line is used to highlight the positive and negative shifts.

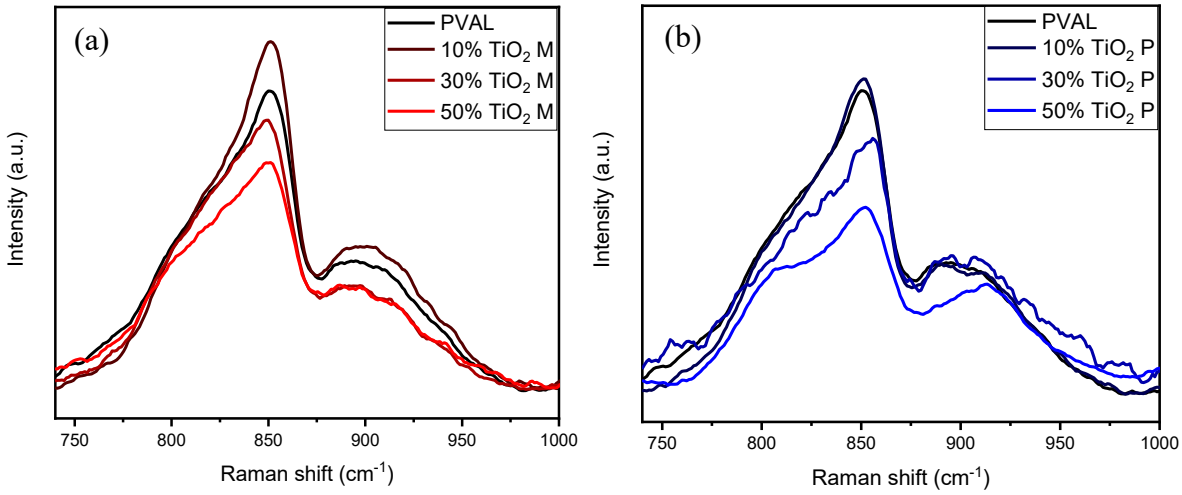


Figure 44: Raman Spectra of PVAL – TiO_2 composite films in the C-C stretching region. (a) Spectra taken in areas where no particles were observed and (b) in areas with visible particles.

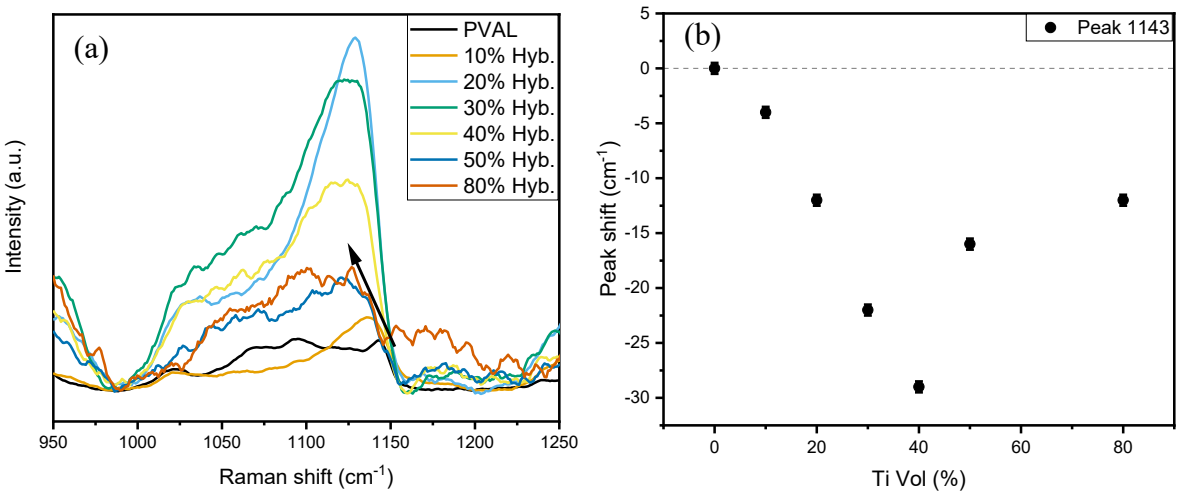


Figure 45: Raman spectra of PVAL / titanium oxide hydrate hybrids in the C-O stretching and O-H bending region (a). The relatively large shift of the 1143 cm^{-1} peak is illustrated in (b). Error bars based on resolution of the apparatus. Further errors due to peak fitting are not represented in the graph. The dashed line is used to highlight the negative shift.

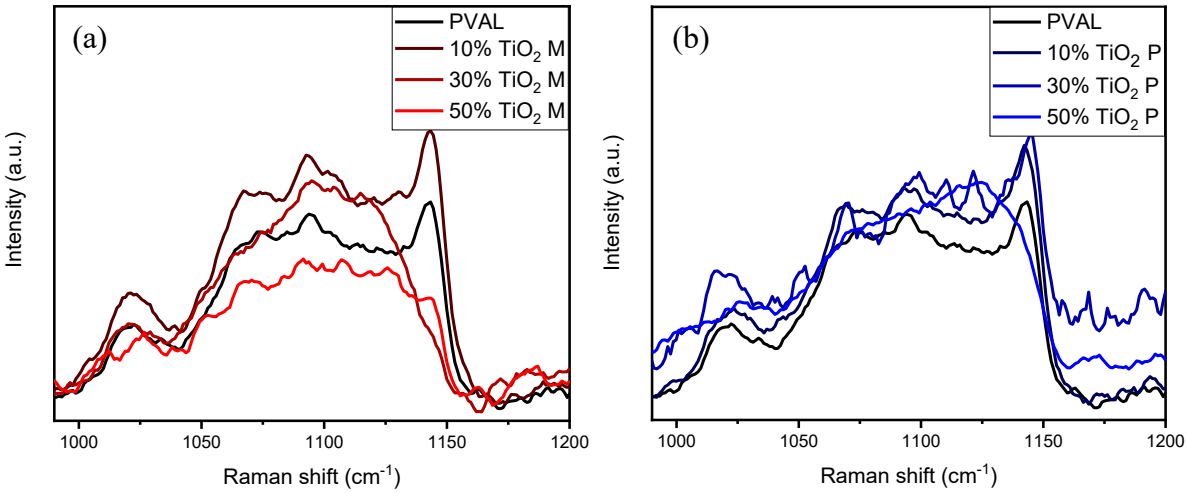


Figure 46: Raman Spectra of PVAL – TiO_2 composite films in the C-O stretching and O-H bending region. (a) Regions where the matrix was dominant and (b) regions with visible particles.

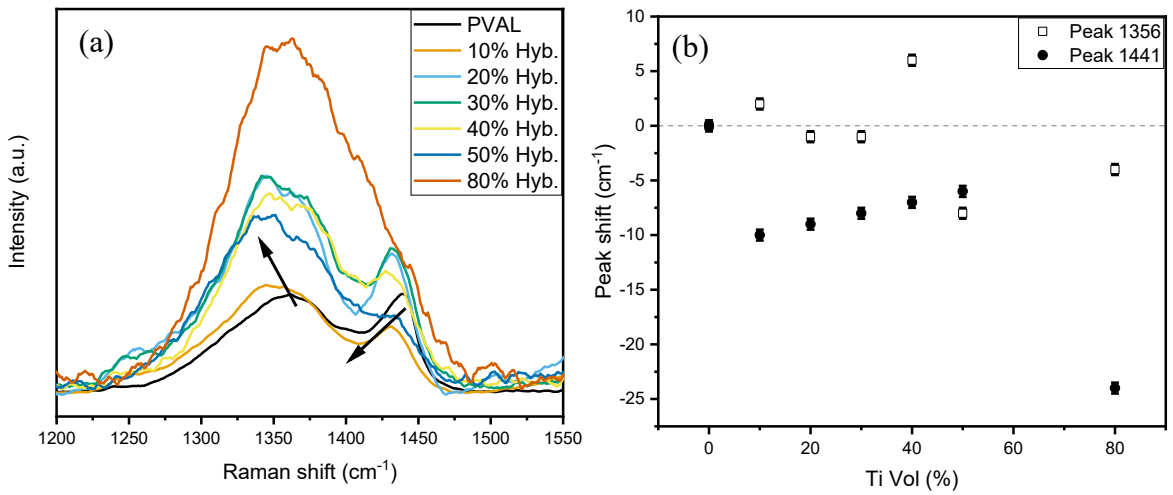


Figure 47: Raman spectra of PVAL / titanium oxide hydrate hybrids in the C-H bending and O-H bending region (a). The peaks appear to be shifted to lower wavenumbers with the 1441 cm[1] showing a larger shift (b). Above 50 vol.% Ti, the two peaks merge into one broad peak. Error bars based on resolution of the apparatus. Further errors due to peak fitting are not represented in the graph. The dashed line is used to highlight the negative shift.

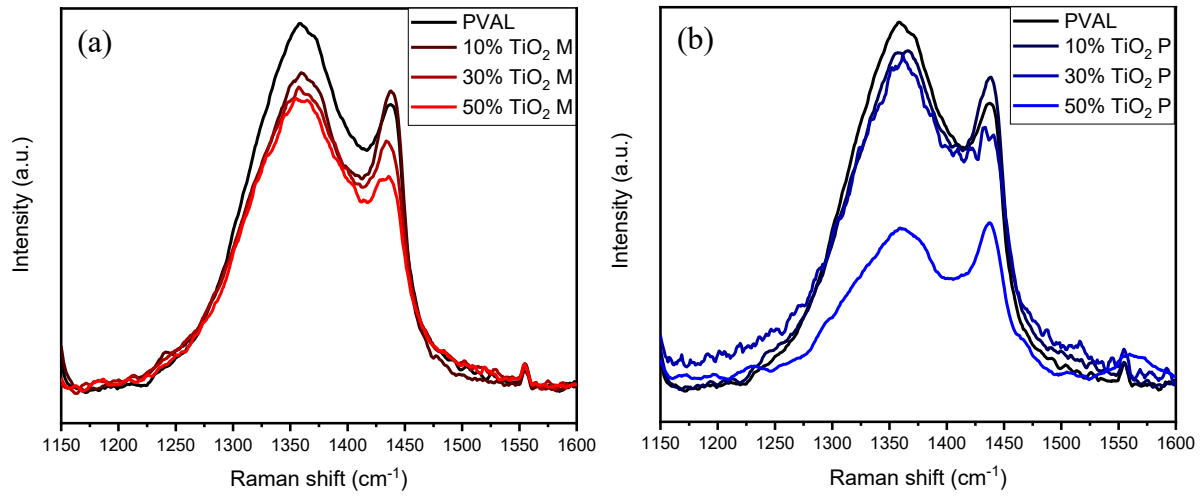


Figure 48: Raman Spectra of PVAL – TiO_2 composite films in the C-H bending and O-H bending region. (a) regions dominated by the matrix and (b) Regions where particles were observed.

The Raman spectra in the lower Raman shifts window of the PVAL / titanium oxide hydrate hybrids films is displayed in Figure 49. Figure 50 and Figure 51 show the Raman spectra of the PVAL - TiO_2 composite films taken from the matrix and particles, respectively.

Taking Raman spectra obtained from the particle as reference, three main characteristic peaks are observed of conventional anatase TiO_2 (Figure 51). These peaks are assigned in Table 7.

Table 7: Peak assignment for anatase TiO_2 based on Raman of PVAL-TiO_2 composites.

Peak Centres (cm^{-1})	**Assignment**	**Reference**
395	O-Ti-O bending	[13, 24, 25]
517	Ti-O antisymmetric stretching	[13, 24, 25]
638	Ti-O symmetric stretching	[13, 24, 25]

For the PVAL / titanium oxide hydrate hybrids, no sharp peaks characteristic for anatase are observed at any composition. One of the changes is the apparent formation of a broad peak centred at 434 cm^{-1}. This peak is centred in the middle between the C-O bending and wagging modes of the neat PVAL (414 and 481 cm^{-1}), and appears to grow in intensity with higher inorganic content. Furthermore, the 634 cm^{-1} peak in PVAL associated with O-H wagging and twisting appears to broaden and reduce in intensity with increasing loading. Remarkably, these spectra do not look like any known crystal structure of TiO_2 which typically give clear and sharp peaks [25]. It is inferred from these traces that an amorphous network of Ti-O with PVAL was created [26, 27]. This is in agreement with previous studies on the PVAL / titanium oxide hydrate hybrids where no crystal structures were observed [4-9].

Conversely, the PVAL – TiO_2 composite films show the sharp peaks typically for anatase crystals. Even at the points were it was considered that only PVAL is present, the peaks at 395, 517 and 638cm^{-1} are apparent in 10 wt.% TiO_2 composites, though they were not as sharp in the 30 and 50 wt.% TiO_2 nanocomposite films. This could be due to the presence of particles much smaller than the optical microscope can resolve. Note that the spectra are in agreement with studies in literature of similar systems [13, 23].

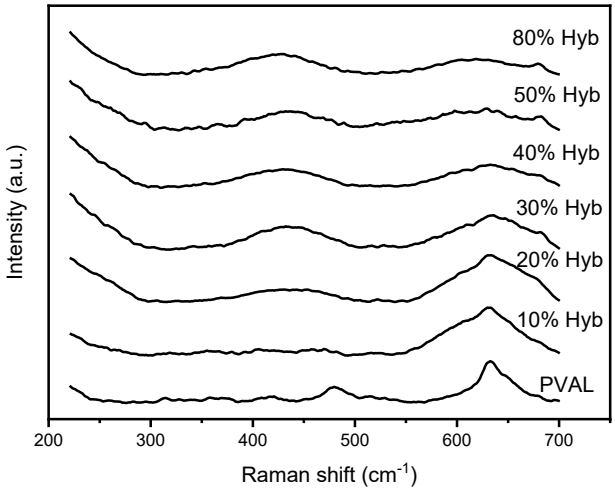


Figure 49: Raman spectra of PVAL / titanium oxide hydrate hybrid films between 220 and 700 cm^{-1}.

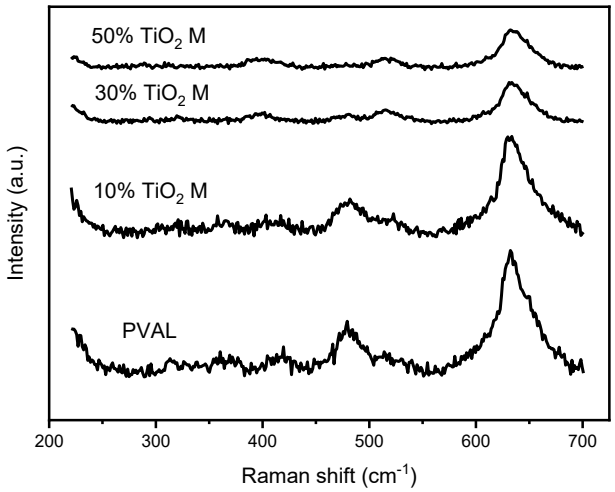


Figure 50: Raman spectra of PVAL – TiO_2 composite films between 220 and 700 cm^{-1} taken where predominantly the matrix was observed.

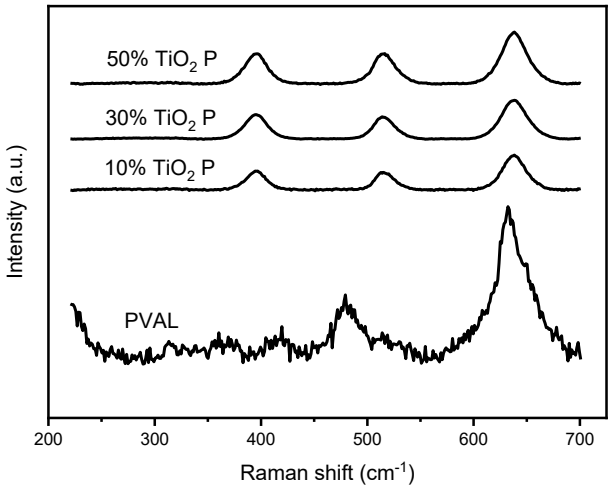


Figure 51: Raman spectra of PVAL – TiO_2 composite films between 220 and 700 cm^{-1} in regions where the particles were observed.

4.2.2 Fourier-Transform Infra-Red (FTIR) Spectroscopy

We recall the assignment of the FTIR bands of neat PVAL film in Table 4. Figure 52 shows the FTIR spectra of a neat PVAL film with relevant bands highlighted and contributors to each band indicated.

Table 8: FTIR band assignments for PVAL.

Band centres (cm^{-1})	Assignment	Reference
3276	O-H stretching inter and intrachain	[28, 29]
2937, 2905	C-H stretching	[28, 29]
1733, 1709	C=O stretching (residual acetate)	[29]
1430	C-H stretching	[28, 29]
1123	C-O stretching (local ordered segments)	[28, 29]
1083, 1051, 1021	C-O-C stretching	[29]

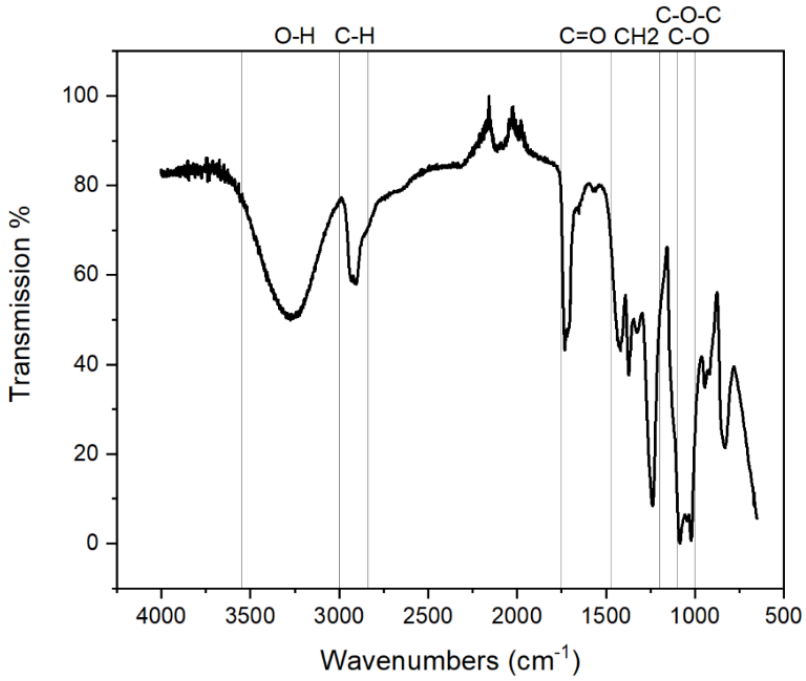


Figure 52: FTIR spectra of PVAL. The spectra is divided into the main regions where characteristic vibrations are observed. The main contributor(s) to each peak are indicated.

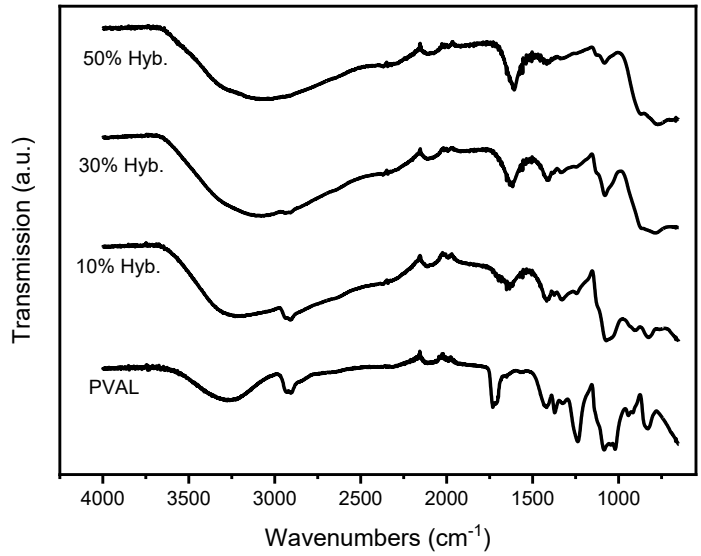


Figure 53: FTIR spectra of PVAL / titanium oxide hydrate hybrid films.

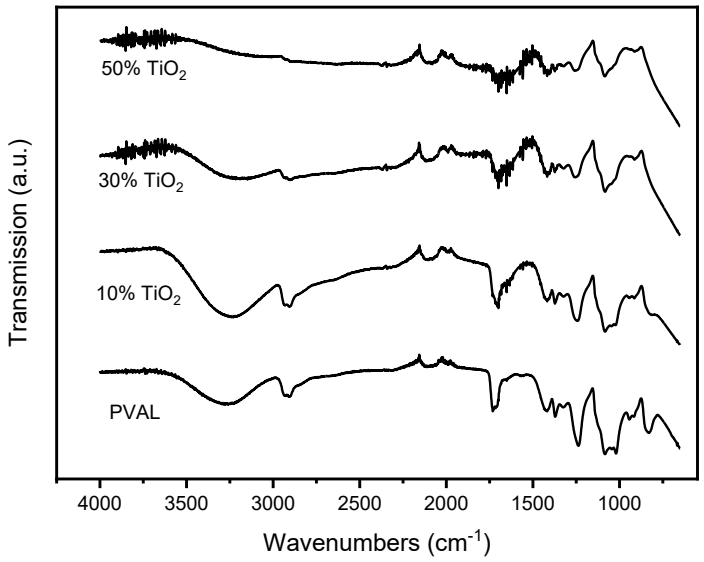


Figure 54: FTIR spectra of PVAL - TiO_2 composite films.

The FTIR spectra of both the PVAL / titanium oxide hydrate hybrids and the PVAL – TiO_2 composite films are presented in Figure 53 & Figure 54, respectively. For the hybrid films, the O-H band that originally is at 3276 cm^{-1} is shifted considerably to lower wavenumbers and with an increase in intensity. The C-H stretching bands at 2937 and 2905 cm^{-1} appear to be overshadowed and merge with the O-H band creating a very broad absorption band. This change is similar to a PVAL crosslinking study using terephthalic acid which complements the cross-linked network of the hybrids [30]. This drastic shift to lower number was also reported in a PVAL / boric acid study when the boron atom links to two consecutive oxygen atoms on the PVAL [31]. This could also indicate strong water absorbance from residual solvent during the film formation [10].

The C=O bands at 1733 and 1709 cm^{-1} assigned to the residual acetate are significantly shifted to lower wavenumbers with increasing inorganic loading (1634, 1616, 1607 cm^{-1}). Form literature, absorption peaks around 1630 cm^{-1} are associated with C=C skeletal stretching and O-H bending from free water molecules [32]. However, it is not expected that C=C would be created in the hybrid films without exposing them to elevated temperatures to observe a thermochromic response [7]. Moreover, the carbonyl group has a wide range in the FTIR spectra and is generally observed between 1800 and 1600 cm^{-1} [33]. It was also observed that a carbonyl group linked to more restricted carbons like an aromatic ring or cross-linked polymers, have a signal closer to 1630 cm^{-1} [34, 35]. This shift to a lower wavenumber was observed in PVAL cross-linked with boric acid where it was shifted to 1658 cm^{-1} [35]. It is likely that a similar structure is created in this organic/inorganic hybrid. Figure 55 describes an illustration of the acetate group linked to a PVAL hybrid network.

The C-H stretching band around 1430 cm^{-1} appears to reduce in intensity with increasing inorganic content. Reduction is similar to the symmetric and asymmetric bands at 2937 and 2905 cm^{-1}. For the C-O stretching region, the hybrid formation seems to restrict that vibration and the intensity of that peak is reduced with higher inorganic content. The strong absorption bands around 475 cm^{-1} assigned to Ti-O stretching and bending and it increases in intensity with increasing inorganic content [10, 36, 37].

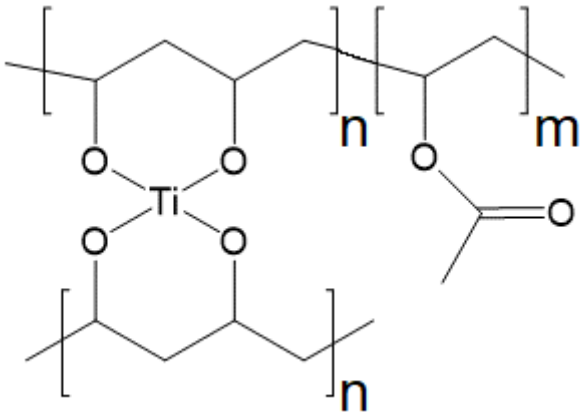


Figure 55: PVAL / titanium oxide hydrate hybrid structure with a residual acetate group.

In strong contrast to the hybrids, the 30 wt.% and 50 wt.% TiO_2 nanocomposite films appear to have a lot of scattering and the signal has much more noise. A shift to lower wave numbers of the O-H stretching can be observed but it is not as significant as the one for the hybrid films. This shift is likely due to the interaction of the hydroxyl group with the TiO_2 nanoparticles and

disrupting the hydrogen bonding in PVAL [10, 36]. Furthermore, the intensity of the peak decreases with increasing amount of TiO_2. This could be due to increased scattering in that range or that the films were not sufficiently thick. The C=O band is slightly shifted to lower number for the 10% TiO_2 film but at the higher loadings, the signal was too noisy to discern any changes. The C-H stretching is reduced in intensity with increasing TiO_2. This could be due to the higher inorganic content in the system. For the C-O band at 1123 cm^{-1}, a deformation of the peak is observed due to the introduction of TiO_2 nanoparticles. The peak is linked with ordered regions of PVAL and the addition of the particles disrupts the formation of crystalline regions in the PVAL film. This complements what is observed with Raman spectra in that region. Moreover, a strong absorption peak is detected at 475 cm^{-1}, which is assigned to the Ti-O stretching mode similar to what was observed in the hybrids films.

4.3 Differential Scanning Calorimetry (DSC)

Figure 56 (a) and (b) show the DSC thermograms for the first heating and first cooling of the PVAL / titanium oxide hydrate hybrid films, respectively. For the hybrid films, two large endotherms are apparent for the different hybrid compositions. However, no characteristic crystallisation peaks are apparent in the cooling cycle signifying that the endothermic reactions observed are irreversible [8]. There are no apparent features in the second heating cycle for the hybrid films presented in Figure 58 supporting the view of an irreversible transition.

From TGA studies of hybrid films performed previously, the endotherms observed in the first heating scan could indeed signify various reactions including: evaporation of residual water, evaporation of residual hydrochloric acid from the titanium oxide hydrate, further hydrolysis reactions of the Ti-Cl followed by evaporation HCl, crosslinking between Ti atoms and hydroxyl groups, and polycondensation of titanium oxide hydrate moieties prior to vaporisation of H_2O molecules [8]. However, the first feature could also be a glass transitions, that increases with increasing inorganic content signifying that the chains in the amorphous region are restricted in motion [38]. Furthermore, the reduction in the melting temperature could signify that the chemical crosslinking increase the inter-chain distances and reduces the crystalline region [21, 39]. T_g and T_m are listed in Table 9.

Figure 57 (a) and (b) show the first heating and cooling cycles for the PVAL – TiO_2 composite films, respectively. The composites show a single large broad endothermic peak in the first heating with a shoulder at lower temperatures. These features are apparent in the consequent cooling and the heating cycle implying that those transitions are reversible. Considering the

shoulder as the T_g and the large endotherms as T_m, the values are presented in Table 9. The glass transition appears to be higher than for neat PVAL in all composites while the melting temperature is reduced in comparison to PVAL. The increase in T_g is linked to increased interaction between the particles and the PVAL chains especially in the amorphous regions [36]. The presence of the filler moreover hinders the crystal formation resulting in a lower melting temperature. This can also be observed in the second heating cycles in Figure 59 where no melting peak is observed and only a glass transition was apparent.

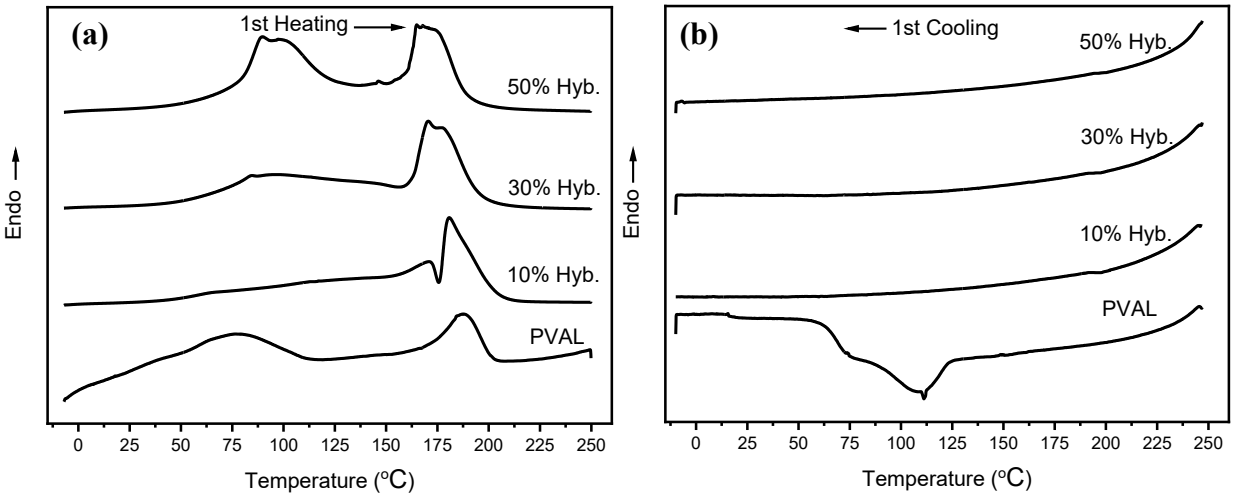


Figure 56: DSC thermograms of PVAL / titanium oxide hydrate hybrids showing the first heating (a) and cooling cycles (b).

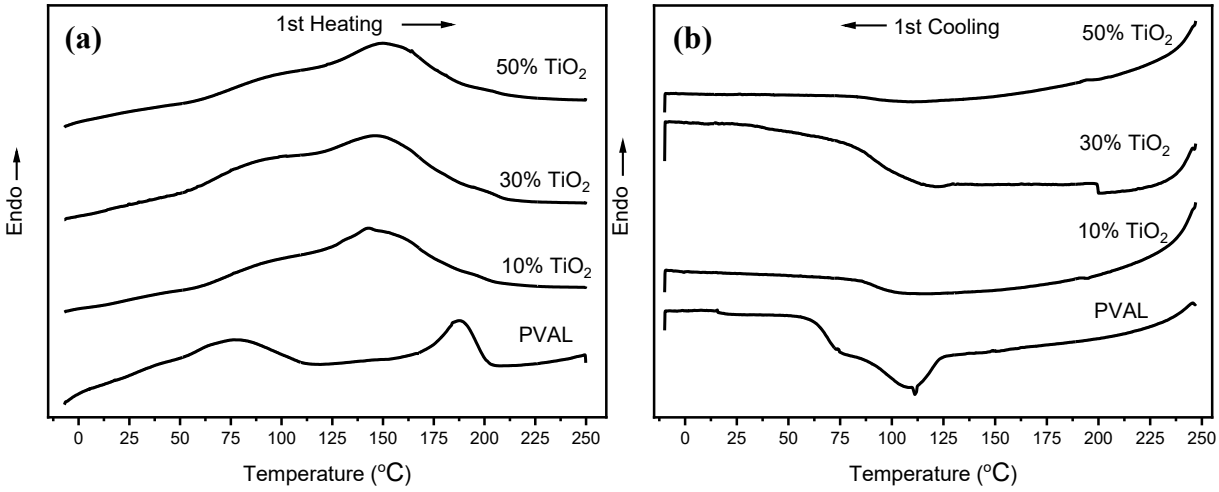


Figure 57: DSC thermograms of PVAL – TiO_2 composites showing the first heating (a) and cooling cycles (b).

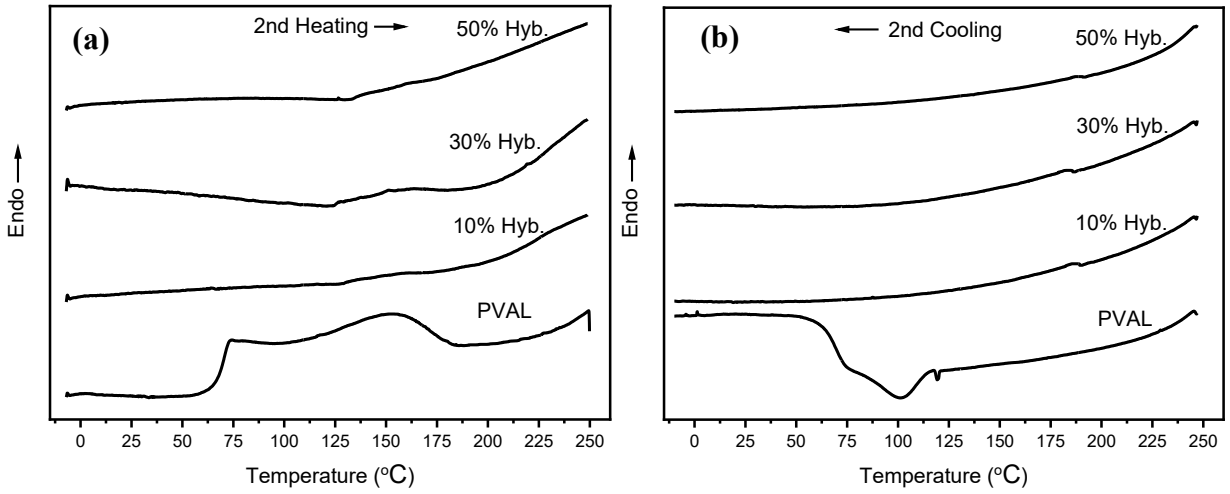


Figure 58: DSC thermograms of PVAL / titanium oxide hydrate hybrids showing the second heating (a) and cooling cycles (b).

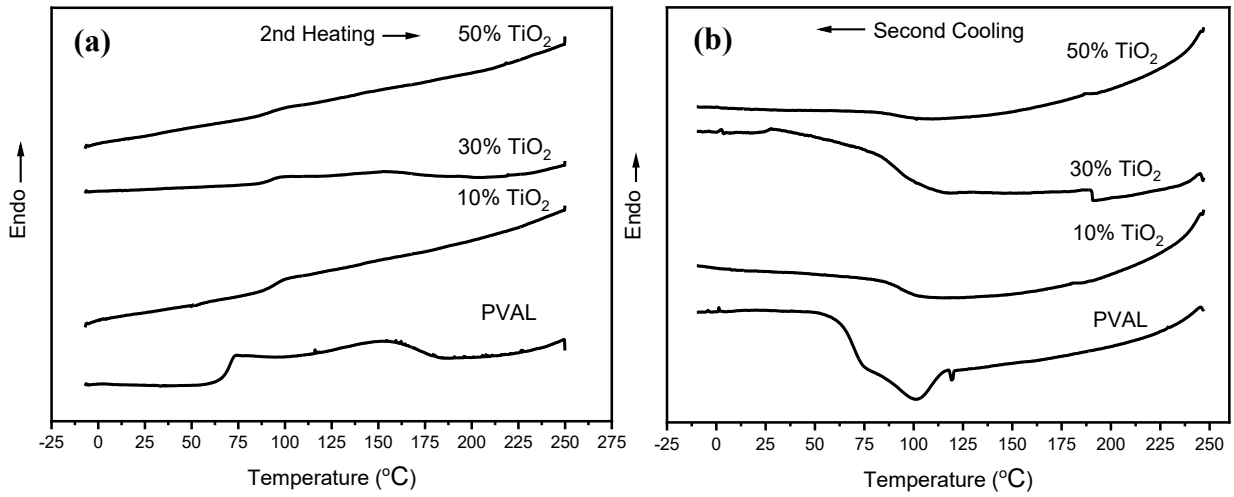


Figure 59: DSC thermograms of PVAL – TiO_2 composites showing the second heating (a) and cooling cycles (b).

Table 9: Measured glass transitions and melting temperatures of PVAL / titanium oxide hydrate hybrid films and PVAL – TiO_2 composite films.

Sample	**T_g (°C) (1st heating)**	**T_g (°C) (2nd heating)**	**T_m (°C) (1st heating)**	**T_m (°C) (2nd heating)**
PVAL	77	65	187	152
10 vol.% Ti hybrid	59*	N/A	180*	N/A
30 vol.% Ti hybrid	93*	N/A	173*	N/A
50 vol.% Ti hybrid	94*	N/A	168*	N/A
10 wt.% TiO_2	94	88	146	N/A
30 wt.% TiO_2	90	87	148	153
50 wt.% TiO_2	102	86	152	N/A

*Hybrid T_g and T_m points may be hidden by different reactions as mentioned in the analysis above.

4.4 X-ray photoluminescence spectroscopy (XPS)

XPS spectra were split in to three main regions of high resolution to simplify the analysis. The regions of interest are carbon, oxygen, and titanium. Figure 60 presents the carbon region of the PVAL / titanium oxide hydrate hybrid films. Three peaks are apparent in the neat PVAL film: at 284.5 eV assigned to CH_2, at 286 eV assigned to C-OH, and at 289 eV assigned to C=O [40]. With the creation of the hybrid network, all peaks are shifted to higher binding energy levels and with lower intensities. It is noted that the C-OH peak is reduced in intensity more significantly with increasing inorganic content signifying that the hydroxyl group was used to create covalent bonds with the titanium oxide hydrate species. This is in agreement with the FTIR and Raman studies. A similar trend was observed in literature crosslinking studies [11, 41, 42] and an experiment preparing PVAL / boric acid systems presented in Appendix D. Furthermore, the peak assigned to C=O has the same percentage of intensity for all hybrid films (Figure 60 (b)). This implies that the hybrid network was created via the hydroxyl groups primarily and not the carbonyl groups from the residual acetate. It is also in agreement with the FTIR spectra where the carbonyl group's signal was detected and only shifted in the formation of hybrid films.

For the PVAL – TiO_2 composite films (Figure 61), the peaks associated with C1s appear to shift slightly to lower binding energies but not significantly. They also appear to reduce in intensity but all with the same magnitude. This could be linked to hydrogen bond formation between the particles and PVAL [43]. Furthermore, the ratio between the peaks appears to be constant over the three different loadings of TiO_2. This probably signifies that hardly any hydroxyl groups were react with the inorganic particles and no covalent bonds are formed [11].

Focusing on the O1s, (Figure 62), the PVAL / titanium oxide hydrate hybrids show an initial reduction in the C-O peak centred around 532.2 eV with the introduction of titanium oxide hydrate. A shoulder then appears to grow at 530.7 eV and transitions to be the main peak at higher inorganic content. This peak is assigned to C-O-Ti bonds as well as Ti-O-Ti bonds as seen from literature [42, 44]. This change is also in agreement with the reduction of the C(OH) peak in the C1s region, indicating that covalent bonds are created between Ti-O-C after the condensation of the titanium oxide hydrate [4, 8].

The signals from the PVAL – TiO_2 composites feature a different trend (Figure 63). No new peak appears to grow, and the main change upon composite formation is a slight shift to lower binding energies with a reduction in intensity. This is possible be due to hydrogen bond formation similar to what is observed in the C1s part of the spectra [43, 45].

In the third window of interest, the titanium's $2p_{3/2}$ and $2p_{1/2}$ electrons were examined. This is presented in Figure 64 for the PVAL / titanium oxide hydrate hybrids where the titanium peaks centred around 458.2 eV and 464 eV are assigned to $Ti2p_{3/2}$ and $Ti2p_{1/2}$, respectively. Furthermore, the energy difference between the two peaks (5.8 eV) relates to the Ti^{4+} state [44]. The peaks appears to be sifted to a higher binding energy (~1 eV difference) with higher inorganic content. The intensity of both peaks also increases reflecting the higher Ti content in the system.

For the composite films, the signals featured a higher noise (Figure 65). This could be linked to the surface sensitivity of the measurement technique. However, at 50 wt.% TiO_2 loading, the two $Ti2p_{3/2}$ and $Ti2p_{1/2}$ peaks are observed. Their centres are found at 458.8 eV and 464.8 eV respectively. This is in agreement to the anatase crystal structure of the TiO_2 particles. However, as both rutile and anatase have similar peaks under XPS, the exact crystal structure cannot be discerned using this technique [46].

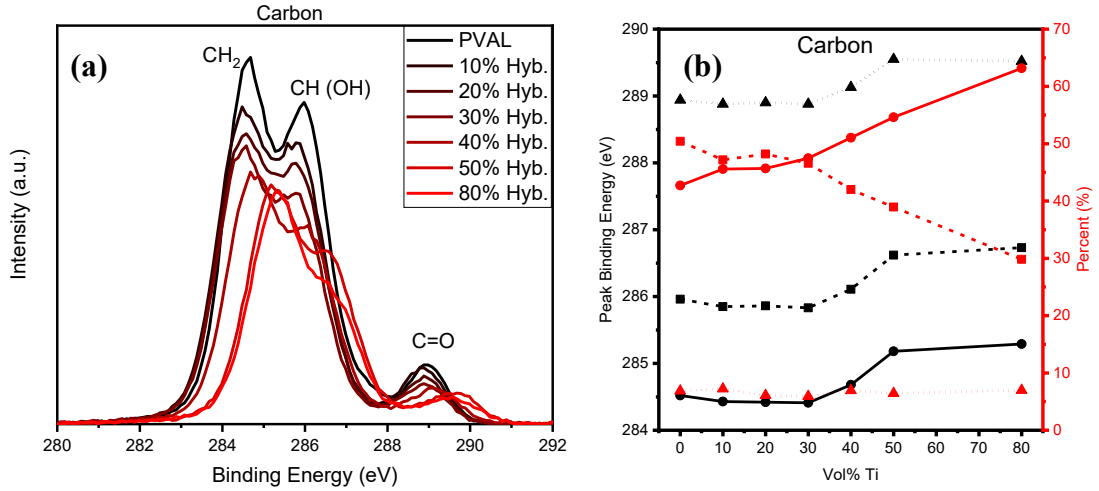


Figure 60: XPS spectra of PVAL / titanium oxide hydrate hybrid films focusing on the C1s region (a). A comparison of the carbon peak intensity is presented in (b) as a function of inorganic content.

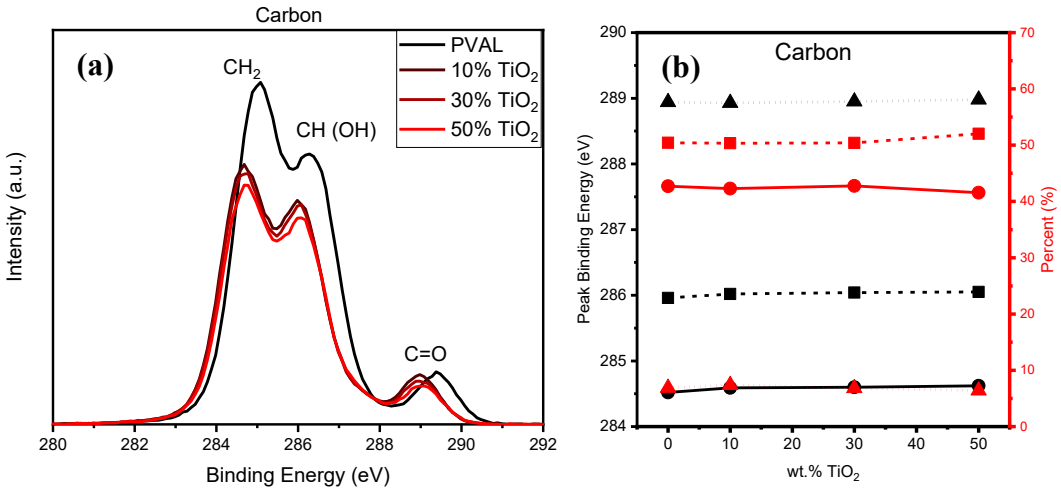


Figure 61: XPS spectra of PVAL – TiO_2 composite films focusing on the C1s region (a). A comparison of the carbon peak intensity is presented in (b) as a function of inorganic content.

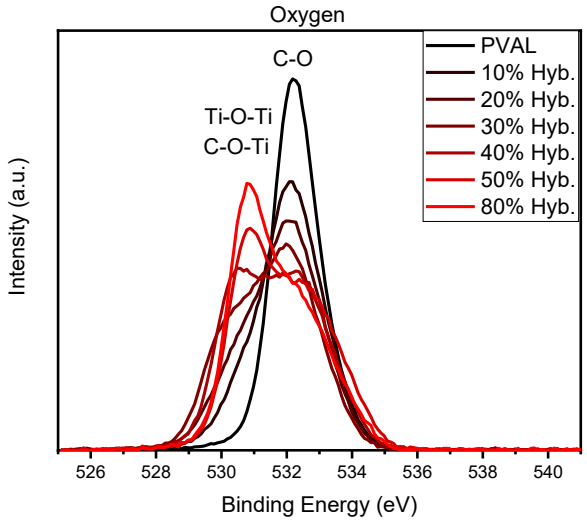


Figure 62: XPS spectra of PVAL / titanium oxide hydrate hybrid films focusing on the O1s region.

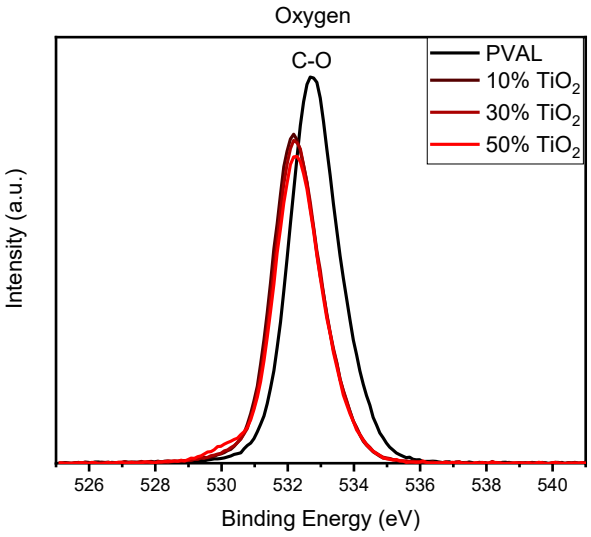


Figure 63: XPS spectra of PVAL – TiO_2 composite films focusing on the O1s region.

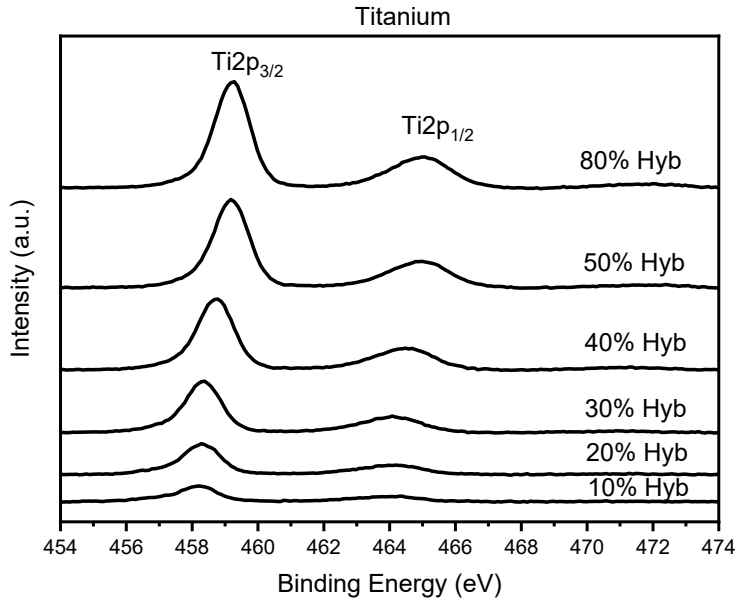


Figure 64: XPS spectra of PVAL / titanium oxide hydrate hybrid films focusing on the Ti2p region.

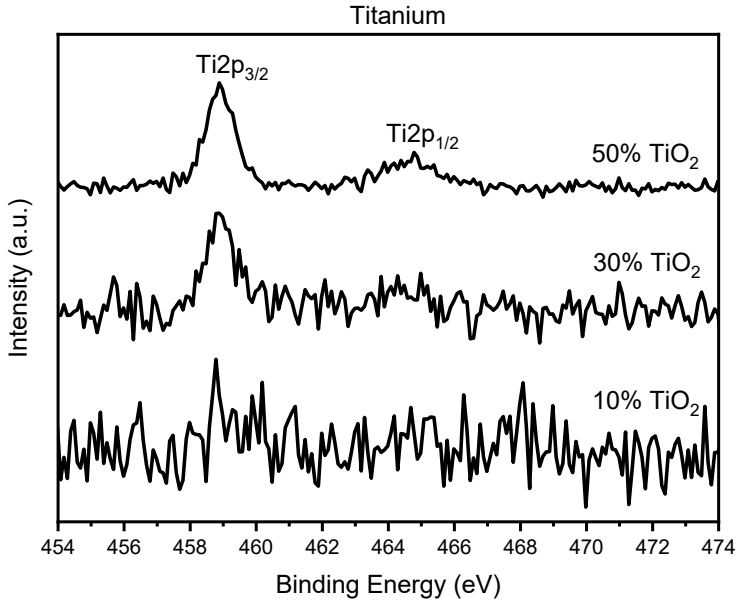


Figure 65: XPS spectra of PVAL – TiO2 composite films focusing on the Ti2p region.

4.5 SEM

Images of the PVAL / titanium oxide hydrate hybrid films using SEM are presented in Figure ***66***. The PVAL – TiO_2 composite films are shown in Figure 67. For the hybrid films, no features are discernible even at 50 vol.% inorganic content. This correlates with the findings of a previous study where no crystal formation was observed up until 80 vol.% titanium oxide hydrate. Indeed, at that loading, the particles that were observed were less than 5 nm and were only seen using TEM [4]. The distribution of the inorganic species is likely homogenous throughout the material and hardly any aggregates are observed at all compositions used in this thesis. For the PVAL – TiO_2 composites in strong contrast, TiO_2 particles can be clearly seen at all the prepared compositions. With increasing TiO_2 content, the amount of particles increases and larger agglomerates with sizes of around 2 µm are found. These larger agglomerates are the ones that could be seen under the Raman microscope. Furthermore, due to the relatively large agglomerates in the composite films, the films appear hazy at 10 wt.% TiO_2 loading, and white and opaque for 50 wt.% TiO_2. This is mainly due to the pronounced scattering of light from the particles [3]. Light scattering was hardly observed in the PVAL / titanium oxide hydrate hybrid films making them attractive optical and photonic applications [4-7, 22, 47].

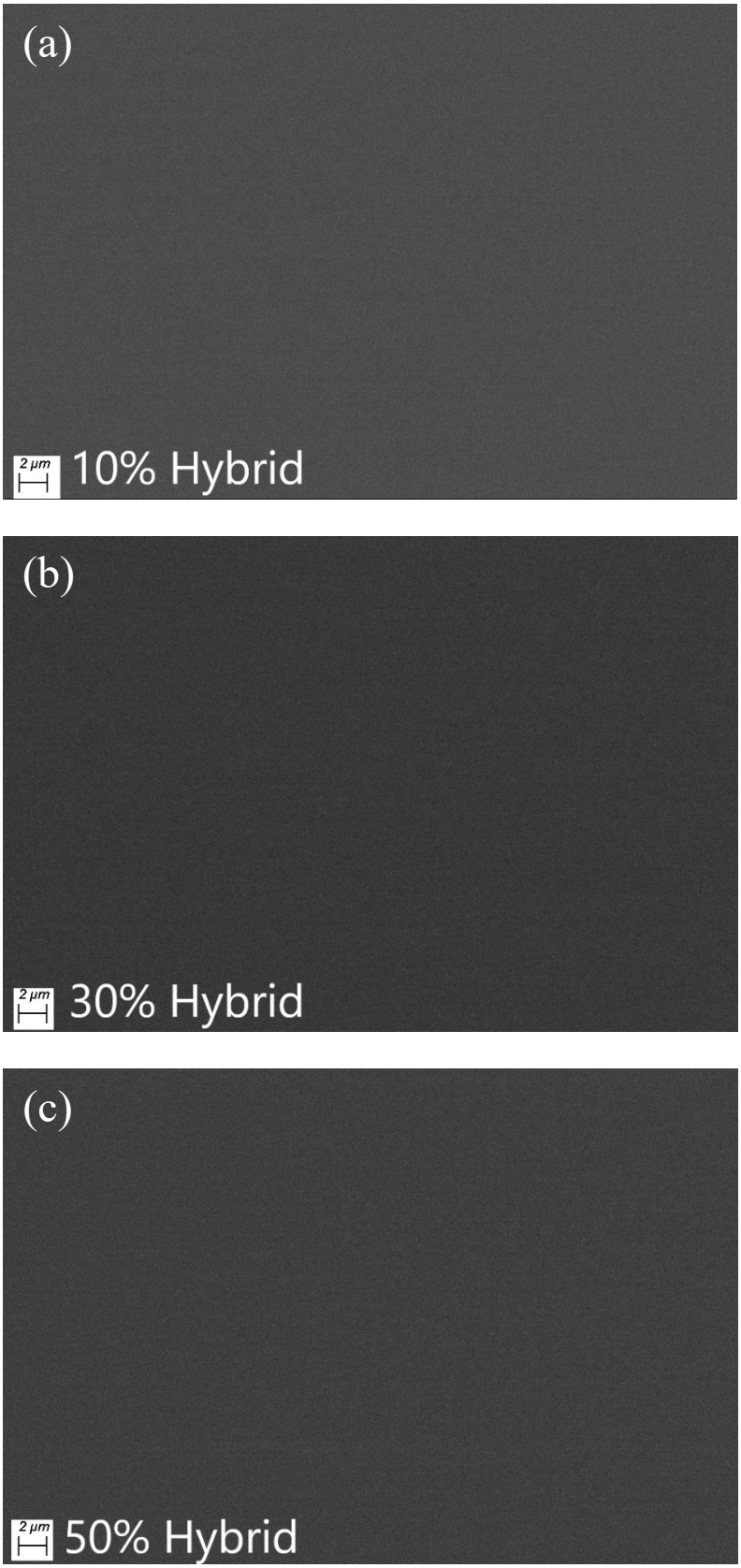


Figure 66: SEM images of hybrid films 10 vol.% (a), 30 vol.% (b), and 50 vol.% titanium oxide hydrate (c) at 5K x magnification.

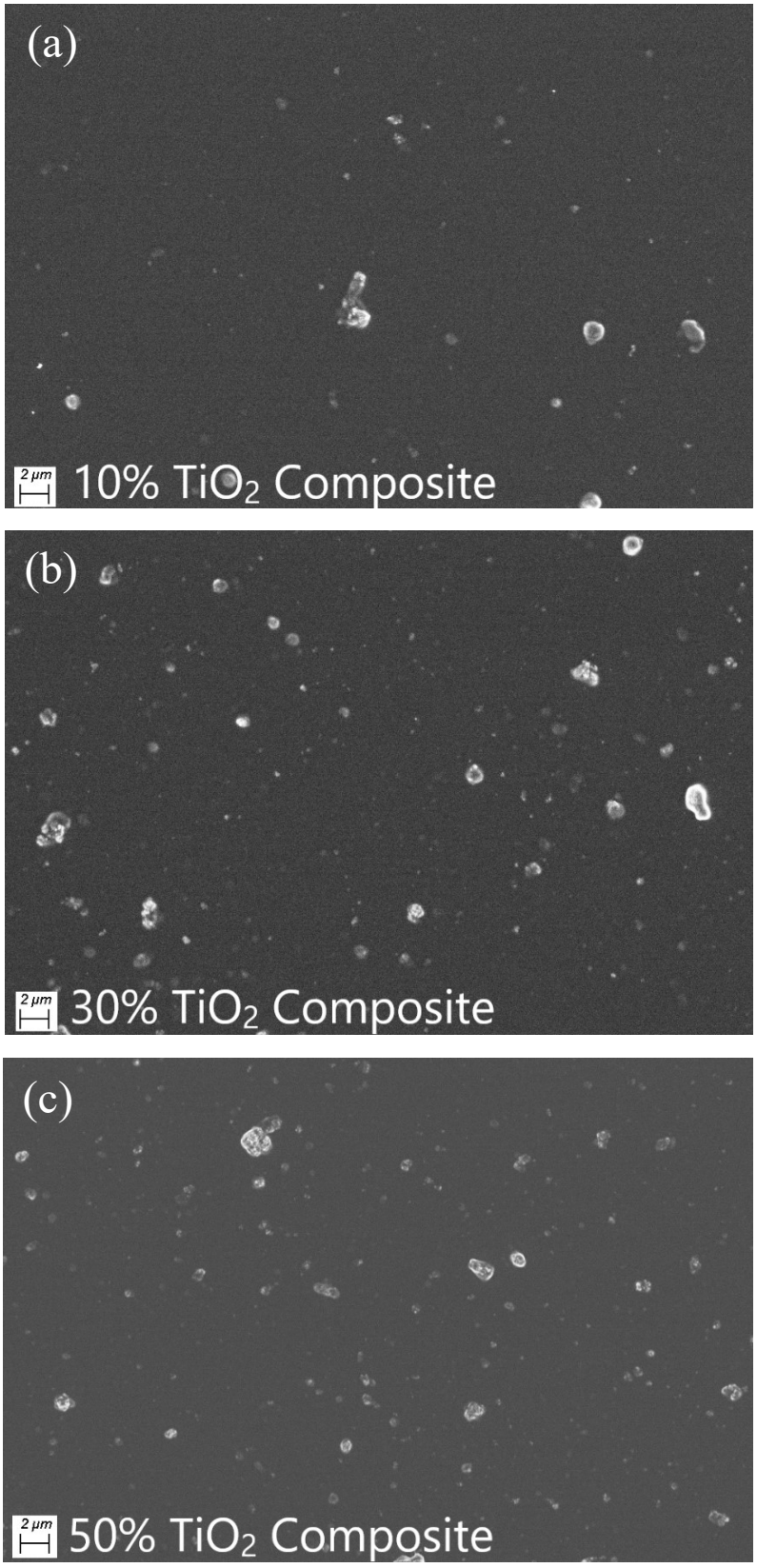


Figure 67: SEM images of nanocomposites of 10 wt.% (a), 30 wt.% (b), and 50 wt.% TiO_2 in PVAL (c) at 5K x magnification.

4.6 Thermal conductivity (3-ω)

Thermal conductivity data measured for PVAL / titanium oxide hydrate hybrid films presented in Figure 68 (squares). At 10 vol.% inorganic content, the TC measured appears to be slightly lower than for the neat PVAL. The measured TC then steadily increases in a linear fashion as a first approximation up to ~0.83 W/m.K in the 80 vol.% titanium oxide hydrate hybrid. The solid line represents the "rule of mixtures" using 0.32 W/m.K as the value for PVAL and 0.9 W/m.K for the / titanium oxide hydrate [48] . The value of K for the titanium oxide hydrate was used based on the value measured of amorphous titania film prepared by sol-gel method [49]. It appears to fit the linear trend of the rule of mixtures with higher inorganic content (>50 vol%) This trend is in agreement to a study on thiolene films cross-linked with TiO_2 nanoparticles [50]. That system is considered as the closest system to the PVAL / titanium oxide hydrate hybrids with thermal conductivity measurements found in literature. The hybrid system studied here could not be fitted with the same Bruggeman model used in that study as it takes into account the particle shape and the thermal resistance, which would not be representative of this system. Furthermore, extrapolating the trend observed using the rule of mixtures, the thermal conductivity of a ~100 vol.% titanium oxide hydrate hybrid film would be 0.9 W/m.K which fits the trend in the experimental data points Despite the fact that the organic / inorganic hybrid network creates a less ordered system, the thermal conductivity increases. This may be attributed to more efficient phonon pathways throughout the material. The formation of this network differs from conventional crosslinking with organic molecules, as in some of those studies, the thermal conductivity increased then decreased with the degree of crosslinking [51-54]. As cited in Section 1.2.3 earlier, the length of the cross-linker plays a significant role in thermal transport within a material [55]. Due to the steadily increased thermal conductivity steadily upon the addition of the titanium oxide hydrate, it is possible that the titanium oxide hydrate bring the PVAL chains closer to each other than the intrinsic hydrogen bonding. Indeed, Raman, FTIR, and XPS spectroscopy revealed the restrictive effect on the polymer backbone. Moreover, from previous studies, particles of less than 5 nm were observed only at very high inorganic content loading in PVAL / titanium oxide hydrate hybrids [4]. This implies that the PVAL polymer chains are greatly restricted in motion due to the hybrid network formation yet they interact closely in creating less scattering points for phonons. Another takeaway from the results is that no apparent step in the measured thermal conductivity is observed with increasing inorganic content. This implies that there is no percolation threshold in this system unlike in conventional composites with TiO_2 particles [56, 57].

The thermal conductivity measured data for PVAL – TiO_2 composite films are presented in Figure 68 (circles). Reassuringly, the TC values are comparable to those of neat PVAL despite TiO2 has a higher intrinsic TC than PVAL. Furthermore, no percolation threshold is observed. This implies that the thermal transport in these films was primarily through the PVAL matrix and not through the TiO_2 particles, as they did not form a percolating network [56]. Therefore, the variation in TC is based primarily on the changes in PVAL due to the introduction of TiO_2 and having a slightly less-ordered pathway for phonons to travel.

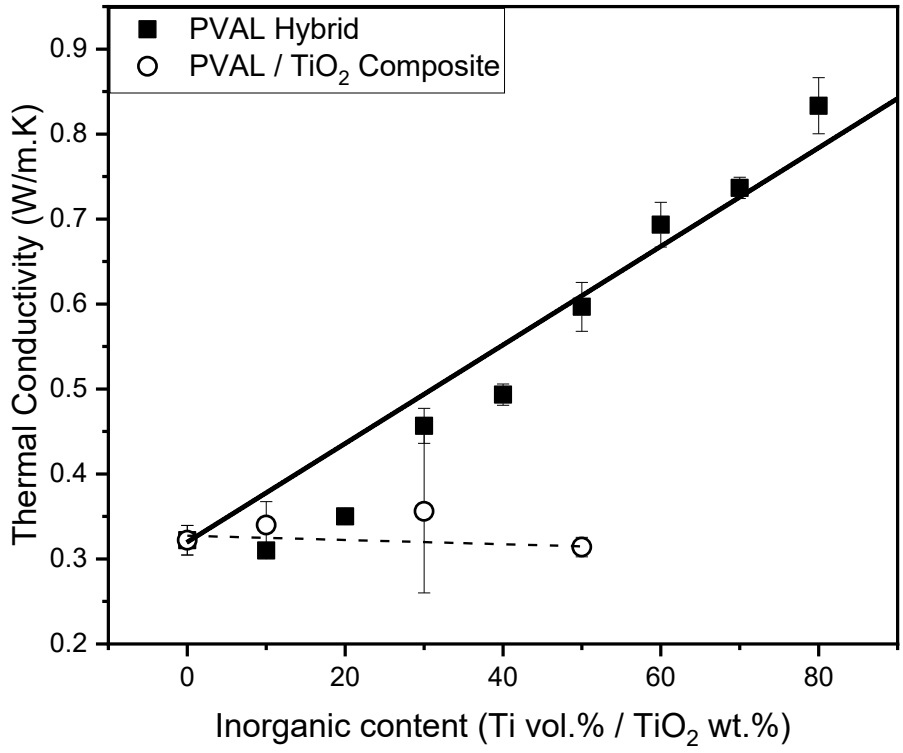


Figure 68: Thermal conductivity measurements for PVAL/titanium oxide hydrate hybrids and PVAL – TiO_2 composite films of varying inorganic content using the 3-ω technique. Error bars are based on measurements of three films for hybrids and two films for composites. Solid line based on rule of mixtures using 0.9 W/m.K as the value for the titanium oxide hydrate. Dashed line represents the relative unchanging TC of the PVAL/TiO_2 composite films with increasing inorganic content.#

4.7 Conclusions

In this chapter, another method to engineer inter-chain interactions was utilised to tune the thermal conductivity of polymer-based systems. PVAL / titanium oxide hydrate hybrid films were compared with conventional PVAL – TiO_2 to differentiate the distinct solid-state structures created. The hybrid films form a covalently bonded network of PVAL chains and titanium oxide hydrate. This was inferred by experiments using Raman, FTIR and XPS spectroscopy. In DSC, due to the crosslinking of the polymer chains, no significant features were observed in the second heating and cooling cycles. This is in strong contrast to the reversible phase transitions found for the PVAL – TiO_2 composites. From FTIR, Raman and XPS spectroscopy, it was deduced that only changes in hydrogen bonding between the polymer and the filler occur and no covalent bonds were form. These dissimilar structures between the hybrid and nanocomposite give rise to different thermal transport pathways. In the PVAL / titanium oxide hydrate hybrid films, phonons have pathways between PVAL chains and the titanium oxide hydrates that link them. This creates a large amorphous macromolecule that is expected to have isotropic thermal conductivity. For the PVAL – TiO_2 composites in contrast, two separate phases are formed where phonons may travel more efficiently through the TiO_2 particles than the polymer chains. However, in the films studied in this thesis, the measured TC of PVAL – TiO_2 composites of different compositions varied slightly from the neat PVAL. No percolation threshold was observed in contrast to reports in literature. It was deduced that the variation in thermal conductivity was due to the changes in PVAL structure which was the primary means of phonon transport in these composite films.

4.8 References

1. Nanko, M., *Definitions and Categories of Hybrid Materials.* Advances in Materials and Processing Technologies, 2009. **11**(1): p. 1-8.
2. Sanchez, C., et al., *Applications of advanced hybrid organic-inorganic nanomaterials: from laboratory to market.* Chemical Society Reviews, 2011. **40**(2): p. 696-753.
3. Caseri, W.R., *Nanocomposites of polymers and inorganic particles: preparation, structure and properties.* Materials Science and Technology, 2006. **22**(7): p. 807-817.
4. Bachevillier, S., *Solution-Processed Photonics for Light and Heat Management*, in *Department of Materials*. 2019, Imperial College London.
5. Strang, A., *Organic/Inorganic Hybrid Material for Solution-Processed Photonics Applications*, in *Department of Materials*. 2015, Imperial College London.
6. Russo, M., et al., *One-pot synthesis of polymer/inorganic hybrids: toward readily accessible, low-loss, and highly tunable refractive index materials and patterns.* Journal of Polymer Science Part B: Polymer Physics, 2012. **50**(1): p. 65-74.
7. Russo, M., et al., *Versatile Chromism of Titanium Oxide Hydrate/Poly(vinyl alcohol) Hybrid Systems.* Advanced Materials, 2012. **24**(22): p. 3015-3019.
8. Votta, I., *Titanium-Oxide-Hydrates Based Organic/Inorganic Molecular Hybrids produced via Sol-Gel Processing*, in *Department of Materials*. 2017, Imperial College London.
9. Russo, M., *Titanium Oxide Hydrates: Optical Properties and Applications*, in *Department of Materials*. 2010, Imperial College London.
10. Abdel-Hady, E.E., et al., *Physical and electrochemical properties of PVA/TiO2 nanocomposite membrane.* Advances in Polymer Technology, 2018. **37**(8): p. 3842-3853.
11. Madhuri, S.N., K.S. Hemalatha, and K. Rukmani, *Preparation and investigation of suitability of gadolinium oxide nanoparticle doped polyvinyl alcohol films for optoelectronic applications.* Journal of Materials Science: Materials in Electronics, 2019. **30**(9): p. 9051-9063.
12. Thomas, P.S. and B.H. Stuart, *A Fourier transform Raman spectroscopy study of water sorption by poly(vinyl alcohol).* Spectrochimica Acta Part A: Molecular and Biomolecular Spectroscopy, 1997. **53**(13): p. 2275-2278.
13. Yang, C.-C., et al., *Study of poly(vinyl alcohol)/titanium oxide composite polymer membranes and their application on alkaline direct alcohol fuel cell.* Journal of Power Sources, 2008. **184**(1): p. 44-51.
14. Dodda, J.M., et al., *Comparative study of PVA/SiO2 and PVA/SiO2/glutaraldehyde (GA) nanocomposite membranes prepared by single-step solution casting method.* Journal of Materials Science, 2015. **50**(19): p. 6477-6490.
15. Gauthier, M.A., et al., *Degree of crosslinking and mechanical properties of crosslinked poly(vinyl alcohol) beads for use in solid-phase organic synthesis.* Polymer, 2004. **45**(24): p. 8201-8210.
16. Yang, C.-C., Y.J. Li, and T.-H. Liou, *Preparation of novel poly(vinyl alcohol)/SiO2 nanocomposite membranes by a sol–gel process and their application on alkaline DMFCs.* Desalination, 2011. **276**(1): p. 366-372.
17. Li, C., et al., *New insight into non-isothermal crystallization of PVA–graphene composites.* Physical Chemistry Chemical Physics, 2014. **16**(40): p. 22145-22158.
18. Prosanov, I.Y. and A.A. Matvienko, *Study of PVA thermal destruction by means of IR and Raman spectroscopy.* Physics of the Solid State, 2010. **52**(10): p. 2203-2206.
19. Hiejima, Y., et al., *Microscopic structural changes during photodegradation of low-density polyethylene detected by Raman spectroscopy.* Polymer Degradation and Stability, 2018. **150**: p. 67-72.
20. Kida, T., Y. Hiejima, and K.-h. Nitta, *Raman Spectroscopic Study of High-density Polyethylene during Tensile Deformation.* International Journal of Experimental Spectroscopic Techniques, 2016. **1**(1): p. 1-6.

21. Martinelli, A., et al., *Structural analysis of PVA-based proton conducting membranes.* Solid State Ionics, 2006. **177**(26–32): p. 2431-2435.
22. Bachevillier, S., et al., *Fully Solution-Processed Photonic Structures from Inorganic/Organic Molecular Hybrid Materials and Commodity Polymers.* Advanced Functional Materials, 2019. **29**(21): p. 1808152 -1808159.
23. Salazar, J.D.R. *Study of Structural, Thermic, μ-Raman and Optic Transformation of PVA/TiO2 Polymeric Membranes*. in *Scientia Et Technica*. 2018. Universidad Tecnológica de Pereira.
24. Lagopati, N., et al., *Effect of nanostructured TiO2 crystal phase on photoinduced apoptosis of breast cancer epithelial cells.* International Journal of Nanomedicine, 2014. **9**: p. 3219-3230.
25. Verma, R., J. Gangwar, and A.K. Srivastava, *Multiphase TiO2 nanostructures: a review of efficient synthesis, growth mechanism, probing capabilities, and applications in bio-safety and health.* RSC Advances, 2017. **7**(70): p. 44199-44224.
26. Zhang, Q., et al., *Anodic Oxidation Synthesis of One-Dimensional TiO₂ Nanostructures for Photocatalytic and Field Emission Properties.* Journal of Nanomaterials, 2014. **2014**: p. 831752 - 831716.
27. Bradley, J.D.B., et al., *Submicrometer-wide amorphous and polycrystalline anatase TiO2 waveguides for microphotonic devices.* Optics express, 2012. **20**(21): p. 23821-23831.
28. Costa, H.S., et al., *Sol–gel derived composite from bioactive glass–polyvinyl alcohol.* Journal of Materials Science, 2007. **43**(2): p. 494-502.
29. Mansur, H.S., et al., *FTIR spectroscopy characterization of poly (vinyl alcohol) hydrogel with different hydrolysis degree and chemically crosslinked with glutaraldehyde.* Materials Science and Engineering: C, 2008. **28**(4): p. 539-548.
30. Sonker, A.K., et al., *Crosslinking of Polyvinyl Alcohol (PVA) and Effect of Crosslinker Shape (Aliphatic and Aromatic) Thereof.* Journal of Polymers and the Environment, 2018. **26**(5): p. 1782-1794.
31. Prosanov, I.Y., et al., *Complex of polyvinyl alcohol with boric acid: Structure and use.* Materials Today Communications, 2018. **14**: p. 77-81.
32. Wei, X.-X., et al., *Advanced visible-light-driven photocatalyst BiOBr–TiO2–graphene composite with graphene as a nano-filler.* Journal of Materials Chemistry A, 2014. **2**(13): p. 4667-4675.
33. Brian, C.S., *The C=O Bond, Part VI: Esters and the Rule of Three.* Spectroscopy, 2018. **33**(7): p. 20–23.
34. Brian, C.S., *The Carbonyl Group, Part I: Introduction.* Spectroscopy, 2017. **32**(9): p. 31–36.
35. Huang, M., et al., *High performances of dual network PVA hydrogel modified by PVP using borax as the structure-forming accelerator.* Designed Monomers and Polymers, 2017. **20**(1): p. 505-513.
36. Hdidar, M., et al., *Influence of TiO2 rutile doping on the thermal and dielectric properties of nanocomposite films based PVA.* Journal of Alloys and Compounds, 2018. **750**: p. 375-383.
37. Liou, G.-S., et al., *Flexible nanocrystalline-titania/polyimide hybrids with high refractive index and excellent thermal dimensional stability.* Journal of Polymer Science Part A: Polymer Chemistry, 2010. **48**(6): p. 1433-1440.
38. Miyazaki, T., et al., *Role of boric acid for a poly (vinyl alcohol) film as a cross-linking agent: Melting behaviors of the films with boric acid.* Polymer, 2010. **51**(23): p. 5539-5549.
39. Park, J.S., J.W. Park, and E. Ruckenstein, *Thermal and dynamic mechanical analysis of PVA/MC blend hydrogels.* Polymer, 2001. **42**(9): p. 4271-4280.
40. Akhter, S., et al., *XPS and IR study of X-ray induced degradation of PVA polymer film.* Applied Surface Science, 1988. **35**(2): p. 241-258.
41. Li, Y., et al., *Preparation and characterization of crosslinked electrospun pullulan nanofiber membrane as a potential for biomaterials.* The Journal of The Textile Institute, 2018. **109**(6): p. 750-756.
42. Woo, J.H., et al., *Effects of the addition of boric acid on the physical properties of MXene/polyvinyl alcohol (PVA) nanocomposite.* Composites Part B: Engineering, 2020. **199**: p. 108205-108216.

43. Flamia, R., et al., *Conformational Study and Hydrogen Bonds Detection on Elastin-Related Polypeptides Using X-ray Photoelectron Spectroscopy.* Biomacromolecules, 2005. **6**(3): p. 1299-1309.
44. Delekar, S.D., et al., *Structural and Optical Properties of Nanocrystalline TiO2 with Multiwalled Carbon Nanotubes and Its Photovoltaic Studies Using Ru(II) Sensitizers.* ACS Omega, 2018. **3**(3): p. 2743-2756.
45. Liu, S., et al., *Surface segregation in polymer blends and interpolymer complexes with increasing hydrogen bonding interactions.* Journal of Polymer Science Part B: Polymer Physics, 2005. **43**(14): p. 1924-1930.
46. Challagulla, S., et al., *Structure sensitive photocatalytic reduction of nitroarenes over TiO2.* Scientific Reports, 2017. **7**(1): p. 8783-8790.
47. Nussbaumer, R.J., P. Smith, and W.R. Caseri, *Transparent, Anatase-Free TiO2 Nanoparticle Dispersions.* Journal of Nanoscience and Nanotechnology, 2006. **7**: p. 2422 - 2432.
48. Nielsen, L.E., *The thermal and electrical conductivity of two-phase systems.* Industrial Engineering Chemistry Fundamentals, 1974. **13**(1): p. 17-20.
49. Fang, J., et al., *Thermal Conductivity of Highly-Ordered Mesoporous Titania Thin Films from 30 to 320 K.* The Journal of Physical Chemistry C, 2011. **115**(30): p. 14606-14614.
50. Schechtel, E., et al., *Elastic Modulus and Thermal Conductivity of Thiolene/TiO2 Nanocomposites.* The Journal of Physical Chemistry C, 2017. **121**(45): p. 25568-25575.
51. Park, Y., et al., *Crosslinking Effect on Thermal Conductivity of Electrospun Poly(acrylic acid) Nanofibers.* Polymers, 2019. **11**(5): p. 858-871.
52. Tang, N., et al., *Thermal Transport in Soft PAAm Hydrogels.* Polymers, 2017. **9**(12): p. 688-700.
53. Yamamoto, O. and H. Kambe, *Thermal Conductivity of Cross-linked Polymers. A Comparison between Measured and Calculated Thermal Conductivities.* Polymer Journal, 1971. **2**: p. 623-628.
54. Kikugawa, G., et al., *Effect of crosslink formation on heat conduction in amorphous polymers.* Journal of Applied Physics, 2013. **114**(3): p. 034302 -034306.
55. Rashidi, V., et al., *Thermal Conductance in Cross-linked Polymers: Effects of Non-Bonding Interactions.* The Journal of Physical Chemistry B, 2017. **121**(17): p. 4600-4609.
56. Guo, Y., et al., *Factors affecting thermal conductivities of the polymers and polymer composites: A review.* Composites Science and Technology, 2020. **193**: p. 108134 - 108159.
57. Sahu, M. and A. Satapathy, *Processing and characterization of TiO2 filled polymer composites.* Materials Today: Proceedings, 2021. **44**: p. 4945-4951.

5 Polymer / polymer nanofiber system

5.1 Motivation

In Chapter 3, it was reported how a small molecule with strong hydrogen bonding capability could influence the PVAL's chain conformation. Molecular dynamics studies were also cited that showed that polymers with stiffer backbones have a positive impact on thermal conductivity [1, 2]. PPTA features a rigid backbone due to the aromatic rings and the amide groups (see Figure 69), and strong inter-chain bonding via hydrogen bonds and π-π stacking can form that give rise to the high modulus and strength of PPTA fibres [3-5]. However, PPTA fibres on the macroscale have poor adhesion to other polymer matrices due to their strong intermolecular interactions between PPTA molecules [6].

Recently, Yang *et al*. have produced a method of obtaining aramid nanofibres (referred to as ANF here) by controlled deprotonation of the amide groups [7]. This was achieved by dispersing PPTA fibres in DMSO / KOH. The electrostatic repulsion and π-π stacking controls the size of the ANFs and prevent full molecular isolation [7]. Since this initial paper, many studies have focused on using these ANFs as building blocks in creating composites with improved properties (mainly mechanical) [3, 5, 6, 8]. In all of these studies, the ANFs are protonated by solvent substitution and then isolated by vacuum assisted filtration. They were then either dispersed in a solvent before mixing with a polymer [6, 8-10], or directly mixed with a resin before curing [3]. In contrast, in this thesis, the ANF dispersion in the DMSO / KOH solution was directly mixed with PVAL pre-dissolved in DMSO in order obtain strong bonding and interactions between the two polymers. This is anticipated to obtain stronger effects on the PVAL chain conformation in comparison to the TEG molecules.

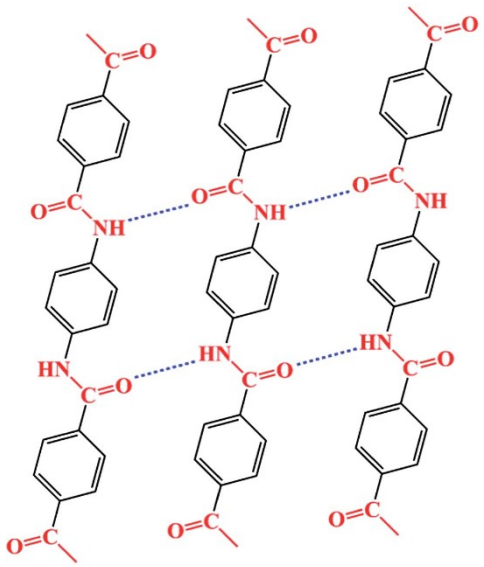


Figure 69: Chemical structure of PPTA. Amide groups are situated between the aromatic rings in the backbone. The hydrogen inter-chain bonding is illustrated with dashed lines. Reproduced from [5] with permission from the Royal Society of Chemistry.

5.2 Solid-State Structure

To study the changes in solid-state structure, a similar set of experiments and techniques were utilised here as in the previous chapters. It is noted that the base PVAL material used here and the solvent differ from the ones used in other parts of this thesis. Here, a PVAL that is 99% hydrolysed was used and the solvent was DMSO. This was to have a common solvent between PVAL and the ANF dispersion.

5.2.1 Raman Spectroscopy

The Raman window used here was the one between 600 and 1750 cm^{-1} to fit the expected peaks of ANFs reported in literature. Raman spectra of neat PVAL and neat ANF films presented in Figure 70. The main contributors assigned to each peak are indicated above the observed bands and details on the vibration modes are presented in Table 10 and Table 11 for PVAL and ANF films, respectively.

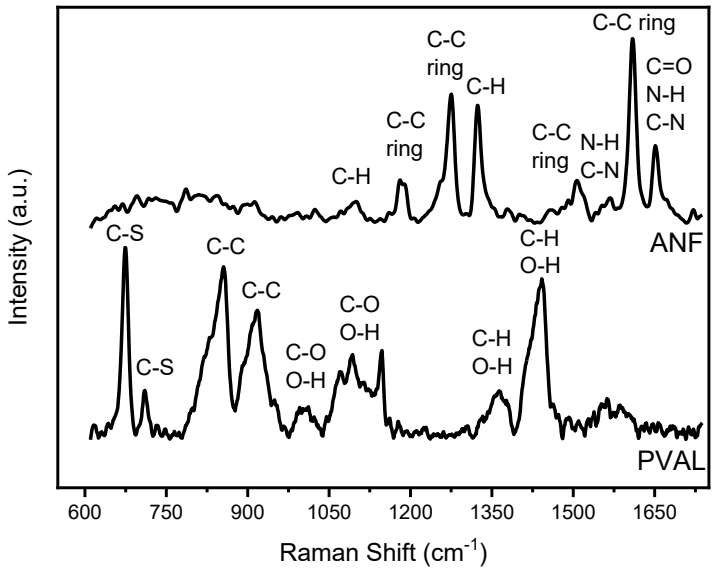


Figure 70: Raman spectra of PVAL and ANF between 600 and 1700 cm^{-1}. Observed peaks assigned to main contributor(s). Further details on peak assignments are described in Table 10 and Table 11.

Table 10: Raman peak position and assignment for PVAL.

Peak Centres (cm^{-1})	Assignment	Reference
674, 710	C-S stretching (residual DMSO)	[11]
855 (shoulders at 833)	C-C stretching	[12-14]
895	C-C stretching	[12, 14]
916 (shoulder at 944)	C-C stretching	[12, 13]
1003	C-O stretching O-H bending	[12, 15]
1068	C-O stretching O-H bending	[12-14]
1092	C-O stretching O-H bending	[12-14]
1120	C-O stretching O-H bending	[12, 14, 16]
1146	C-O stretching C-O stretching	[12-14, 16, 17]
1360	C- bending O-H bending	[12, 13, 15, 17]
1441	C- bending O-H bending	[12, 13, 15, 17]

Table 11: Raman peak position and assignment for ANF.

Peak Centres (cm^{-1})	Assignment	Reference
1101	C-H bending	[18]
1180 (1190 shoulder)	C-C ring stretching	[18, 19]
1275 (1258 shoulder)	C-C ring stretching	[18, 19]
1324	C-H in-plane bending	[18, 19]
1509	C-C ring stretching	[18, 19]
1568	N-H bending C-N stretching	[18, 19]
1609	C-C ring stretching	[18, 19]
1652	C=O stretching, C-N stretching, N-H bending	[18, 19]

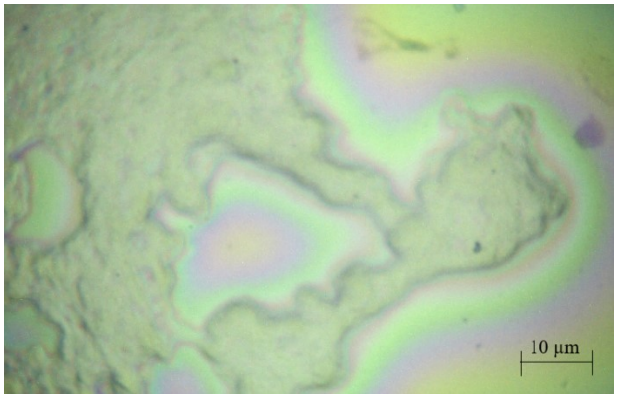


Figure 71: Optical micrograph of a 2.5 wt.% ANF sample in PVAL. Film formation at this ANF loading was poor and separated islands seemed to form on the substrate.

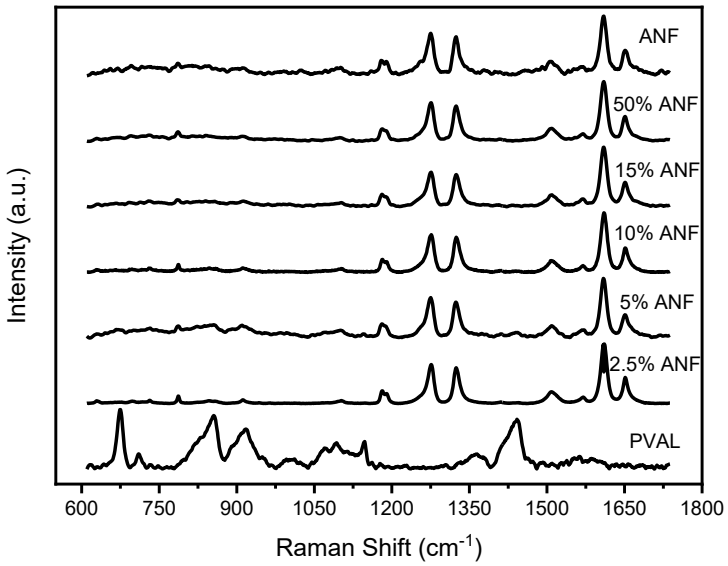


Figure 72: Raman spectra of PVAL / ANF films between 600 cm^{-1} and 1700 cm^{-1}. The signal of the ANF appears to overshadow the PVAL signal at all composite compositions.

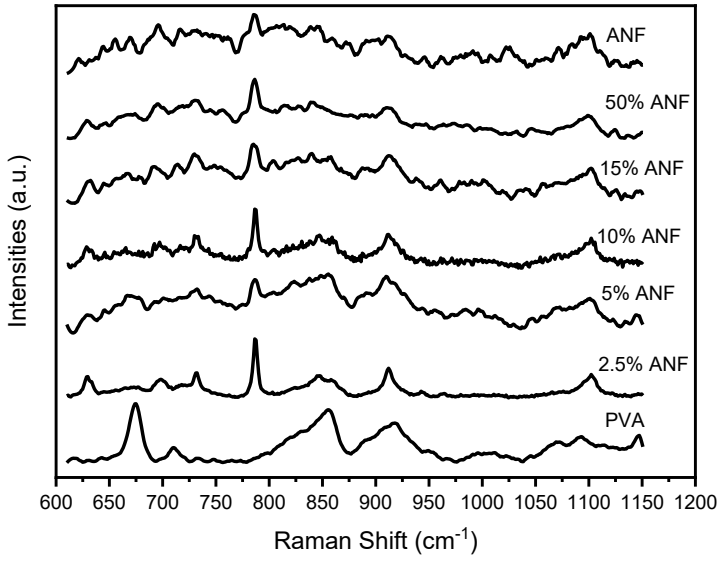


Figure 73: Raman spectra of PVAL / ANF films between 600 cm^{-1} and 1150 cm^{-1}.

Figure 70 displays the Raman spectra of distinctly different PVAL and ANF films. The same PVAL peak assignments were used as in Chapters 3 and 4 with minor changes due to the solvent used and its hydrolysis level. The first two peaks observed at 674 and 710 cm^{-1} are not assigned to PVAL. Rather, these peaks are characteristic of C-S-C stretching in DMSO [11]. This could be due to some residual solvent that was not fully evaporated before the measurements. However, no other peaks attributed to DMSO are apparent in the rest of the spectra and mainly PVAL signals are observed. It is noticeable that the 1146 cm^{-1} peak is sharper and higher in intensity than the for 88% hydrolysed PVAL studied in Chapters 3 and 4. This is probably due to a more ordered chain arrangement because of the lack of bulky acetate groups [20, 21]. This is also reflected in the higher intensity of the 1441 cm^{-1} peak compared to the 1360 cm^{-1}, which was attributed to a more ordered system [12, 22].

For the neat ANF film, characteristic peaks were used here based on ANF studies in literature as well as studies on macro PPTA fibres that have the same bonds [8, 9, 18, 19]. The strong signals are primarily coming from the C-C stretching in the aromatic rings. The amide group bands are coupled, centred at 1568 cm^{-1} and 1652 cm^{-1}.

An important note is the poor film formation of the 2.5 wt.% ANF/PVAL composition. This can be visualised using the optical microscope of the Raman apparatus shown in Figure 71. Isolated islands are created after solvent evaporation on the substrates, no continuous film was formed. It was also noticed that at this concentration the solution turns into a gel-like system within ~1 hour of mixing the two solutions, rendering it challenging to create homogenous films. However, where signals could be obtained from these islands, they were recorded and analysed as the rest of the PVAL/ANF composites.

Raman spectra for PVAL / ANF films of different compositions are presented in Figure 72. It can be seen that with as little as 2.5 wt.% ANF/PVAL, the signals from PVAL chains are completely overshadowed. This is observed at all ANF concentrations in PVAL. Hardly any variations are observed in those peaks with increasing ANF loadings. A similar observation was made in PVAL/ANF and PVAL/ polybenzimidazole (PBI) studies in literature where no Raman signals could be discerned [8, 23]. This is likely due to the signal coming from the aromatic rings which is multiple times stronger than those from PVAL vibrations [23].

Due to that large difference in signal intensities, the detector was limited to the region between 600 cm^{-1} and 1150 cm^{-1} as an attempt to observe parts of the PVAL signals (Figure 73). The 2.5 wt.% ANF composite has the clearest signal in comparison with the rest of the systems.

Peaks are detected at 630, 700, 732, and 787cm^{-1} that are assigned to different ring vibrations. A double peak is observed at 847 and 860 cm^{-1} that is assigned to ANF C-H bending and aromatic ring vibrations, respectively. The sharp peak at 1102 cm^{-1} is also attributed to C-H bending [18]. The sharp peak at 912 cm^{-1} could be linked to the C-C stretching of PVAL that was centred at 917 cm^{-1}. This shift by ~5cm^{-1} is observed for all ANF compositions but with varying degrees of clarity. With increasing ANF loadings, the signal appear to have a higher noise. Nevertheless, this slight shift to lower wavenumbers in the C-C stretching mode could be due to tensile extension similar to what was observed in PVAL / TEG blends and studies on PE [24, 25]. However due to the large signal noise, this cannot be confidently resolved.

5.2.2 Fourier-Transform Infra-Red (FTIR) Spectroscopy

FTIR spectra of neat PVAL and ANF films are depicted in Figure 74. The assignment of the observed bands are presented in Table 12 and Table 13 for PVAL and ANF, respectively.

Table 12: FTIR band assignments for PVAL.

Band centres (cm^{-1})	Assignment	Reference
3276	O-H stretching inter and intrachain	[26, 27]
2937, 2905	C-H stretching	[26, 27]
1733, 1709	C=O stretching (residual acetate)	[27]
1430	C-H stretching	[26, 27]
1123	C-O stretching (ordered segments)	[26, 27]
1083, 1051, 1021	C-O-C stretching	[27]

Table 13: FTIR band assignments for ANF.

Band centres (cm^{-1})	Assignment	Reference
3314	N-H stretching	[7, 28, 29]
1644	C=O stretching	[7, 28, 29]
1538	N-H deformation coupled with C-N stretching	[7, 28, 29]
1511	C=C stretching	[7, 28, 29]
1316	Aromatic C-N stretching	[7, 28, 29]
1017	C-H in-plane stretching	[7, 28, 29]

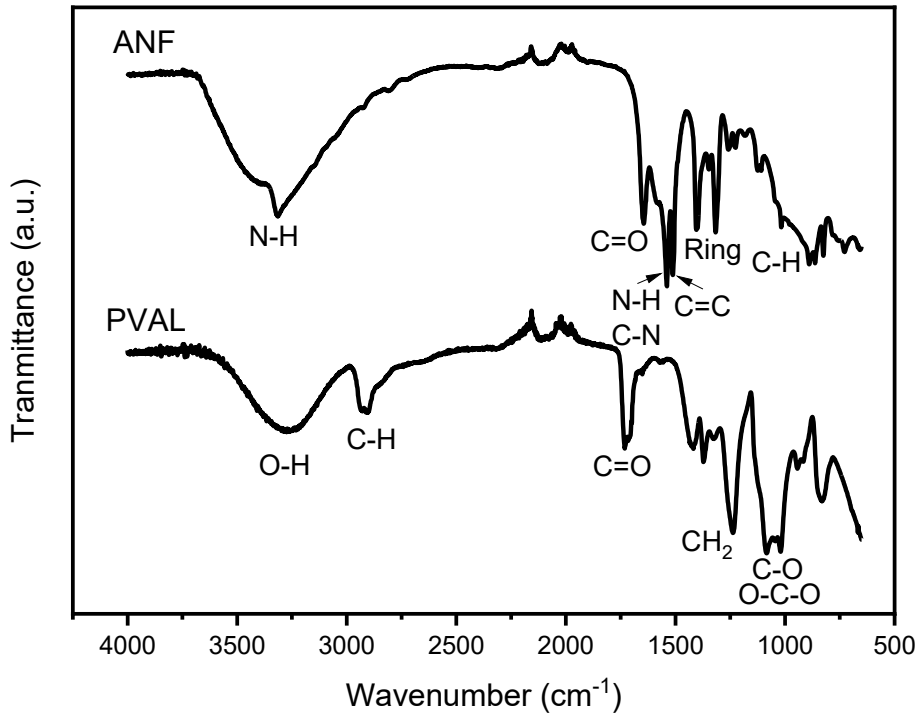


Figure 74: FTIR spectra of neat ANF and PVAL. Contributors to each peak are indicated below the peaks. For detailed peak positions, see Table 12 and Table 13.

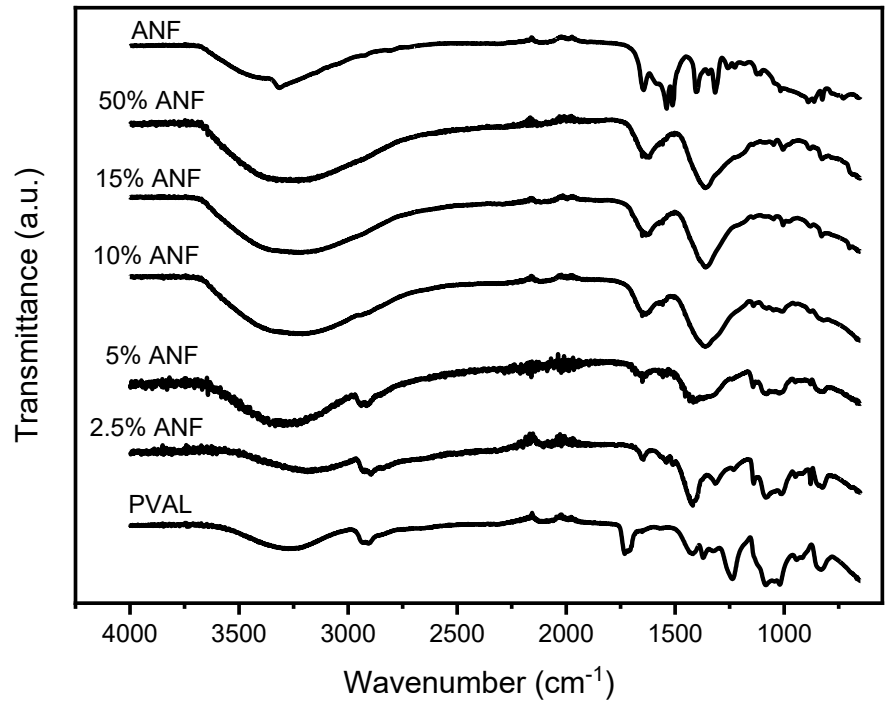


Figure 75: FTIR spectra of PVAL / ANF films of different composite compositions.

FTIR spectra of PVAL / ANF films of different compositions are presented in Figure 75. Compared to the neat PVAL, the O-H band is shifted considerably to lower wavenumbers and the C-H stretching peak has merged with that large band. This could be due to hydrogen bond formation between the hydroxyl group from PVAL and the amine group from ANFs, or to disruptions of inter-chain hydrogen bonding in PVAL due to the introduction of ANFs [30]. A study in literature on PVAL / ANF blends, which were prepared by isolating ANF suggested this shift to higher wavenumber of the O-H stretching band to result from the incorporation of ANF into PVAL matrix [6]. The shift of this peak and the coalescence with the C-H peak was similarly observed in the PVAL / titanium oxide hydrate films discussed in Chapter 4, which could indicate crosslinking of PVAL with ANF via condensation of the hydroxyl group.

It should be noted here that PVAL's FTIR spectra is from a 88% hydrolysed polymer. The C=O stretching peak at 1733 cm^{-1} is due to that residual acetate. However, the PVAL used in the ANF blended films was 99% hydrolysed and the peak that appears at 1645 cm^{-1} in the PVAL/ANF composite films is attributed to the C=O from the ANF. The band grows in intensity with increasing amount of ANFs. Furthermore, the C-N stretching and the N-H bending from the amide groups is situated at 1538 cm^{-1} and the C=C stretching is at 1511 cm^{-1} in the neat ANF films. In the PVAL / ANF films, all three of those peaks appear to merge into one broad feature that is centred around 1640 cm^{-1}. This could signify that significant changes occur in the blends relating to the amide group.

Another significant peak is the one assigned to the aromatic ring stretching which is observed at 1419 cm^{-1} in the 2.5 wt.% ANF/PVAL blend, then at 1360 cm^{-1} in systems of higher ANF loadings. Furthermore, in the neat ANF film, ring stretching vibrations appear as multiple peaks, while for the PVAL / ANF films, this is observed as a single broad peak. In the 10, 15 and 50 wt.% ANF/PVAL films, only three broad absorption peaks are observed. These could have contributions from multiple different vibration modes. It is intriguing to note that no such observations were made in ANF composites reported in literature, signifying that a likely a different structure is produced in the films prepared in this thesis [6, 8-10, 30].

Finally, it is highlighted, that the C-O and C-O-C absorption bands are reduced in intensity upon addition of ANF. This band is indicative of molecularly ordered regions in the PVAL [26, 27]. Due to strong interactions and hydrogen bond formation between PVAL and ANF, this band is observed to disappear with increasing ANF loading. This implies significant changes

in the structure. The changes in all of these vibrations could not be detected with Raman likely due to the nature of the signal acquisition and its strength.

5.3 Differential Scanning Calorimetry (DSC)

DSC thermograms of PVAL / ANF films are displayed in Figure 76 showing the first heating and cooling cycle. The range used in this experiment covers 25 ºC to 300 ºC. A few observation can be made. PVAL used in this chapter had a higher melting point than the PVAL cast from water in the Chapters 3 and 4. A comparison between the 99% hydrolysed PVAL cast from DMSO and 88% hydrolysed PVAL from water is presented in Figure 77. This difference in hydrolysis level is the probable reason for the higher melting temperature of the 99% hydrolysed PVAL [21]. This is likely due to better crystal formation as there are hydroxyl groups on every other carbon atom in the polymer chain in the 99% hydrolysed and hardly any bulky residual acetate [20, 21, 31]. Furthermore, there is an increase in the measured glass transition temperature from 77 ºC to 79 ºC in the 99% hydrolysed PVAL. Analogously, this is attributed to the higher number of hydroxyl groups in the PVAL used here, resulting in increased inter-chain hydrogen bonding and increased restriction of chain movement [20, 21, 31]. Another feature observed in the 99% PVAL, is the large endotherm centred around 272 ºC. This may be due to the degradation of PVAL chains. A measurement using DSC / TGA of a similar film is presented in Figure 78 (a). The DSC thermograms is drawn in black with the endothermic peaks pointing downwards instead of upwards here. The TGA curve is drawn in red. Figure 78 (b) shows the first derivative of the TGA curve. The first minima in the TGA curve at 175 ºC, is attributed to the evaporation of residual DMSO, which has a boiling point at 189 ºC [32]. There is no loss of mass at 227 ºC, which corresponds to the melting peak observed in DSC. After melting, a sharp reduction in weight is observed with the midpoint at 279 ºC. This is characteristic of decomposition of polymer chain [6, 33].

For the PVAL / ANF DSC thermograms, the large endotherm peak associated with melting of PVAL is shifted to lower temperatures with increasing ANF loading. Furthermore, it is noted that previously, the addition of ANFs in PVAL has led to a higher thermal stability of the system [6]. Therefore, it could be that the decomposition endotherm is above 300 ºC and the peaks observed in Figure 76 are related to melting of different phases of PVAL, PVAL/ANF, or ANF structures. For the 2.5 wt.% ANF/PVAL, the melting endotherm appears to have two contributions that start to merge, while a shoulder evolves with increasing ANF loading before separating in the 50 wt.% ANF/PVAL system. This could be an indication of the miscibility of the two phases at 50 wt.% ANF. Clear is that there is a melting point depression of PVAL when

adding ANF which indicates significant interactions between the two components [34, 35]. The reduction in the melting temperatures results from smaller PVAL crystals due to the incorporation of the ANFs. The glass transition (T_g), the two melting temperatures seen in the thermograms (denoted as T_{m1} and T_{m2}) and the enthalpy of fusion for PVAL are presented in Table 14. However, these changes in phase behaviour cannot be discerned with DSC alone. It could further be clarified with temperature dependant X-ray measurements. Note ANFs, similar to the microfibers of PPTA, do not have a melting point [4, 8, 36, 37]. This can also be observed in the ANF DSC thermogram, where the only feature detected is a small endothermic peak at 194 °C, which corresponds to the evaporation of residual DMSO.

For the cooling curves, presented in Figure 76 (b), no discernible features where detected except some instrumentational noise, which is attributed to the decomposition of PVAL at 300 °C as mentioned previously.

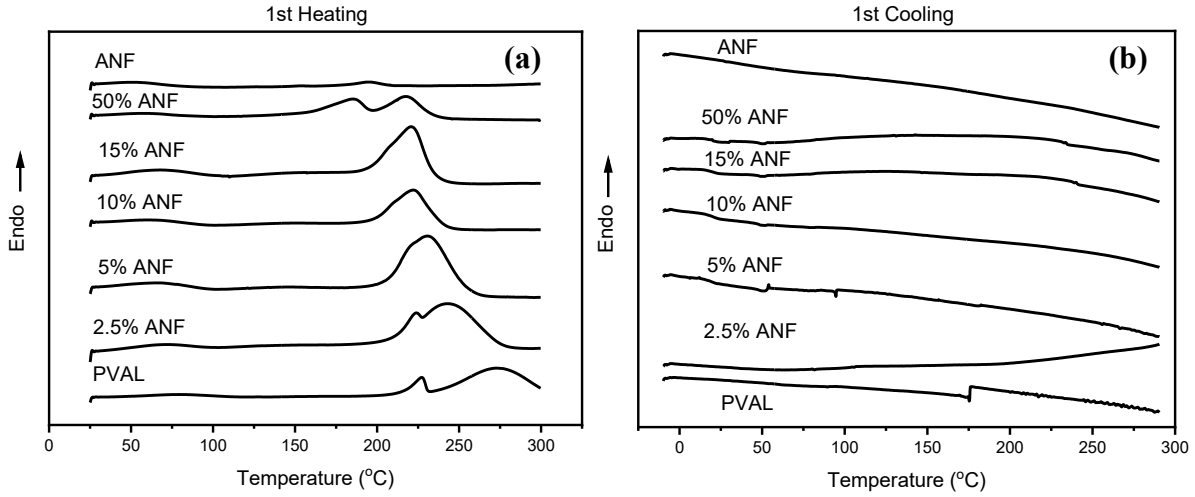


Figure 76: DSC thermograms of PVAL / ANF films of the first heating (a) and the first cooling (b) cycles.

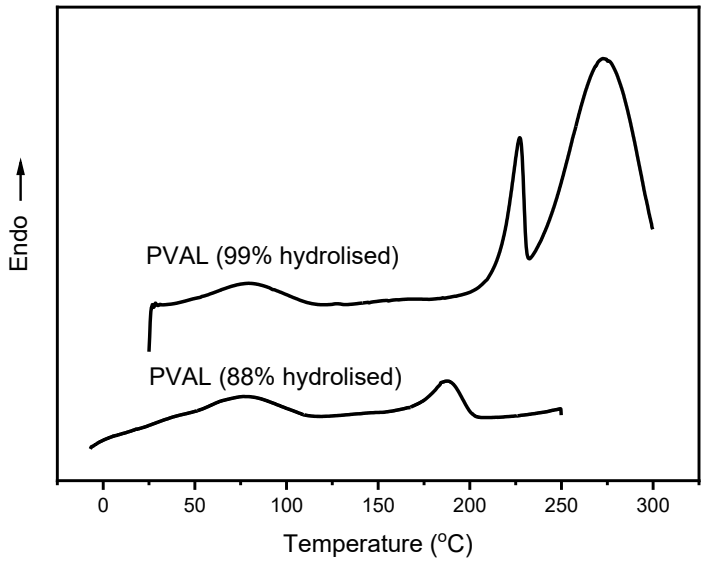


Figure 77: DSC first heating thermograms of PVAL films with 88% and 99% degrees of hydrolysis.

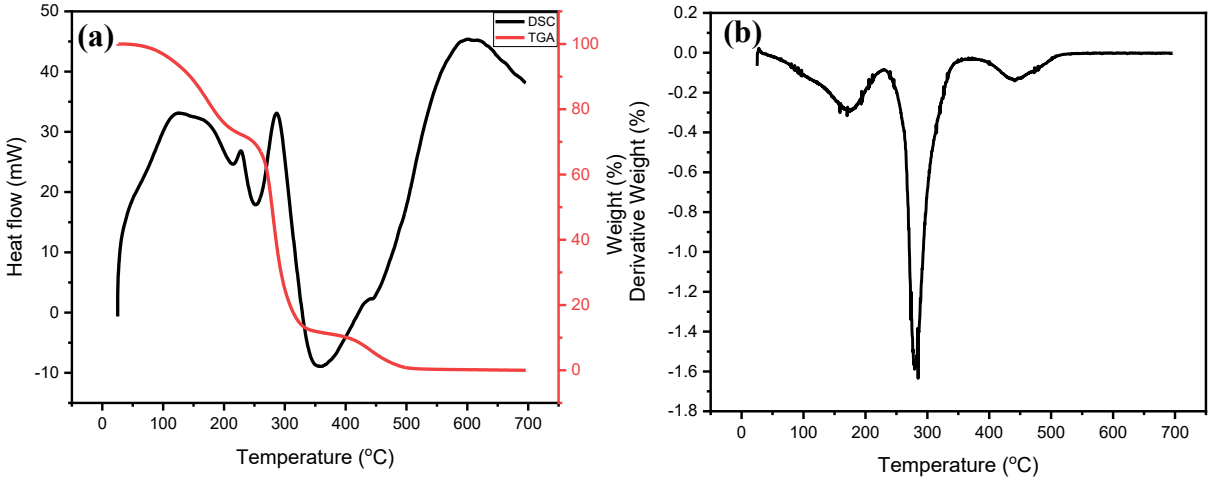


Figure 78: DSC/TGA of 99% hydrolysed PVAL film drop cast from DMSO (a). DSC themrogram shown in black and TGA curve shown in red. First derivative of TGA curve (b).

Table 14: Observed glass transition, melting temperatures of PVAL / ANF films

Sample	**T_g (°C)**	**T_{m1} (°C)**	**T_{m2} (°C)**	**T_d (°C)****	**Enthalpy ΔH_{PVAL} (J/g)*****
PVAL*	79	227	N/A	272	190
2.5 wt.% ANF	71	223	242	N/A	347
5 wt.% ANF	66	217	232	N/A	272
10 wt.% ANF	61	211	221	N/A	218
15 wt.% ANF	67	209	221	N/A	182
50 wt.% ANF	58	185	217	N/A	396
ANF	N/A	N/A	N/A	N/A	N/A

*PVAL used here is 99% hydrolysed. **T_d = degradation temperature only observed with PVAL. *** Measured enthalpy of both endotherms in first heating and normalised by weight fraction of PVAL.

5.4 X-ray photoluminescence spectroscopy (XPS)

XPS spectra were split in to three main regions of high resolution to simplify the analysis. The regions of interest are carbon, oxygen, and nitrogen. For the C1s region, this is presented in Figure 79. Several peaks are apparent in this window of the spectra. Three peaks are apparent in the neat PVAL: 285.1 eV assigned to CH_2, 286 eV assigned to C-OH, and 289 eV assigned to C=O [38]. It is noted that this spectra was obtained from the 88% hydrolysed PVAL and not the 99% hydrolysed used in the PVAL / ANF films. That is why the residual acetate content that gives rise to the C=O is not observed in the PVAL / ANF films. Furthermore, two new peaks appear to grow with higher loading of ANF in the PVAL / ANF films at 292.8 eV and 295.6 eV. These are assigned to $K2p_{3/2}$ and $K2p_{1/2}$, respectively [39]. This is due to residual potassium from the ANFs suspension in DMSO / KOH, indeed the peak intensity increases with ANF loading. With the addition of ANF, the CH_2 peak is shifted to lower binding energies to 284.7 eV which is assigned to C-C or C=C from an aromatic ring [8, 40]. The C-N peak is very close to the C-OH peak at 286 eV. That peak appears to decrease in intensity with increasing ANF loadings. The peak at 287.8 eV is assigned to N-C=O, because the only nitrogen and the carbonyl groups are present in the ANFs [8, 40]. Speculations on hydroxyl groups being consumed to create covalent bonds with the PVAL could not be discerned as the C-N peak overlaps the C-OH peak. Other spectroscopic or resonance techniques could discern this further.

In the O1s region displayed in Figure 80, the C-O peak of the PVAL was positioned at 532.7 eV. With the addition of ANFs, the C=O bond give rise to a peak at 532.2 eV [41, 42]. At 50 wt.% ANF loading and the neat ANF film, a peak at 530 eV is detected which is assigned to the amide group [41, 42]. This is similar to the amide group peak that rose in the C1s region. As the peaks overlap, it was difficult to observe hydrogen bonding between the two components. However, the shift to lower binding energies could signify hydrogen bond formations [43, 44]. The magnitude of the shift is similar to what was observed with the addition of TiO_2 particles in Chapter 4.

In the third part of the spectra, the N1s is presented in Figure 81. A single peak at 399.9 eV was increasing in intensity with the addition of ANFs. This is assigned to the amide group from the ANFs. [41, 42].

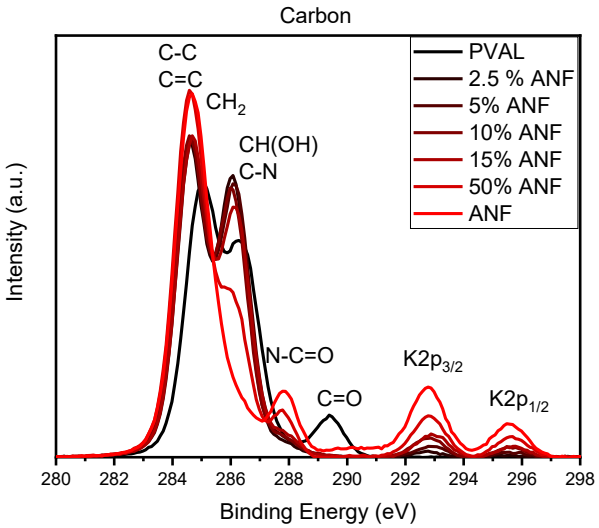


Figure 79: XPS spectra of PVAL / ANF films in the C1s region.

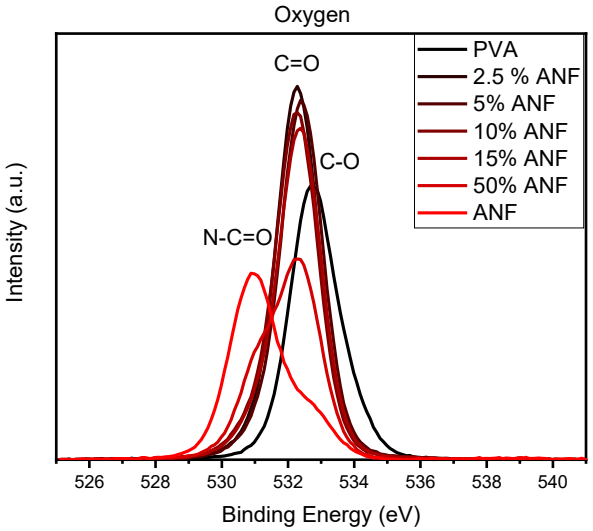


Figure 80: XPS spectra of PVAL / ANF films in the O1s region.

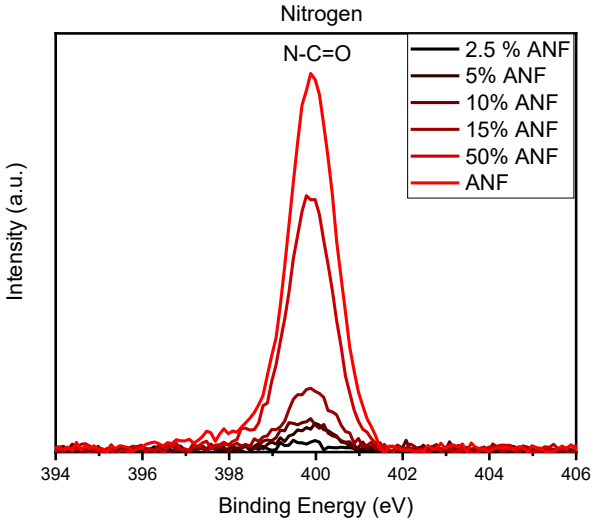


Figure 81: XPS spectra of PVAL / ANF films in the N1s region.

5.5 SEM

SEM images of all PVAL / ANF films and for comparison neat ANF are presented in Figure ***82*** and Figure 83. They were all taken at 1000x magnification except the 2.5 wt.% ANF/PVAL film, which was taken at 150x. This was to show the island growth of the film similar to the optical image in Figure 71. The 5, 10, 15 wt.% ANF in PVAL films appear to be homogenous with minor observable features. Noteworthy are the inorganic particulates that are apparent on the films. They are considered inorganic due to the high contrast in comparison with the polymers. These could be particulates of residual potassium or a reactant from the chromium coating, as they were not observed optical microscopy. In the 50 wt.% ANF/PVAL film, agglomerates are seen that are around 1-1.5 μmin size and are homogenously distributed. As they are much darker than the inorganic particles, it was considered that they are organic in nature. Further investigation is required to understand these structures. Clear is that ANF film consist of the homogenously distributed darker areas at this relatively low resolution using SEM. These may be due to a variation in thickness or due to the surface roughness of the film. To obtain a better indication of the ANF distribution in PVAL films a higher resolution microscope such as TEM could be used.

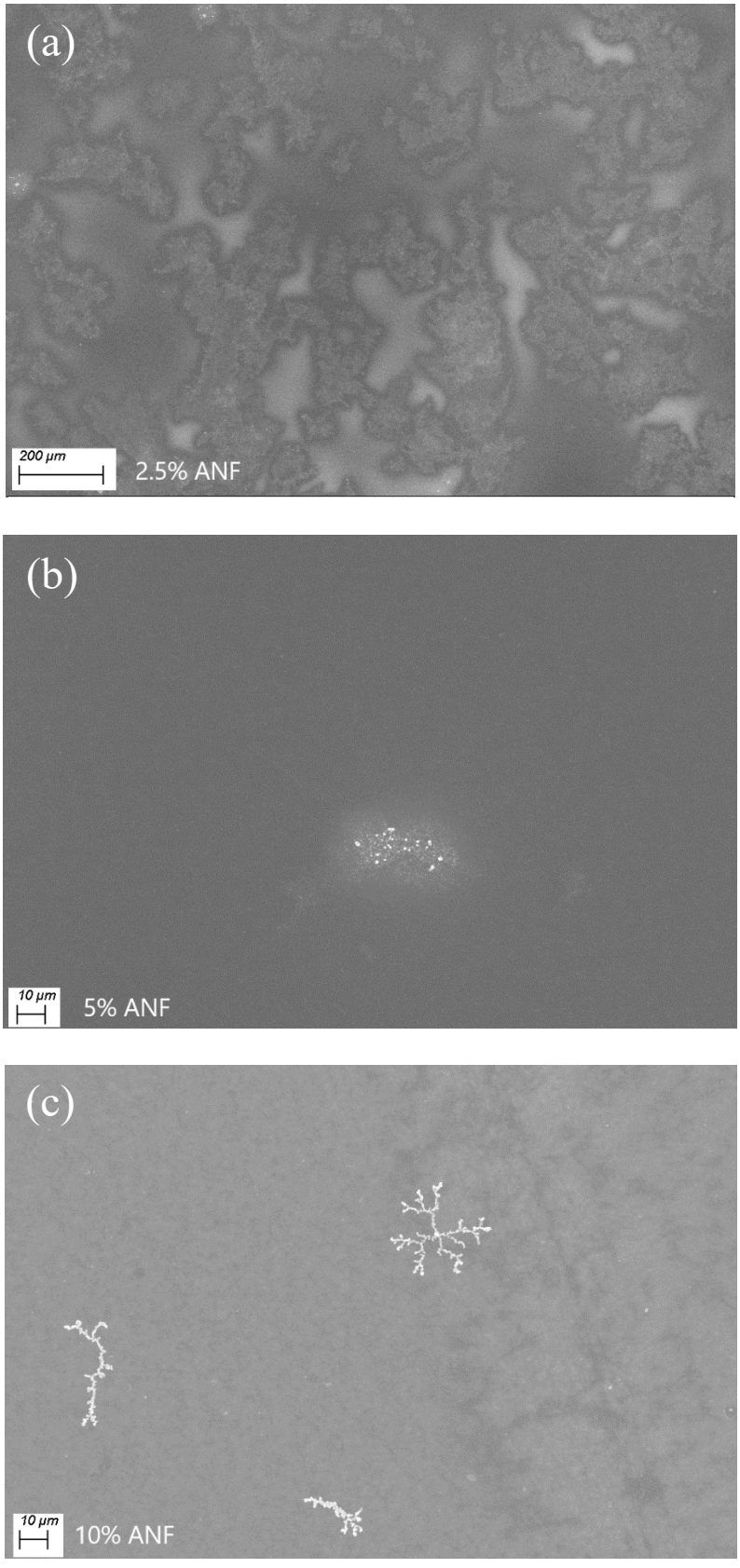


Figure 82: SEM images of 2.5 wt.% ANF/PVAL (a), 5 wt.% ANF/PVAL (b), and 10 wt.% ANF/PVAL (c).

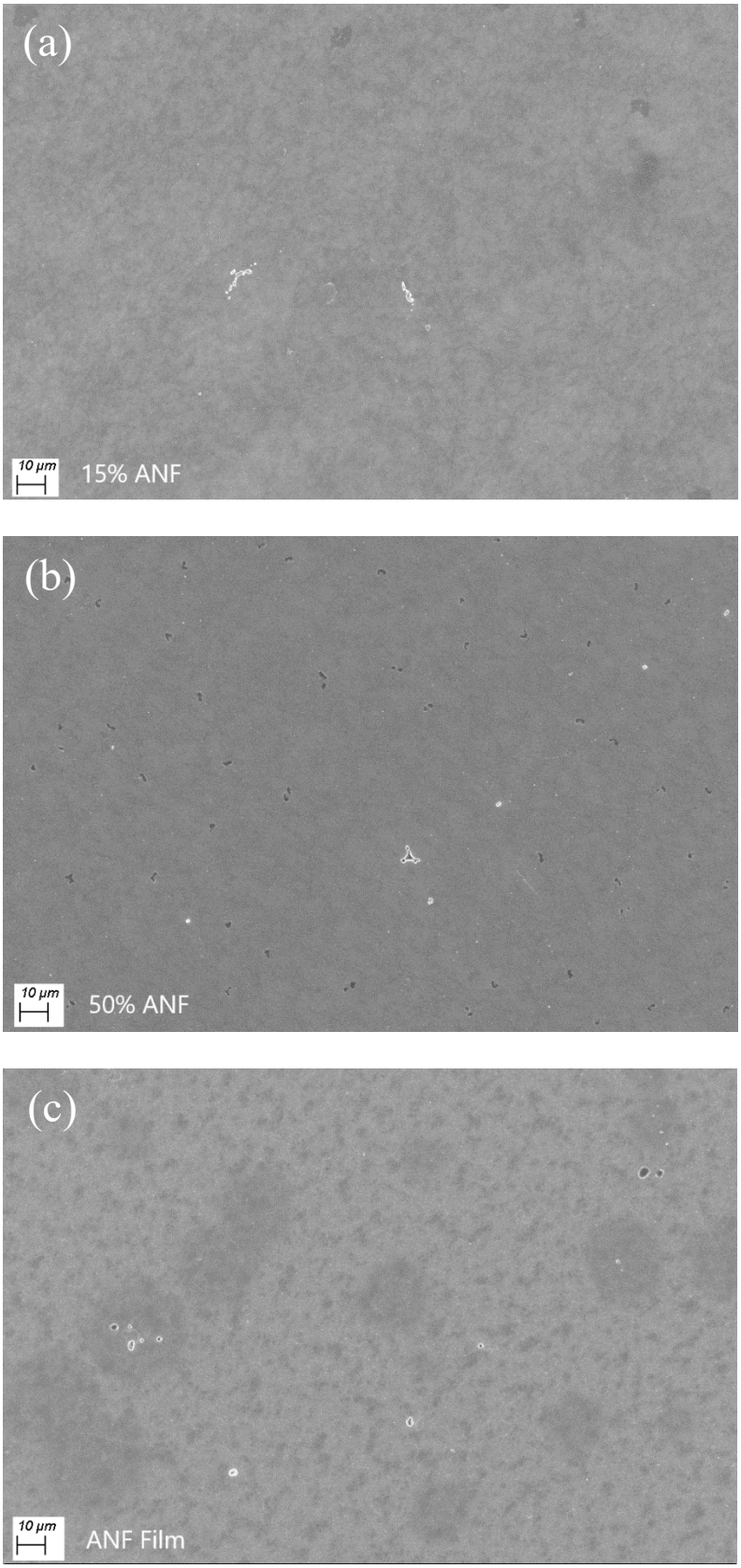


Figure 83: SEM images of 15 wt.% ANF/PVAL (a), 50 wt.% ANF/PVAL (b), and neat ANF film (c).

5.6 Thermal conductivity (3-ω)

Thermal conductivity measurements made on PVAL / ANF films are presented in Figure 84. The 2.5 wt.% ANF /PVAL sample could not be measured due to the nature of the island growth that was observed on the substrates. A continuous film is required for the 3-ω measurements and the deposition of the electrodes. Furthermore, there were difficulties in depositing the electrodes on the ANF films due to the surface roughness of the films. The deposition did not form continuous heater lines making measurements unattainable. Similar to what was observed in the PVAL / titanium oxide hydrate hybrid films in Chapter 4, the measured TC is observed to initially decrease slightly (5 wt.% ANF/PVAL: 0.276 W/m.K) before increasing significantly to reach 1.53 W/m.K at the 50 wt.% ANF/PVAL. The reduction observed at 5 wt.% ANF/PVAL film could be based on the errors of the measurement and the small sample size as only two films were measured. The TC value of 50 wt.% ANF/PVAL is similar to electrospun PVAL nanofibers which was reported in literature to be 1.58 W/m.K [45]. As observed from the DSC measurements, the melting temperature of PVAL is reduced with increasing ANF loading and that usually leads to lower thermal conductivity [45-47]. However, here, the thermal conductivity increased with ANF loading. This could be due to the increased local order of PVAL chains due to the addition of the stiffer ANFs, similar to what was observed with the PVAL / TEG films. Another possibility would be that the ANFs have an intrinsically higher thermal conductivity than PVAL. The measured values appear to follow the rule-of-mixtures between the two components. The Lewis-Nielsen model is a variation of a the rule-of-mixtures that takes in to account the shape of the fillers and packing factors in predicting the effective thermal conductivity (K_{eff}) of a composite system [48]. It is given by the following equation:

$$\frac{K_{eff}}{K_m} = \frac{1+AB\varphi_f}{1-B\psi\varphi_f} \tag{5.1}$$

Where K_m is the matrix' thermal conductivity. A is parameter based on the length (L) and the diameter (D) of the filler and is given as $A = 2L/D$. B is a parameter based on the thermal conductivities of the matrix (K_m) and the filler's (K_f) and was defined as:

$$B = \frac{(K_f/K_m-1)}{(K_f/K_m+A)} \tag{5.2}$$

The parameter ψ is based on the filler's volume fraction (φ_f) and the maximum packing factor (φ_{max}) and is given as :

$$\psi = 1 + [\frac{1-\varphi_{max}}{\varphi_{max}^2}]\varphi_f \quad (5.3)$$

In this calculation, K_m was taken as 0.32 W/m.K from the 3-ω measurements in this thesis. K_f had different values based on how the measurement was conducted and the nature of the sample. For example, the thermal conductivity of Kevlar fibres, measured along the fibre's axis, has a value of 3.1 W/m.K [49]. However, in commercial data sheets, the value of TC for Kevlar was indicated as 0.04 W/m.K [50]. In some of the recent work in literature, ANF films prepared by vacuum assisted filtration had a thermal conductivity of 0.183 W/m.K [51]. The model used K_f as 3.1 W/m.K and a 0.04 W/m.K as an upper and lower limit. Furthermore, the length of the fibre was assumed to be 10 μm, with diameter of 30 nm, based on the original ANF isolation study [7]. The maximum packing factor of random fibres was given as 0.82 by Nielsen [48]. As the PVAL / ANF films were prepared by weight percentage and not volume fraction, those values needed to be converted. The ANFs was assumed to have similar density to Kevlar (1.44 g/cm^3)[4]. PVAL's density was taken as 1.19 g/cm^3 [52]. The measured thermal conductivities were plotted with the Lewis-Nielsen model using the two different TC values of Kevlar as upper and lower limits in Figure 85. It can be observed that thermal conductivities of the 10, 15 and 50 wt.% ANF/PVAL films fall on the model using the higher limit. With 5 wt.% ANF/PVAL, the measured value seems to be closer to the lower bound limit. It must be noted that only two film samples were able to be measured and the difference between the lower and upper limit in the model at that volume fraction is relatively small. Another possibility could be that with the 5 wt.% ANF/PVAL sample, the distribution and concentration of the ANFs was not sufficient to create efficient phonon transport pathways throughout the film. Indeed, due to the addition of the ANFs, the observed thermal conductivity was lower than for a neat PVAL film. In contrast, for 15 and 50 wt.% ANF/PVAL films, that the primary means of phonon transport may be along the ANFs and not the PVAL chains. This in turn renders the system to behave as a two-phase system. However, as the measurements are done through-plane and the distribution of the ANF fibres was deemed random and homogenous, the measured thermal conductivity could be considered as isotopic. Further investigations are required to elucidate this detail.

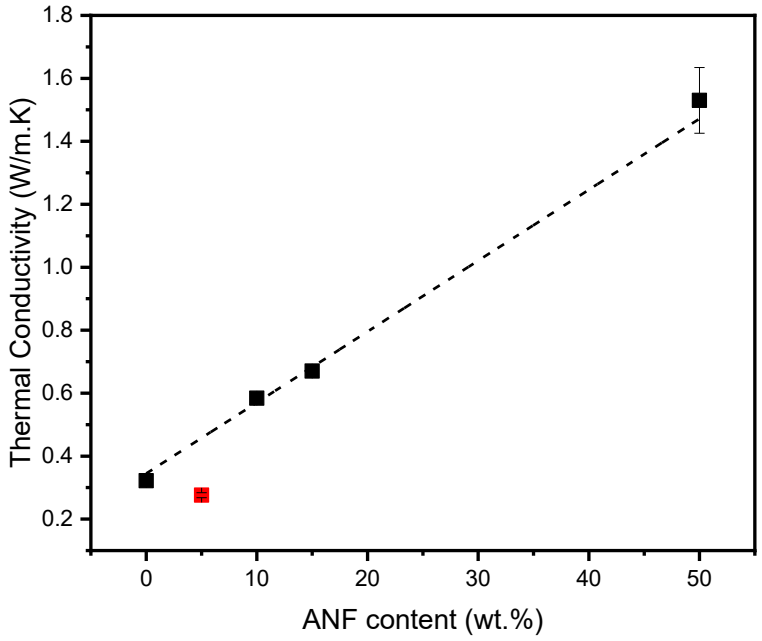


Figure 84: Thermal conductivity of PVAL / ANF films based plotted as a function of ANF concentration using the 3-ω technique. The 2.5 wt.% ANF/PVAL film and neat ANF film values are missing, as measurements could not be performed due to poor film quality. Error bars based on measurements of two films. Dashed line added as a guide by fitting a linear function. 5 wt.% ANF/PVAL film was masked in linear fit.

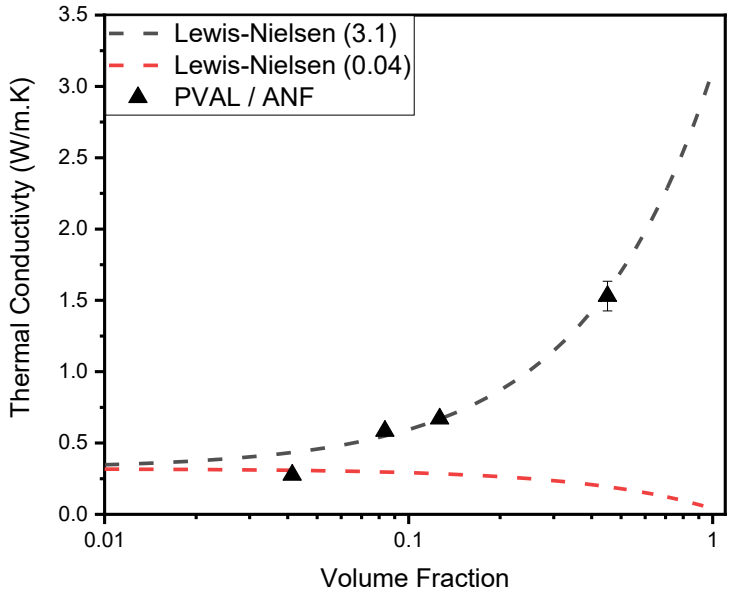


Figure 85: PVA / ANF thermal conductivity compared to Lewis - Nielsen model for composite using a 3.1 W/m.K value (black dashed line) and 0.04 W/m.K (red dashed line) as upper and lower limits, respectively.

5.7 Conclusions

By adding ANFs to PVAL, broad tuning of the system's thermal conductivity was achieved. This could be due to changes in solid-state structure as well as the addition of a highly conductive filler as seen from the modelled thermal conductivity. From Raman spectroscopy, possible localised extension of PVAL backbone was observed. However, this was challenging to discern to due to the nature of the signals and ANF signals overshadowing PVAL features. FTIR spectroscopy showed how the functional groups interacted with each other with most significant changes occurring with the hydroxyl and amide groups. The miscibility of the blend and the effect ANF introduction to the polymer chain mobility were observed from DSC data. No reduction in the crystallinity was observed however, the melting point for PVAL was found to be reduced upon addition of ANF. From XPS, strong interactions between PVAL and ANF were observed and the possibility of covalent bonding was discussed. Observing the films via SEM, they appeared to be homogenous and without isolated phases except for the 2.5 wt.% ANF/PVAL sample. Beneficially, the introduction of ANFs to PVAL was observed to have a positive effect on the overall thermal conductivity. The measured values were compared to a model of a binary system and the experimental results appear to be in agreement with the upper bound limit considered here. It is considered that ANF filler was homogenously dispersed within the PVAL matrix and the observed TC values could be isotropic. Most importantly, this system had combined the good film formation properties of PVAL with the high thermal conductivity of ANFs.

5.8 References

1. Liu, J. and R. Yang, *Length-dependent thermal conductivity of single extended polymer chains.* Physical Review B, 2012. **86**(10): p. 104307-104315.
2. Zhang, T. and T. Luo, *Role of Chain Morphology and Stiffness in Thermal Conductivity of Amorphous Polymers.* The Journal of Physical Chemistry B, 2016. **120**(4): p. 803-812.
3. Lin, J., et al., *Isolation of Aramid Nanofibers for High Strength and Toughness Polymer Nanocomposites.* ACS Applied Materials & Interfaces, 2017. **9**(12): p. 11167-11175.
4. Lefevre, J., *Ultra-high-performance polymer foils*. 2008, ETH Zurich: Switzerland.
5. Fan, J., et al., *Aramid nanofiber-functionalized graphene nanosheets for polymer reinforcement.* Nanoscale, 2012. **4**(22): p. 7046-7055.
6. Guan, Y., et al., *Aramid nanofibers and poly (vinyl alcohol) nanocomposites for ideal combination of strength and toughness via hydrogen bonding interactions.* Composites Science and Technology, 2017. **144**: p. 193-201.
7. Yang, M., et al., *Dispersions of Aramid Nanofibers: A New Nanoscale Building Block.* ACS Nano, 2011. **5**(9): p. 6945-6954.
8. Songfeng, E., et al., *Enhancing mechanical strength and toughness of aramid nanofibers by synergetic interactions of covalent and hydrogen bonding.* Composites Part A: Applied Science and Manufacturing, 2020. **137**: p. 106031-106042.
9. Huang, J., et al., *Improved mechanical and ultraviolet shielding performances of hydroxyethyl cellulose film by using aramid nanofibers as additives.* Carbohydrate Polymers, 2021. **255**: p. 117330-117338.
10. Yang, M., et al., *Aramid nanofiber-reinforced transparent nanocomposites.* Journal of Composite Materials, 2015. **49**(15): p. 1873-1879.
11. Martens, W.N., et al., *Raman spectroscopy of dimethyl sulphoxide and deuterated dimethyl sulphoxide at 298 and 77 K.* Journal of Raman Spectroscopy, 2002. **33**(2): p. 84-91.
12. Thomas, P.S. and B.H. Stuart, *A Fourier transform Raman spectroscopy study of water sorption by poly(vinyl alcohol).* Spectrochimica Acta Part A: Molecular and Biomolecular Spectroscopy, 1997. **53**(13): p. 2275-2278.
13. Yang, C.-C., et al., *Study of poly(vinyl alcohol)/titanium oxide composite polymer membranes and their application on alkaline direct alcohol fuel cell.* Journal of Power Sources, 2008. **184**(1): p. 44-51.
14. Dodda, J.M., et al., *Comparative study of PVA/SiO2 and PVA/SiO2/glutaraldehyde (GA) nanocomposite membranes prepared by single-step solution casting method.* Journal of Materials Science, 2015. **50**(19): p. 6477-6490.
15. Gauthier, M.A., et al., *Degree of crosslinking and mechanical properties of crosslinked poly(vinyl alcohol) beads for use in solid-phase organic synthesis.* Polymer, 2004. **45**(24): p. 8201-8210.
16. Yang, C.-C., Y.J. Li, and T.-H. Liou, *Preparation of novel poly(vinyl alcohol)/SiO2 nanocomposite membranes by a sol–gel process and their application on alkaline DMFCs.* Desalination, 2011. **276**(1): p. 366-372.
17. Madhuri, S.N., K.S. Hemalatha, and K. Rukmani, *Preparation and investigation of suitability of gadolinium oxide nanoparticle doped polyvinyl alcohol films for optoelectronic applications.* Journal of Materials Science: Materials in Electronics, 2019. **30**(9): p. 9051-9063.
18. Washer, G., T. Brooks, and R. Saulsberry, *Characterization of Kevlar Using Raman Spectroscopy.* Journal of materials in civil engineering, 2009. **21**(5): p. 226-234.
19. Yang, B., et al., *Timesaving, High-Efficiency Approaches To Fabricate Aramid Nanofibers.* ACS Nano, 2019. **13**(7): p. 7886-7897.
20. Hdidar, M., et al., *Effect of hydrolysis degree and mass molecular weight on the structure and properties of PVA films.* Ionics, 2017. **23**(11): p. 3125-3135.
21. Maria, T.M.C., et al., *The effect of the degree of hydrolysis of the PVA and the plasticizer concentration on the color, opacity, and thermal and mechanical properties of films based on PVA and gelatin blends.* Journal of Food Engineering, 2008. **87**(2): p. 191-199.

22. Salazar, J.D.R. *Study of Structural, Thermic, μ-Raman and Optic Transformation of PVA/TiO2 Polymeric Membranes*. in *Scientia Et Technica*. 2018. Universidad Tecnológica de Pereira.
23. Herranz, D., et al., *Poly (vinyl alcohol) and poly (benzimidazole) blend membranes for high performance alkaline direct ethanol fuel cells.* Renewable Energy, 2018. **127**: p. 883-895.
24. Hiejima, Y., et al., *Microscopic structural changes during photodegradation of low-density polyethylene detected by Raman spectroscopy.* Polymer Degradation and Stability, 2018. **150**: p. 67-72.
25. Kida, T., Y. Hiejima, and K.-h. Nitta, *Raman Spectroscopic Study of High-density Polyethylene during Tensile Deformation.* International Journal of Experimental Spectroscopic Techniques, 2016. **1**(1): p. 1-6.
26. Costa, H.S., et al., *Sol–gel derived composite from bioactive glass–polyvinyl alcohol.* Journal of Materials Science, 2007. **43**(2): p. 494-502.
27. Mansur, H.S., et al., *FTIR spectroscopy characterization of poly (vinyl alcohol) hydrogel with different hydrolysis degree and chemically crosslinked with glutaraldehyde.* Materials Science and Engineering: C, 2008. **28**(4): p. 539-548.
28. Zhao, Y., et al., *Electrochromic polyaniline/aramid nanofiber composites with enhanced cycling stability and film forming property.* Journal of Materials Science: Materials in Electronics, 2019. **30**(13): p. 12718-12728.
29. Lee, J. and H.S. Whang, *Poly(vinyl alcohol) blend film with m-aramid as an N-halamine precursor for antimicrobial activity.* Journal of Applied Polymer Science, 2011. **122**(4): p. 2345-2350.
30. Guo, Y., X. An, and Z. Fan, *Aramid nanofibers reinforced polyvinyl alcohol/tannic acid hydrogel with improved mechanical and antibacterial properties for potential application as wound dressing.* Journal of the Mechanical Behavior of Biomedical Materials, 2021. **118**: p. 104452.
31. Cassu, S.N. and M.I. Felisberti, *Poly(vinyl alcohol) and poly(vinyl pyrrolidone) blends: miscibility, microheterogeneity and free volume change.* Polymer, 1997. **38**(15): p. 3907-3911.
32. Smallwood, I., *Solvent recovery handbook*. 1993, London: Edward Arnold.
33. Yang, H., et al., *Thermal Decomposition Behavior of Poly (Vinyl Alcohol) with Different Hydroxyl Content.* Journal of Macromolecular Science, Part B, 2012. **51**(3): p. 464-480.
34. Liu, J., N. Hameed, and Q. Guo, *Eutectic crystallization and hydrogen bonding interactions in polymer/surfactant blends.* Journal of Polymer Science Part B: Polymer Physics, 2009. **47**(10): p. 1015-1023.
35. Matrone, G.M., et al., *The hole in the bucky: structure–property mapping of closed- vs. open-cage fullerene solar-cell blends via temperature/composition phase diagrams.* Journal of Materials Chemistry C, 2021. **9**(45): p. 16304-16312.
36. Zhang, Z., et al., *Nanoparticle-Infused UHMWPE Layer as Multifunctional Coating for High-Performance PPTA Single Fibers.* Scientific Reports, 2019. **9**(1): p. 7183-7192.
37. Zhang, H., et al., *Effects of solar UV irradiation on the tensile properties and structure of PPTA fiber.* Polymer Degradation and Stability, 2006. **91**(11): p. 2761-2767.
38. Akhter, S., et al., *XPS and IR study of X-ray induced degradation of PVA polymer film.* Applied Surface Science, 1988. **35**(2): p. 241-258.
39. Sawyer, R., H.W. Nesbitt, and R.A. Secco, *High resolution X-ray Photoelectron Spectroscopy (XPS) study of K2O–SiO2 glasses: Evidence for three types of O and at least two types of Si.* Journal of Non-Crystalline Solids, 2012. **358**(2): p. 290-302.
40. Zeng, L., et al., *Surface Modification of Aramid Fibres with Graphene Oxide for Interface Improvement in Composites.* Applied Composite Materials, 2018. **25**(4): p. 843-852.
41. Shiju, J., F. Al-Sagheer, and Z. Ahmad, *Thermal Mechanical Properties of Graphene Nano-Composites with Kevlar-Nomex Copolymer: A Comparison of the Physical and Chemical Interactions.* Polymers, 2020. **12**(11): p. 2740-2762.
42. Radtke, M. and A. Ignaszak, *Grafting of the carbon allotropes and polypyrrole via a Kevlar-type organic linker: the correlation of carbon structure/morphology with electrochemistry of*

the composite electrode. Materials for Renewable and Sustainable Energy, 2016. **6**(1): p. 1-16.
43. Flamia, R., et al., *Conformational Study and Hydrogen Bonds Detection on Elastin-Related Polypeptides Using X-ray Photoelectron Spectroscopy.* Biomacromolecules, 2005. **6**(3): p. 1299-1309.
44. Liu, S., et al., *Surface segregation in polymer blends and interpolymer complexes with increasing hydrogen bonding interactions.* Journal of Polymer Science Part B: Polymer Physics, 2005. **43**(14): p. 1924-1930.
45. Zhang, Y., et al., *Thermal transport in electrospun vinyl polymer nanofibers: effects of molecular weight and side groups.* Soft Matter, 2018. **14**(47): p. 9534-9541.
46. Shen, S., et al., *Polyethylene nanofibres with very high thermal conductivities.* Nature Nanotechnology, 2010. **5**(4): p. 251-255.
47. Henry, A., *Thermal Transport in Polymers*. Vol. 17. 2014.
48. Nielsen, L.E., *The thermal and electrical conductivity of two-phase systems.* Industrial Engineering Chemistry Fundamentals, 1974. **13**(1): p. 17-20.
49. Wang, X., et al., *Thermal Conductivity of High-Modulus Polymer Fibers.* Macromolecules, 2013. **46**(12): p. 4937-4943.
50. DuPont. *Kevlar Aramid Fiber Technical Guide*. 2019 11/3/2019 [cited 2021 28/12/2021]; Available from: https://www.dupont.com/content/dam/dupont/amer/us/en/safety/public/documents/en/Kevlar_Technical_Guide_0319.pdf.
51. Zhuo, L., et al., *Toward high thermal conductive aramid nanofiber papers: Incorporating hexagonal boron nitride bridged by silver nanoparticles.* Polymer Composites, 2021. **42**(4): p. 1773-1781.
52. Wypych, G., *Handbook of Polymers*. 2016, Scarborough: ChemTec Publishing.

6 Summary and outlook

6.1 Summary

This thesis investigated how different macromolecular structures influence thermal transport. The principal concepts of thermal transport in materials, and in particular, polymers were first described and presented in Chapter 1. The different approaches of tuning polymer thermal conductivity were highlighted in the form of polymer blends, mechanical stretching and the preparation of polymer composites. PVAL was chosen as a model polymer with a functional group to create distinct solid-state structures with varying effects on overall thermal conductivity. In Chapter 3, PVAL was blended with an oligomer to influence the local order of PVAL chains via hydrogen bonding, and in turn, influencing the thermal transport. An organic / inorganic hybrid system based on PVAL / titanium oxide hydrate was investigated in Chapter 4 while drawing contrasts with a conventional PVAL – TiO_2 composite. In Chapter 5, a novel preparation of PVAL / ANF films was studied and the effect on thermal conductivity was investigated. The preparation methods and experimental techniques described reported in Chapter 2.

With the PVAL / TEG blend in Chapter 3, it was observed that at low concentrations (5-15 wt.%) a localised stretching of the PVAL bonds occurred. However, with higher TEG concentrations, the main change observed was a plasticising effect and disruption of the ordered segments in PVAL. These changes in structure identified with Raman and FTIR spectroscopy as well as DSC, affected the film's speed of sound transmission and thermal conductivity. The structure with low TEG content led to a more efficient phonon pathway through the material, which is closely correlated to both the TC and speed of sound of the films. However, the improvement of the thermal conductivity was not pronounced, from 0.32 W/m.K in neat PVAL, to 0.36 W/m.K in with 5 wt.% TEG. This could be due to the nature of the TEG molecules, which are relatively flexible, and the weak restrictions they impose on the PVAL chains.

The PVAL / titanium oxide hydrate hybrid structure was investigated in Chapter 4. Various spectroscopic techniques were used here to complement the previous studies on this hybrid system as well to provide new insights on their chemical structure. The side-by-side comparison with conventional polymer/nanoparticle composites assisted in identifying the

changes in solid-state structure upon hybrid formation. That in turn, improved the understanding on where the different properties of the hybrid stem from. It was observed from Raman spectroscopy how the backbone was compressed and became more restricted due to the hybrid network formation. From FTIR spectroscopy, changes in the pendant groups of PVAL were found, while with XPS the nature of the hybrid formation was investigated to compliment the other findings. The changes observed in these spectroscopic methods were reflected in the measured thermal conductivity of the films showing a relatively linear response with the inorganic species content. This was notably different from findings made in literature with other conventional crosslinking methods and their effect on thermal transport further highlighting the unique structure of the PVAL / titanium oxide hydrate hybrids. The hybrid structure indeed appeared to improve the phonon pathways in the system without adding inorganic particles and despite having a lesser ordered molecular structure. This change in structure expands on the thermal transport in macromolecules and provides new design rules to tune polymeric systems' thermal conductivity to fit the required applications.

As the final system, a polymer / polymer nanofiber composite system was investigated. Using a different preparation method than reported in literature, a more intimate interaction between the ANF and the PVAL chain was obtained, as revealed by FTIR and XPS spectroscopy. Due to the nature of the measurements, Raman spectroscopy was not suitable to study the changes in structure similar to the other systems as the ANFs signals overshadowed the ones from the PVAL. The introduction of ANF to the PVAL matrix appeared to reduce the size of PVAL crystals as deduced from the DSC analysis. The changes to the thermal conductivity were more significant compared to the other systems studied throughout the thesis. The observed thermal conductivities appeared to follow a two-phase composite system with the ANF being of higher intrinsic thermal conductivity. As the thermal conductivity measurements gave through-plane TC values, this change in TC was considered isotropic.

6.2 Outlook and future work

The results obtained in this thesis have produced new insight on design rules of how the solid-state structure of polymer-based materials can influence the thermal transport. It was revealed how hydrogen bonding can be utilised between long polymer chains and oligomers to tune the properties of a polymer film. Organic / inorganic hybrid networks have shown intriguing properties for their optical properties, here the structure has been studied for their thermal transport properties. Hybrid-formation was identified to be yet another highly useful method of tuning thermal properties via manipulation of polymer chain confirmation and structure. An additional method was proposed, introducing ANF to PVAL. Having a more reactive amide sites in the system has produced films with promising thermal transport properties. The results further highlight how the interaction between different constituents affect a two-phase system and its properties.

The measurements and experiments performed throughout this thesis focused on small-scale interactions and corresponding changes in structure were inferred based on a local and short-range order. Further investigations on how long-range order and the overall microstructure effects on thermal properties may be performed via X-ray scattering. Complementing experiments using wide-angle X-ray scattering (WAXS) as well as small-angle X-ray scattering (SAXS) would assist to observe the change in phase morphology and microstructure in a more definitive manner. WAXS can deliver information on the changes in films complementing the DSC measurements. SAXS would be useful in the two component systems such as the hybrids and the PVAL/ANF composites to identify length-scales of phase separation.

BLS proved to be very useful in gaining understanding the changes in the phonons' pathways as the speed of sound measurements are directly related to the phonons' group velocity. However, only the PVAL – TEG system was measured using that technique, as those were the only system that could be produced with sufficient thickness using the same concentration of solutions and deposition method as for the rest of measurements. With PVAL / titanium oxide hydrate hybrids, PVAL – TiO_2 composites and the PVAL / ANF films, it was challenging to prepare relatively thick films using the solution concentrations of previous measurements. Dip coating or wire bar coating could be utilised with solutions of higher concentrations and viscosity to prepare films for both BLS and 3-ω measurements to obtain a meaningful comparison. These methods typically allow for slower solvent evaporation rates, which would produce different structures than spin coating, and could be studied with those differences

considered. However, the hybrid structure is less sensitive to the variation in thickness as it forms a cross-linked network.

Solid-state nuclear magnetic resonance (SSNMR) would also be valuable in understanding the different structures. It may reveal the different interactions that form between PVAL and the blend / hybrid / composite components. This would give further insight on the possible reactions between the titanium oxide hydrate as well as the deprotonated ANFs, which would complement the other spectroscopic techniques utilised in this thesis.

The thermal conductivity measurements conducted in this thesis measured the through-plane TC. The structures in this thesis are believed to be isotropic. However, to confirm this, in-plane thermal conductivity techniques should be used to complement and confirm this. Such techniques could include suspended film 3-ω or frequency domain thermoreflectance (FDTR).

For the PVAL / titanium oxide hydrate systems, a distinct structure with a cross-linked network between PVAL chains and inorganic moieties was found. This network produced a promising thermal pathway within the material. Building on the XPS experiments with PVAL / boric acid systems, it would be beneficial to identify those changes in this system using the spectroscopic techniques and thermal conductivity measurements as used in this thesis. It could present a similar network but with boron instead of titanium as the inorganic constituent. Moreover, recent studies have shown that a PVAL / silica hybrid structure could be produced using tetraethoxysilane (TEOS) as a precursor. Comparing those three organic / inorganic hybrid systems would allow observing the influences due to the size of the inorganic atom in the system as well as gaining a more detailed understanding of such structures.

Furthermore on the PVAL / ANF system, the 99% hydrolysed PVAL should be used in all measurements. This would present a clearer comparison using all the techniques provided. DSC measurements may indicate some degradation as observed in the PVAL samples. However, only PVAL was analysed using TGA. With the PVAL / ANF films, two features were observed and a possibility of two molecular arrangements were proposed. Using temperature dependant X-ray diffraction techniques could clarify that further. Furthermore, as the cooling cycles did not have any distinct features, TGA measurements of PVAL / ANF films would highlight where the degradation occurs to establish possible reasons for the lack of signals. In SEM, some particulates were observed that could not be explained clearly. It was suggested that it could be a reaction between the conductive chromium layer and residual potassium in the system or other molecules. Energy dispersive X-ray analysis (EDS)

measurements on those particles under SEM could clarify where they originate from. TEM imaging of the PVAL / ANF films would also be useful to elucidate of the overall structure and how the ANFs assemble within PVAL matrix. Moreover, as some of the films' thermal conductivity could not be measured, film processing should be optimised to produce smoother films. Finally, understanding whether the PVAL matrix provides a suitable medium for assembling the ANFs in an isotropic, high thermal conductivity material could assist further materials design.

Appendix A

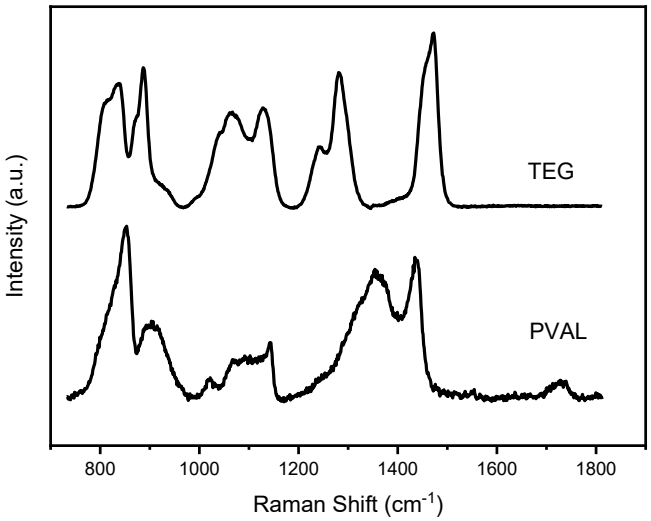


Figure 86: Raman spectra of neat TEG and neat PVAL between 750 and 1850 cm^{-1}. TEG is liquid at room temperature and a droplet was used to capture spectra. PVAL film cast from 6 wt.% solution.

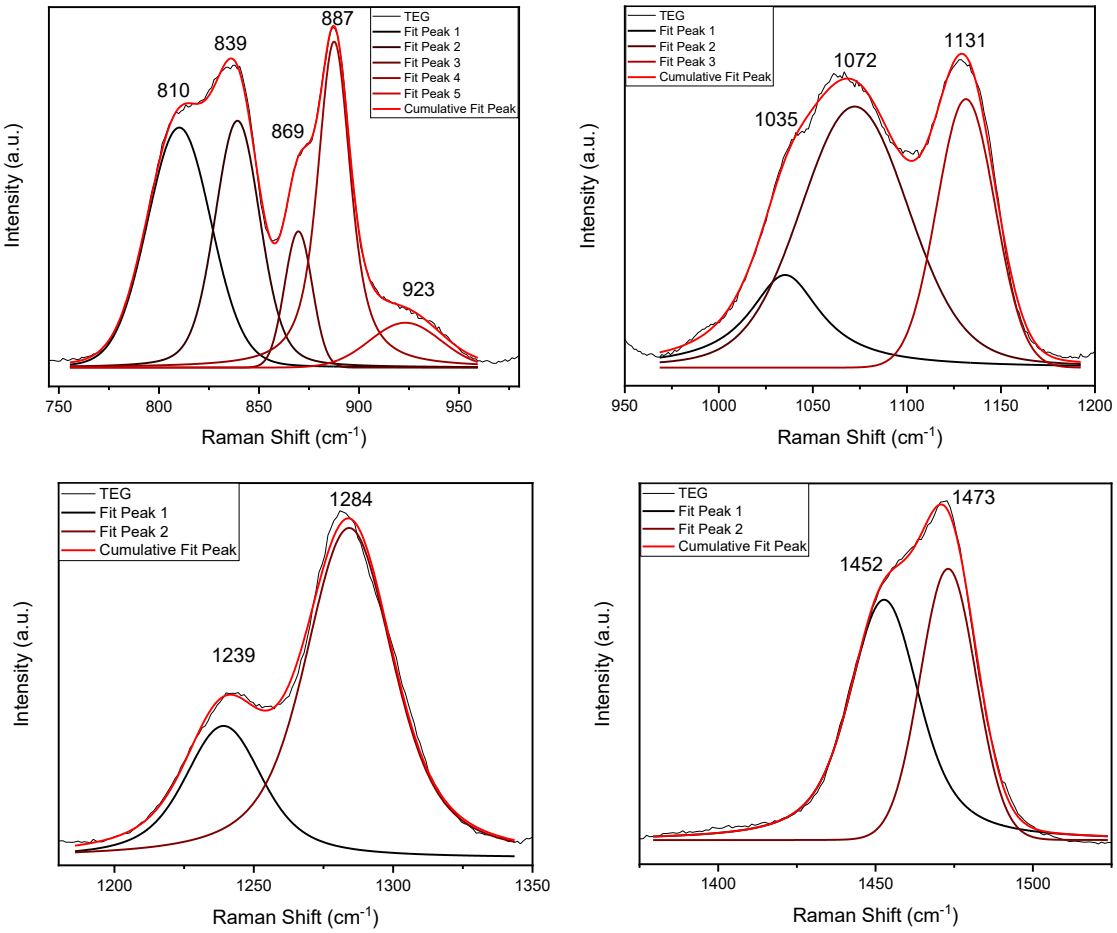


Figure 87: Raman spectra of neat TEG showing the peak fittings at each of the main band regions.

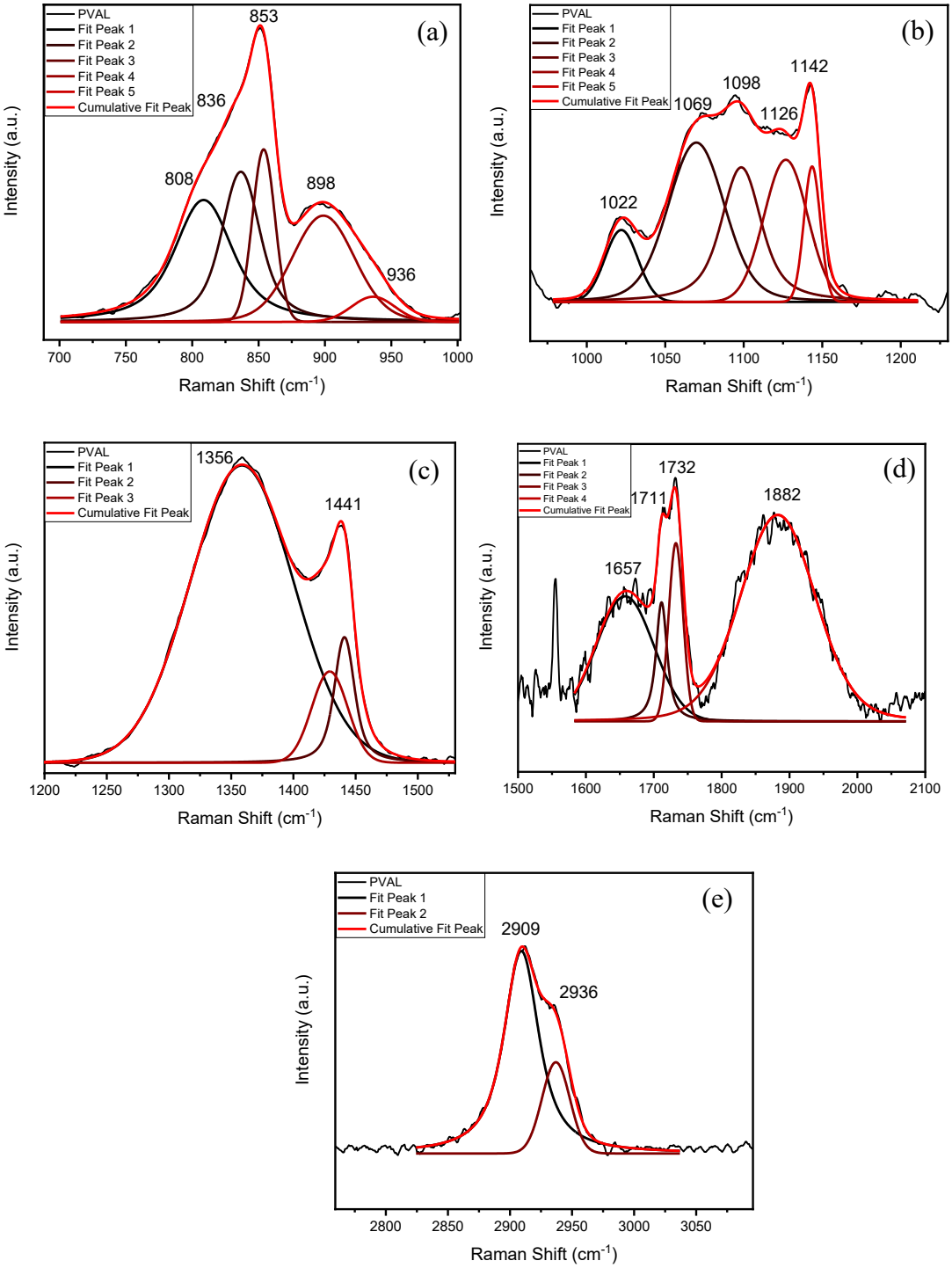


Figure 88: Raman spectra peak fitting of neat PVAL at different regions: (a) C-C stretching, (b) C-O stretching and O-H bending, (c) C-H and O-H bending, (d) C=O stretching and C-O asymmetric stretching, and (e) C-H stretching. Peak assignments are used in Chapter 3 and 4.

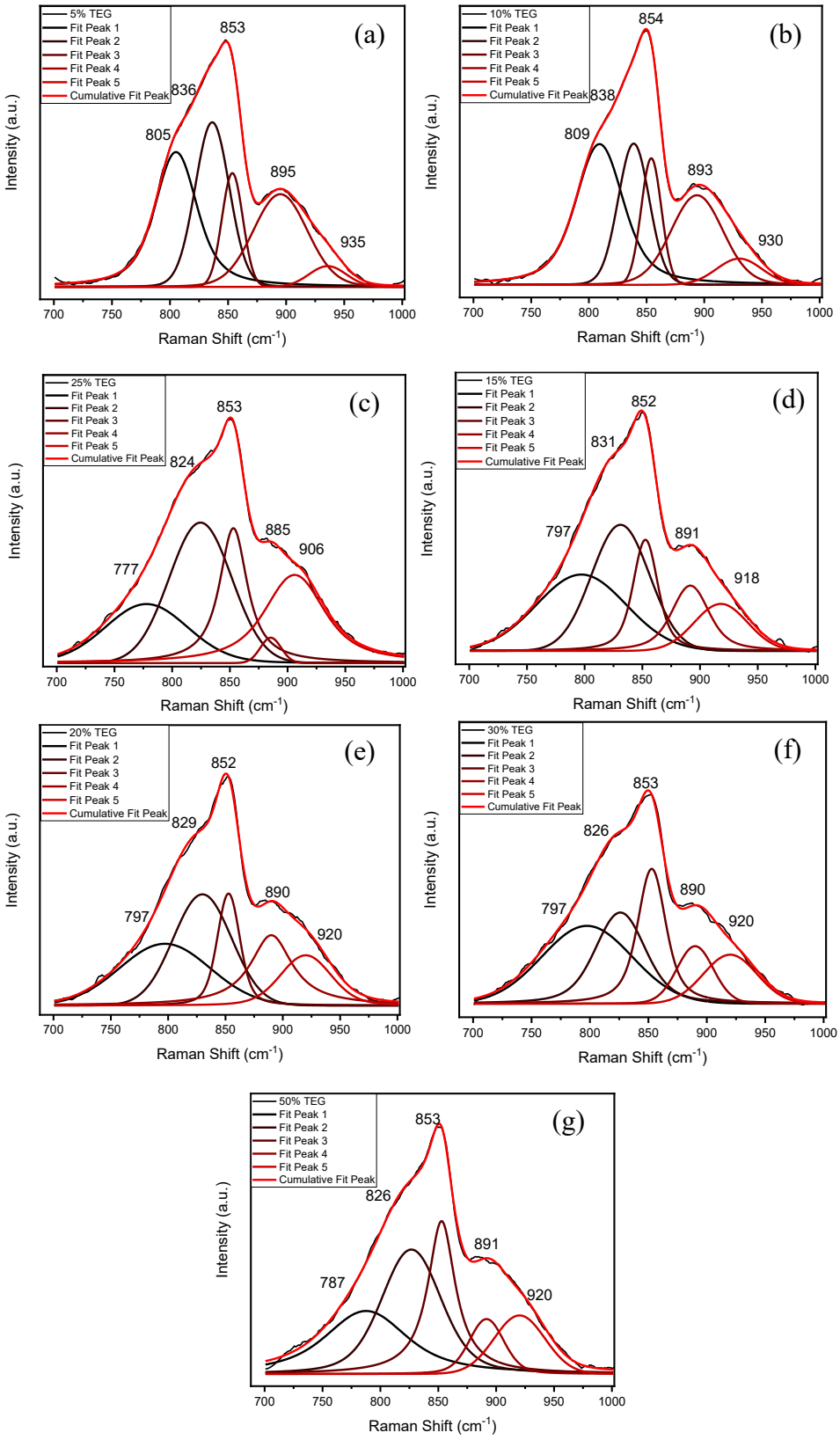


Figure 89: Raman spectra peak fitting of PVAL/TEG blends of different concentrations at the C-C stretching region. (a) 5 wt.% TEG, (b) 10 wt.% TEG, (c) 15 wt.% TEG, (d) 20 wt.% TEG, (e) 25 wt.% TEG, (f) 30 wt.% TEG, and (g) 50 wt.% TEG in PVAL.

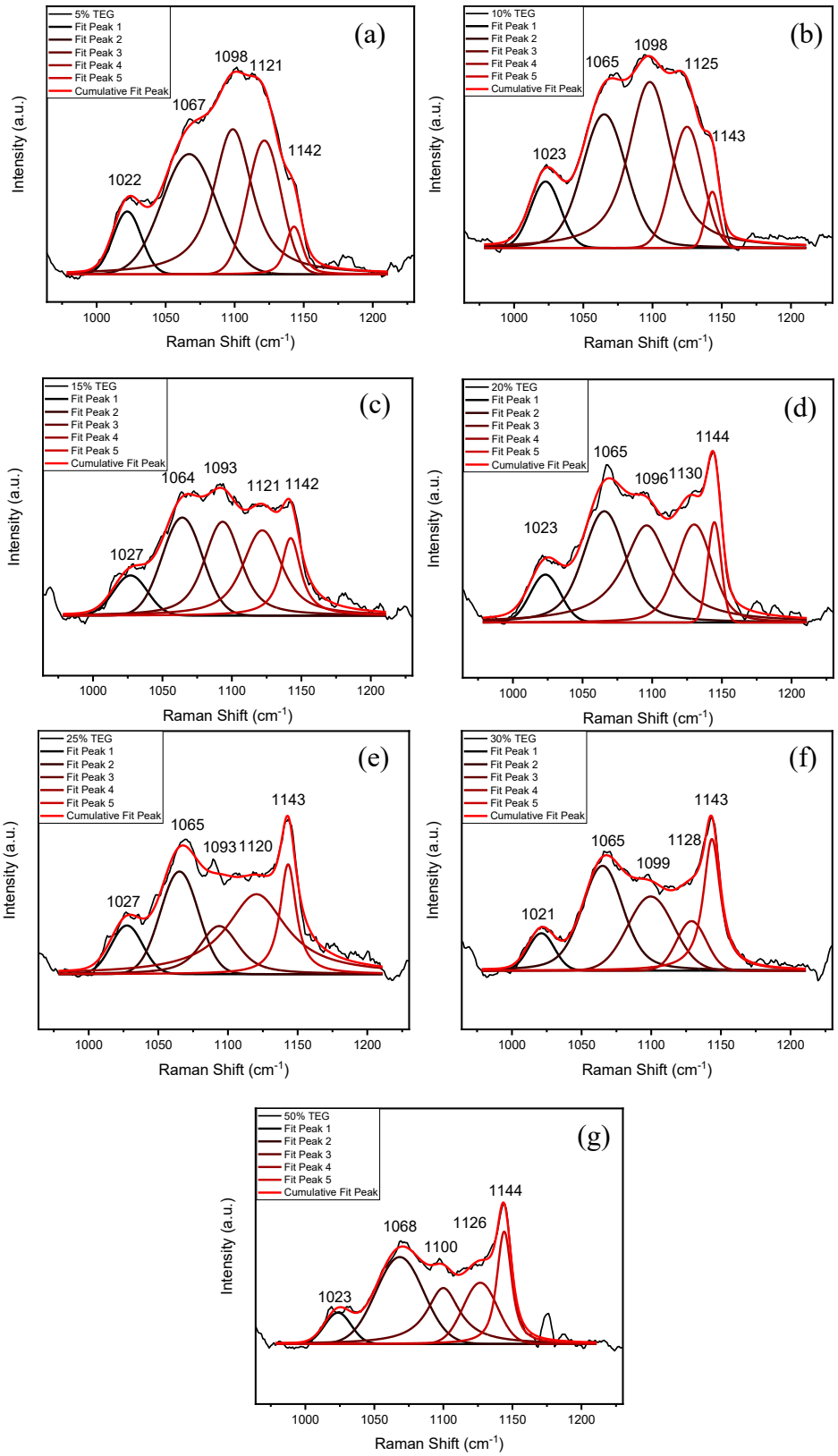


Figure 90: Raman spectra peak fitting of PVAL/TEG blends of different concentrations at the C-O stretching and O-H bending region. (a) 5 wt.% TEG, (b) 10 wt.% TEG, (c) 15 wt.% TEG, (d) 20 wt.% TEG, (e) 25 wt.% TEG, (f) 30 wt.% TEG, and (g) 50 wt.% TEG in PVAL.

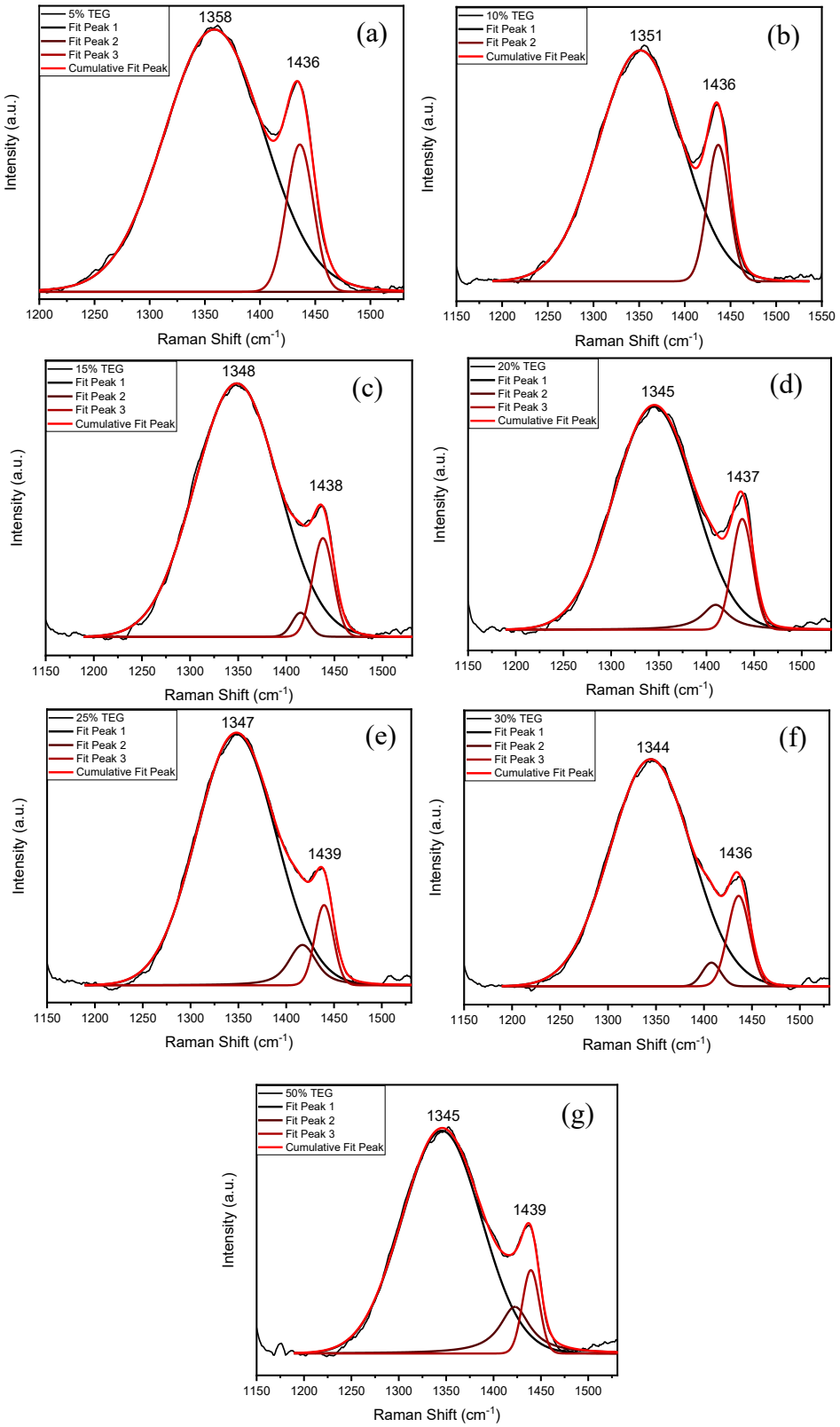


Figure 91: Raman spectra peak fitting of PVAL/TEG blends of different concentrations at the C-H bending and O-H bending region. (a) 5 wt.% TEG, (b) 10 wt.% TEG, (c) 15 wt.% TEG, (d) 20 wt.% TEG, (e) 25 wt.% TEG, (f) 30 wt.% TEG, and (g) 50 wt.% TEG in PVAL.

Table 15: Raman peak fitting statistics for PVAL/TEG blends of different concentrations at the C-C stretching region.

Sample	Reduced χ	R squared
PVAL	0.00148	0.9993
5% TEG	0.00199	0.99947
10% TEG	0.00175	0.99954
15% TEG	0.00317	0.99907
20% TEG	0.00496	0.99828
25% TEG	0.0025	0.99928
30% TEG	0.00472	0.99816
50% TEG	0.00259	0.99869

Table 16: Raman peak fitting statistics PVAL/TEG blends of different concentrations at the C-O stretching and O-H bending region.

Sample	Reduced χ	R squared
PVAL	0.00065	0.99785
5% TEG	0.00178	0.99639
10% TEG	0.0018	0.99597
15% TEG	0.00194	0.9907
20% TEG	0.0028	0.99141
25% TEG	0.00286	0.98429
30% TEG	0.00111	0.99366
50% TEG	0.00249	0.98261

Table 17: Raman peak fitting statistics for PVAL/TEG blends of different concentrations at the C-H bending and O-H bending region.

Sample	Reduced χ	R squared
PVAL	0.00405	0.99934
5% TEG	0.00707	0.99909
10% TEG	0.0103	0.99781
15% TEG	0.01502	0.99819
20% TEG	0.01944	0.9964
25% TEG	0.01669	0.99828
30% TEG	0.01478	0.99779
50% TEG	0.0129	0.99695

Appendix B

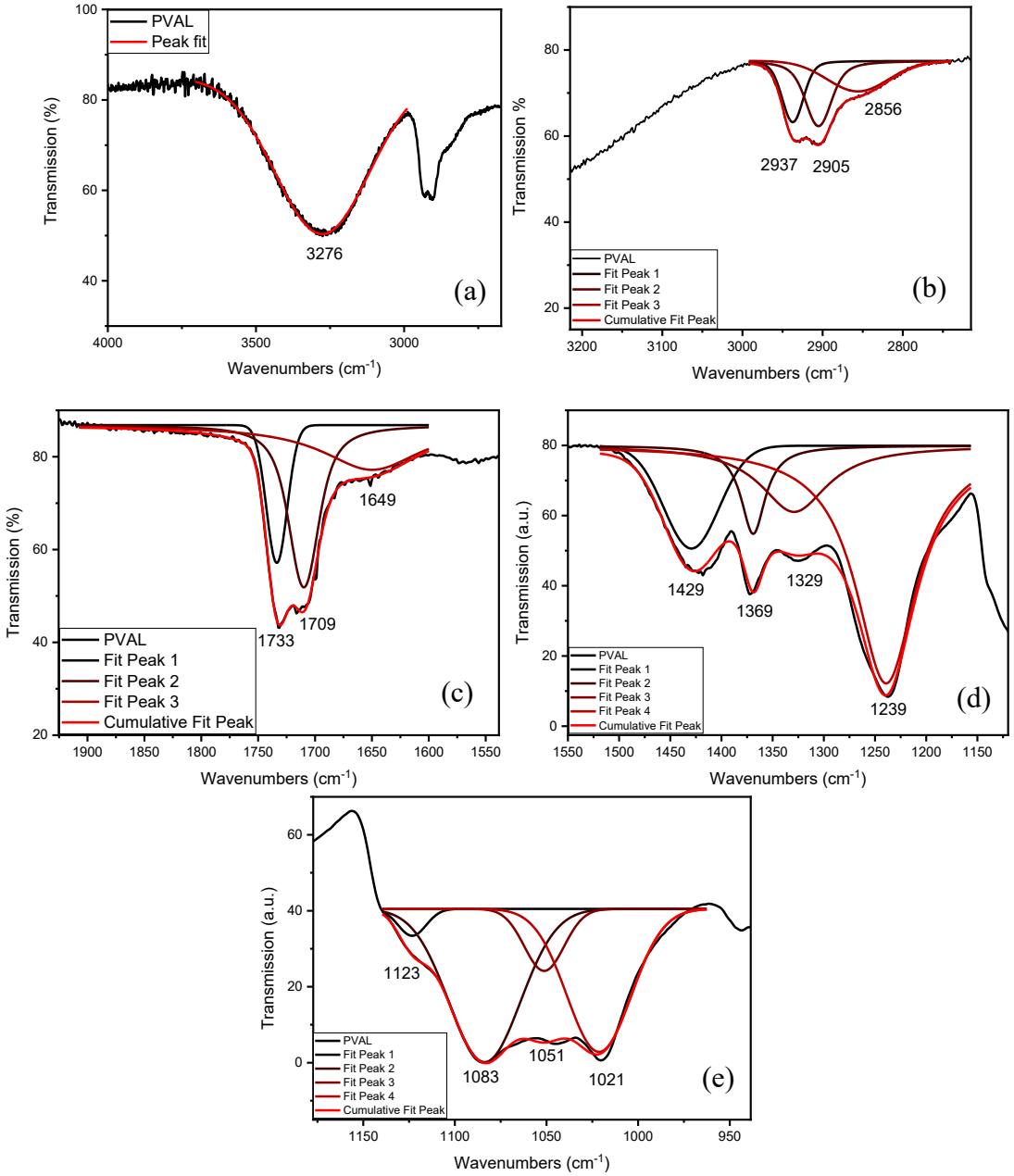


Figure 92: FTIR spectra peak fitting of PVAL at different regions of the spectrum: (a) O-H stretching, (b) C-H stretching, (c) C=O stretching, (d) C-H stretching, and (e) C-O and C-O-C stretching.

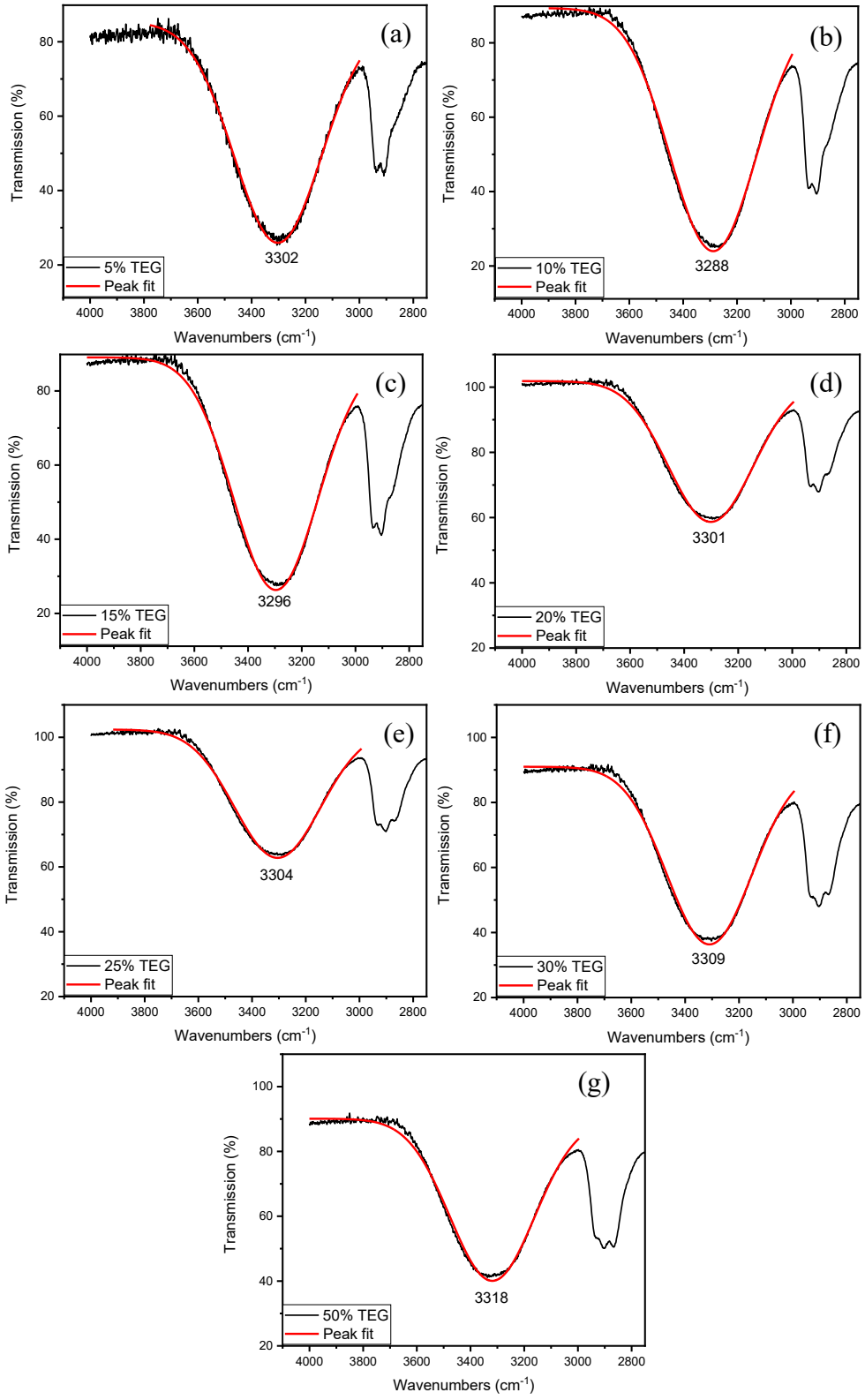


Figure 93: FTIR spectra peak fitting of PVAL/TEG blends for the O-H stretching band. (a) 5 wt.% TEG, (b) 10 wt.% TEG, (c) 15 wt.% TEG, (d) 20 wt.% TEG, (e) 25 wt.% TEG, (f) 30 wt.% TEG, and (g) 50 wt.% TEG in PVAL.

Appendix C

Raman peak fitting between 100 and 700 cm^{-1}

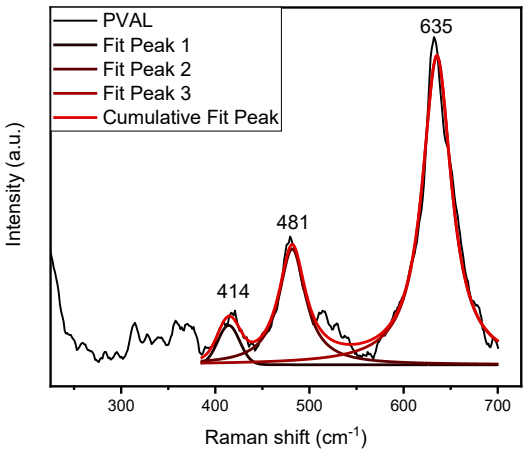


Figure 94: Raman spectra peak fitting of PVAL in the region between 100 and 700 cm-1

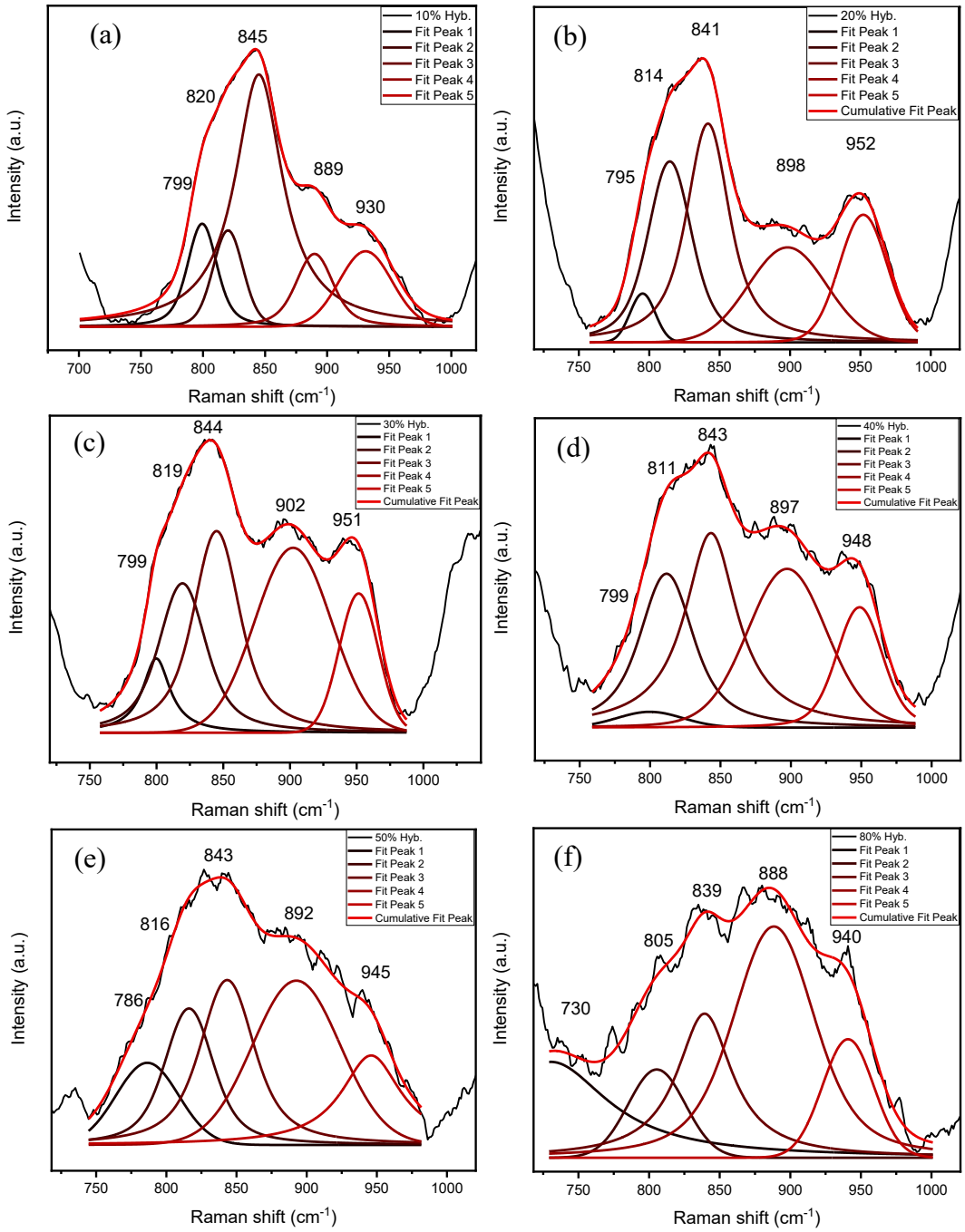


Figure 95: Raman spectra peak fitting of PVAL/titanium oxide hydrate hybrid film of different compositions at the C-C stretching region. (a) 10 vol.%, (b) 20 vol.%, (c) 30 vol.%, (d) 40 vol.%, (e) 50 vol.%, and (f) 80 vol.% titanium oxide hydrate in PVAL.

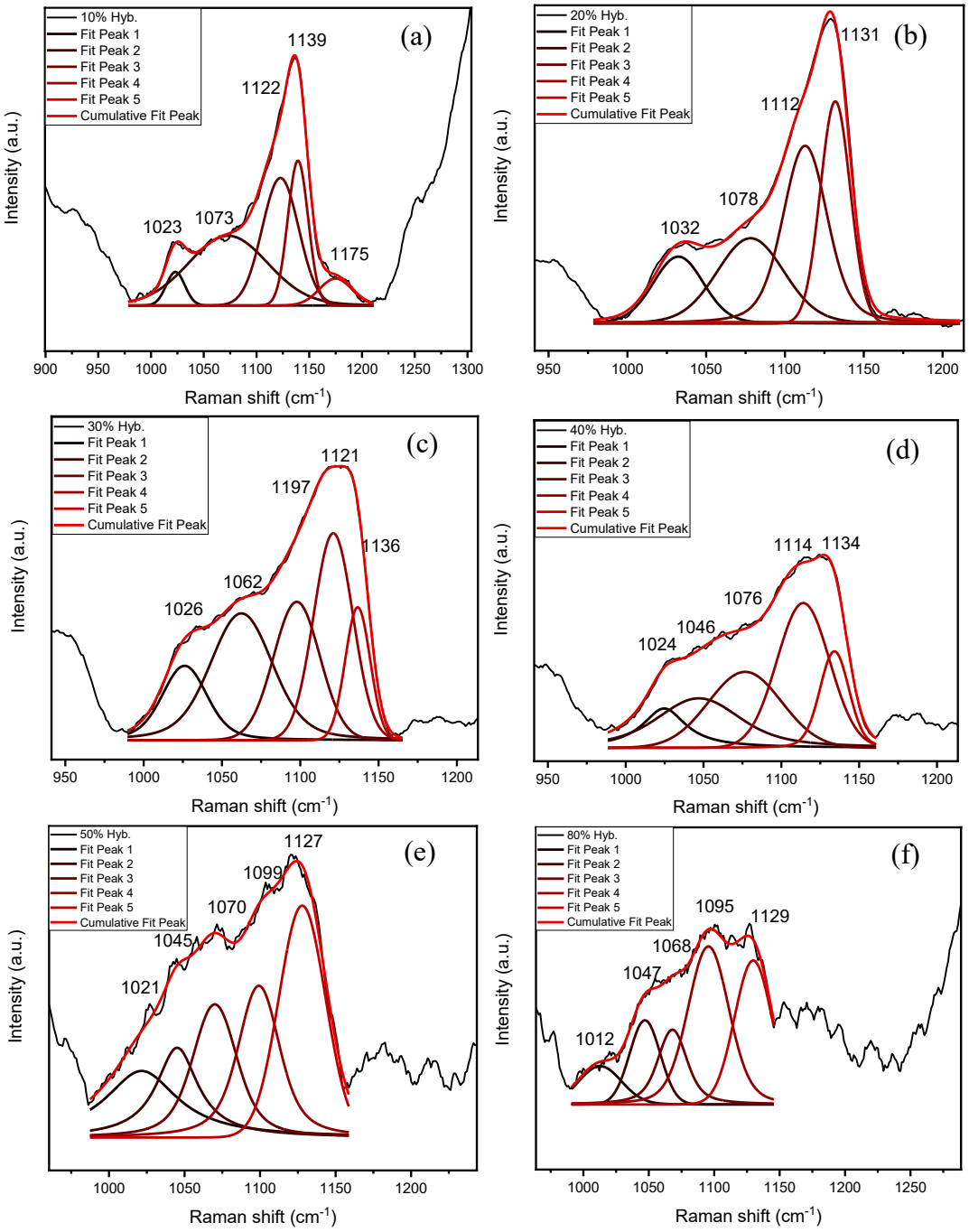


Figure 96: Raman spectra peak fitting of PVAL/titanium oxide hydrate hybrid film of different compositions at the C-O stretching and O-H bending region. (a) 10 vol.%, (b) 20 vol.%, (c) 30 vol.%, (d) 40 vol.%, (e) 50 vol.%, and (f) 80 vol.% titanium oxide hydrate in PVAL.

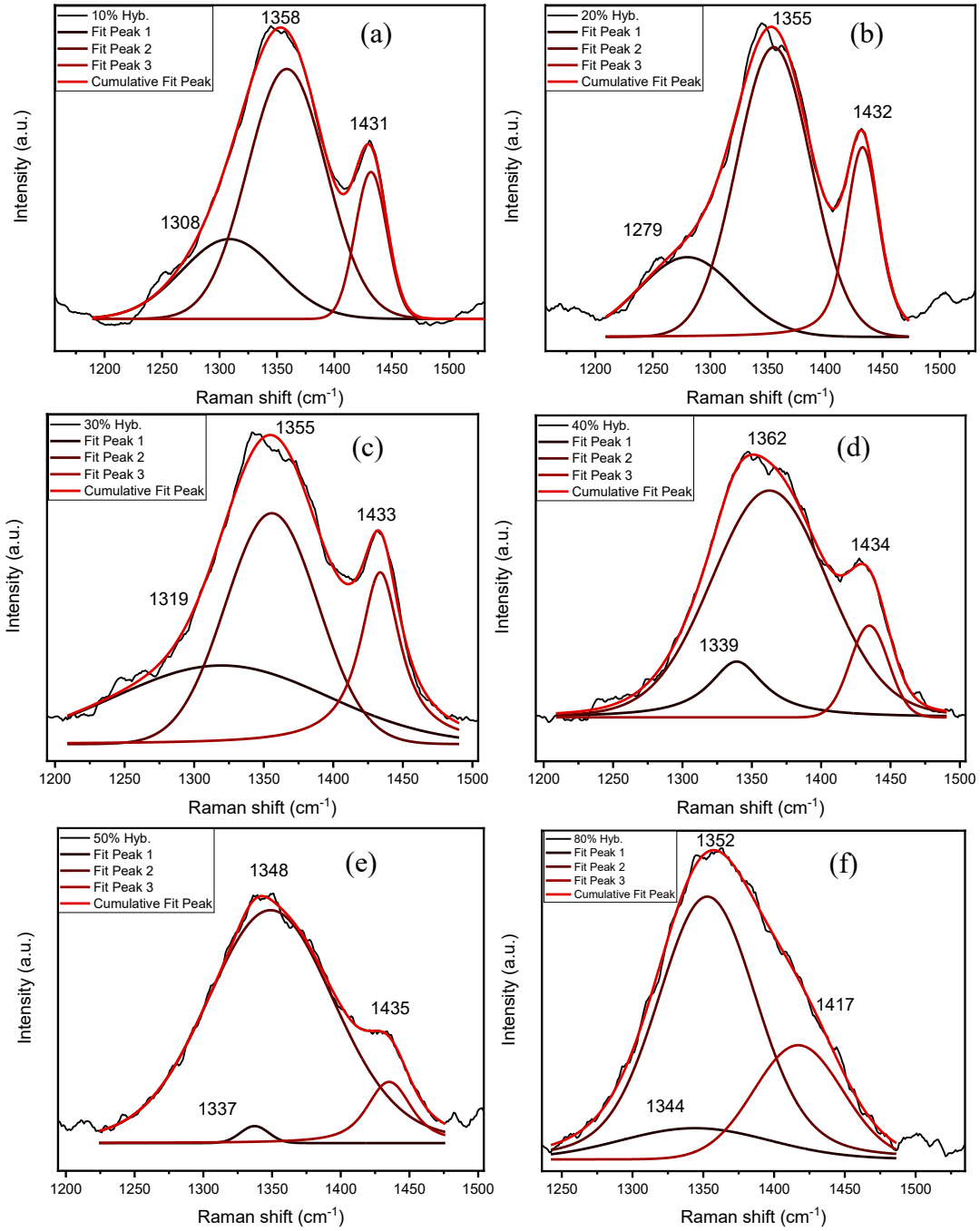


Figure 97: Raman spectra peak fitting of PVAL/titanium oxide hydrate hybrid film of different compositions at the C-H and O-H bending region. (a) 10 vol.%, (b) 20 vol.%, (c) 30 vol.%, (d) 40 vol.%, (e) 50 vol.%, and (f) 80 vol.% titanium oxide hydrate in PVAL.

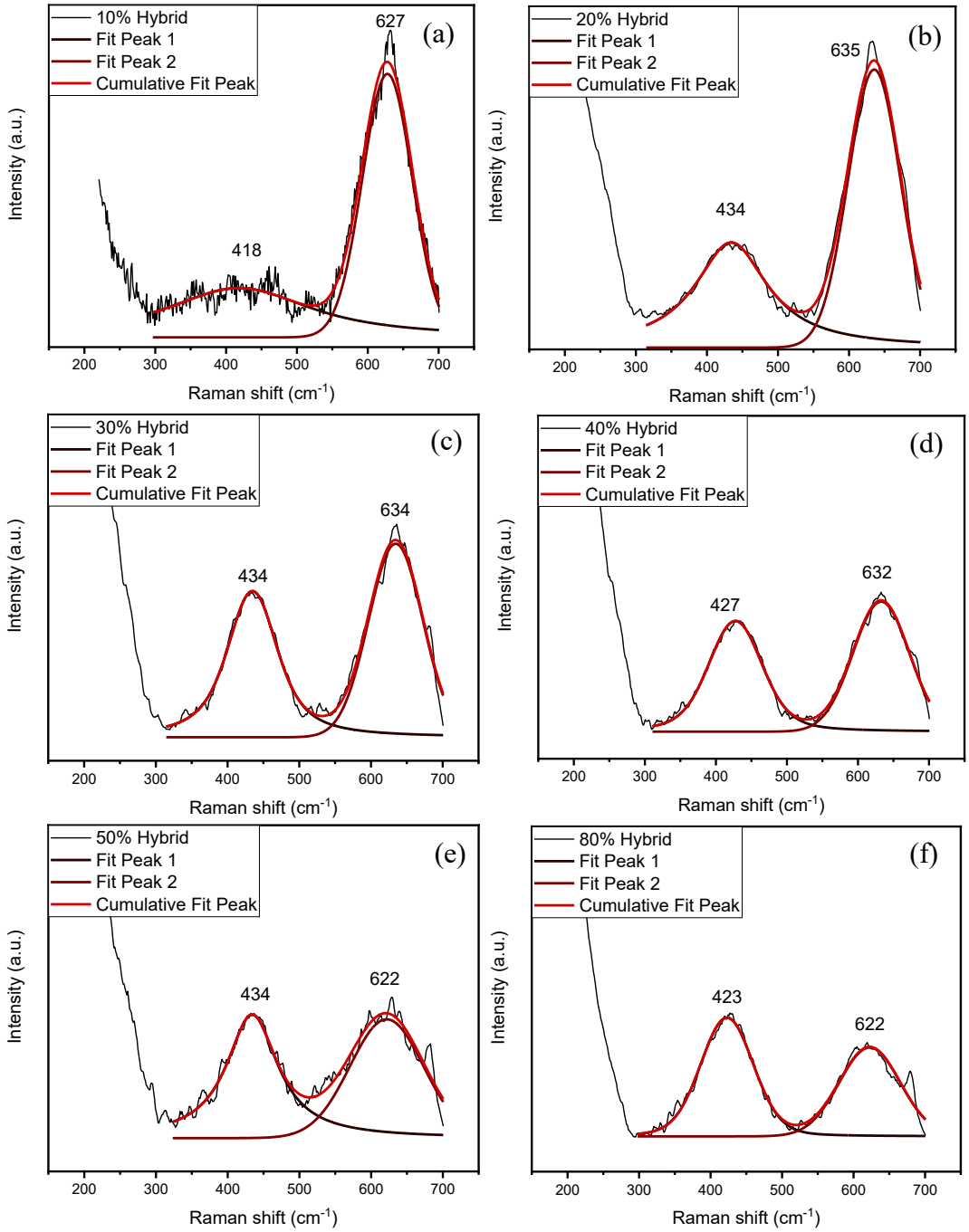


Figure 98: Raman spectra peak fitting of PVAL/titanium oxide hydrate hybrid film of different compositions between 300 and 700 cm^{-1}. (a) 10 vol.%, (b) 20 vol.%, (c) 30 vol.%, (d) 40 vol.%, (e) 50 vol.%, and (f) 80 vol.% titanium oxide hydrate in PVAL.

Table 18: Raman peak fitting statistics for PVAL/titanium oxide hydrate hybrid film of different compositions at the C-C stretching region.

Sample	Reduced Chi	R squared
PVAL	0.00148	0.9993
10% Hybrid	0.00938	0.98306
20% Hybrid	0.00414	0.99768
30% Hybrid	0.00801	0.9975
40% Hybrid	0.00877	0.99475
50% Hybrid	0.0122	0.9919
80% Hybrid	0.07765	0.98045

Table 19: Raman peak fitting statistics PVAL/ titanium oxide hydrate hybrid film of different compositions at the C-O stretching and O-H bending region.

Sample	Reduced Chi	R squared
PVAL	0.00065	0.99785
10% Hybrid	0.00107	0.99746
20% Hybrid	0.02644	0.99771
30% Hybrid	0.00808	0.99927
40% Hybrid	0.01087	0.99779
50% Hybrid	0.01065	0.99115
80% Hybrid	0.01451	0.99162

Table 20: Raman peak fitting statistics for PVAL/ titanium oxide hydrate hybrid film of different compositions at the C-H bending and O-H bending region.

Sample	Reduced Chi	R squared
PVAL	0.00405	0.99934
10% Hybrid	0.01627	0.99543
20% Hybrid	0.057256	0.99532
30% Hybrid	0.07331	0.99441
40% Hybrid	0.03219	0.99733
50% Hybrid	0.019	0.99779
80% Hybrid	0.07551	0.998

Table 21: Raman peak fitting statistics for PVAL/ titanium oxide hydrate hybrid film of different compositions at the between 300 and 700 cm^{-1}.

Sample	Reduced χ	R squared
PVAL	**0.94423**	**0.97841**
10% Hybrid	**1.6467**	**0.98069**
20% Hybrid	**0.86302**	**0.98989**
30% Hybrid	**0.754**	**0.98341**
40% Hybrid	**0.2847**	**0.98736**
50% Hybrid	**0.99058**	**0.93829**
80% Hybrid	**0.50678**	**0.97027**

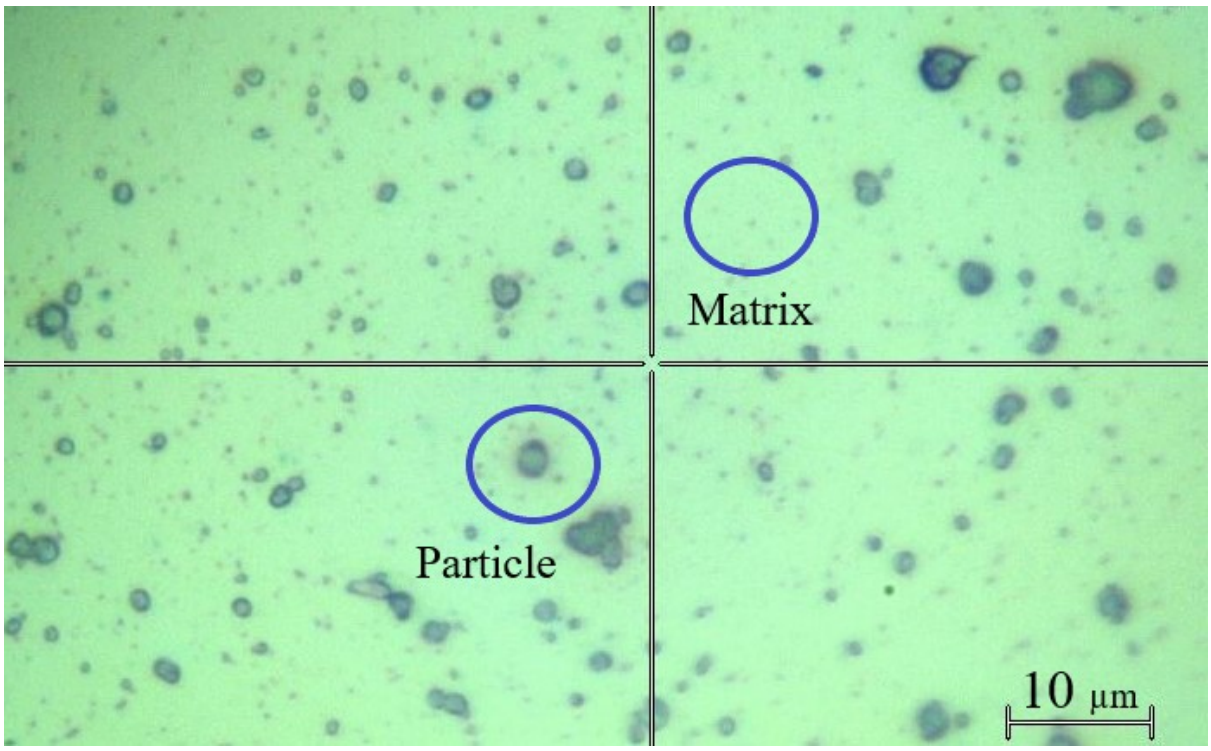


Figure 99: Optical micrograph taken using Raman microscope of PVAL – TiO_2 composite. Points where it was considered to be predominantly the matrix or particle are indicated.

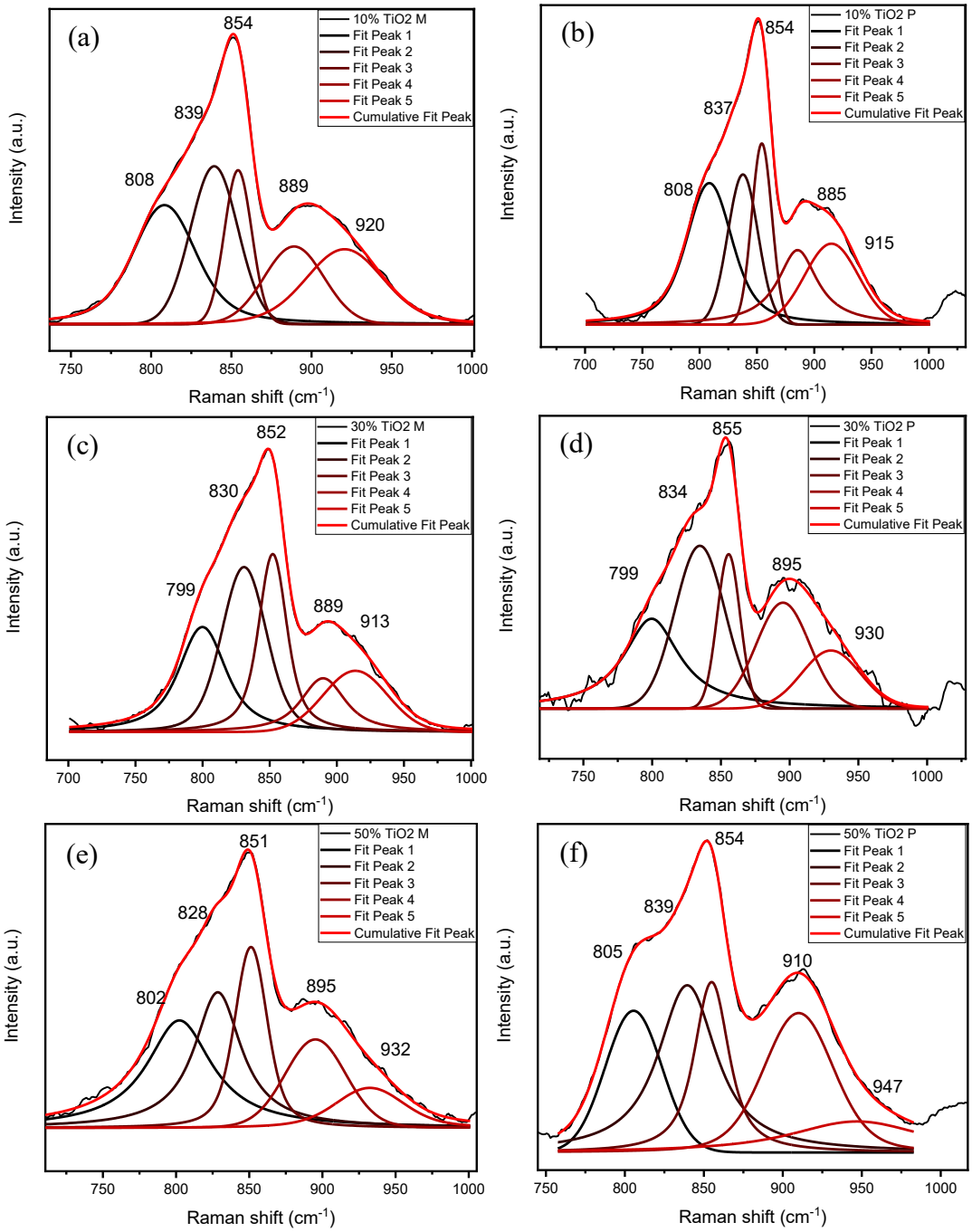


Figure 100: Raman spectra peak fits for PVAL - TiO2 composites of different compositions and taken where matrix "M" or particle "P" were observed in the C-C stretching region. (a) 10% TiO2/PVAL M, (b) 10% TiO2/PVAL P, (c) 30% TiO2/PVAL M, (d) 30% TiO2/PVAL P, (e) 50% TiO_2/PVAL M, and (f) 50% TiO_2/PVAL P.

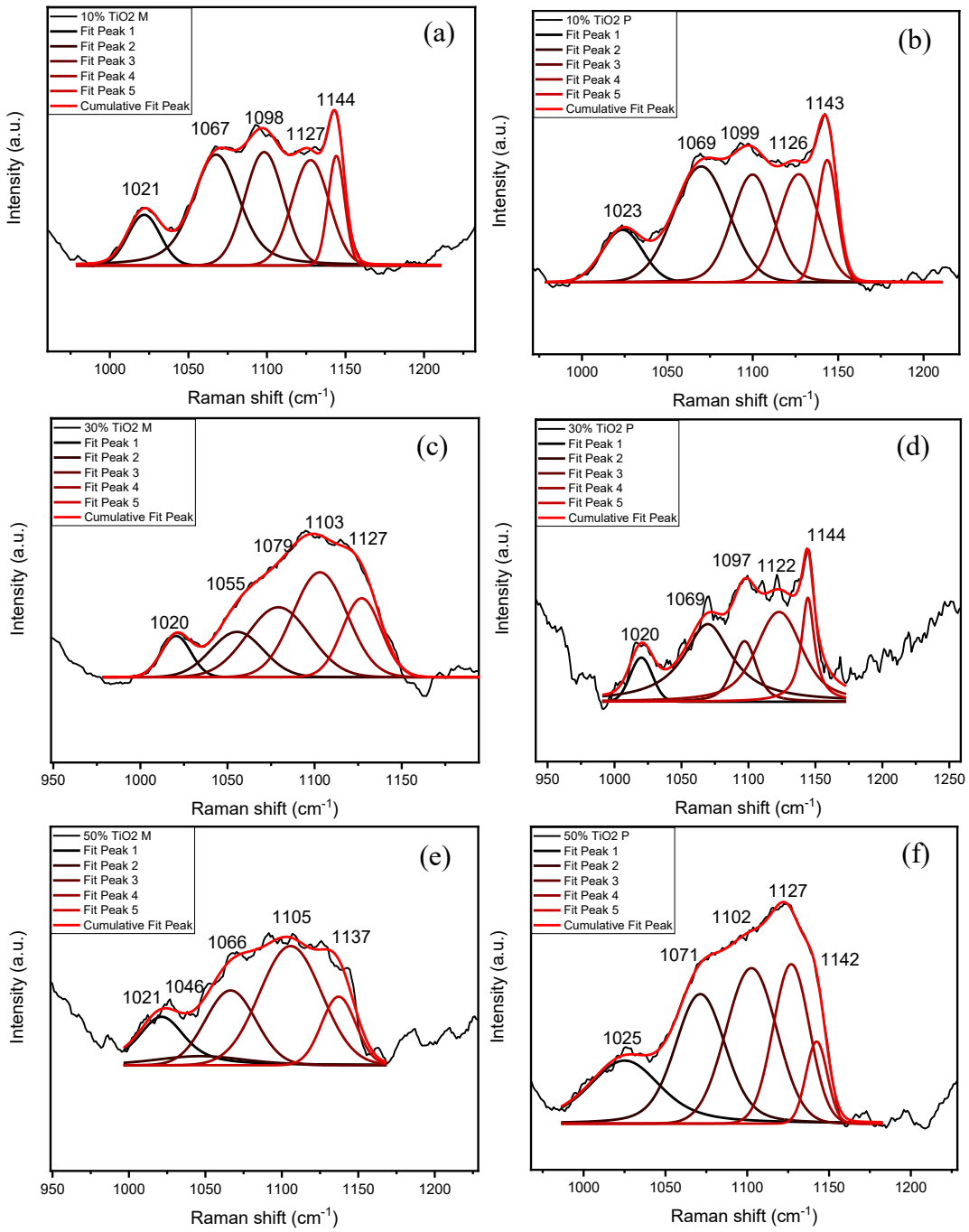


Figure 101: Raman spectra peak fits for PVAL - TiO2 composites of different compositions and taken where matrix "M" or particle "P" were observed in the C-O stretching and O-H bending region. (a) 10% TiO2/PVAL M, (b) 10% TiO2/PVAL P, (c) 30% TiO2/PVAL M, (d) 30% TiO2/PVAL P, (e) 50% TiO_2/PVAL M, and (f) 50% TiO_2/PVAL P.

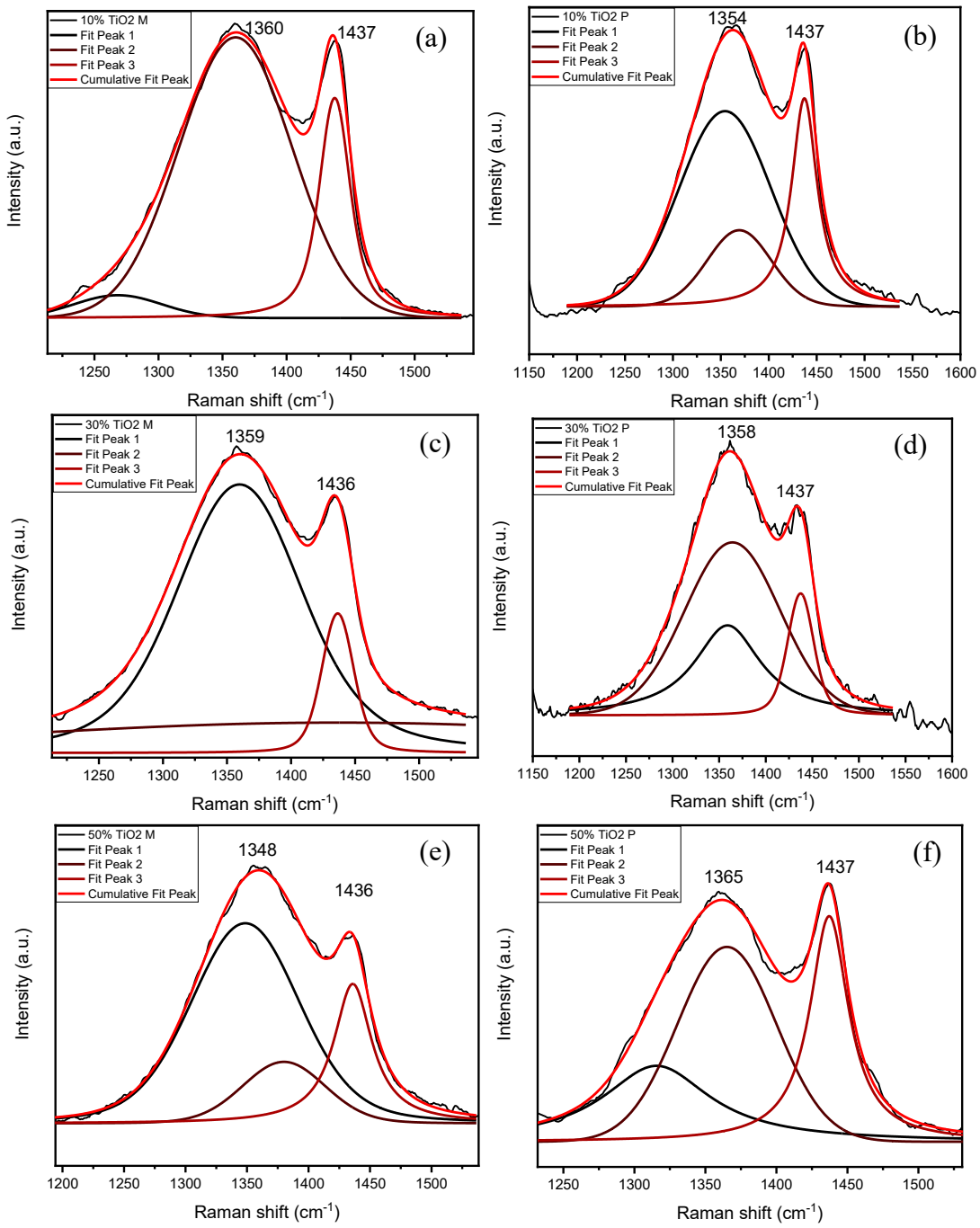


Figure 102: Raman spectra peak fits for PVAL - TiO2 composites of different compositions and taken where matrix "M" or particle "P" were observed in the C-O stretching and O-H bending region. (a) 10% TiO2/PVAL M, (b) 10% TiO2/PVAL P, (c) 30% TiO2/PVAL M, (d) 30% TiO2/PVAL P, (e) 50% TiO_2/PVAL M, and (f) 50% TiO_2/PVAL P.

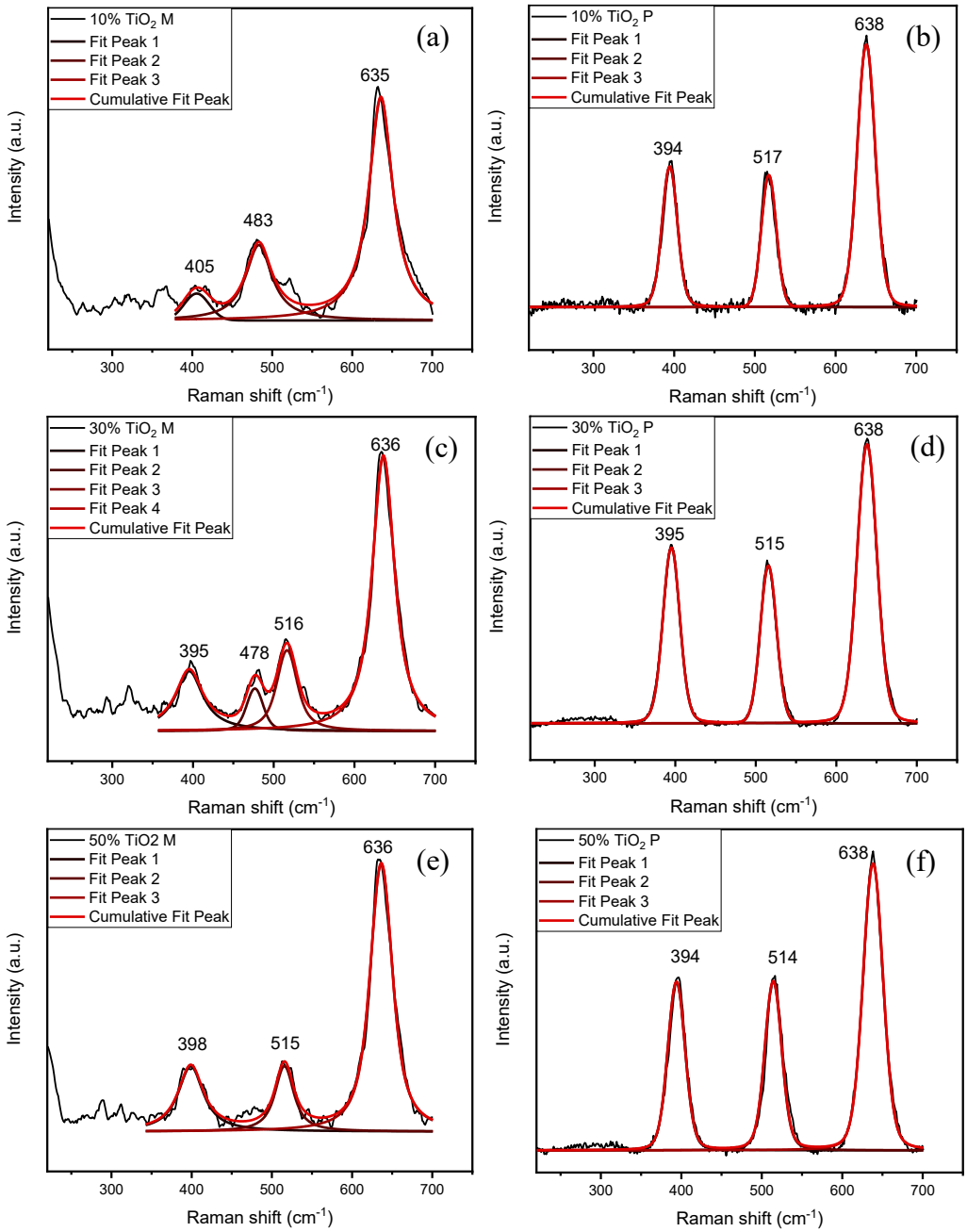


Figure 103: Raman spectra peak fits for PVAL - TiO_2 composites of different compositions and taken where matrix "M" or particle "P" were observed between 300 and 700 cm^{-1}. (a) 10% TiO_2/PVAL M, (b) 10% TiO_2/PVAL P, (c) 30% TiO_2/PVAL M, (d) 30% TiO_2/PVAL P, (e) 50% TiO_2/PVAL M, and (f) 50% TiO_2/PVAL P.

Table 22: Raman peak fitting statistics for PVAL - TiO_2 composites of different compositions at the C-C stretching region.

Sample	Reduced χ	R squared
PVAL	0.00148	0.9993
10% TiO_2 M	0.00212	0.99936
10% TiO_2 P	0.00872	0.99672
30% TiO_2 M	0.00164	0.99927
30% TiO_2 P	0.01582	0.98888
50% TiO_2 M	0.00228	0.99852
50% TiO_2 P	0.00731	0.99909

Table 23: Raman peak fitting statistics PVAL - TiO_2 composites of different compositions at the C-O stretching and O-H bending region.

Sample	Reduced χ	R squared
PVAL	0.00065	0.99785
10% TiO_2 M	0.00244	0.99424
10% TiO_2 P	0.00223	0.99385
30% TiO_2 M	0.00366	0.98727
30% TiO_2 P	0.00613	0.96794
50% TiO_2 M	0.00296	0.97265
50% TiO_2 P	0.00548	0.99739

Table 24: Raman peak fitting statistics for PVAL - TiO_2 composites of different compositions at the C-H bending and O-H bending region.

Sample	Reduced χ	R squared
PVAL	0.00405	0.99934
10% TiO_2 M	0.01826	0.99718
10% TiO_2 P	0.2144	0.99702
30% TiO_2 M	0.00498	0.99908
30% TiO_2 P	0.01661	0.99695
50% TiO_2 M	0.00735	0.99853
50% TiO_2 P	0.00557	0.99634

Table 25: Raman peak fitting statistics for PVAL – TiO_2 composites of different compositions between 300 and 700 cm^{-1}.

Sample	Reduced χ	R squared
PVAL	0.94423	0.97841
10% TiO_2 M	0.78712	0.97323
10% TiO_2 P	0.01599	0.99243
30% TiO_2 M	0.05259	0.98848
30% TiO_2 P	0.00906	0.99709
50% TiO_2 M	0.05091	0.98802
50% TiO_2 P	0.04251	0.99201

Appendix D

PVAL / Boric acid XPS

PVAL / Boric acid films were prepared from solution by spin coating. Measured as in the PVAL / titanium oxide hydrate hybrids. It is noted in Figure 104 that the C-OH peak is reduced in intensity with increasing inorganic content signifying that the hydroxyl group was used to create covalent bonds with the boric acid species similar to what was observed in the PVAL / titanium oxide hydrate hybrids. Figure 105 shows the O1s part of the spectra of the same films. A new peak attributed to B-O is only apparent with the 50 wt.% H_3BO_3/PVAL film and a slight shift of binding energy in the C-O peak is observed.

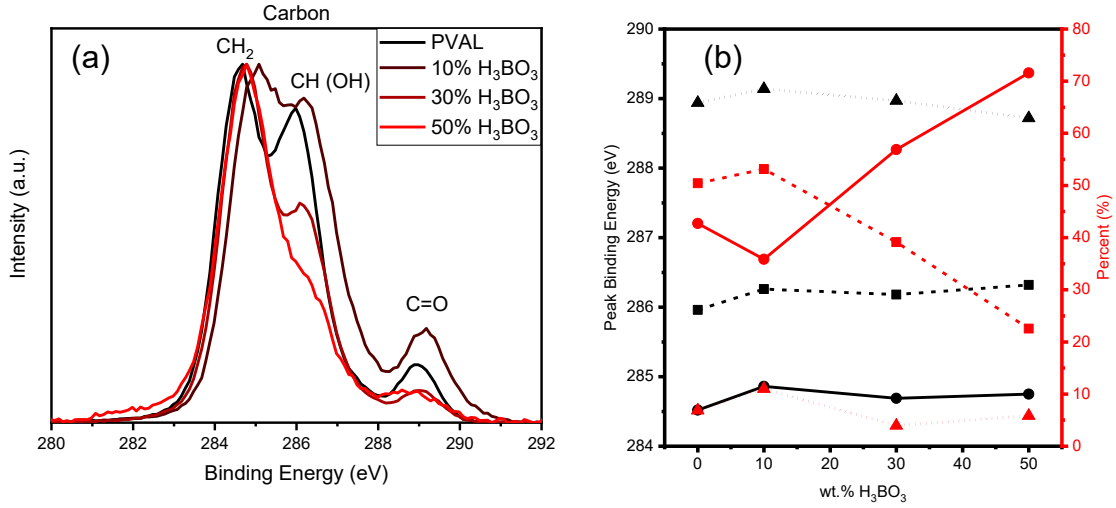


Figure 104: XPS spectra of PVAL / boric acid films focusing on the C1s region (a). A comparison of the carbon peak intensity is presented in (b) as a function of inorganic content.

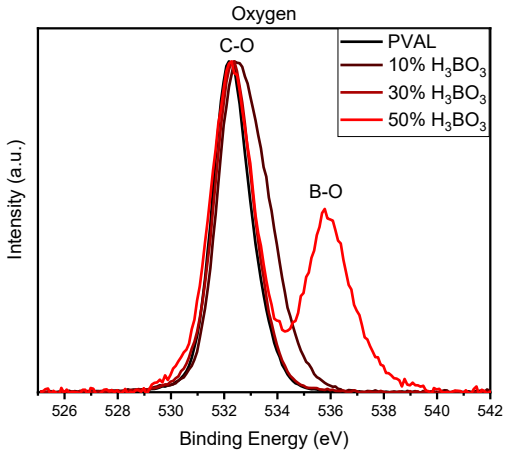


Figure 105: XPS spectra of PVAL / boric acid films focusing on the C1s region.

* Thank you to Alex Balzer, Department of Chemical and Bimolecular Engineering, Georgia Institute of Technology, GA, USA, for the of PVAL / boric acid film preparation and XPS measurements.

Appendix E

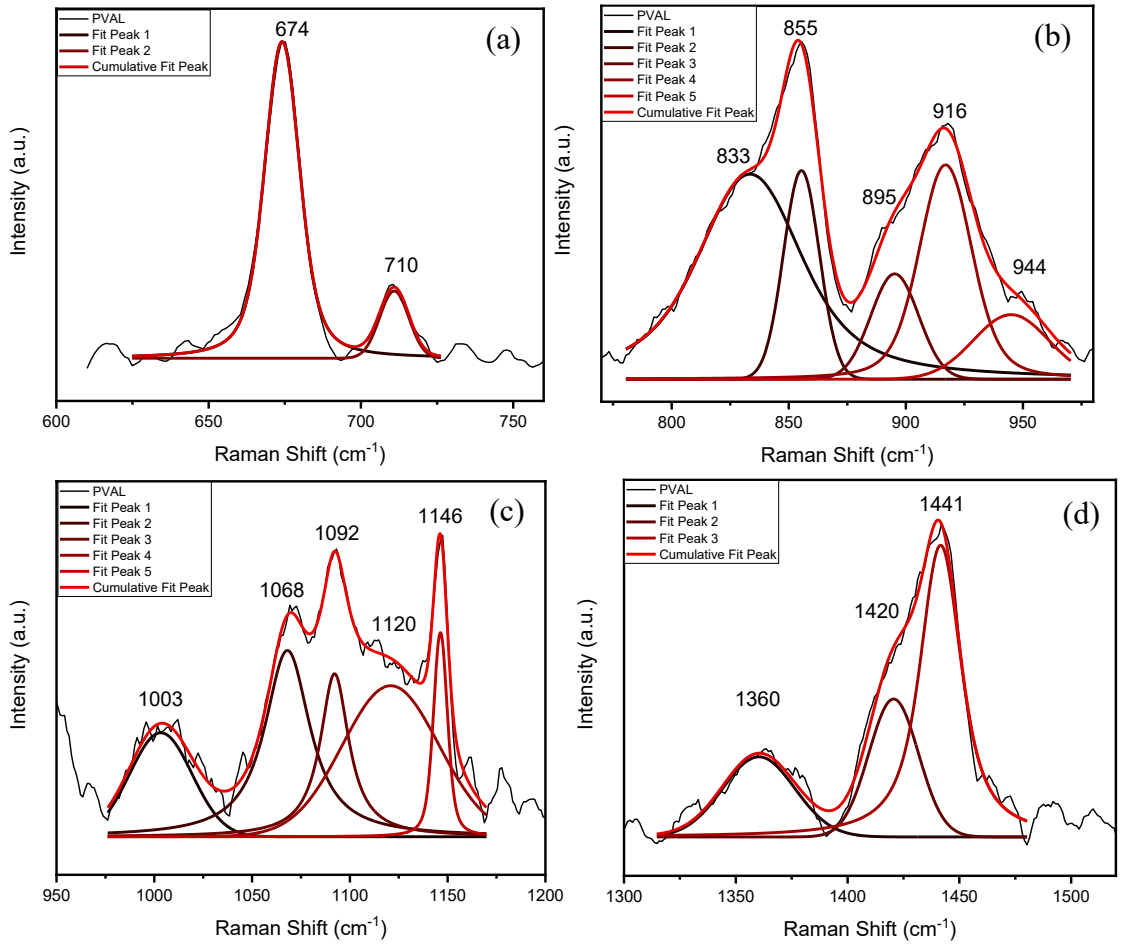


Figure 106: Raman spectra peak fitting of neat PVAL films 99% hydrolysed at different regions: (a) C-S stretching, (b) C-C stretching, (c) C-O stretching and O-H bending, (d) C-H and O-H bending .Peak assignments are used in Chapter 5.

Table 26: Raman peak fitting statistics for PVAL 99% hydrolysed at different regions of the spectrum

Sample	Reduced χ	R squared
PVAL (625 - 725 cm^{-1})	0.00148	0.9993
PVAL (750 -1000 cm^{-1})	0.00212	0.99936
PVAL (1000-1200 cm^{-1})	0.00872	0.99672
PVAL (1300 - 1500 cm^{-1})	0.00164	0.99927

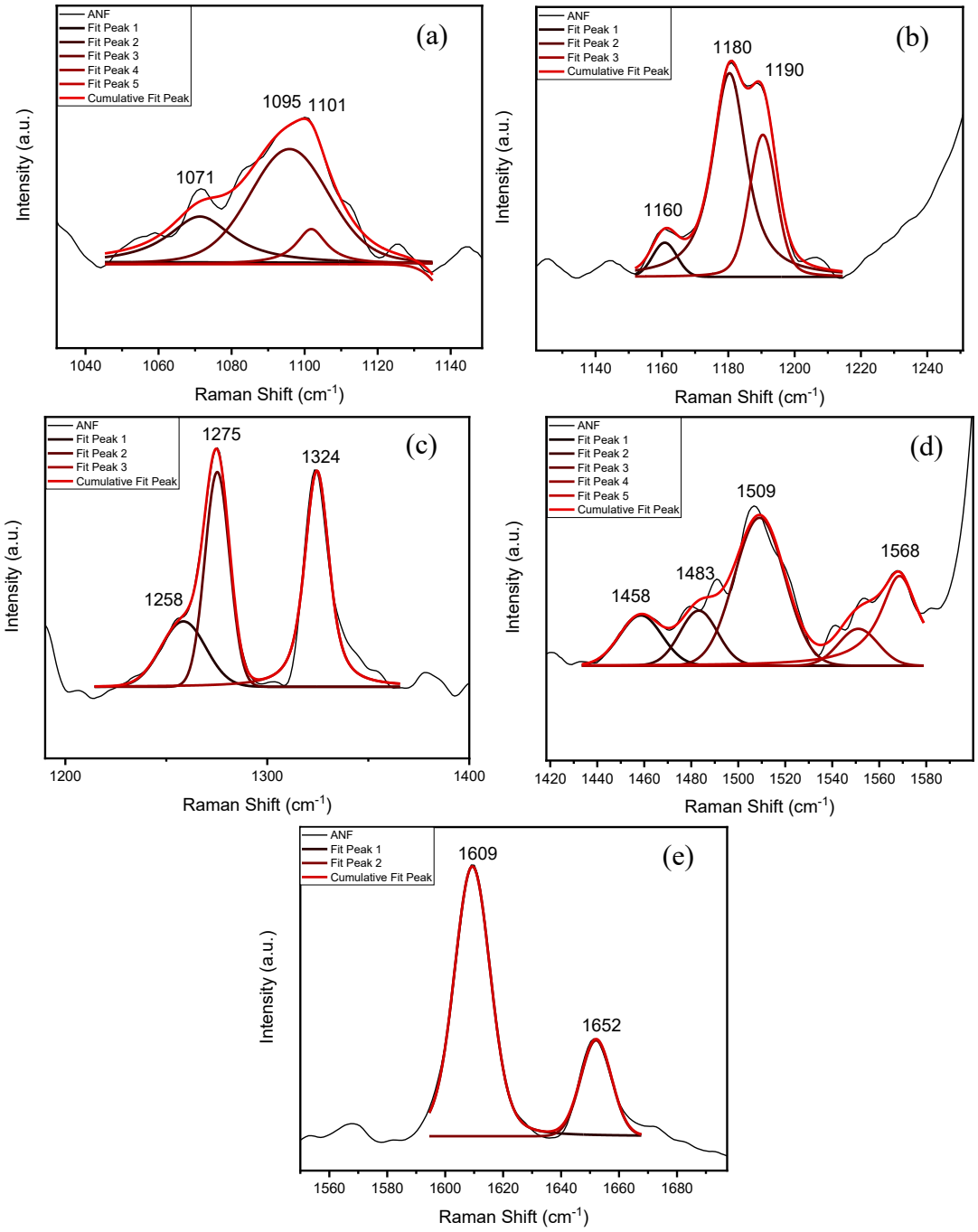


Figure 107: Raman spectra peak fitting of neat ANF at different regions: (a) C-H bending, (b) C-C ring stretching, (c) C-C ring stretching and C-H in-plane bending, (d) C-C ring stretching and N-H bending and C-N stretching, (e) C-C ring stretching C=O stretching, C-N stretching, and N-H bending.

Table 27: Raman peak fitting statistics for PVAL 99% hydrolysed at different regions of the spectrum

Sample	Reduced χ	R squared
ANF (1040-1140 cm^{-1})	0.29242	0.97902
ANF (1140-1220 cm^{-1})	0.18126	0.9975
ANF (1200-1375 cm^{-1})	6.05667	0.98418
ANF (1420 – 1580 cm^{-1})	1.00974	0.96868
ANF (1560 – 1680 cm^{-1})	2.31735	0.99687

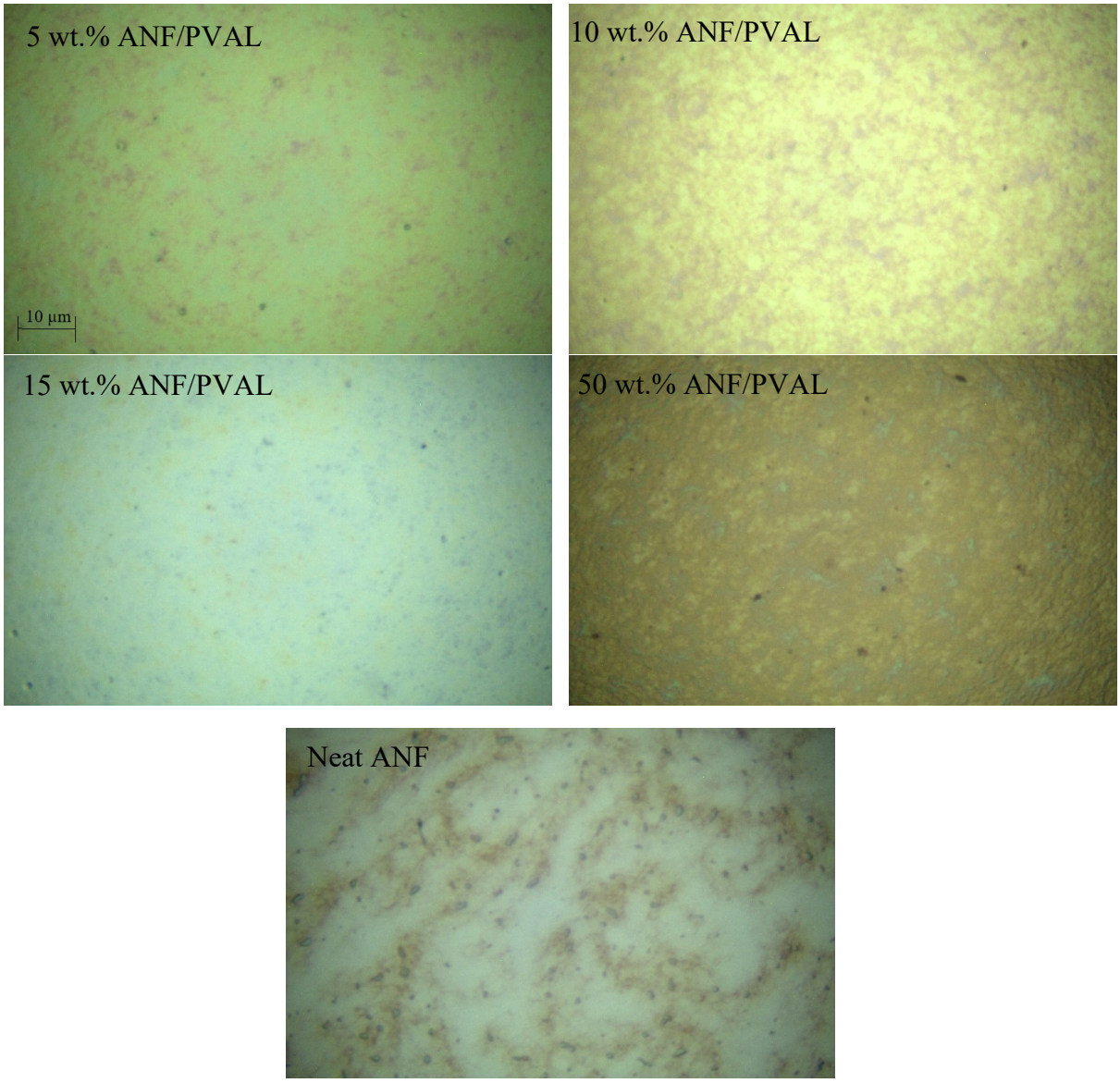


Figure 108: Optical micrographs of PVAL/ANF composite films with different concentrations. Images taken using Raman microscope lens with 100x objective.

Talks, Posters, and Prizes

Talks

Chain Morphology Effect on Thermal Conductivity of Polymer-Based Materials. November 2018, MRS 2018 Fall Meeting, Boston, MA, USA.

Posters

- *Chain Morphology Effect on Thermal Conductivity of Polymer-Based Materials,* March 2019, Interfaces in Organic and Hybrid Thin-Film Optoelectronics Conference INFORM 19, Valencia, Spain.
- *Chain Morphology Effect on Thermal Conductivity of Polymer-Based Materials,* March 2019, Imperial College London – Materials Postgraduate Research Day, London, U.K.
- *Chain Morphology Effect on Thermal Conductivity of Polymer-Based Materials,* July 2019, Imperial College London – Functional Materials Theme, PhD Student Day, London, U.K.

Prizes

1st Prize for Best scientific content for a poster, March 2019, Imperial College London – Materials Postgraduate Research Day, London, U.K.